



Theses and Dissertations

---

2005-08-12

## Effects of Pressure on Coal Pyrolysis at High Heating Rates and Char Combustion

Dong Zeng  
*Brigham Young University - Provo*

Follow this and additional works at: <https://scholarsarchive.byu.edu/etd>



Part of the [Chemical Engineering Commons](#)

---

### BYU ScholarsArchive Citation

Zeng, Dong, "Effects of Pressure on Coal Pyrolysis at High Heating Rates and Char Combustion" (2005). *Theses and Dissertations*. 659.

<https://scholarsarchive.byu.edu/etd/659>

This Dissertation is brought to you for free and open access by BYU ScholarsArchive. It has been accepted for inclusion in Theses and Dissertations by an authorized administrator of BYU ScholarsArchive. For more information, please contact [scholarsarchive@byu.edu](mailto:scholarsarchive@byu.edu), [ellen\\_amatangelo@byu.edu](mailto:ellen_amatangelo@byu.edu).

EFFECTS OF PRESSURE ON COAL PYROLYSIS AT HIGH HEATING RATES  
AND CHAR COMBUSTION

by  
Dong Zeng

A dissertation submitted to the faculty of  
Brigham Young University  
in partial fulfillment of the requirements for the degree of  
Doctor of Philosophy

Department of Chemical Engineering  
Brigham Young University  
Decemeber 2005

BRIGHAM YOUNG UNIVERSITY

GRADUATE COMMITTEE APPROVAL

of a dissertation submitted by

Dong Zeng

This dissertation has been read by each member of the following graduate committee and by a majority votes has been found satisfactory.

\_\_\_\_\_

Date

\_\_\_\_\_

Thomas H. Fletcher, Chair

\_\_\_\_\_

Date

\_\_\_\_\_

Merrill W. Beckstead

\_\_\_\_\_

Date

\_\_\_\_\_

William C. Hecker

\_\_\_\_\_

Date

\_\_\_\_\_

John L. Oscarson

\_\_\_\_\_

Date

\_\_\_\_\_

Dale R. Tree

BRIGHAM YOUNG UNIVERSITY

As chair of the candidate's graduate committee, I have read the dissertation of Dong Zeng is in its final form and have found that (1) its format, citations, and bibliographical style are consistent and acceptable and fulfill university requirements; (2) its illustrative materials including figures, tables, and charts are in place; and (3) the final manuscript is satisfactory to the graduate committee and is ready for submission to the university library.

---

Date

---

Thomas H. Fletcher  
Chair, Graduate Committee

Accepted for the Department

---

William G. Pitt  
Graduate Coordinator

Accepted for the College

---

Alan R. Parkinson  
Dean, Ira A. Fulton College of Engineering  
and Technology

## ABSTRACT

### EFFECTS OF PRESSURE ON COAL PYROLYSIS AT HIGH HEATING RATES AND CHAR COMBUSTION

Dong Zeng

Department of Chemical Engineering

Doctor of Philosophy

Clean coal technologies are now becoming popular because of their high efficiencies and minimal environmental impact. Higher operating pressures have been applied to clean coal technologies. The effect of pressure on coal pyrolysis and char combustion has been extensively studied but still remains to be further explored. The objective of this project was to characterize high pressure, high heating rate coal pyrolysis and char combustion, with emphasis on improving coal/char high pressure combustion models.

A flat-flame burner was used in a high pressure laminar flow facility to conduct high temperature, high heating rate pyrolysis and combustion experiments for four coals. The high-heating-rate ( $10^5$  K/s), high-temperature atmosphere can better simulate industrial conditions than the conventional drop tube facility. Pressure and heating rate have a significant impact on the total volatiles, char physical structure including morphology, and char internal surface areas. The high heating rate decreases the swelling ratios of chars at pressures from 2.5 to 15 atm. TGA char oxidation reactivities were measured at the same total pressure as the char preparation pressure. The general trend was that the TGA reactivity on a gram per gram available basis decreased with increasing char formation pressure. When the reactivity was normalized by either the  $N_2$  or  $CO_2$  surface area, the normalized reactivity was found to be relatively constant with increasing pressure.

Char burnout was measured at different pressures and  $O_2$  concentrations at high temperature in the pressurized flat flame burner facility. For a given pressure, the particle diameter ratio based on coal ( $d/d_{coal,0}$ ) decreased with increasing  $O_2$  concentration. Two char kinetic models (CBK 8 and CBK/E) were used to fit the char burnout data, and the modeling results showed that the intrinsic char oxidation rate increased with increasing total pressure at constant oxygen partial pressure.

## ACKNOWLEDGMENTS

I would like to thank my academic advisor, Dr. Thomas H. Fletcher, for his support, for guiding me to think scientifically, for inspiring me to design a good experiment, for helping me come to my own conclusions. I have learned many things through his conduct and leadership. I would like to thank Dr. William C. Hecker for providing many ideas for this research. I gratefully acknowledge Dr. Robert Hurt at Brown University for providing the source code of the CBK model. Thanks to US Department of Energy through the DOE/UCR program for sponsoring this project.

I would like to thank those who helped me in preparing and performing experiments, namely Todd Gunderson, Michael Clark, Brent Crenshaw, and Lee Reynolds; this project could not be finished without their help. I would like to thank my parents for their support and encouragement throughout my education, and my master advisor Prof. Song Cai at Southeast University of China, who brought me into combustion research area. And most importantly, I would like to thank my wife Yuan Gao for her patience, concern, and support.

## Table of Contents

List of Tables .....	x
List of Figures .....	xii
Nomenclature .....	xvi
Glossary .....	xx
1. Introduction.....	vi
2. Literature Review .....	3
2.1 Effects of Pressure on Coal Devolatilization and Resulting Char Properties ...	3
2.1.1 Effects of Pressure on Coal Devolatilization.....	4
2.1.1.1 TGA Reactor.....	4
2.1.1.2 Wire-Mesh Reactor.....	5
2.1.1.3 Drop-Tube Reactor .....	6
2.1.2 Effects of Pressure on Resulting Char Physical Properties .....	8
2.1.3 Effects of Pressure on Resulting Char Reactivity.....	15
2.2 Effects of Reaction Pressure on Char Combustion Kinetics.....	16
2.3 Mechanism of Char Oxidation .....	20
2.3.1 The Three-Zone Theory.....	20
2.3.2 Semi-Global Intrinsic Kinetics for Char Combustion Modeling.....	23
2.3.3 Pore Diffusion and Effectiveness Factor .....	34
2.4 Summary .....	38
3. Objectives and Approach.....	41
4. Description of Experiments .....	45
4.1 High-Pressure Facility at BYU.....	45
4.1.1 Review of Char Oxidation Facilities.....	46
4.1.2 BYU HPDT Reactor .....	48
4.1.3 High Pressure Flat-Flame Burner (HPFFB) Reaction System .....	52



4.1.4	High Pressure Thermogravimetric Analyzer (HPTGA) .....	55
4.2	Coal Selection.....	57
4.3	Sample Preparation and Characterization .....	58
4.3.1	Coal Preparation.....	58
4.3.2	Proximate Analysis .....	59
4.3.3	Ultimate Analysis.....	60
4.3.4	Tracer Analysis to Calculate Mass Release.....	61
4.3.5	Apparent Density .....	62
4.3.6	Specific Surface Area Measurements .....	62
4.3.7	Scanning Electron Microscope (SEM) Analysis .....	64
5.	Coal Pyrolysis and Resulting Char Properties.....	65
5.1	Coal Characterization .....	65
5.2	Reaction Conditions for the Pyrolysis Experiments.....	66
5.3	Mass Release during Coal Pyrolysis .....	69
5.4	Elemental Composition of Chars Prepared at Different Pressures.....	73
5.5	Effects of Pressure on Coal Swelling Ratios.....	76
5.6	Effects of Pressure on Char Morphology .....	81
5.7	Char Surface Area .....	89
5.8	Summary of Coal Pyrolysis and Resulting Char Properties.....	90
6.	Intrinsic Reactivity of Char Formed at Elevated Pressure.....	93
6.1	Conditions of TGA Combustion Tests.....	93
6.1.1	Char Preparation .....	93
6.1.2	HPTGA Test Procedure .....	94
6.1.3	Kinetic Analysis.....	95
6.2	Results and Discussion.....	99
6.2.1	Char Intrinsic Reactivity.....	99
6.2.2	Discussion of TGA Reactivities.....	105
6.2.3	Activation Energy and Oxygen Order in the N-th Order Kinetic Rate Expression.....	107
6.2.4	The Relationship between Surface Area and Char Reactivity.....	109
6.3	Summary of Intrinsic Reactivities of Char Formed at Different Pressures...	112

7.	Elevated Pressure, High Temperature Coal Oxidation Experiments and Modeling	115
7.1	Conditions of Combustion Tests .....	115
7.1.1	Experimental Conditions .....	115
7.1.2	Gas Temperature Profile .....	116
7.2	Experimental Results and Discussion .....	118
7.2.1	Variations in Char Burnout during Combustion .....	118
7.2.2	Variations in Char N <sub>2</sub> BET Surface Area during Combustion .....	120
7.2.3	Variations in Char d/d <sub>0</sub> Ratio during Combustion .....	122
7.3	High Temperature Char Combustion Modeling .....	123
7.3.1	Modeling of Gas and Particle Temperature Profiles .....	123
7.3.2	Modeling of Char Combustion Process using n-th Order Kinetic Expressions .....	127
7.3.3	Modeling of Char Combustion Process using 3-Step Kinetics .....	134
7.3.4	Discussion of Modeling Results of High Temperature Char Oxidation .....	138
7.4	Summary of High Temperature Char Combustion Experimental and Modeling Results .....	142
8.	Summary and Conclusions .....	145
8.1	Accomplishments .....	145
8.2	Summary of Results .....	147
8.2.1	Effects of Pressure on Char Properties .....	147
8.2.2	Effects of Pressure on Char Intrinsic Reactivity .....	148
8.2.3	Effects of Pressure on High Temperature Char Characteristics .....	149
8.2.4	The Modeling of High-Temperature Char Combustion .....	150
8.3	Principal Conclusions .....	151
8.4	Limitations and Recommendations .....	152
	References .....	155
	Appendices .....	165
Appendix A:	Temperature Correction .....	167
Appendix B:	Operation Procedure of HPFFB .....	171
Appendix C:	Experimental Pyrolysis and Combustion Conditions .....	175
Appendix D:	Tabulation of Experimental Data of High-pressure Pyrolysis .....	177

Appendix E:	Tabulation of Experimental Data of High-temperature Combustion .	181
Appendix F:	Gas Field Simulations for HPFFB Tests.....	189
Appendix G:	Detailed HPTGA Tests Results .....	197
Appendix H:	Additional HPTGA Tests Results.....	211
Appendix I:	Sample CPD Model Input Files .....	217
Appendix J:	Sample CBK Model Input Files.....	219

## List of Tables

Table 2.1 Comparison of Experimental Conditions for Two Pressurized Drop Tube Experiments .....	11
Table 2.2 Char Classification System.....	13
Table 2.3 Test Conditions for Various High Pressure Oxidation Rate Measurements.....	17
Table 2.4 Global and Semi-Global Mechanisms and Corresponding Rate Laws.....	24
Table 2.5 Summary of Controlling Mechanisms and Rate Expressions for Each Temperature Range .....	32
Table 5.1 Characteristics of Coals .....	66
Table 5.2 Coal Structure Parameters Used in CPD Modeling.....	71
Table 5.3 Comparisons of Experimental Conditions.....	78
Table 6.1 Matrix of Experiments in the HPTGA.....	95
Table 6.2. Effects of Pressure on Resulting Char Reactivities .....	106
Table 6.3 Activation Energies and Oxygen Orders of Pitt #8 Coal Chars .....	108
Table 6.4 Activation Energies and Oxygen Orders of Ill #6 Coal Chars .....	108
Table 7.1 Matrix of Coal Oxidation Experiments <sup>a</sup> .....	116
Table 7.2 Gas Flow Rates Used in the HPFFB.....	117
Table 7.3 Pre-exponential Factor (A) Used in CBK8.....	130
Table 7.4 Relative Error between Calculations and Measured Values of Mass Release Using the CBK8 Model .....	132
Table 7.5 Kinetic Parameters Used in CBK/E.....	135
Table 7.6 Relative Error between Calculations and Measured Values of Mass Release Using the CBK/E Model.....	137



## List of Figures

Figure 2.1. Published results for total volatile yields as a function of pressure. ....	8
Figure 2.2. Swelling vs. heating rate at 1 atm.....	10
Figure 2.3. Effect of total pressure on oxygen order (left) and activation energy (right) of the NDL and Pitt 8 char reactivity.....	20
Figure 2.4. Rate-controlling zones for heterogeneous char oxidation.....	22
Figure 2.5. The effectiveness factor curves for first order and zero-th order reactions in Cartesian Coordinates.....	37
Figure 4.1. Schematic of high pressure drop tube reactor. ....	49
Figure 4.2. Schematic of drop tube reactor sample collection configuration.....	50
Figure 4.3. Measured gas temperature profiles in the HPDT. ....	52
Figure 4.4. Schematic of the HPFFB.....	53
Figure 4.5. Schematic of the high pressure flat flame burner flow system. ....	55
Figure 4.6. Schematic of the DMT high pressure Thermogravimetric Analyzer. ....	56
Figure 4.7. Parent coal compositions plotted on a coalification diagram.....	58
Figure 5.1. Measured gas temperature profiles in the HPFFB.. ....	68
Figure 5.2. Calculated early particle temperature histories for the different pressure conditions in the HPFFB.....	69
Figure 5.3. Measured mass release due to pyrolysis for chars obtained at different pressures. ....	71
Figure 5.4. Predicted and measured mass release as a function of pressure.....	72
Figure 5.5. Elemental compositions of chars as a function of pressure.....	74
Figure 5.6. Hydrogen content in the chars after pyrolysis as a function of pressure (left) and fraction of the initial amount of nitrogen that remains in the char (right).75	

Figure 5.7. Fraction of initial nitrogen remaining in the char ( $m_{N,char}/m_{N,coal}$ ) after pyrolysis as a function of pressure.....	76
Figure 5.8. Apparent densities for chars prepared in the HPFFB.....	77
Figure 5.9. Swelling ratios of four coal chars as a function of preparation pressure.....	77
Figure 5.10. Comparison of swelling ratio in the HPFFB with other studies.....	78
Figure 5.11. SEM micrograph of char produced from pyrolysis of Pitt #8 coal and Knife River Lignite.....	83
Figure 5.12. SEM micrograph of char cross section produced from pyrolysis of Pitt #8 coal.....	84
Figure 5.13. SEM micrograph of char cross section produced from pyrolysis of Knife River Lignite.....	85
Figure 5.14. SEM micrograph of char produced from pyrolysis of Ken #9 coal. ..	86
Figure 5.15. SEM micrograph of char cross section produced from pyrolysis of Ken #9 coal.....	87
Figure 5.16. The proposed mechanism of char structure evolution by Yu et al. ....	88
Figure 5.17. Surface area of chars prepared at different pressures.....	90
Figure 6.1. Measured and fitted data set obtained from a HPTGA test.....	96
Figure 6.2. Char oxidation reactivity normalized by $m_{avail}$ as a function of burnout.....	96
Figure 6.3. Char oxidation reactivity per initial mass as a function of burnout .....	97
Figure 6.4. Pitt #8 char oxidation reactivity as a function of burnout and total pressure.....	100
Figure 6.5. Ill #6 char oxidation reactivity as a function of burnout and total pressure.....	100
Figure 6.6. KRL char oxidation reactivity as a function of burnout and total pressure.....	101
Figure 6.7. Pitt #8 char oxidation reactivity as a function of burnout and total pressure.....	102
Figure 6.8. Char HPTGA reactivity vs. Burnout and $P_{tot}$ , Char: Pitt #8 10 atm. ....	104
Figure 6.9. Ill #6 char reactivity and normalized reactivity.....	110
Figure 6.10. Pitt #8 Char reactivity and normalized reactivity.....	111

Figure 6.11. KRL char reactivity and normalized reactivity. ....	111
Figure 7.1. Measured gas temperature profiles in the HPFFB at different pressures and oxygen concentrations. ....	117
Figure 7.2. Measured mass release of Pitt #8 coal (90-125 $\mu$ m) during combustion experiments at different pressures and O <sub>2</sub> concentrations.....	118
Figure 7.3. Measured mass release of Pitt #8 coal (63-76 $\mu$ m) during combustion experiments at different pressures and O <sub>2</sub> concentrations.....	119
Figure 7.4. Measured mass release of Ill #6 coal (short reaction distance) during combustion experiments at different pressures and O <sub>2</sub> concentrations. ....	119
Figure 7.5. Measured mass release of Ill #6 coal (long reaction distance) during combustion experiments at different pressures and O <sub>2</sub> concentrations. ....	120
Figure 7.6. Nitrogen surface areas of char particles during combustion experiments at different pressures and O <sub>2</sub> concentrations. ....	121
Figure 7.7. Diameter ratios of char particles (d/d <sub>coal</sub> ) during combustion experiments at different pressures and O <sub>2</sub> concentrations. ....	123
Figure 7.8. Diameter ratios of char particles (d/d <sub>char</sub> ) during combustion experiments at different pressures and O <sub>2</sub> concentrations. ....	124
Figure 7.9. Geometry and particle trajectory used in the FLUENT calculations. ..	125
Figure 7.10. Measured and predicted centerline gas temperature profiles for Pitt #8 coal at 6 atm.....	126
Figure 7.11. Predicted centerline particle velocity profiles for Pitt #8 coal. ....	127
Figure 7.12. Comparison of swelling ratios of Benfell's model and measured swelling ratios during devolatilization. ....	129
Figure 7.13. Modeled burnouts using of CBK8 versus measured burnouts for the four combustion conditions.....	131
Figure 7.14. Modeled Activation Energy (E) determined from best fits of the data at different pressures.....	132
Figure 7.15. Comparison of Modeled Activation Energy (E) from CBK 8 with measured Activation Energy (E) from HPTGA experiments. ....	133



Figure 7.16. Predicted burnouts using CBK/E versus measured burnouts for the  
four combustion conditions..... 137

Figure 7.17. Best-fit values of  $A_{30}$  for the four combustion conditions. .... 138

## Nomenclature

<u>Variable</u>	<u>Definition</u>
$A$	Pre-exponential factor
$A$	Surface area, $\text{m}^2 \text{g}^{-1}$
$B$	Blowing factor $\left( c_{pg} \left( -\frac{dm_p}{dt} \right) / (2\pi d_p k_g) \right)$
$C$	Carbon mass fraction.
CBK	Carbon Burnout Kinetics model
CPD	Chemical Percolation Devolatilization model
$c_0$	Initial char bridge fraction, used in CPD model
$c_{og}$	Bulk stream oxygen concentration
$c_p$	Heat capacity, $\text{J g}^{-1} \text{K}^{-1}$
$D_e$	The effective diffusivity.
$d$	Diameter, m
daf	Dry, ash-free basis
$E$	Activation energy, kcal/mol
$E_{obs}$	Observed activation energy
$E_0$	Energy of adsorption of the standard adsorbate
$f_c$	The correction function for effectiveness factors.
$H$	Hydrogen mass fraction.
$\Delta H_{pyr}$	Heat of pyrolysis, $\text{J g}^{-1}$

$h$	Convective heat transfer coefficient, $\text{W m}^{-2} \text{K}^{-1}$
$K$	Kinetic parameter used in Langmuir rate equation
$k$	kinetic parameters
$k_g$	Thermal conductivity of gas, $\text{W m}^{-1} \text{K}^{-1}$
$L$	Characteristic length
MW	Molecular weight.
$m$	Mass, g
$m$	Intrinsic (true) reaction order
$N$	The total number of oxides
$N_{av}$	Avogadro's number
$n$	The reaction order in the n-th order rate equation
$n$	Number of records
$M_T$	Thiele module.
$M_\delta$	Molecular weight per side chain, used in CPD model.
$MR$	Mass release.
$N$	Nitrogen mass fraction.
$Nu$	Nusselt number
$O$	Oxygen mass fraction.
$P$	Pressure.
$p_0$	Initial fraction of attachments that are bridges, used in CPD model
$p_i^p$	burnout prediction for the $i^{\text{th}}$ record
$p_i^0$	measured burnout value
$R$	Ideal gas constant $8.314 \text{ J/mol-K}$
$S$	Sulfur mass fraction.
$S_{int}$	Particle interior surface area
$S_{ext}$	Particle exterior surface area

$SC$	The total carbon site density
$S_w$	Swelling ratio
$T$	Temperature
$V$	Volume
$V_m$	monolayer volume,
$R$	Reaction rate.
$r''_{normalized}$	Char oxidation rate normalized by internal surface area (Eq. 3), $\text{g m}^{-2} \text{s}^{-1}$
$r_{intrinsic}$	Intrinsic char oxidation rate, $\text{g g}_{avail}^{-1} \text{s}^{-1}$
$Sw$	Swelling ratio.
$T$	Temperature, K
$t$	Time, s
$v$	Velocity, $\text{m s}^{-1}$
$\nu_0$	The stoichiometric coefficient of oxygen.
$W$	Weight.
$z$	Axial distance, m
$\alpha$	Power index
$\beta$	similarity coefficient
$\eta$	Effectiveness factor
$\rho$	Particle density, $\text{g cm}^{-3}$
$\varepsilon$	Emissivity
$\varepsilon$	The second effectiveness factor
$\theta$	Fraction of sites.
$\sigma$	Stefan Boltzman constant
$\sigma+1$	Coordination number (i.e., attachments per cluster), used in CPD model

## Subscripts

A	Ash.
ads	Adsorption
avail	Available (instantaneous, rather than initial)
C	Carbon
<i>C</i>	Oxygen concentration, mol/m <sup>3</sup>
<i>cl</i>	Molecular weight per cluster, used in CPD model.
<i>daf</i>	Dry, ash free basis.
des	Desorption
f	Free site
g	Gas
in	Intrinsic
o	Initial
obs	Observed
<i>o<sub>s</sub></i>	External surface oxygen
p	Particle
<i>p<sub>0</sub></i>	Initial Particle
rxn	Reaction
Tot	Total
w	Wall

## Glossary

	Definition
CO <sub>2</sub> surface area	Internal surface area measured using CO <sub>2</sub> adsorption.
Coalification	The process of converting living biomass into coal.
Hydro-pyrolysis	A method of effecting the pyrolysis of a fuel by contacting it with hot hydrogen.
Inertinite	An organic component of coal that is inert, or partially inert, during coking processes.
Maceral	A maceral is a component of coal. The term is analogous to the term mineral, as applied to igneous or metamorphic rocks. Examples of macerals are inertinite, vitrinite and exinite.
Mesopore	Pore of intermediate size with width from 2 to 50 nm.
Macropore	Pore with width exceeding about 0.05 $\mu\text{m}$ or 50 nm.
Metaplast	The finite polymer fragments that remain in the condensed phase during pyrolysis.
Micropore	Pore with width not exceeding about 2.0 nm
N <sub>2</sub> surface area	Internal surface area measured using N <sub>2</sub> adsorption.
Oxyreactivity	Reaction rate of sample with oxygen.
Petrography	Description of rocks and their textures.
Steam reactivity	Reaction rate of sample with steam.
Vitrinite	Vitrinite is the most common and most important maceral group in bituminous coals. Vitrinite is considered a reactive maceral, burning readily during combustion and becoming fluid during carbonization.







# 1. Introduction

Clean coal technologies are now becoming popular because of their high efficiencies and minimal environmental impact. Several technologies, such as Integrated Gasification Combined Cycle (IGCC), Pressurized Fluidized Bed Combustor (PFBC) and Pulverised Coal Injection (PCI), have been identified as the most viable alternatives for the clean utilization of coal due to the use of combined cycles (Smoot, 1998; Smoot and Smith, 1985). These advanced clean coal technologies have gained increased technological and scientific interest over the last few decades. Higher operating pressures have been applied to these technologies, for example, 10-15 atm for PFBC, 15-25 atm for IGCC, and less than 5 atm for PCI. Operations at higher pressure will inherently result in an increase in coal throughput, a reduction in pollutant emissions, and an enhancement in the intensity of reaction (Harris and Patterson, 1995; Takematsu and Maude, 1991).

The effect of pressure on coal pyrolysis and char combustion has been extensively studied previously but many questions remain. Coal combustion is usually divided into two consecutive processes: pyrolysis and char combustion. The effect of pressure on these two processes is usually studied independently. However, it is well known that chars made at different pressures have different physical and chemical properties. There is therefore a need for high-pressure char reactivity data on chars produced at high pressure. One of major goals of this project is to determine the effect of pressure on coal

pyrolysis and char oxidation behavior. Reliable high-temperature, high-pressure coal oxidation data were obtained in this project. The ultimate goal was to improve a char oxidation model to satisfactorily describe char oxidation as a function of time, bulk oxygen concentration, and pressure.

A high-pressure flat-flame burner (HPFFB) was developed to conduct high-temperature, high heating rate coal pyrolysis and char combustion experiments at different total pressures. Char was formed at different pressures in the flat-flame reactor, and then oxidized in a high-pressure thermogravimetric analyzer (HPTGA). High-temperature char reactivity experiments were also performed in the HPFFB.

A char oxidation model called CBK (Char Burnout Kinetics) was used to analyze the experimental results and explore char oxidation kinetics. Kinetic parameters were fitted using an optimization technique.

## **2. Literature Review**

This literature review summarizes previous studies of coal devolatilization and char oxidation, with emphasis on issues related to the effects of total gas pressure. These include (1) effects of pressure on coal devolatilization and resulting char properties; (2) effects of reaction pressure on char combustion kinetics; and (3) the mechanism of char oxidation.

### **2.1 Effects of Pressure on Coal Devolatilization and Resulting Char Properties**

Coal pyrolysis at elevated pressure has been extensively investigated over the last few decades. Effects of pressure on coal devolatilization have been observed for different coal ranks over a wide range of operating conditions. This chapter will review three aspects, including effects of pressure on (1) coal devolatilization; (2) resulting char physical properties; and (3) resulting char low-temperature oxidation reactivities.

### 2.1.1 Effects of Pressure on Coal Devolatilization

Coal pyrolysis at elevated pressure is reviewed here for three categories of reactors: Thermogravimetric Analyzer (TGA), Wire-mesh, and Drop-tube reactors.

#### 2.1.1.1 TGA Reactor

The TGA provides the most precise measurements of mass release of reacting material. However, the technique used with this instrument suffers from disadvantages such as low operating temperatures and low heating rates ( $\sim 1$  K/s). Seebauer and Staudinger (1997) used a TGA to investigate the effects of pressure, particle size, and heating rate on coal pyrolysis. They indicated that the total volatile yield decreased with increasing pressure, with a significant decrease in tar yield and a slight increase in light gas yield with increasing pressure. The TGA experiment alone is insufficient to derive kinetic parameters for pyrolysis reactions due to (a) the low heating rate, and (b) large effects from the bed of particles. Sun et al. (1997) studied the pyrolysis of two Chinese coals (0.4-4 mm) as a function of pressure (1-13 atm) using a pressurized dual-chamber TGA with heating rates as low as 0.33 K/s. Their results showed that the total volatiles yield decreased with increasing pressure when temperature was above a certain temperature ( $560^{\circ}\text{C}$  for a Chinese bituminous coal and  $680^{\circ}\text{C}$  for a Chinese anthracite coal), while the total volatiles yields were almost independent of pressure at lower temperatures. Arendt and van Heek (1981) performed high-pressure pyrolysis for five German coals using a wire mesh reactor and TGA respectively, and found similar trends with respect to pressure.

### 2.1.1.2 Wire-Mesh Reactor

The electrical grid or wire mesh reactor has been widely applied to coal pyrolysis due to well-controlled heating rates. Anthony and Howard (1976) and Suuberg et al. (1979) showed that in 1,000K/s experiments with 30 sec hold, increasing pressure from  $10^{-4}$  to 69 atm reduced total volatile yield by roughly 5 wt% for lignite and 15 wt% for bituminous coal. Arendt and van Heek (1981) found that with increasing pressure, tar repolymerised and cracked more significantly, resulting in increased yields of char and hydrocarbon gases. Hydrogen was found to influence devolatilization significantly at increased pressures. Additional amounts of aromatic products were released by hydrogenation of coal itself, particularly between 773 and 973 K, and the yields of light products such as  $\text{CH}_4$  and  $\text{C}_2\text{H}_6$  increased significantly in these pressurized hydrogen atmosphere pyrolysis experiments.

Griffin et al. (1994) studied the effects of pressure (1-10 atm) and temperature (750-1230 K) on pyrolysis of pulverized Pittsburgh No. 8 bituminous coal under a helium atmosphere, using an electrical screen heater reactor at a heating rate of  $10^3$  K/s. They found that volatile yields decreased slightly with increasing pressure, the effect being more pronounced at higher temperature. Below 970 K, pressure had little effect on yields. This is similar to the results obtained by Anthony and Howard (1976) and Bautista (1986), who studied high pressure pyrolysis for four different coals using an electric grid reactor at heating rates from 100-10,000 K/s. They found that the weight loss of Pittsburgh coal decreased rapidly with increasing pressures of helium and hydrogen, up to an apparent limiting value at 10 atm. The decrease in weight loss with increasing pressure was attributed to diminishing tar yields, only slightly compensated by increasing gas yields.

The tar yields were identical in the inert and reducing atmospheres, so consistently higher gaseous yields under hydrogen resulted in the increased mass release. Cai et al. (1996) studied coal pyrolysis with a hydrogen pressure up to 70 atm in a wire-mesh pyrolysis reactor, with heating rates ranging from 1 to 5000 K/s. They observed an increase of total volatile yield with increasing H<sub>2</sub> pressure, while tar yields decreased. The degree of reduction in tar yields decreased with increasing pressure. Cai's results showed that the influence of pressure on volatiles yields and tar yields became more significant at higher temperatures.

#### 2.1.1.3 Drop-Tube Reactor

Lee et al. (1991) investigated the rapid pyrolysis behavior of a bituminous coal under rapid heating ( $10^3$ - $10^4$  K/s) and elevated pressure (up to 3.8 atm). They found that increasing pressure slowed the global release of volatiles, lowered the asymptotic volatile yields, and promoted secondary reactions of the volatiles, which reduced the tar yields and changed the gas yields. Fatemi (1987) investigated the effect of pressure on devolatilization of pulverised coal particles in an entrained flow reactor at temperatures up to 1373 K and pressures of 68 atm. The results showed that tar yield is affected by pressure, decreasing significantly with increasing pressure up to 13.8 atm. Weight loss and gas yield decreased with increasing pressure up to 13.8 atm. Above this pressure there was no significant effect. Yeasmin et al. (1999) studied the high-pressure devolatilization of brown coal using a pressurized drop tube furnace. The residence time of coal particles in the furnace was calibrated based on the effect of pressure and temperature. Partially devolatilized coal or char particles were collected using a collection tube, which was able to move up and down to control the residence time in the

furnace. Weight loss decreased with increasing pyrolysis pressure. In a recent study, Matsuoka et al. (2003) examined three Japanese coals using a drop tube reactor, with temperature ranging from 600 to 700°C. The effect of pressure was significant on CH<sub>4</sub> and C<sub>2</sub>-C<sub>6</sub> hydrocarbon fractions. The yields of CH<sub>4</sub> and CO<sub>2</sub> increased with increasing pressure, whereas C<sub>2</sub>-C<sub>6</sub> yields monotonically decreased with increasing pressure. Niksa et al. (2003) reviewed several published high-pressure coal devolatilization data, and evaluated these data using the FLASHCHAIN (Niksa, 1995) model. Manton et al. (2004) and Liu et al. (2004) performed coal pyrolysis experiments in a Pressurized Radiant Coal Flow Reactor (p-RCFR) at 0.1 and 1.0 Mpa. The detailed product distributions, which included major noncondensable gases, C1-C4 hydrocarbons, oils, CO, CO<sub>2</sub>, H<sub>2</sub>, H<sub>2</sub>O, fuel-N, tar-N, and char-N, were measured for the devolatilization of five coals during transient heating at a rate of 7000 K/s and two pressures at 0.1 and 1.0 Mpa.

#### 2.1.1.1 Summary

In summary, the effects of pressure on devolatilization behavior vary with coal rank, gas environment and operating conditions, and Figure 2.1 shows published data of total volatile yield with increasing pressure. General trends observed from experiments can be summarized as follows:

The total volatile and tar yields decrease with increasing pressure, tar yield being more distinctly dependent on pressure. The reduction in tar and total volatile yields appears to be most significant for bituminous coals, but less pronounced for lignite. The effect of pressure on tar and total volatile yields appears to be more pronounced at higher temperature. The effect of pressure on the tar and total volatile yields appears to be less pronounced at high pressure. With increasing pressure, tar molecular weights are lower.

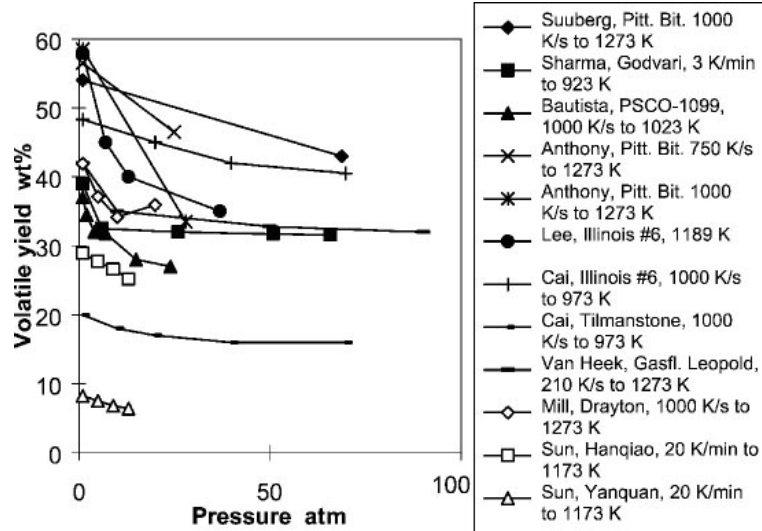


**Figure 2.1.** Published results for total volatile yields as a function of pressure. (Shan, 2000)

Although the effect of pressure on coal pyrolysis has been extensively studied, entrained flow high pressure coal pyrolysis research is still needed. TGA pyrolysis tests are limited by low temperature and low heating rate. Wire-mesh reactors have the drawback of interaction between coal particles and the wire mesh. Many current drop tube reactors can not achieve high temperatures ( $>1200\text{ }^{\circ}\text{C}$ ) at high pressure, and the article heating rates typically only reaches  $10^4\text{ K/s}$  compared to  $10^6\text{ K/s}$  in industrial facilities. A high-pressure flat flame burner was therefore developed in this study to overcome these problems.

### 2.1.2 Effects of Pressure on Resulting Char Physical Properties

Coal devolatilization affects the combustion performance of pulverized fuel boilers in many different ways. Two primary characteristics of the coal devolatilization



process are (a) the amount of mass released as volatile matter, and (b) the heating value of the pyrolysis products. Coal mass release during devolatilization has been discussed in section 2.1.1. The coal devolatilization also influences the properties of the remaining char. The physical structure of char subsequent to devolatilization (i.e. diameter, internal surface area, pore size, and porosity) greatly affects the rate of char oxidation. This section focuses on how coal devolatilization at elevated pressure affects the physical structure of the resulting char. Coal swelling, morphology, surface area, and pore size will be discussed.

#### 2.1.2.1 Coal Swelling Ratio during Devolatilization

Particle swelling may be the most distinct phenomenon of coal physical structure transformation during devolatilization, which can affect char particle size, pore size, porosity, density, and reactivity. The swelling ratio is defined as the diameter ratio of char to coal, which can be affected by coal properties such as initial particle size, coal type, and devolatilization process such as maximum temperature, heating rate, and oxygen content. The effect becomes more complicated when considering the diversity of the behavior of individual particles due to the variation of the coal maceral constituents among the particles within the same coal sample (Benfell et al., 2000). Instead of a comprehensive review of coal swelling research, this section only focuses on pulverized coal swelling at elevated pressure.

Direct observations (Essenhigh and Yorke, 1965; Gao et al., 1997; Strezov et al., 2003) of coal swelling at low heating rates are relatively easy to accomplish compared to observations at harsh industrial flame conditions. At low heating rates, it was observed that coal particles undergo significant changes of swelling and shrinking (transient size

oscillations) until resolidification occurred. Fletcher (1993), Gale et al. (1995), and Zygorakis (1993) measured the transient swelling of fuel particles collected at high heating rates during pyrolysis at 1 atm. The general trend of coal particle swelling ratio with heating rate is shown in Figure 2.1. Coal particle swelling ratio increased with increasing heating rate to  $10^3\sim 10^4$  K/s, and then decreased at higher heating rates.

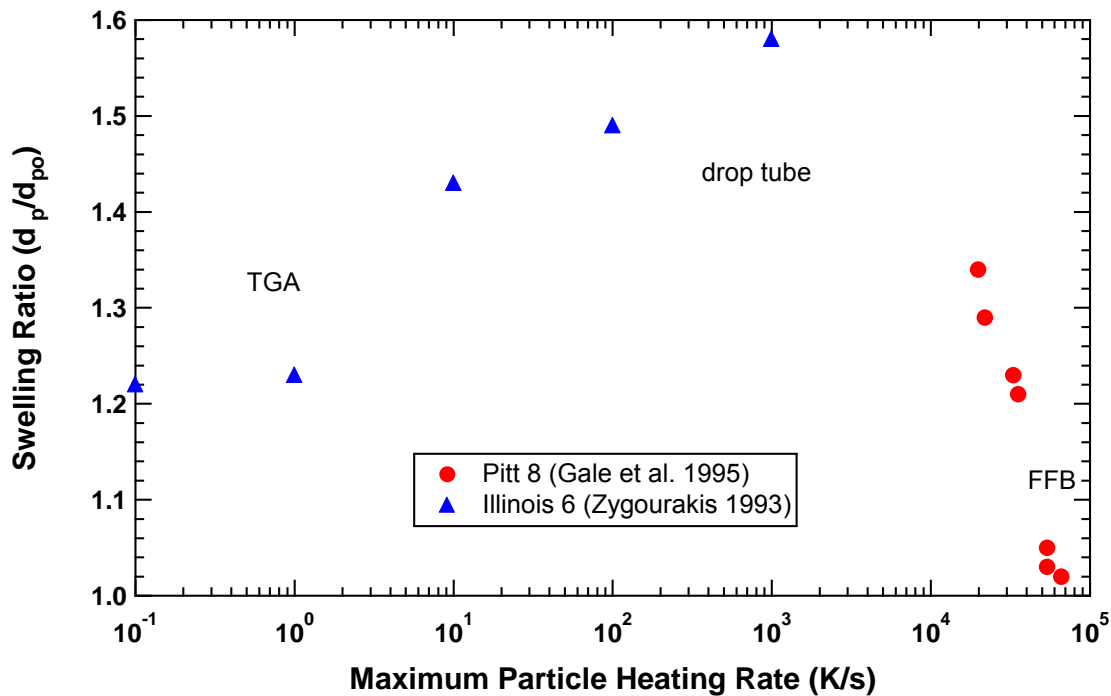


**Figure 2.2.** Swelling vs. heating rate at 1 atm (Gale et al., 1995).

Lee et al. (1991) studied the effect of pressure on the swelling behavior of Illinois #6 coal pyrolysed at 1189 K in an inert nitrogen atmosphere. At 1 atm, coal particle swelling was not significant. At 8 atm, the swelling ratio ( $d_p/d_{p0}$ ) increased about three times at 0.3 s and thirty times at 0.8 s, suggesting that swelling may occur during late stages of pyrolysis. However, at 22 atm, the extent of swelling dropped significantly, and

swelling occurred in the early stage of pyrolysis (<0.5 s), and swelling was not obvious between 0.5 s and 1.0 s when significant mass release occurred.

Wu et al. (2000) studied an Australian bituminous coal using a pressurized drop tube furnace. The char characteristics were found to be influenced significantly by the system pressure. Their results indicated that coal and char fragmentation might have occurred during devolatilization at high pressure. The char size (as characterized by the swelling ratio) was also observed to increase with system pressure. The measured swelling ratios of the char sample fell well below the data of Lee et al. (1991) at all system pressures. This may be caused by differing furnace temperatures or heating rates, which are compared in Table 2.1. Yu et al. (2003) studied the effect of initial coal density fractions on their swelling ratio. The mass release, swelling ratio, and the porosity decreased with increasing parent coal density. Results from size fractionated samples suggested that larger swelling occurred in a DTF (drop-tube furnace) when the initial particle size was decreased.

**Table 2.1 Comparison of Experimental Conditions for Two Pressurized Drop Tube Experiments**

	Lee et al.(1991)	Wu et al. (2000)
Coal	Illinois No.6	Australian Bituminous coal
Particle size	62 $\mu\text{m}$ mean particle diameter	63-90 $\mu\text{m}$
Apparatus	HEF (high-pressure entrained-flow furnace)	PDTF (pressurized drop-tube furnace)
Heating rate	$\sim 10^4$ K/s	$\sim 10^4$ - $10^5$ K/s

Temperature	1189 K	1573 K
Pressure	0.1-3.8 MPa	0.1-1.5 MPa
Atmosphere	N <sub>2</sub>	N <sub>2</sub> with small amounts of O <sub>2</sub>




A number of attempts have been made to model the coal swelling (Oh et al., 1989; Sheng and Azevedo, ; Solomon and Hamblen, 1985; Yu et al., 2002). It is commonly agreed that metaplast fluidity and bubbles formed during coal devolatilization play an important role on determining coal swelling ratio and char structure. The fluidity of the metaplast of the softening coal can be increased by elevated pressure, due to the retention of volatiles which act as a plasticizing agent (Khan and Jenkins, 1984). The increased fluidity facilitates bubble transport to the particle surface. Elevated pressure also increases the resistance to expansion of the plastic coal melt. The maximum swelling ratio occurs at the point that the initial pressure build-up inside the coal melt achieves a balance with the bulk pressure. Contraction was observed at extended residence times when devolatilization had been completed (Lee et al., 1991). Bubble growth and coalescence can also be used to explain char physical structure change with density (Yu et al., 2002).

#### 2.1.2.2 Char Morphology and Surface Area during Devolatilization

Char morphology has been extensively studied during the past decade (Alvarez et al., 1997; Cloke et al., 1997; Lester and Cloke, 1999; Lester et al., 1996). Recently, Wu et al. (2000) and Benfell et al. (2000) studied the effect of pressure on char morphology. By analyzing char SEM (Scanning Electron Microscopy) photos, chars were categorized based on criteria shown in Table 2.2.

Typically, Group I particles have a very porous structure, with large voids inside the particle and a thin wall, Group II particles have a medium porosity and wall thickness, and Group III char particles have low porosity. This classification is the first attempt to classify char particles into representative groups. The effects of coal rank and density on coal morphology were also studied by Bailey et al. (1990) and Benfell et al. (2000). Essentially, coal rank and density are indices of coal petrography. The morphology of the chars shows a strong relationship with increasing vitrinite content (Benfell et al., 2000).

**Table 2.2 Char Classification System (Benfell et al., 2000; Wu et al., 2000)**

Char groups	Group I	Group II	Group III
Two-dimensional schematic representation			
Porosity (%)	>70	Variable, 40–70	<50
Average wall thickness (mm)	<5	>5	>5
Shape	Spherical subspherical	Subspherical	Angular
Typical swelling ratio	>1.3	<1.0	<0.9
Typical residual mass ratio	0.1–0.5	0.1–0.5	1.0

Pressure has a strong influence on char morphology. When furnace pressure increases, the overall proportion of Group I chars formed increases, while the proportions of Groups II and III chars decrease. Mean diameter and porosity of an Australia coal increased when pressure was increased from 5 to 10 atm, and then decreased at pressures ranging from 10 to 15 atm, probably due to char fragmentation. Microscopic observation of this char showed that the group I particles had thinner walls and a more spherical

structure than those of lower pressure chars, factors which made these samples more susceptible to fragmentation within the furnace and during handling (Benfell et al., 2000). The average macro-porosity of high-pressure chars was higher than that of low pressure chars, and the high pressure chars had more bubbles with smaller sizes (Yu et al., 2003).

The internal surface area of char is one of the significant parameters sometimes used in modeling char combustion and gasification. Only two data sets have been presented for the surface areas of chars produced under high-pressure conditions. Lee et al. (1991) investigated the development of CO<sub>2</sub> surface area of char as a function of mass release and pressure for Illinois No. 6 bituminous coal under a moderate heating rate condition (See Table 2.1). The surface area of char was generally lower under higher pressure pyrolysis conditions. A recent study presented the CO<sub>2</sub> surface area for chars produced from Australian bituminous coals in a pressurized drop tube furnace at various pressures (Benfell et al., 2000). Generally, the surface areas of chars decreased as pressure is increased. The effect of pressure on char surface area is believed to be related to the fluid behavior during devolatilization (Lee et al., 1991).

#### 2.1.2.3 Summary

In summary, pressure has a significant effect on coal swelling and char morphology. Coal swelling increases with pressure increased to 5-10 atm then decreases with further increase of pressure. Char formed at high-pressure tends to be more porous. The surface areas of chars are lower at elevated pressure than chars formed at low pressure.

### 2.1.3 Effects of Pressure on Resulting Char Reactivity

The pressure at which the parent coal is devolatilized may play an important role in the reactivity of the resulting char. Sha et al. (1990) noted a significant decrease in the reactivity of the char as pressure was increased, postulating that reactivity was affected by changes in pore structure. Van Heek and Mühlen (1991) noted that the steam reactivity for chars is not affected by pressure if pyrolysis is performed under inert conditions. Under a hydrogen atmosphere, increased pressure resulted in a decrease in the steam reactivity of the resulting char. Cai et al. (1996) found combustion reactivities (calculated as the maximum TGA rate observed during the conversion profile at 773 K) decreased during hydro-pyrolysis at pressures up to 40 atm, but increased at pressures above 40 atm. The eventual increase in reactivity was reportedly the result of some char conversion by H<sub>2</sub> at the higher pressure, which exposed a fresh and enlarged carbon surface. Lee et al. (1992) investigated the structure and reactivity (g/g-s) of Illinois No.6 coal char following pyrolysis at elevated pressure. Their data demonstrated how pressure hinders the development of the mesopore system that develops after the coal passes through the plastic phase of pyrolysis. The increased fluidity that results during higher-pressure pyrolysis led to enhanced ordering of carbon layers and the subsequent loss of gasification reactivity in the char residue.

Roberts et al. (2000) measured the apparent and intrinsic gasification rates of an Australian coal char collected from a pressurized drop tube furnace (PDTF) under various pressures. Char gasification reactivity varied significantly with pressure, whereas the intrinsic rates, which were obtained by normalizing the apparent rate by internal surface area, were almost independent of pressure over a range of 1 to 15 atm. Comparisons of

the initial apparent and intrinsic gasification rates of vitrinite- and inertinite-rich char samples from the same coal were given by Benfell et al. (2000). The inertinite-rich sample had a faster apparent gasification rate than the vitrinite-rich sample when made at 5 atm, but a slower apparent gasification rate when made at 15 atm. However, it was shown that the intrinsic reaction rates of these char samples did not systematically show large variations with pressure or maceral concentrations in the parent coal. This suggests that the pressure significantly influences the physical structure of coal chars, as discussed above, but has little effect on the chemical structure of char, which largely determines the intrinsic char reactivity. Such a conclusion has significant implications for interpreting char reaction rates and mathematical modeling of char burnout.

In summary, chars produced at different pressures were reported to have different apparent reaction rates, but similar intrinsic rates. However, pressure may have a significant influence on char morphology. High pressure pyrolysis forms more porous char particles. The change of morphology with pressure affects the apparent reactivity due to changes in internal surface area and other properties. Chemical structures of chars formed at different pressures seem similar, as long as the char preparation temperature is low. Further studies are needed to determine the effects of high pyrolysis temperatures (>1673 K) and high pressures on the properties of char.

## **2.2 Effects of Reaction Pressure on Char Combustion Kinetics**

A review of published data from high pressure coal combustion and char oxidation experiments is listed in Table 2.3. Reviews of research by Hong (1999) are not repeated in this dissertation.



**Table 2.3 Test Conditions for Various High Pressure Oxidation Rate Measurements**

Investigator (year)	Fuel	diameter ( $\mu\text{m}$ )	$T_p$ (K)	$P_{\text{total}}$ (atm)	$x_{\text{O}_2}$ (%)
Monson (1992)	chars	63-75	1300-2100	1-15	5~21
Mathias (1996)*	Coals, chars	6, 9 mm	900-1300	0.86-5	6-18
Ranish and Walker (1993)*	graphite	flakes	733-842	1-64	100
Banin et al. (1997)*	chars	~6	1200-1800	8	0-100
Croiset et al. (1996)*	chars	90-106	850-1200	2-10	1.5-10
Moors, J.H.J (1999)	char	<10	1300-3000	6-11	0-100
Roberts and Harris (2000)	chars	600-1000	723	15	50
Hecker et al. (2002)	chars	64-76	598-723	1-32	2.5-80

\* See review by Hong (1999).

Monson (1992) investigated high-pressure and high-temperature char oxidation using a high-pressure controlled-temperature profile drop-tube reactor. The measurements were performed using Utah and Pittsburgh coals at reactor temperatures between 1000 and 1500 K and total pressures of 1, 5, 10 and 15 atm. All chars were formed at 1 atm. At constant oxygen mole fractions (0.05, 0.10 and 0.21), increasing total pressure from 1 to 5 atm led to a slight increase in the reaction rate, with the rate decreasing with further increases in total pressure from 5 to 15 atm. Monson (1992) used a global  $n$ -th order char oxidation model to fit his data. The calculated apparent rate coefficients showed significant pressure dependence, since both the activation energy and frequency factor decreased with increasing pressure. Since these rate coefficients should not vary significantly with pressure, this appears to show that the global  $n$ -th order approach is inadequate in modeling char oxidation rates when total pressure is varied.

Moors (1998) investigated combustion of Göttelborn char in a high temperature and high pressure shock tube. The particle temperature varied between 1300 and 3000 K. The total gas pressure varied between 0.6 and 1.1 MPa. He concluded that the combustion of Göttelborn char particles occurs in the rough-sphere regime (defined by Moors as regime in which the external surface area of the particle is much larger than the internal surface area involved in the combustion process). The penetration of oxygen into the pores was small. Internal transport of reactant had no influence on the apparent kinetics. Based on an energy balance, a mass balance and a carbon dioxide production calculation, the kinetics were found to be of a Langmuir type. Adsorption of oxygen at active sites determines the overall reaction rate at partial pressures higher than about 0.4 MPa. The reaction order decreased from unity to zero when the oxygen partial pressure increased. When internal transport influenced the apparent combustion kinetics, the reaction order decreased to one half as the pressure increased. Moors also found that the particle size distribution and the temperature history of the particles influenced the kinetic reaction rates obtained. The shock tube gave smaller activation energies than other reactors. This difference was apparently due to a difference in burnout time and a more pronounced influence of thermal annealing for the reactors with a longer burnout time.

Roberts and Harris (2000) measured the intrinsic reactivities of two Australian coal chars (produced at 1100°C nitrogen for 3 hr) to O<sub>2</sub>, CO<sub>2</sub>, and H<sub>2</sub>O at pressures up to 30 atm. Measured reaction orders in CO<sub>2</sub> and H<sub>2</sub>O were not constant over the pressure range investigated, whereas reaction order in O<sub>2</sub> was unchanged. The differences in reaction order transition appeared to be related to the rate of the reaction. Activation energies of all three reactions were not found to vary as the pressure was increased.

These results demonstrated that a physical rather than a chemical change is the reason for the observed variations in the apparent reaction order. However, the authors pointed out a need for high-temperature high-pressure measurements of reactivities in order to validate their conclusion.

Hecker et al. (2003) examined the intrinsic oxidation of two coal chars Pitt #8 and North Dakota lignite prepared at high temperature and high heating rate at atmospheric pressure. High pressure TGA experiments were conducted over a pressure range of 1 to 32 atm, a temperature range of 598 to 823 K, a range of oxygen partial pressures from 0.03 to 12.8 atm, and a char burnout range of 20 to 60%. Under these conditions, it was found that intrinsic char oxidation rate, determined on a  $g/g_{\text{available}}\text{-s}$  basis, was independent of total pressure and char burnout level, and that kinetic parameters ( $E_A$ ,  $n$ ) were not affected by changes in total pressure. More specifically, under the conditions of this study, intrinsic char oxidation rate, activation energy, and oxygen reaction order were found to be independent of total pressure (see Figure 2.3). It was also reported that the  $n$ th order kinetic model fits both atmospheric and elevated pressure char oxidation data very well, with  $n = 0.7$  for both chars studied.

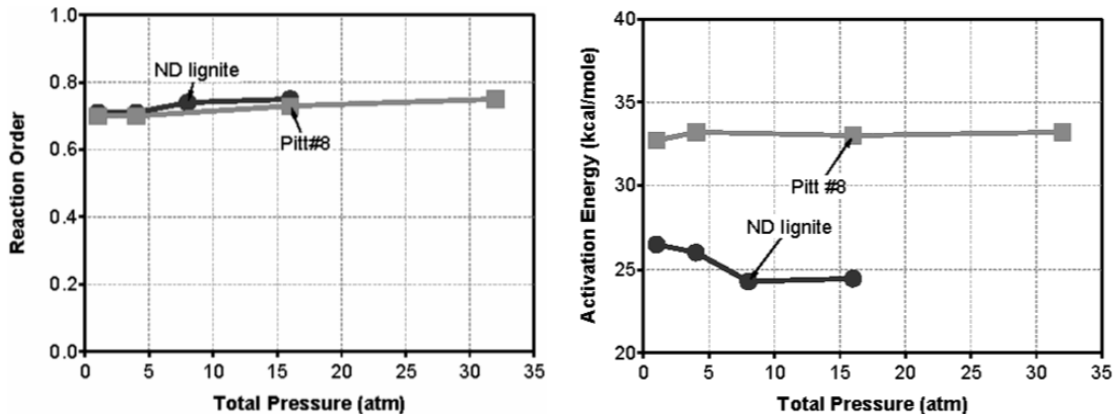


**Figure 2.3.** Effect of total pressure on oxygen order (left) and activation energy (right) of the NDL and Pitt 8 char reactivity. (Hecker et al., 2003)

In summary, elevating reaction pressure increases char oxidation reactivity up to moderate pressure. The reaction rate may be almost independent of total pressure at high pressure. Char oxidation rates at elevated pressure may increase with an increase in total pressure from atmospheric pressure to almost 10 atm, and then decrease at even higher pressure. However, there are inconsistent trends in the literature.

More work should be performed in order to firmly establish the kinetics of high pressure char oxidation. One particular area that should be studied is the intrinsic kinetics of chars produced at elevated pressure. Chars produced at elevated pressures may exhibit different behavior compared to chars produced at atmosphere pressure. In addition, it is possible that the internal surface area of the char changes significantly as experimental conditions vary. Many mechanistic models of intrinsic reactivity normalize the reactivity by the internal surface area. Changes in the internal surface area may account for the changes in reactivity with total pressure or burnout predicted by some of these models.

## **2.3 Mechanism of Char Oxidation**

### **2.3.1 The Three-Zone Theory**

The rate of char oxidation is controlled by the sequential or parallel processes of boundary layer diffusion of O<sub>2</sub>, surface chemical reaction, and pore diffusion. Several investigators, such as Walker et al. (1959) and Gray et al. (1976) have postulated the existence of three different temperature zones or regimes in which one or more different

processes control the overall reaction rate. This classic “three-zone” theory has been widely accepted and used to interpret experimental data in the char oxidation literature.

In Zone I, which occurs when the chemical reaction rate is slow compared to the diffusion rate (i.e. at low temperature and for small particles), the chemical reaction is the rate-determining step. In Zone II, the reaction rate is controlled by both chemical reaction and pore diffusion. Zone III, which occurs at high temperatures, is characterized by mass-transfer limitations in the boundary layer of the particle. Figure 1 illustrates these zones graphically and indicates the theoretical dependence of the reaction rate on oxygen concentration (Smoot and Smith, 1985).

It should be noted that the three-zone theory as shown in Figure 2.4 idealizes and simplifies the actual variation of reaction rate with temperature. First, the three-zone theory assumes that boundary layer diffusion (BLD) resistance dominates in Zone III, is present during the transition from Zone II to Zone III, and is totally absent from Zone I to Zone II.

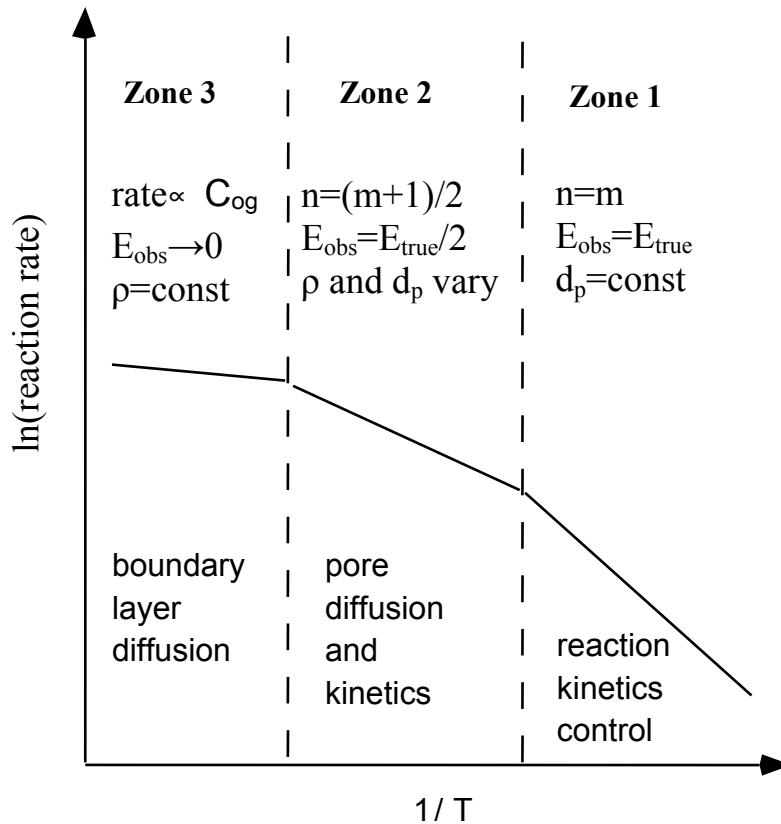


**Figure 2.4.** Rate-controlling zones for heterogeneous char oxidation.

In reality, BLD resistance is often present in Zone II. In other words, char oxidation rate is typically influenced by all three processes: BLD, pore diffusion, and chemical kinetics. Second, the three-zone theory applies only to  $n$ -th order kinetics, and fails to predict the variation of reaction rate with temperature for Langmuir-Hinshelwood kinetics. For example, Essenhigh (1991) suggested that the true activation energy of the char-oxygen reaction changed from 32.95 kcal/mol to 10.04 kcal/mol (corresponding to desorption control and adsorption control, respectively) as temperature increased. Third, the three-zone theory assumes that the combustion rate contributed from the external surface area is negligible compared to the rate contributed from the internal surface area. This assumption is true for most cases, since the internal surface area is typically much

larger than the external surface area. However, the external surface area can become important under some conditions, such as low internal surface area (typically in highly ordered carbons) or severe pore diffusion limitations, which lead to extremely low effectiveness factors (Hurt, 1998). For very small particles, Banin and Veeffkind (1997) assumed a “rough sphere” approximation to incorporate the effects of external surface area, although this approximation was not needed in later modeling by Hong, et. al. (2000b).

### 2.3.2 Semi-Global Intrinsic Kinetics for Char Combustion Modeling

The carbon-oxygen reaction is probably the most important reaction in industrial application, playing a very important role in industries such as ironmaking, coal or biomass fired power plants, gasification, etc. This reaction still remains very intriguing in spite of several decades of studies of this reaction. Stoichiometrically, the reaction is simple; oxygen reacts with carbon to form carbon dioxide or carbon monoxide:



The general features of the kinetics were well documented (Marsh, 1978), but a general mechanism that can describe the rate over a range of temperature, of oxygen partial pressure, and other conditions is still under study. The difficulties are: (1) the variation of properties of carbon in its graphitic form, which depends heavily on the source of carbon and the method of preparation; and (2) the elementary processes of adsorption, migration, rearrangement, dissociation, and dispersion, which make overall reaction hard to be correlated into a general mechanism (Back, 1997). However, a

reliable, simple carbon oxygen reaction mechanism is still needed. Several semi-global intrinsic kinetic mechanisms have been proposed to meet this need.

Table 2.4 gives four candidate kinetic models (Campbell et al., 2002; Haynes, 2001; Hurt and Calo, 2001; Mitchell, 2003); they will be discussed in detail below.

**Table 2.4 Global and Semi-Global Mechanisms and Corresponding Rate Laws**

Model 1. Global power-law 1. $C + O_2 \rightarrow CO / CO_2$	$r_{gas} = kP_{O_2}^n$
Model 2. Langmuir-Hinshelwood 1. $C + O_2 \rightarrow 2C(O)$ 2. $C(O) \rightarrow CO$	$r_{gas} = \frac{k_1 k_2 P_{O_2}}{k_1 P_{O_2} + k_2}$ (non-dissociative form)
Model 3. Three-step semi-global 1. $C + O_2 \rightarrow 2C(O)$ 2. $C(O) + O_2 \rightarrow CO_2 + C(O)$ 3. $C(O) \rightarrow CO$	$r_{gas} = \frac{k_1 k_2 P_{O_2}^2 + k_1 k_3 P_{O_2}}{k_1 P_{O_2} + k_3 / 2}$ $CO / CO_2 = \frac{k_3}{k_2 P_{O_2}}$
Model 4. Four-step semi-global (Turnover model) 1. $2C + O_2 \rightarrow 2C(O)$ 2. $C + C(O) + O_2 \rightarrow CO_2 + C(O) + C$ 3. $C + C(O) + O_2 \rightarrow CO + C(O) + C(O)$ 4. $C(O) \rightarrow CO + C$	$r_{ic} = MW_C (S / N_{av})$ $\{(k_2 + k_3)(S / N_{av})\theta_f [O_2] + k_4\} (1 - \theta_f)$ $CO / CO_2 = \frac{k_3 (SC / N_{av})\theta [O_2] + k_4}{k_2 (SC / N_{av})\theta [O_2]}$

### 2.3.2.1 The Global n-th Order Rate Equation

An empirical n-th order rate equation is often used to describe kinetics of char oxidation at typical industrial boiler temperatures (Hurt and Mitchell, 1992; Monson et al., 1995; Smith, 1982). The most common form of the n-th order rate equation is

$$q_{rxn} = k_s P_{os}^n = A \exp\left(\frac{-E_{obs}}{RT_p}\right) P_{os}^n \quad (2.3)$$



This simple equation provides a basis for estimating char oxidation rates, and has often been adequate for practical use at atmospheric pressure over small temperature ranges (Smoot, 1998). Due to its simplicity, the global n-th order rate equation is often used in comprehensive computer models. However, this rate equation does not explicitly account for pore diffusion effects on kinetics. Pore diffusion effects are often implicitly included in the observed activation energy and the pre-exponential factor.

The global n-th order rate equation has been criticized for lack of theoretical basis and inadequacy for predicting rates over wide ranges of experimental conditions, especially for high pressure char oxidation modeling (Essenhigh and Mescher, 1996; Monson, 1992). One weakness of this equation is that it cannot be extrapolated between Zone I and Zone II. In addition, the reaction order is often observed to vary as experimental conditions vary, with limits of zero and unity (Suuberg et al., 1988).

In a recent study, Hurt and Haynes (2004) suggested that persistent, high fractional order in the carbon/oxygen reaction is due to surface heterogeneity. Simple surface reaction models including surface heterogeneity predicted power-law behavior over wide ranges of partial pressure if the breadth of the activation energy distribution for adsorption and/or desorption is large. However it is impractical to carry out the detailed surface characterization or fully define heterogeneous surface models for each carbon material of technological interest. Their theory proves that Haynes's turnover model is capable of predicting the lower orders and the gradual change in reaction order with pressure for graphitized carbon black, a behavior that is intermediate between power-law and Langmuir kinetics..

### 2.3.2.2 Langmuir-Hinshelwood Kinetics

Fundamental studies show that the carbon-oxygen reaction involves chemisorption, oxygen surface diffusion, and desorption of surface oxygen complexes (Du et al., 1991; Essenhig, 1981; Essenhig, 1991). The n-th order rate equation fails to reflect the adsorption-desorption nature of this reaction. A more mechanistically meaningful representation of the intrinsic reaction rate is a Langmuir-Hinshelwood form (Laurendeau, 1978), which in its simplest form becomes the Langmuir rate equation:

$$r_{in}'''(C) = \frac{k_1 C}{1 + KC} \quad (2.4)$$

where  $k_1$  and  $K$  are two kinetic parameters. It should be noted that 1) the product of  $K$  and  $C$  is non-dimensional; 2) there are different possible mechanisms leading to Eq. 2.4; 3) the physical meanings of the two parameters  $k_1$  and  $K$  depend on the mechanism leading to Eq. 2.4. The discussion in this review is general and independent of mechanisms. The above equation is also referred to as a “Langmuir adsorption isotherm” (Essenhig, 1988), a shifting order rate equation (Robert and Bartholomew, 1997) and more specifically, a non-dissociative, single-adsorbed-species Langmuir rate equation (Hill, 1977). The Langmuir rate equation (Eq.2.4) can be re-written as:

$$\frac{1}{r_{in}'''} = \frac{1}{k_1 C} + \frac{1}{k_0} \quad (2.5)$$

where  $k_0$  is the ratio of  $k_1$  to  $K$ . The Langmuir rate equation is the simplest form of all Langmuir-Hinshelwood kinetic expressions capable of modeling apparent reaction order shifting between zero and unity.

In an attempt to treat the effects of pressure, Essenhig et al. (1999) proposed a so-called “second effectiveness factor” to account for the internal (pores) combustion.

This method uses some approximations to achieve a simple form of the final rate expression. The second effectiveness factor ( $\varepsilon$ ) is calculated from the power index ( $\alpha$ ) of a normalized density-diameter relationship in the following manner (Essenhigh et al., 1999; Laurendeau, 1978):

$$\varepsilon = 1 + \alpha/3 \quad (2.6)$$

$$\frac{\rho}{\rho_o} = \left( \frac{d}{d_o} \right)^\alpha \quad (2.7)$$

Hong (1999) identified several weaknesses in the second effectiveness factor approach. First, the second effectiveness factor approach requires density and diameter data, which are often not available a priori, in order to determine the power index  $\alpha$ . Hence, this method is not truly predictive in nature. Second, the power index  $\alpha$  is very difficult to determine accurately, since it can vary over several orders of magnitude. For example, Essenhigh (1988) reported a value of  $\alpha$  around 1 for high temperature char oxidation and values of  $\alpha$  in the range of  $10^4 \sim 10^5$  for low temperature char oxidation. Third, this approach assumes that the power index  $\alpha$  remains constant throughout the whole range of burnout. In a typical pulverized char combustor, a single char particle travels through different zones of the reactor and interacts with different combustion environments, leading to varying burning modes (corresponding to  $\alpha$  between zero and infinity), and a constant value of  $\alpha$  is no longer realistic; hence it is inadequate to account for internal combustion. The original effectiveness factor approach, however, has the potential to overcome all these difficulties associated with the second effectiveness factor approach.

Hong (2000b) applied the Langmuir rate equation to graphite flake data of Ranish and Walker (1993). Oxidation rates of some highly crystalline graphite flakes were measured in pure oxygen at pressures between 1 and 64 atm and temperatures between 733 and 842 K. The best fit of Langmuir desorption activation energy ( $E_{des}$ ) was 41.0 kcal/mol. Adsorption activation energy  $E_{ads}$  was 51.1 kcal/mol, and  $E_{ads} > E_{des}$ . This inverted activation energy contradicts previous experimental observations (Essenhigh, 1988). Langmuir-Hinshelwood kinetics are also unable to describe the persistent n-th order behavior observed by Hecker et al. (2003) over a range of  $P_{O_2}$  from 0.025 to 12.80 atm, and by Suuberg et al. (1988) over a range of  $P_{O_2}$  from about 0.2 to 100 atm. Rearrangement of the Langmuir-Hinshelwood kinetic mechanism gives a reaction order of (Hong, 1999):

$$m_{obs} = \frac{1}{1 + A_p e^{-E_p/RT} P_{os}} \quad (2.8)$$

At constant temperature, Langmuir-Hinshelwood kinetics can not predict constant order with change of  $P_{O_2}$ , as observed by Hecker et al. (2003) and Suuberg et al. (1988). This implies Langmuir-Hinshelwood kinetics can not be used as a general kinetic form, even though it has more theoretical basis than n-th order kinetics.

### 2.3.2.3 Three-Step Semi-Global Kinetics

A three-step intrinsic kinetic mechanism was proposed to resolve the problems in the reaction order for conventional char oxidation kinetics (Hurt and Calo, 2001; Niksa et al., 2003):





The corresponding rate laws for each step are:

$$R_1 = k_1 P_{O_2} (1 - \theta) \quad (2.12)$$

$$R_2 = k_2 P_{O_2} \theta \quad (2.13)$$

$$R_3 = k_3 \theta \quad (2.14)$$

where  $\theta$  represents the fraction of sites occupied by the adsorbed oxygen complex,  $P_{O_2}$  is the  $O_2$  partial pressure on the carbon surface, and,  $k_1$ ,  $k_2$ , and  $k_3$  denote the rate constants for Step 1, Step 2 and Step 3 in Eq. (2.9-2.11), respectively. These laws can be combined to yield the steady-state expression for the overall oxidation rate and primary CO/CO<sub>2</sub> ratio, which are:

$$r_{gas} = \frac{k_1 k_2 P_{O_2}^2 + k_1 k_3 P_{O_2}}{k_1 P_{O_2} + k_3 / 2} \quad (2.15)$$

$$CO / CO_2 = \frac{k_3}{k_2 P_{O_2}} \quad (2.16)$$

The difference between three-step semi-global kinetics and the Langmuir form is the reaction involving gas phase oxygen with surface complexes:



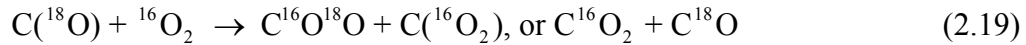
This mechanism is better than n-th order and Langmuir-Hinshelwood kinetics in three aspects (Hurt and Calo, 2001):

1. Many recent studies provide direct proof that this reaction is important step. Haynes (2001), Haynes and Newbury (2000) studied oxyreactivity of carbon surface

oxides using isotopically-labeled oxygen, temperature-programmed desorption (TPD). The overall reaction proceeds as



The contribution of reaction (2.10) to the overall rate of carbon gasification under their experimental ranges is from 45% at 873 to 4% at 1083 K. Zhuang et al. (1996) also found following reaction



is responsible for <sup>18</sup>O-labeled carbonyl and ether. Both Zhuang et al. (1996), and Haynes and Newbury (2000) find that the O<sub>2</sub>-complex reaction proceeds even on the thermally stable complexes, which in the absence of O<sub>2</sub> would not turn over fast enough at the reaction temperature to contribute significantly to the observed gasification. Thus in the presence of a broad distribution of desorption activation energies, the most stable complexes turn over preferentially by the oxyreactivity Eq. 2.18, while on the same surface the labile complexes turn over preferentially by the thermal desorption, producing a mixed reaction mode (Haynes and Newbury, 2000).

2. This semi-global “mechanism” may be a lumped description of several more elementary steps. Hurt and Calo (2001) found that this mechanism may represent anyone of three aspects: (a) Direct collisional interaction between gaseous oxygen and a surface complex; (b) The attack of sites adjacent to an existing complex, resulting in complex destabilization and rapid desorption of CO<sub>2</sub>. The rapid desorption makes this process first order in molecular oxygen; and (c) Some modes of induced or intrinsic heterogeneity (Ranish and Walker, 1993), in which adsorption activation energy increases and desorption activation energy decreases with increasing coverage. This trend can lead to

partial or complete adsorption control at low temperatures where fractional coverage is very high.

3. A number of observations support step 2 above as the primary pathway to CO<sub>2</sub>, rather than



which is the favored explanation for CO<sub>2</sub> formation in all but the most recent literature. These observations include the high CO/CO<sub>2</sub> ratios seen during vacuum TPD relative to gasification conditions (Du et al., 1990; Ranish and Walker, 1993; Zhuang et al., 1996), the recent quantification of C<sup>18</sup>O<sup>16</sup>O in isotope tracer studies (Haynes and Newbury, 2000; Zhuang et al., 1995; Zhuang et al., 1996), and the inability of Eq. 2.20 to predict high reaction order at low temperature without additional model complexity (Hurt and Calo, 2001).

Table 2.5 gives rate expressions of the three-step mechanism (Eq. 2.15) at different temperature ranges. It can be found that the three-step mechanism is able to describe the change of global reaction order with increasing temperature. Global reaction order shifts from high (O<sub>2</sub>-complex control) to low (desorption control) and back to high again (adsorption control).

Unlike the classic Langmuir-Hinshelwood form, which describes a first order and zeroth order process in series, this parallel mechanism gives zeroth order behavior at low pressure, and transitions to first order behavior at higher pressure (Hurt and Calo, 2001). This transition is summarized in Table 2.5.

**Table 2.5 Summary of Controlling Mechanisms and Rate Expressions for Each Temperature Range (Hurt and Calo, 2001)**

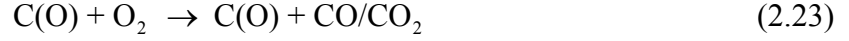
Particle temperature range	Simplified burning rate	Controlling mechanisms
Low temperature ( $k_3$ small)	$r_{gas} = k_2 P_{O_2}$	O <sub>2</sub> -complex reaction control
Low-moderate temperature ( $k_1 P_{O_2} \gg k_3$ )	$r_{gas} = k_2 P_{O_2} + k_3$	Mixed desorption/O <sub>2</sub> /complex control
Moderate temperature ( $k_1 P_{O_2} \gg k_3 \gg k_2 P_{O_2}$ )	$r_{gas} = k_3$	Desorption control
High-moderate temperature ( $k_1 P_{O_2} \gg k_3 \gg k_2 P_{O_2}$ )	$r_{gas} = \frac{k_1 k_3 P_{O_2}}{k_1 P_{O_2} + k_3 / 2}$	Langmuir–Hinshelwood-type, mixed adsorption/desorption control
Very high temperature: ( $k_3$ large)	$r_{gas} = 2k_1 P_{O_2}$	Adsorption control

#### 2.3.2.4 Four Step Semi-Global Kinetics

Three-step semi-global kinetics are simple but very effective; they describe the trends in global reaction, CO/CO<sub>2</sub> ratio, and global activation energy. However, three-step kinetics fail to predict a number of other known features of the carbon-oxygen, including those pointed out by Hurt and Calo (2001): (1) the production of CO<sub>2</sub> is a second product of thermal desorption (Du et al., 1990; Haynes and Newbury, 2000; Zhuang et al., 1995); (2) site heterogeneity [30]; (3) constant nth-order behavior over two orders of magnitude of oxygen partial pressure (Hecker et al., 2003; Suuberg et al., 1988); (4) increases in oxide surface density with increasing temperature or with the onset of gasification (Du et al., 1990; Walker et al., 1959); and (5) the measurement by Du et al. (1990) of fractional order for the CO producing reactions alone, specifically  $n_{CO} = 0.7$ ;  $n_{CO_2} = 1$ .

Haynes (2001) developed a turn-over carbon-oxygen reaction model:





This model contains explicit descriptions of the broad heterogeneity of types of complexes (C(O) site). Their activation energies for the thermal decomposition process gives a wide diversity and flexibility to the calculated results. Haynes (2001) successfully predicted spherocarb burning rates at 2.7 Pa from 873-1073 K. The turn-over kinetic model can be expressed using pseudo-steady equations (Haynes, 2001; Hurt and Haynes, 2004):

$$R_{\text{ads}} = A_{\text{ads}} e^{(-E_{\text{ads}}/RT)} P_{\text{O}_x} (1 - \theta) \quad (2.24)$$

Where  $\theta$  is the fraction coverage and  $A_{\text{ads}}$  comes from gas kinetic theory as:

$$A_{\text{ads}} = S / (2\pi M_{\text{O}_2} RT)^{1/2} \quad (2.25)$$

The activation energy,  $E_{\text{ads}}$ , is coverage-dependent, according to:

$$E_{\text{ads}} = a + b \ln(N) \quad (2.26)$$

where  $N$  is the total number of oxides. The parameters  $a$  and  $b$  are determined by TPD experiment. The desorption rate is obtained by integration over a distribution of sites of varying desorption activation energy:

$$R_{\text{des}} = A_{\text{des}} \int_0^{\infty} e^{(-E_{\text{des}}/RT)} q(E_{\text{des}}) f(E_{\text{des}}) dE_{\text{des}} \quad (2.27)$$

where  $A_{\text{des}}$  is  $10^{14} \text{ sec}^{-1}$  and site density  $f(E_{\text{des}})$  distribution is determined by TPD experiments with variable isothermal soak time. A Gaussian form distribution is adopted by Haynes (2001).

The overall gasification rate is :

$$R_{\text{global}} = R_{\text{ads}} + R_{\text{g-c}} \quad (2.28)$$

where  $R_{\text{ads}}=R_{\text{des}}$  at pseudo-steady state.  $R_{\text{g-c}}$  is the rate of gas/complex reaction step (2.23), which is not well understood.

This model has been applied to spherocarb, which is an amorphous, macroporous synthetic char of high purity (Haynes, 2001), and to several sets of coal char TGA data (Hurt and Haynes, 2004). A qualitative consistency of rates, reaction orders, and pressure dependence was achieved by perturbing original parameters determined experimentally for spherocarb (Haynes, 2001).

Although this model provides theoretical understanding of the observed power-law kinetic behavior, it is impractical to carry out the detailed surface characterization to fully define heterogeneous surface models of each carbon material of technological interest.

### 2.3.3 Pore Diffusion and Effectiveness Factor

The effectiveness factor is widely used to account for the intra-particle diffusion effects on kinetics in catalytic pellets and solid fuel particles. The effectiveness factor is defined as follows:

$$\eta = \frac{\text{actual } O_2 \text{ consumption rate}}{\text{maximum possible } O_2 \text{ consumption rate}} \quad (2.29)$$

The reaction rate in a particle can therefore be conveniently expressed by its rate based on surface reactant concentrations, multiplied by the effectiveness factor:

$$r_{\text{obs}}'''(C_s) = -\frac{dn_c}{V_p dt} = \frac{1}{V_p} (\eta S_{\text{int}} + S_{\text{ext}}) r_{\text{in}}'''(C_s)$$

$$\begin{aligned}
&= \frac{S_{\text{int}}}{V_p} \left( \eta + \frac{S_{\text{ext}}}{S_{\text{int}}} \right) r_{\text{in}}''(C_s) = \left( \eta + \frac{S_{\text{ext}}}{S_{\text{int}}} \right) \frac{S_{\text{int}}}{S_{\text{tot}}} \frac{S_{\text{tot}}}{V_p} r_{\text{in}}''(C_s) \\
&= \left( \eta + \frac{S_{\text{ext}}}{S_{\text{int}}} \right) \frac{S_{\text{int}}}{S_{\text{tot}}} r_{\text{in}}'''(C_s) \tag{2.30}
\end{aligned}$$

It is commonly observed that the external surface area is negligible compared to the internal surface area. Therefore, the above equation becomes:

$$r_{\text{obs}}'''(C_s) = \eta r_{\text{in}}'''(C_s) \tag{2.31}$$

The intrinsic char oxidation rate can be represented by an intrinsic  $m$ -th order rate equation in the form of

$$r_{\text{in}}''' = kC^m \tag{2.32}$$

where  $k$  is the kinetic coefficient in  $(\text{mol C/m}^3)^{1-m} \text{sec}^{-1}$ , and  $m$  is the intrinsic reaction order. Correspondingly, the observed reaction rate becomes

$$r_{\text{obs}}''' = \eta k_m C_s^m \tag{2.33}$$

Alternatively the intrinsic char oxidation rate can be represented by the Langmuir rate equation (Eq. 2.4), and the observed reaction rate becomes:

$$r_{\text{obs}}'''(C_s) = \eta r_{\text{in}}'''(C_s) r_{\text{obs}}''' = \eta \frac{k_1 C_s}{1 + K C_s} \tag{2.34}$$

It has been established that the effectiveness factor can be approximately (except that it is exact for first order reactions) predicted by (Bischoff, 1965; Thiele, 1939):

$$\eta = \frac{\tanh(M_T)}{M_T} \quad \text{in Cartesian coordinates} \tag{2.35}$$

$$\eta = \frac{1}{M_T} \left( \frac{1}{\tanh(3M_T)} - \frac{1}{3M_T} \right) \quad \text{in spherical coordinates} \tag{2.36}$$

where

$$M_T = \frac{L v_o r_{in}'''(C_s)}{\sqrt{2}} \left[ \int_0^{C_s} D_e(C) v_o r_{in}'''(C) dC \right]^{\frac{1}{2}} \quad (2.37)$$

and  $L$  is the characteristic length of the particle (Aris, 1957), which is equal to  $V_p/S_g$ ,  $C$  is the local concentration of oxidizer in the particle,  $r_{in}'''$  is the intrinsic molar reaction rate in any form,  $v_o$  is the stoichiometric coefficient of oxygen for each mole of carbon consumed, which converts the carbon consumption rate into oxygen consumption rate, and  $D_e$  is the effective diffusivity, which can be a function of oxygen concentration. In particular, the general modulus for the  $m$ -th order rate equation (Eq. 2.32) becomes (Bischoff, 1965):

$$M_T = L \sqrt{\frac{(m+1) v_o k_m C_s^{m-1}}{2 D_e}} \quad (2.38)$$

This general modulus has been widely used in the chemical engineering literature (Aris, 1957; Bischoff, 1965; Carberry, 1976; Fogler, 1992; Froment and Bischoff, 1979; Hill, 1977; Laurendeau, 1978; Levenspiel, 1993; Levenspiel, 1999; Mehta and Aris, 1971).

For the Langmuir rate equation, a general modulus was obtained by Hong et al. (2000a):

$$M_T = L \sqrt{\frac{v_o k_1}{2 D_e}} \frac{K C_s}{1 + K C_s} [K C_s - \ln(1 + K C_s)]^{-\frac{1}{2}} \quad (2.39)$$

Eqs. (2.35) to (2.37) were originally referred to as the general asymptotic solution of the effectiveness factor for general reaction rate forms. As shown in Figure 2.5, by

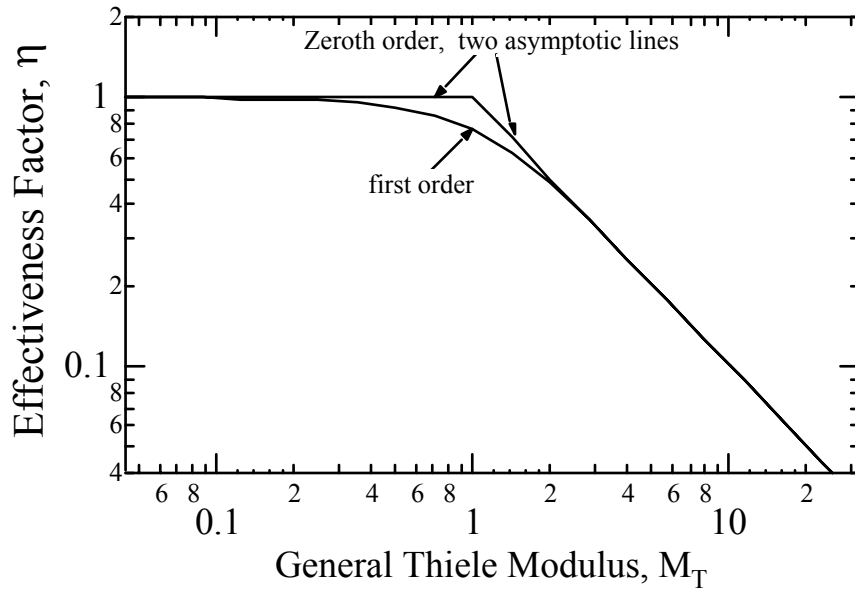


**Figure 2.5.** The effectiveness factor curves for first order and zero-th order reactions in Cartesian Coordinates. For reactions between zero-th order and first order limits ( $0 < m < 1$  or  $0 < KC_s < \infty$ ), the curves lie in the narrow band bounded by the first order and the zeroth order curves. (Hong, 1999)

using the general modulus defined in Eq. (2.37), all of the  $\eta$  vs.  $M_T$  curves lie within a narrow region, bounded by the first order and zero-th order reactions. The general asymptotic solution uses the known analytical expression for first order reactions (Eq. 2.35 or 2.37) to approximate all other curves, since analytical expressions for these other curves are usually not known (except for the zero order curve in Cartesian coordinates). The general asymptotic solution, as the name indicates, tends to be accurate when  $M_T$  approaches either zero or infinity, where the general asymptotic solution approaches the two asymptotic lines ( $\eta = 1$  and  $\eta = 1/M_T$ ). Generally speaking, when  $M_T$  is less than 0.2,  $\eta$  can be approximated as unity (this situation is referred to as Zone I in the char combustion literature). When  $M_T$  is greater than 5,  $\eta$  can be approximated as  $1/M_T$  (this

situation is referred to as Zone II; (Smoot and Smith, 1985)). However, the general asymptotic solution is inaccurate in the intermediate range of the general modulus ( $0.2 < M_T < 5$ ), which was recognized by Bischoff (1965). In Cartesian coordinates, the error of the general asymptotic solution can be as high as -24% on a relative basis.

Hong et al. (2000a) developed a correction function to improve accuracy of general asymptotic solution for  $m$ -th order, and Langmuir rate equation effectiveness effectors. The general form of correction function is:

$$f_c(M_T, m_{obs}) = \left\{ 1 + \frac{\sqrt{1/2}}{2M_T^2 + \frac{1}{2M_T^2}} \right\}^{\frac{1}{2}(1-m_{obs})^2} \quad (2.40)$$

Where,  $m_{obs} = m$  for  $m$ -th order rate equations, and  $m_{obs} = 1/(1+KC_s)$  for Langmuir rate equations.

These correction functions can effectively decrease error of general asymptotic solution from 17% to 2%, but these correction functions can only be applied to limited kinetic expressions.

## 2.4 Summary

In this chapter, the effects of pressure on coal pyrolysis and char combustion were reviewed. Recent developments in char combustion modeling were also reviewed. Most of the research on high pressure char oxidation has been performed on chars prepared at atmospheric pressure. However, increasing pressure decreases pyrolysis yield, and also affects physical char structure. The chemical structure of the chars from high pressure pyrolysis may also be different than that at low pressure, since some of the heavy hydrocarbons apparently crosslink with the char. Studies of high pressure char oxidation

are needed that utilize chars prepared under pressurized conditions. The detailed objectives and approaches are presented in next chapter.





### 3. Objectives and Approach

The objective of this project was to characterize high pressure, high heating rate coal pyrolysis and char combustion, with emphasis on improving coal/char high pressure combustion models. The results of this project will be useful in designing high-pressure, entrained flow gasifiers and other advanced coal conversion systems. This project is divided into the follow tasks:

- *Develop a high-pressure flat flame burner to conduct devolatilization and high temperature reactivity tests.* The ability to achieve high temperature at high pressure in a drop tube is challenging due to reduced insulation performance with increasing pressure (Monson, 1992). An alternative is to use a flat flame burner to create a high temperature condition. A high-pressure flat flame burner (HPFFB) was developed to generate chars from pulverized coals as a function of pressure and temperature at high heating rates.
- *Generate high temperature chars from four typical coals at different pressures.* High heating-rate pyrolysis tests were performed in the HPFFB, at four different pressures (2.5-15 atm) for four coals from a wide range of rank and origin. The products of these pyrolysis experiments were quenched with cold nitrogen gas after a short residence time at high

temperature (250-1300 ms). These devolatilization products were characterized using elemental analysis, inductively coupled plasma (ICP) atomic absorption analysis, and surface area analysis. At each condition, gas temperature profiles were measured in order to calculate particle temperature histories. The evolution of the chemical and structural characteristics of the resulting char was determined during rapid pyrolysis at different pressures for coals of varying rank.

- *Determine intrinsic reactivities of chars using high-pressure TGA tests to find the influence of pressure on char reactivity.* Coal char intrinsic reactivities (i.e., at low temperatures) were measured as a function of pressure using a high-pressure thermogravimetric analyzer (HP-TGA).
- *Determine high temperature oxidation reactivities of char.* Coal char reactivities at high temperatures were measured using the high-pressure flat flame burner.
- *Model the process of high-temperature, high-pressure coal combustion.* An n-th order intrinsic kinetics model and a three-step intrinsic kinetics model were both used to correlate the data collected in this study. The effect of pressure on char reactivity was analyzed.

The results obtained from this study are presented in the following manner. Chapter 4 presents the description of the facility and the experimental procedure. Chapter 5 presents the results of experiments regarding the high pressure coal pyrolysis process, as well as properties of the resulting char. Chapter 6 presents the low-temperature reactivities of char generated at high temperatures and high pressures. Chapter 7 presents

results of the high-pressure, high-temperature coal combustion experiments, along with associated char oxidation modeling. In Chapter 8, a summary and list of conclusions drawn from this study are presented, followed by limitations and recommendations for future work.



## 4. Description of Experiments

High pressure, high temperature pyrolysis and combustion experiments for four coals were performed in a newly developed high-pressure flat flame burner (HPFFB). Low temperature coal char combustion experiments were performed in a high-pressure thermogravimetric analyzer (HPTGA). This chapter describes the HPFFB and HPTGA systems, along with the sample characterization techniques used in this study. The experimental processes and matrix for pyrolysis, TGA combustion, and high temperature combustion experiments are described in Chapters 5-7.

### 4.1 High-Pressure Facility at BYU

The conditions required for high temperature, high pressure coal pyrolysis and oxidation experiments place strict demands on the test facility, especially when simulating industrial-scale pulverized coal combustion conditions. Basically, the following conditions need to be met for a realistic experiment:

1. High particle heating rates ( $10^4\sim 10^6$  K/s);
2. High gas temperature for coal pyrolysis and high particle temperature (1400~2000 K) for char combustion;
3. Stable temperature zone for coal particles to react during the oxidation process;

4. Stable and adjustable reaction residence times and gas compositions for particle oxidation;
5. Single particle reaction behavior.

The difficulties associated with implementing these requirements are reasons that there is a lack of reliable high temperature, high pressure coal combustion data.

#### 4.1.1 Review of Char Oxidation Facilities

Coal pyrolysis and char oxidation experiments have been conducted for over several decades, and have mainly been studied in heated grids and thermogravimetric analyzers (TGAs). Some coal pyrolysis and char combustion experiments are also performed with flat flame burners or shock tubes. The previous chapter evaluated the advantages and disadvantages of drop-tube furnaces, heated grids, and TGAs. Flat flame burners (FFBs) have been used widely in atmospheric coal combustion studies (Fletcher, 1993; Mitchell, 2003), since they can closely approximate pulverized fuel combustor conditions, have high heating rates and high gas temperatures, and are easy to start up. On the other hand, flat flame burners use methane or carbon monoxide as fuel, limiting the gas compositions of combustion products (e.g., there are significant concentrations of steam from the methane flame). Isothermal temperature profiles in FFBs are also difficult to maintain.

Shock tubes can be operated at elevated pressure without being too expensive, but several drawbacks limit their usefulness: (1) The short reaction time (several milliseconds) result in very nonsteady particle temperature histories (Lester et al., 1981); (2) particles cannot be sampled in various stages of burnout; (3) the range of gas concentrations is

limited, and particle dispersion and agglomeration have proven to be problematic (Essenhigh, 1981).

Although one apparatus may be better than others in one or several aspects, certain prerequisites need to be satisfied to achieve a reasonable simulation of pulverized coal combustion. For the elevated pressure coal combustion study, basic prerequisites are:

1. Pressure: a uniform pressure should be maintained through the entire reaction process.
2. Thermal history: Sufficient information must be available to assign the temperature of the samples as a function of time throughout an entire process. High particle heating rates ( $>10^5$  K/s) are needed at coal/char initial heating stage, and high gas temperature ( $>1400$  K) is needed for char combustion experiments.
3. O<sub>2</sub> partial pressure: Uniform O<sub>2</sub> levels in the free stream throughout the combustion history can only be imposed with very dilute coal suspensions. O<sub>2</sub> partial pressure must be controlled.

These prerequisites may be closely approximated by a drop-tube furnace. A drop-tube furnace consists of a long, vertical reaction tube, through which, passes a laminar flow of gas. Two gas flows are introduced at the reactor entrance. The primary flow is introduced at the center of the reaction tube through an injection probe. The secondary flow, preheated to a certain temperature, enters the reaction zone through the annulus between the reaction tube and the injection tube. Carried by the primary flow, the small stream of particles enters the reaction zone, and flows along the reaction tube axis, reacting with the surrounding gases. These reactions are quenched as the particles enter

the cooled collection probe, located at the reactor exit. The injection tube or the collection probe is moveable to allow various particle residence times. Electric wall heaters are normally used to provide heat to the reaction tube, and the preheating is achieved by either a plasma, a combusting flame, or electric heaters.

Drop-tube furnaces have been widely used in high-pressure coal pyrolysis and char combustion studies (Lee et al., 1991; Monson, 1992; Reichelt et al., 1998; Wu et al., 2000). There are several drawbacks related to drop-tube furnaces. The heating rate of a particle in a drop tube furnace can only be as high as  $10^4$  K/s, due to the slow heat transfer rate from the secondary flow to the coal particles. It has also been observed that insulating characteristics of the refractory degraded sharply with increasing pressure (Monson, 1992), which make it very difficult to achieve high temperatures. One possible solution to this dilemma is to introduce a flat flame burner in the drop tube furnace. This attempt was implemented in the current project and will be described in the following section.

#### 4.1.2 BYU HPDT Reactor

A high pressure drop tube (HPDT) reactor was previously designed and constructed for use in both devolatilization and char oxidation tests (Monson, 1992). This drop tube reactor was later upgraded by changing from molybdenum disilicide heating elements to an Iron-Chrome-Aluminum ceramic high temperature heater, which had greater longevity than the original heating elements (Hambly, 1998).



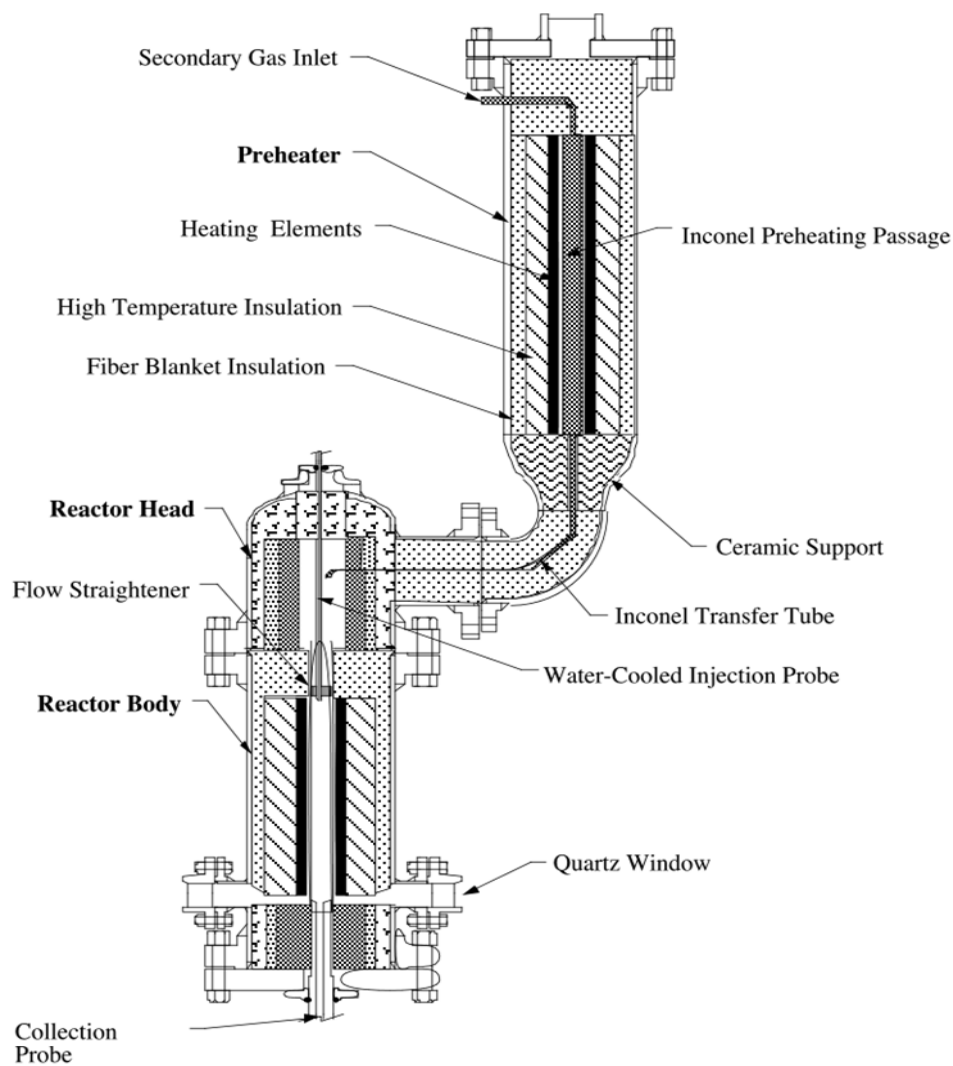


**Figure 4.1.** Schematic of high pressure drop tube reactor (Hambly, 1998).

Figures 4.1 and 4.2 show schematics of the high pressure drop tube reactor. The drop tube reactor (Figure 4.1) is an electrically-heated, laminar flow, drop tube which heating rates were about  $10^4$  K/s. Separate cylindrical electrical resistance heaters were used in the preheater and drop tube sections, each with separate set points and control thermocouples. Each control thermocouple was kept at a constant operating temperature by a PID controller. The pre-heater section heated the (secondary) nitrogen stream to about 625 K before it entered the drop tube. A water-cooled injection probe entrained the

coal particles in a small (primary) nitrogen flow, and prevented the particles from being heated until they left the probe. The residence time was changed by either raising or lowering the injection probe, or by changing the gas flow rate. The particles were injected at a slow rate ( $\sim 1\text{g/hr}$ ) in order to approximate single particle behavior. The secondary (pre-heated) and primary (injection probe) nitrogen flows were set so as to attempt to match their radially-averaged gas velocities (about  $0.7\text{-}0.85\text{ m/s}$ ). In this way it was hoped to minimize turbulence at the point of injection so that the particles would flow down the center axis of the drop tube with minimal radial dispersion. The direct observation of particle flow near the reaction tube exit showed that particles flowed along the centerline.

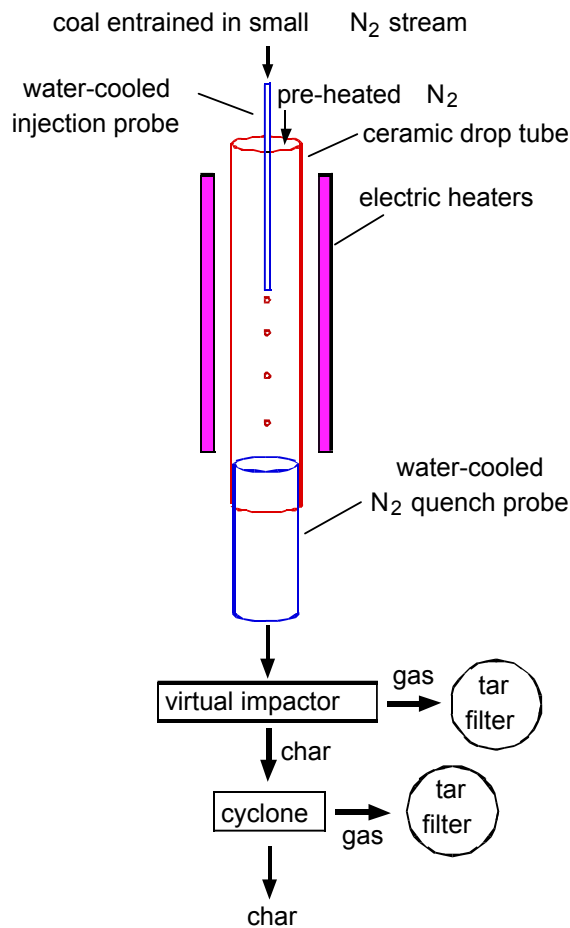


**Figure 4.2.** Schematic of drop tube reactor sample collection configuration (Perry, 1999).

Gas temperatures along this center axis can be measured with the injection and collection systems in place (except for the cyclone) using a type S thermocouple inserted from beneath the virtual impactor. Measured gas temperatures need to be corrected for radiative losses from the thermocouple bead. Pyrolysis products in the drop tube were immediately quenched by dilution with cool (300 K) nitrogen gas upon entering a water-cooled collection probe. Char was separated from most of the tar by a virtual impactor followed by a one-inch cyclone (Perry, 1999).

The HPDT could not achieve high temperatures at elevated pressures. Figure 4.3 shows the centerline temperature profiles of HPDT at different total pressure and a fixed gas flow rate. By adjusting the set point of the heaters, the temperature profiles were maintained at 1200 K. At 15 atm total pressure, the set point of the preheater had to be lowered to 580 °C to avoid failure of the controller unit. More heat loss was observed at elevated pressure, since denser gas promoted heat loss through the insulation on the reactor wall.

A series of devolatilization tests of Pitt #8 coal were conducted as part of this project in the HPDT at 1, 6, and 11 atm total pressures to evaluate the performance of the original high-pressure drop tube system. The hydrogen contents of the chars collected were around 2 wt%, which is much higher than the hydrogen content (0.5 wt%) of char normally collected from a flat flame burner. Since it was not possible to obtain fully pyrolyzed chars in the HPDT at elevated pressures, due to the heat loss limitations, it was necessary to develop another system.

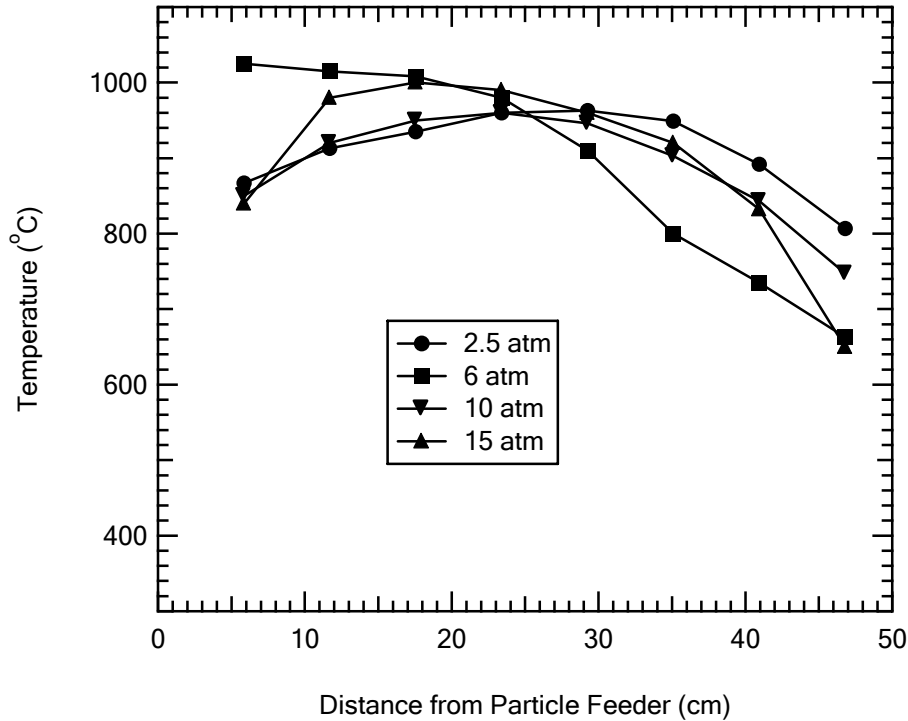


**Figure 4.3.** Measured gas temperature profiles in the HPDT.

#### 4.1.3 High Pressure Flat-Flame Burner (HPFFB) Reaction System

The high-pressure flat flame burner developed in this project was designed based on an atmospheric pressure FFB used by Ma (1996). The atmospheric FFB was also used for some comparison tests in this project. A schematic of the HPFFB is shown in the Figure 4.4.

The high-pressure flat flame burner uses the hot products of methane combustion to heat the particles. As shown in Figure 4.4, methane flows through hypodermic tubes and burns with oxidizer, which is either air or a mixture of air/O<sub>2</sub>. The “flat-flame” therefore, consists of an array of small diffusion flamelets located about 1 mm from the burner surface.

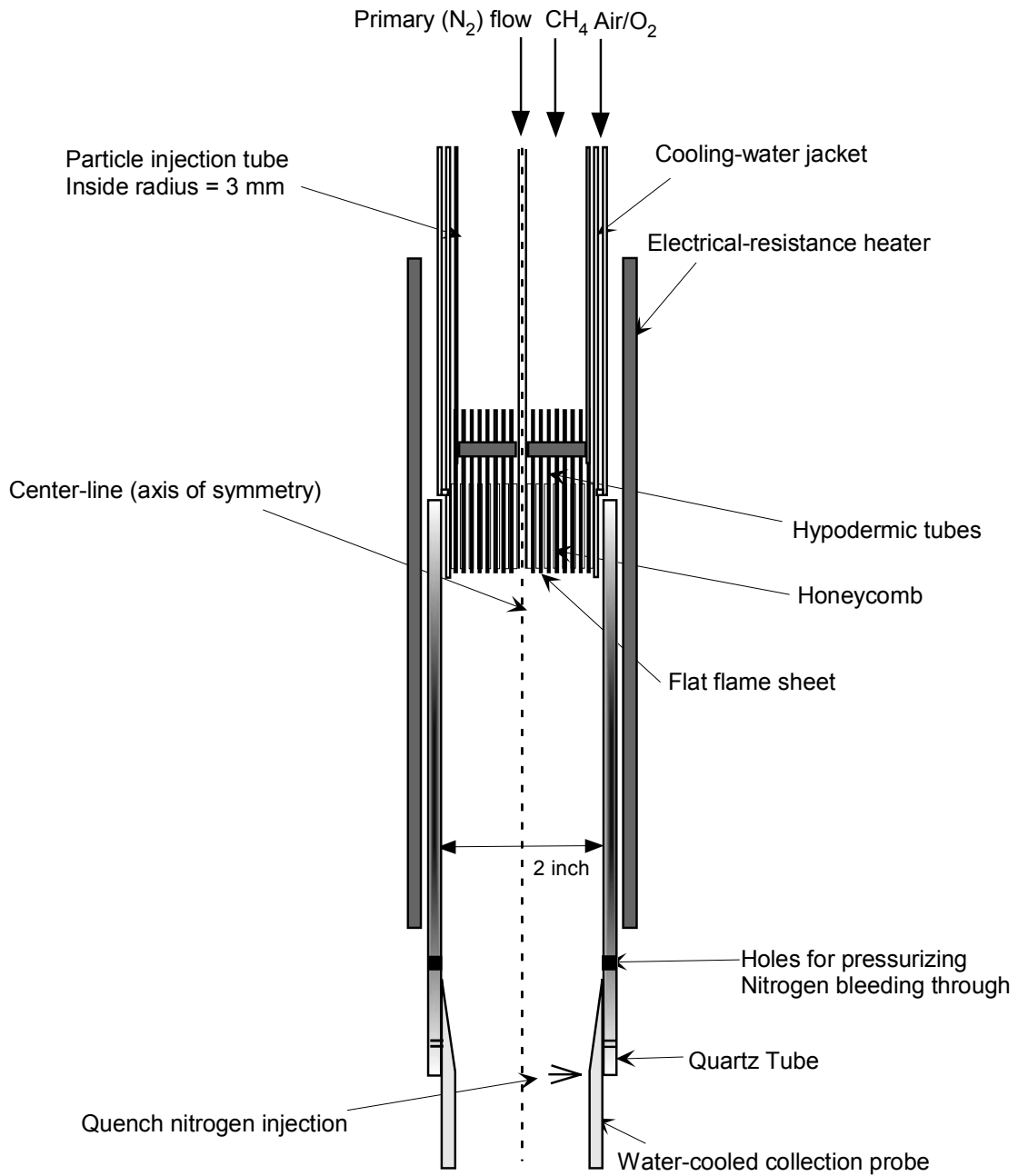


**Figure 4.4.** Schematic of the HPFFB.

The combustion in these flamelets is completed quickly (flame thicknesses of 0.5 to 1 mm), providing a uniform post-flame environment. Post-flame gas temperature and compositions can be adjusted by changing the equivalence ratio or oxidizer stream composition. Residence time can be changed by raising or lowering the burner relative to the collection probe. Coal particles were injected along the center axis of a 2 inch diameter quartz tube. In order to approximate single particle behavior (i.e. no particle-particle interactions), the coal particles were fed at a rate of less than 1 g/hr by entrainment in a small stream of nitrogen. Maximum particle heating rates in the flat flame reactor were about  $10^5$  K/s.

Figure 4.5 is a flow diagram of the HPFFB facility. High pressure nitrogen, air, oxygen, and methane were provided by a reservoir of high pressure gas bottles, with pressure regulators set to 400 psig. Four Porter flow controllers were used to control the flow rates of primary gas ( $N_2$ ), methane, air, and oxygen. Nitrogen flow used to pressurize the system was monitored by a flow meter, and the flow rate was manually adjusted. Nitrogen quench flow was also controlled in the same manner. Air and oxygen were premixed during char oxidation experiments to increase oxygen concentration. The  $O_2$  concentration in the reactor exit stream was monitored with an  $O_2$  sensor before each coal experiment. An Omega PID controller read the reactor pressure from a pressure transducer, and then controlled the system pressure by adjusting orifice size of a valve located in the reactor exhaust line (after the particle collection system). An electronic heater was used to decrease the heat loss from the reactor walls at elevated pressure. Platinum-rhodium thermocouples were installed along the length of reaction tube to

monitor gas temperature, and a PID controller was used to control the temperature of the heater.

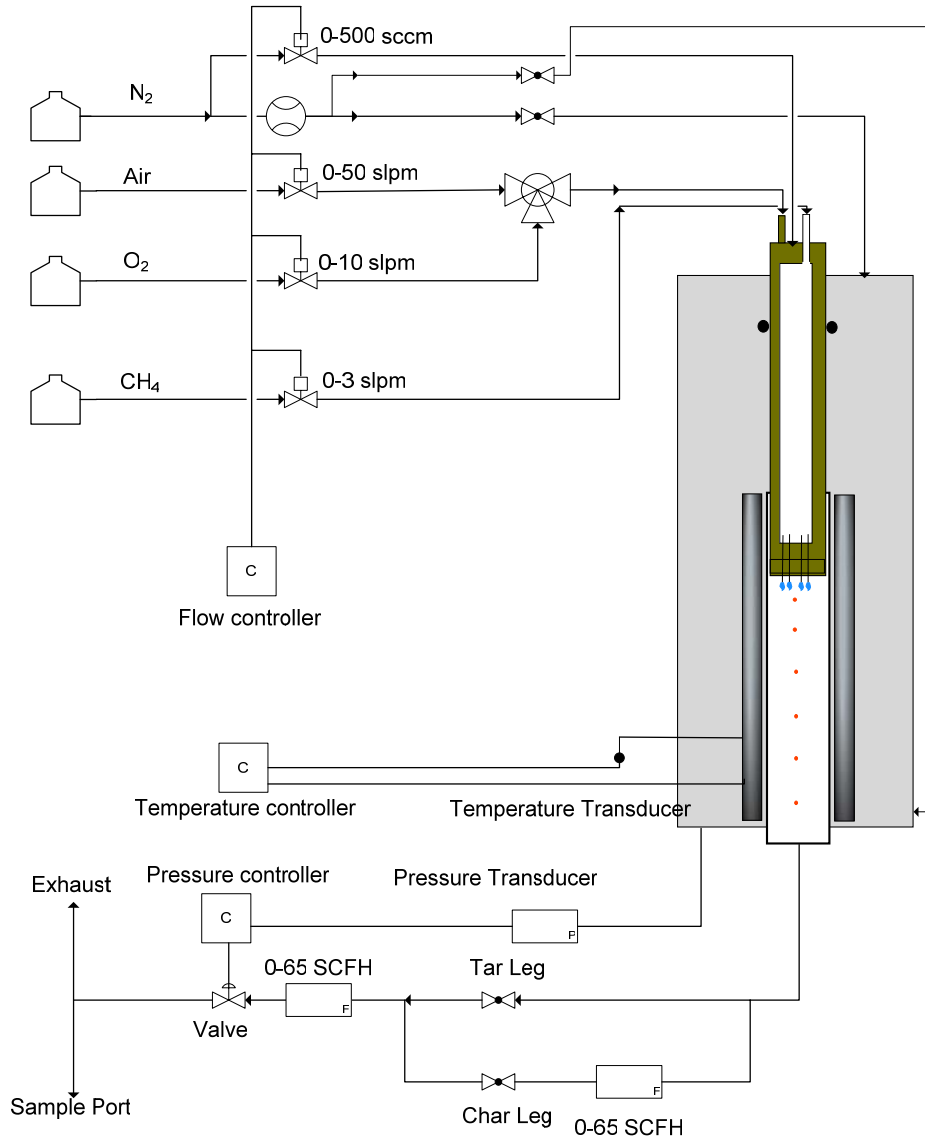


**Figure 4.5.** Schematic of the high pressure flat flame burner flow system.

#### 4.1.4 High Pressure Thermogravimetric Analyzer (HPTGA)

The Deutsche Montan Technologie (DMT) high pressure Thermogravimetric analyzer (HPTGA) (Figure 4.6) is an electrically-heated apparatus that allows the control

of temperature, pressure, gas concentrations, and flow rates. A sample is placed into a basket that is suspended from a chain attached to the microbalance, and is lowered into the furnace. The weight of the sample is then measured and recorded throughout the experiment by a computer. Time, temperature, and pressure are also recorded at a function of time. The temperature is monitored with thermocouples.

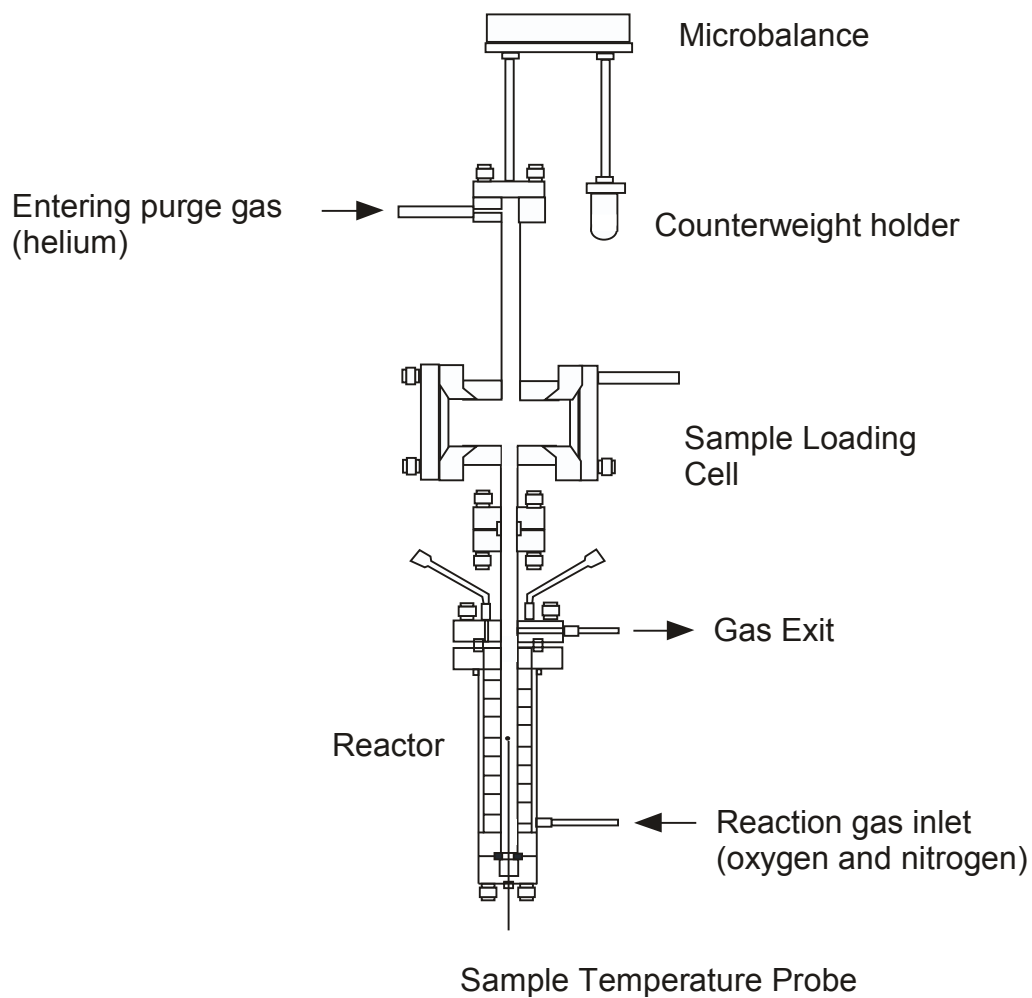


**Figure 4.6.** Schematic of the DMT high pressure Thermogravimetric Analyzer.



Pressure is controlled by a PID controller, with an accuracy of  $\pm 1\%$ . The gas compositions and flow rates are controlled by mass flow controllers, with flow rates ranging from 0.1 to 10 L/min. The maximum reactor temperature is 1100°C. The maximum heating rate achievable in the reactor is 100°C/min. The entire vessel is rated at a maximum pressure of 100 bar. Some of the gases that have been used in the HPTGA include helium, nitrogen, oxygen, carbon dioxide, carbon monoxide, argon, hydrogen, and methane.

The HPTGA was characterized by Hecker et al. (2003) to ensure that the experiments were carried out under conditions such that the reaction rate was controlled only by chemical processes and was not affected by mass or heat transfer effects. Temperature ranges, carrier gas, gas flow rates, and sample amount were chosen accordingly. Helium was chosen as the inert gas environment due to its high thermal conductivity and low density, which minimized the thermal delay and buoyancy effects, and hence increased the accuracy of the data. A 4 mg sample size was used for all of the HPTGA tests and reported here.

## **4.2 Coal Selection**

Coal rank is an important factor that affects coal devolatilization and char combustion behavior. The four coals used in this study cover a wide range of coal rank, and are typical US coals used for combustion research. These coals, were Pittsburgh #8 (hva-bituminous), Kentucky #9 (hvb-bituminous), Illinois #6 (hvc-bituminous), and Knife River (Lignite).

Figure 4.7 displays the coal compositions on a coalification diagram. The H/C atomic ratios for these coals ranged from 0.777 to 0.865, and the O/C atomic ratios ranged from 0.033 to 0.189. The three coals to the left in Figure 4.7 are higher rank, while the lower rank lignite appears on the right.

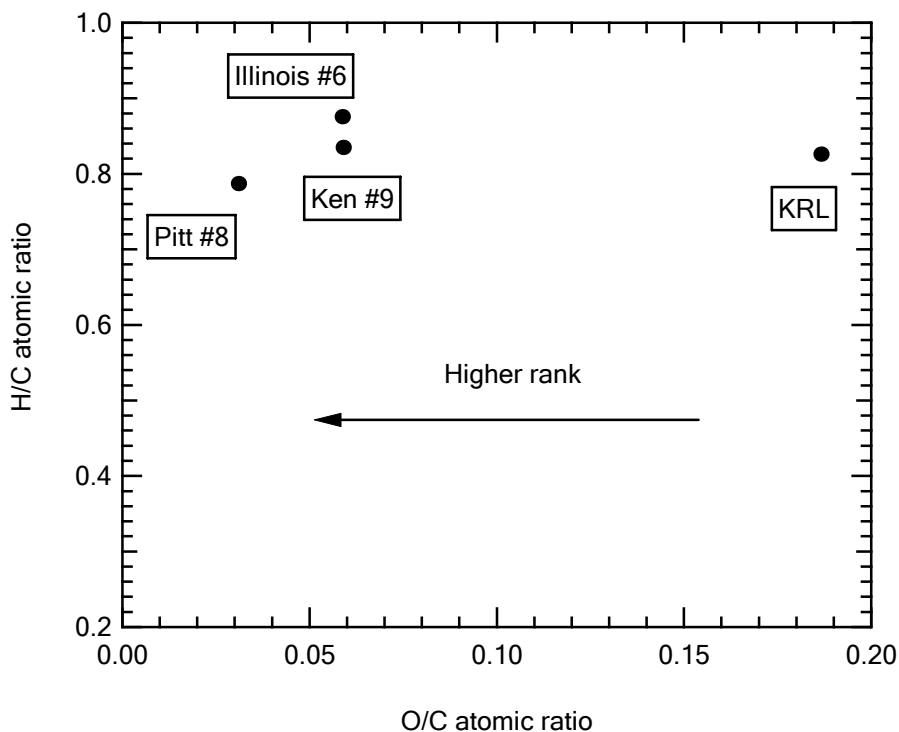


**Figure 4.7.** Parent coal compositions plotted on a coalification diagram.

### 4.3 Sample Preparation and Characterization

#### 4.3.1 Coal Preparation

All parent coals were ground and sieved in an inert atmosphere to obtain coal particles in the size range of 45-120 microns ( $\mu\text{m}$ ) for use in the devolatilization and combustion experiments. Variable size samples were used to study the effect of particle

size. All coal samples were stored in glass bottles, sealed with argon, and kept at  $-10\text{ }^{\circ}\text{C}$  until used. This prevented oxidation of the pulverized coal.

Parent coal, char, and combustion residue samples were characterized with several techniques. Each of these characterization techniques is discussed in detail in the sections that follow in this chapter.

#### 4.3.2 Proximate Analysis

The proximate analysis, as defined by ASTM (American Society for Testing Materials), is the prescribed method to determine the percentages of moisture, volatile matter, fixed carbon (by difference), and ash. These standards were carefully followed in the analysis performed as part of this study.

Moisture was measured by drying the sample in a platinum crucible at  $105\text{ }^{\circ}\text{C}$  in a hood for two hours (ASTM). The difference in weight before and after the drying procedure gives the moisture content of the sample.

The dried sample was placed back into the oven, and the oven temperature was ramped up to  $500^{\circ}\text{C}$  in one hour. The sample was flooded with air every 30 minutes by briefly opening the oven door. The temperature was then ramped up to  $750^{\circ}\text{C}$  in another hour. Finally, the sample was soaked at  $750^{\circ}\text{C}$  for at least 12 hours before the sample was cooled down and weighed again. The weight loss was used to calculate the ash content of the sample.

About one gram of coal was placed in a small (about 10 ml) tared ceramic crucible and dried for 1 hour at  $105\text{ }^{\circ}\text{C}$ . Then the crucible was cooled, weighed, and covered with a loose fitting cover. The covered crucible was placed inside a larger crucible to allow manipulation with tongs. Finally the crucibles were placed in a  $950\text{ }^{\circ}\text{C}$

muffle furnace for exactly 7 minutes and then cooled for 15 minutes before weighing. The weight loss from this analysis was used to calculate the volatile matter of the sample.

#### 4.3.3 Ultimate Analysis

A LECO CHNS-932 elemental analyzer was used to obtain the mass fraction of carbon, hydrogen, nitrogen and sulfur of the coal, char and residue samples. Each sample was weighed in a tared silver crucible before being totally burned by pure oxygen in the oxidation furnace in the analyzer. The products of combustion in the CHNS analyzer are  $\text{CO}_2$ ,  $\text{H}_2\text{O}$ ,  $\text{N}_2$ , and  $\text{SO}_x$ . The gases, which are carried through the system by the helium carrier, are swept through the oxidation tube packed by with copper sticks, which removes oxygen, to complete the conversion to  $\text{SO}_2$ . The  $\text{H}_2\text{O}$  is swept through the non-dispersive infrared adsorption detection system, then the  $\text{H}_2\text{O}$  is removed by Anhydron. The remaining gases are swept through the  $\text{SO}_2$  and  $\text{CO}_2$  analyzers. The  $\text{N}_2$  is measured by thermal conductivity after  $\text{CO}_2$  and  $\text{H}_2\text{O}$  are removed. Adjustment for blank, calibration and sample weight are applied to the final integrated signal. Oxygen content was calculated by difference.

Five replicates of each sample were analyzed in succession and the results were averaged. An appropriate standard (blank and standard run) was used between each test to account for the possible machine drift. It was observed that the measurement error for carbon and hydrogen were very small, usually within 1% (relative). Nitrogen and sulfur analyses were also quite accurate, usually with 1% (relative).

#### 4.3.4 Tracer Analysis to Calculate Mass Release

The ICP (Inductively Coupled Plasma) atomic emission spectroscopy technique was used to accurately determine the oxidative burnout or devolatilization mass release of a char sample relative to its parent coal (Fletcher and Hardesty, 1992). This technique is based on the assumption that the tracer element does not get released during pyrolysis.

Using Ti as an example, %Ti<sub>coal</sub>, %Ti<sub>char</sub>, and %Ti<sub>ash</sub> are defined as the weight percent of Ti in the parent coal, char, and ash, respectively. Coal, char and ash weights are defined as (dry basis) W<sub>coal</sub>, W<sub>char</sub>, and W<sub>ash</sub> respectively. Based on the conservation of tracer assumption:

$$(\%Ti_{coal})W_{coal} = (\%Ti_{char})W_{char} = (\%Ti_{ash})W_{ash} \quad (4.1)$$

$$W_{char} = \frac{(\%Ti_{coal})}{(\%Ti_{char})} W_{coal}, \quad \text{and} \quad W_{ash} = \frac{(\%Ti_{coal})}{(\%Ti_{ash})} W_{coal} \quad (4.2)$$

The mass release during devolatilization reaction is:

$$\%MR = \frac{W_{coal} - W_{char}}{W_{coal} - W_{ash}} \quad (4.3)$$

After mathematical manipulation, the mass release on a dry, ash-free basis is obtained:

$$\%MR = \left( \frac{\%Ti_{char} - \%Ti_{coal}}{\%Ti_{ash} - \%Ti_{coal}} \right) \left( \frac{\%Ti_{ash}}{\%Ti_{char}} \right) \quad (4.4)$$

The mass release determined by the Ti or Al tracer technique was used in this study, based on recommendation of Zhang (2001). These results were also compared with those obtained using the ash as a tracer. The final mass release reported is the averaged value of the three measurements using the Ti tracer, Al tracer, and ash tracer.

#### 4.3.5 Apparent Density

The method used to determine apparent density ratios is similar to that used by Tsai and Scaroni (1987). A graduated cylinder is filled with particles and tapped gently to allow uniform packing. The bulk density is measured, and the packing factor is assumed to be the same for the both the parent coal and the char particles. The bulk density ratio is therefore equivalent to the apparent density ratio. The mass mean diameter of the char sample is determined from a combination of the extent of mass release and the apparent density, using the following relationship (Fletcher, 1993):

$$m/m_0 = (\rho/\rho_0)(d/d_0)^3 \quad (4.5)$$

where  $d$  is the particle diameter,  $m$  is the mass of the particle,  $\rho$  is apparent density of particle, and the subscript 0 refers to the parent coal sample. The error in this experimental method has been estimated at roughly 10% (Tsai and Scaroni, 1987).

The particle swelling ratio can be calculated using the following equation transformed from equation 4.5:

$$d/d_0 = [m/m_0 / (\rho/\rho_0)]^{1/3} \quad (4.6)$$

#### 4.3.6 Specific Surface Area Measurements

Internal surface areas of coal and char samples were measured via isothermal gas adsorption using a Micromeritics Tristar 3000 instrument with either  $N_2$  or  $CO_2$  as the adsorption gas.  $N_2$  and  $CO_2$  are two adsorbates that are widely used for coal and char surface area studies.

N<sub>2</sub> adsorption is conducted at 77 K (the normal boiling point of N<sub>2</sub>). The small micropores can not be adequately accessed at this temperature because the activation energy of diffusion is too high, and because of thermal shrinkage of pores at this temperature. Therefore N<sub>2</sub> surface area is a measure of the surface area of larger pores only. N<sub>2</sub> adsorption isotherms are used to calculate surface area by the BET equation (Brunauer et al., 1938):

$$\frac{P}{V(P_0 - P)} = \frac{1}{V_m c} + \left(\frac{c-1}{V_m c}\right)\left(\frac{P}{P_0}\right) \quad (4.7)$$

where P is the pressure of a given data point, P<sub>0</sub> is the saturation vapor pressure of the adsorbate, V is the volume absorbed at a given pressure, V<sub>m</sub> is the monolayer volume, and c is a constant. Surface area can be calculated by linearizing the data by plotting P/(V(P<sub>0</sub>-P)) vs. 1/(V<sub>m</sub>c) and using a linear regression analysis to calculate the values for V<sub>m</sub> and c. The surface area can be calculated by using the density to determine the number of moles in the monolayer and assuming that each molecule covers 0.162 nm<sup>2</sup> (Smith, 1981).

CO<sub>2</sub> adsorption measurements were conducted at 273 K. Because CO<sub>2</sub> adsorption temperatures are much higher than N<sub>2</sub> adsorption temperatures, and since CO<sub>2</sub> has a slightly smaller minimum dimension than nitrogen, CO<sub>2</sub> is more suitable for measuring micropore and mesopore volume and the total surface area. The CO<sub>2</sub> adsorption isotherms are calculated using the Dubinin-Polanyi equation (Marsh and Siemieniewska, 1967).

$$\ln(W) = \ln(W_0) - D(\ln(P_0 / P))^2 \quad (4.8)$$

where W is the amount adsorbed at a given temperature, W<sub>0</sub> is micropore capacity, and  $D=(T/(\beta E_0))^2$ . Here T = the temperature of adsorption, β = a similarity coefficient that

relates the adsorbate used to the standard adsorbate (benzene), and  $E_0$  = energy of adsorption of the standard adsorbate. The surface area is calculated from the DP equation by linearizing the data by plotting  $\ln(W)$  vs.  $(\ln(P_0/P))^2$  and then using linear regression to determine the micropore capacity  $W_0$ . The surface area is then related to the micropore capacity by assuming that  $W_0$  is the monolayer volume and thus can be calculated.

#### 4.3.7 Scanning Electron Microscope (SEM) Analysis

The physical features of the surface of coal and char particles were examined using a scanning electron microscope. The SEM micrographs were obtained by Environmental Scanning Electronic Microscopy (ESEM, XL 30 ESEMFEG, Philips) in the SEM laboratory in the Biology Department at BYU. The internal structure of coal particles was examined by sectioning the particles. The detailed process can be found elsewhere (e.g. (Fletcher, 1991)).



## **5. Coal Pyrolysis and Resulting Char Properties**

High-temperature, high-pressure pyrolysis experiments were conducted on four bituminous coals. The resulting chars were collected and analyzed to find the effect of pressure on the coal pyrolysis process and char structure properties. This chapter focuses on the following aspects: mass release during pyrolysis, char elemental composition, char swelling ratio, char physical structure, and char surface area.

### **5.1 Coal Characterization**

The main body of pyrolysis experiments was conducted on the four coals listed in Table 5.1, ranging from lignite to high-volatile bituminous coal. The size of the coal particles used ranged from 45 to 130  $\mu\text{m}$ . Typical particles used in pulverized coal furnace applications have a mean diameter of  $\sim 50 \mu\text{m}$ . Oxygen content was determined by difference. Because the sulfur values as determined by the elemental analyzer include both organic and inorganic sulfur, the oxygen values are somewhat underestimated.

**Table 5.1 Characteristics of Coals**

Coal	Rank	d (µm)	Proximate Analysis (Wt %)			Ultimate Analysis (wt%, daf)				
			Moisture	Ash (dry)	VM (daf)	C	H	N	S	O <sup>a</sup>
Pitt #8	HvA-Bit	63-90	1.44	10.72	34.34	84.58	5.47	2.00	0.49	7.44
Ken #9	HvB-Bit	44-74	8.21	8.43	42.11	76.72	5.27	1.81	3.72	12.48
Ill #6	HvC-Bit	74-90	3.31	9.35	53.83	78.02	5.45	1.36	4.14	10.59
Knife River	Lignite	45-75	11.91	20.38	47.86	62.23	4.23	0.95	1.28	31.30

a.  $O = 100 - (C + H + N + S)$

## 5.2 Reaction Conditions for the Pyrolysis Experiments

All of the elevated pressure char preparation experiments were conducted using the methane-air high-pressure flat flame burner (HPFFB, see Figure 4.4). Maximum gas temperatures were about 1300 °C at pressures of 2.5 to 15 atm, with particle heating rates of  $10^5$  K/s. Atmospheric pressure (0.85 atm) char preparation was conducted using an atmospheric flat flame burner.

In ideal experiments, the pressure could be changed without changing temperature history, residence time, or heating rate. However, this is not possible in an entrained flow experiment. When pressure is increased, gas velocity decreases when mass flow rate is held constant. Gas velocity can be adjusted by increasing the total mass flow rate of entrainment gas, but this changes the heating characteristics (i.e., gas temperature) in the reactor. Residence time is adjusted by changing the reaction length, which was changed here by moving the burner up and down. However, excessive heat was lost to the water-cooled burner when the burner was lowered significantly into the furnace, thus limiting the use of this measure.

The high-temperature coal pyrolysis process is usually completed in less than 50 ms, after which little reaction occurs. In this study, all pyrolysis experiments had a residence time longer than 120 ms, and hence collected samples were fully pyrolyzed.

The initial plan was to conduct all of the pyrolysis experiments under fuel-rich post-flame conditions, since this worked well in atmospheric FFB experiments. However, the fuel-rich CH<sub>4</sub> flame produced soot at elevated pressures, which contaminated the char samples and affected the experimental results. To avoid this, all of the pyrolysis experiments were conducted in a slightly oxidizing condition (0.2~0.5 mol% O<sub>2</sub> in the post-flame gases). Such a low concentration of O<sub>2</sub> had a negligible effect on resulting char properties. An oxygen analyzer was used to monitor the composition of the gases exiting the reactor.

The desired flow rates of the combustion gases were determined by computing the adiabatic flame temperatures, then comparing the measured temperature profiles and O<sub>2</sub> concentrations at different pressures. Table C.1 (See Appendix C) lists the flow rates of CH<sub>4</sub> and air at different pressures.

The centerline gas temperature profile was measured using a type S platinum/rhodium thermocouple inserted from the bottom of reactor. The thermocouple bead diameter was 200 μm. Figure 5.1 shows the measured gas temperature profiles for the four pressures. Thermocouple readings were corrected for radiation losses (Appendix A). Temperature decreased dramatically at longer distances from the burner as pressure increased. This was caused by larger heat loss at high pressure.

The particle velocity was modeled using Fluent, and the particle velocity profile and gas temperature profile were modeled using the CPDCP code (Fletcher et al., 1990).

The effect of primary gas was considered with the Fluent modeling (the detailed modeling is described in Appendix F). The particle energy conservation equation used in the CPDCP code is:

$$v_p m_p c_p \frac{dT}{dz} = h A_p (T_g - T_p) \frac{B}{e^B - 1} - \sigma \epsilon_p A_p (T_p^4 - T_w^4) - v_p \frac{dm}{dz} \Delta H \quad (5.1)$$

where  $h = Nu k_g / d_p$ . In this equation, particle properties are known, and velocity ( $v_p$ ) was obtained from the Fluent modeling results. Gas properties changed with CH<sub>4</sub>/air flow rates, temperature, and pressure, and were modeled using a chemical equilibrium code. Particle temperature histories calculated at early residence times, characteristic of

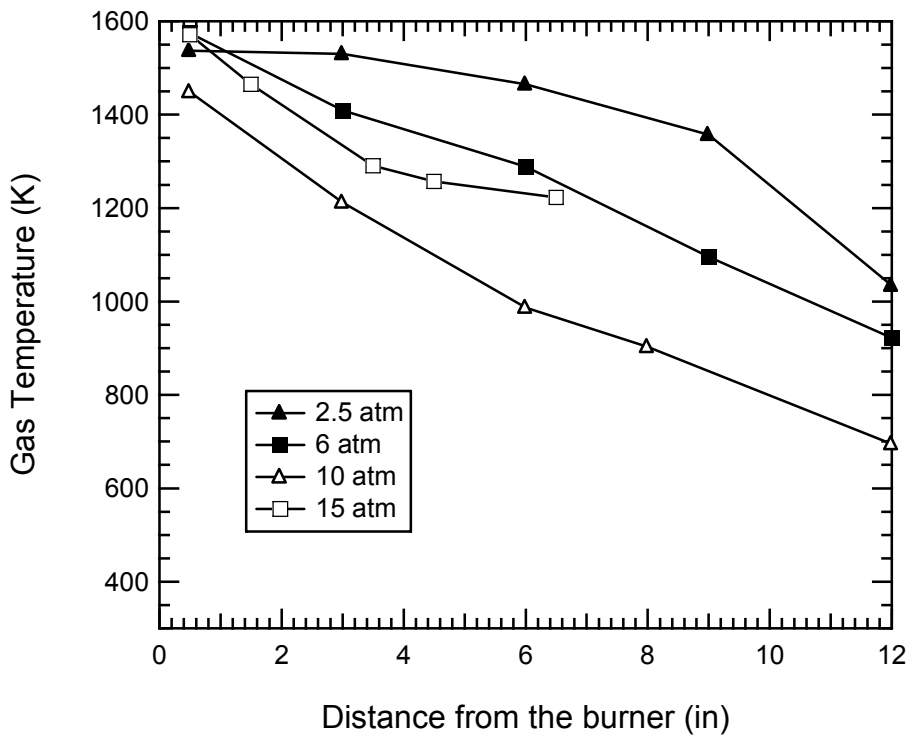


**Figure 5.1.** Measured gas temperature profiles in the HPFFB. These conditions are referred as the “1573 K” condition, since they all have a maximum temperature close to 1573 K.

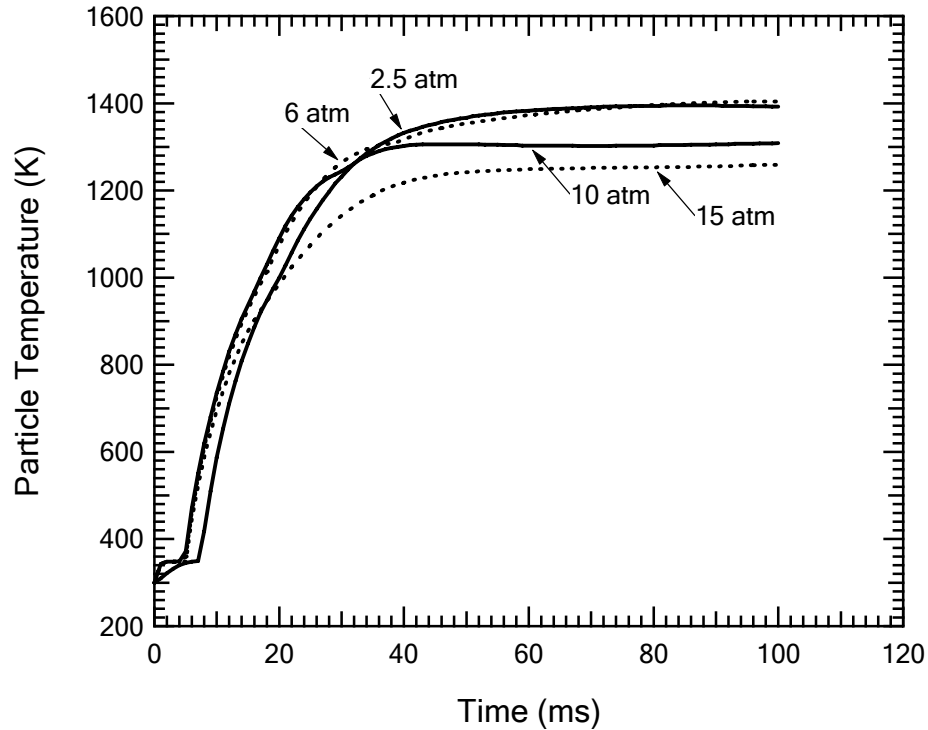


**Figure 5.2.** Calculated early particle temperature histories for the different pressure conditions in the HPFFB. These particular calculations were for the Ill #6 coal.

pyrolysis times, are shown in Figure 5.2 for each pressure. Each condition had a maximum particle heating rate of  $10^5$  K/s.

### 5.3 Mass Release during Coal Pyrolysis

The HPFFB coal pyrolysis data were obtained in the 1573 K gas condition at residence times ranging from 231 ms to 2 sec and pressures ranging from 2.5 atm to 15 atm. The atmospheric pressure data (actually 0.85 atm in Utah) were obtained at 1300 K in a separate atmospheric flat-flame burner facility (Zhang and Fletcher, 2001) where the char samples were collected immediately above the luminous devolatilization zone. The total volatiles yield data for the four coals are shown in Figure 5.3 as a function of

pressure. The measured volatiles yields exceeded the ASTM total volatiles yields (see Table 5.1) for all coals at low to moderate pressures (< 7 atm). This is apparently caused by the high pyrolysis temperature, the high heating rate, and the single particle behavior in the HPFFB experiment. The measured volatiles yields of all four coals decreased with increasing pressure. The effect of coal rank on coal mass release is not very clear in this figure, due to the changes in particle temperature profiles and residence times for the different conditions.

The decreased volatiles yield at increased pressure during devolatilization is commonly thought to be caused by two physical processes: vapor-liquid equilibrium effects and transport effects (Fletcher et al., 1990). Bituminous coal tars exhibit a broad molecular weight distribution. As total pressure is increased, tar precursors with high molecular weights no longer have sufficient vapor pressure to evaporate, and are retained in the condensed phase (Solomon and Fletcher, 1994). Elevated pressure also increases the resistance of volatiles leaving the coal particle, possibly decreasing the total volatiles yield (Lee et al., 1991).

The Chemical Percolation Devolatilization (CPD) model (Fletcher et al., 1990; Fletcher, 1989; Grant et al., 1989) was developed to predict devolatilization behavior of rapidly heated coal, based on the chemical structure of the parent coal. In this study, coal-dependent input parameters for the CPD model were calculated using proximate and ultimate analysis data using a correlation of previous <sup>13</sup>C NMR analyses (Genetti et al., 1999). These input parameters are listed in Table 5.2. Model constants were not tuned to match the volatiles yield data.

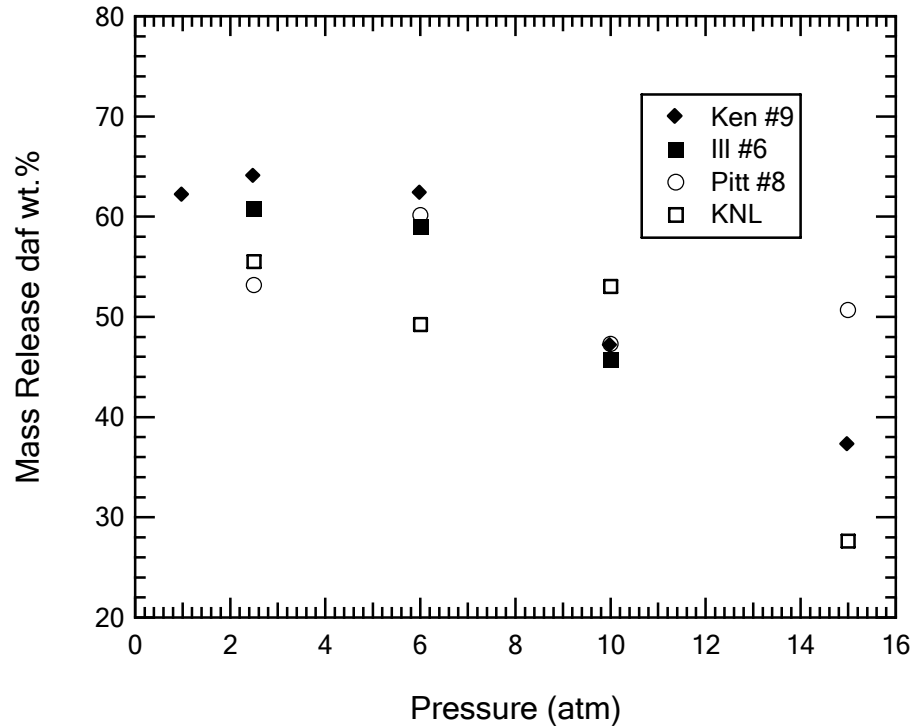


**Figure 5.3.** Measured mass release due to pyrolysis for chars obtained at different pressures.

**Table 5.2 Coal Structure Parameters Used in CPD Modeling**

Coal	$M_{\delta}$	$MW_{cl}$	$p_0$	$\sigma+1$	$c_0$
Pitt #8	29.1	344.4	0.5	4.8	0.0
Ken #9	39.2	386.7	0.5	5.2	0.0
Ill #6	40.5	381.4	0.5	5.2	0.0
Knife River	53.3	337.3	0.7	3.7	0.2

In the CPD model, a vapor-liquid equilibrium submodel, based on the molecular weight of tar precursors, accounts for the change in tar yield observed as the total pressure is changed. The CPD model was used to predict the coal mass release using the measured gas temperature profile, the gas velocities predicted using FLUENT software, and the aforementioned particle energy balance (Eq. 5.1). CPD model predictions are

shown in Figure 5.4, including predicted tar yields. Each pressure condition was modeled using the appropriate particle temperature history, although lines are drawn through the modeling results for convenience. Modeling results are generally comparable to the experiments for pressures up to 6 atm, and slightly overestimate the measured amount of mass release at higher pressures.

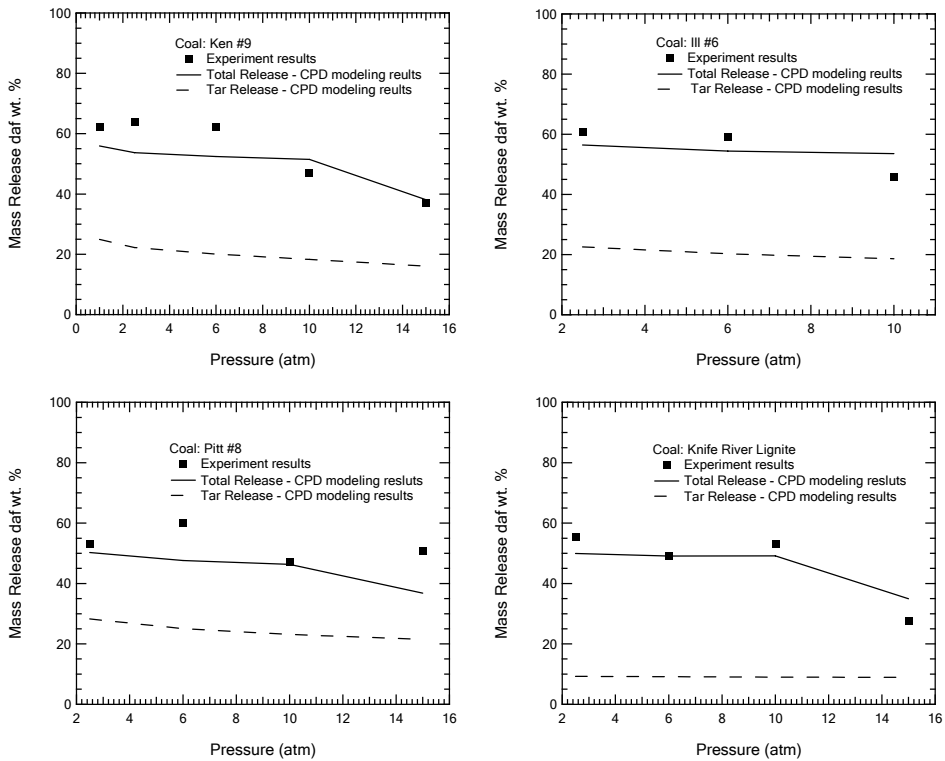


**Figure 5.4.** Predicted and measured mass release as a function of pressure. The solid lines represent predicted volatiles yields using the CPD model, while the dashed lines represent predicted tar yields. (a) Ken #9, (b) Ill #6, (c) Pitt #8, (d) Knife River Lignite.



#### 5.4 Elemental Composition of Chars Prepared at Different Pressures

The elemental composition ratios of coal chars collected at different pressures are shown in Figure 5.5. For the Kentucky #9 coal, the decrease in H/C ratio between 0.85 and 2.5 atm was due to the difference in temperature between the two experiments (1300 K at 0.85 atm vs. 1573 K at elevated pressures). The hydrogen contents in chars and fraction of the initial amount of hydrogen that remains in the char are shown in Figure 5.6. At higher pressures, the H/C and O/C ratios increased because less tar escaped from the char due to vapor pressure effects at elevated pressures (the tar is enriched in hydrogen). Although a decrease in mass release was observed when pressure was increased from 10 atm to 15 atm, both H/C and O/C ratios remained relatively stable when pressure was higher than 6 atm. For the Illinois #6 coal, both H/C and O/C ratios were relatively stable, though the measured mass release decreased slightly with increasing pressure.

The stable H/C ratio in the chars at elevated pressure can be explained based on several competing phenomena. First, at increased pressure, the tar yield decreases due to vapor pressure effects in the high molecular weight tar precursors. Thus, the heavier tars are only vaporized at lower pressures. Second, the heavier tars are enriched in carbon and depleted in hydrogen, due to their higher carbon aromaticity than the lighter tars. The tar that vaporizes at elevated pressure is therefore enriched in hydrogen (Solomon and Fletcher, 1994) beyond the tar evolved at low pressure, but less tar yield is observed at the higher pressure. The tar molecules that would have vaporized at lower pressures, but that stay in the char at elevated pressure, are slightly higher in hydrogen content than the char. These heavier tar precursors that remain in the coal particle serve as light gas precursors, and the evolution of light gas from the char removes hydrogen-rich side

chains. Thus, the light gas yield increases as pressure increases, and the light gases are enriched in hydrogen compared to the char. The net effect is that the char H/C ratio remains relatively constant at the elevated pressures.

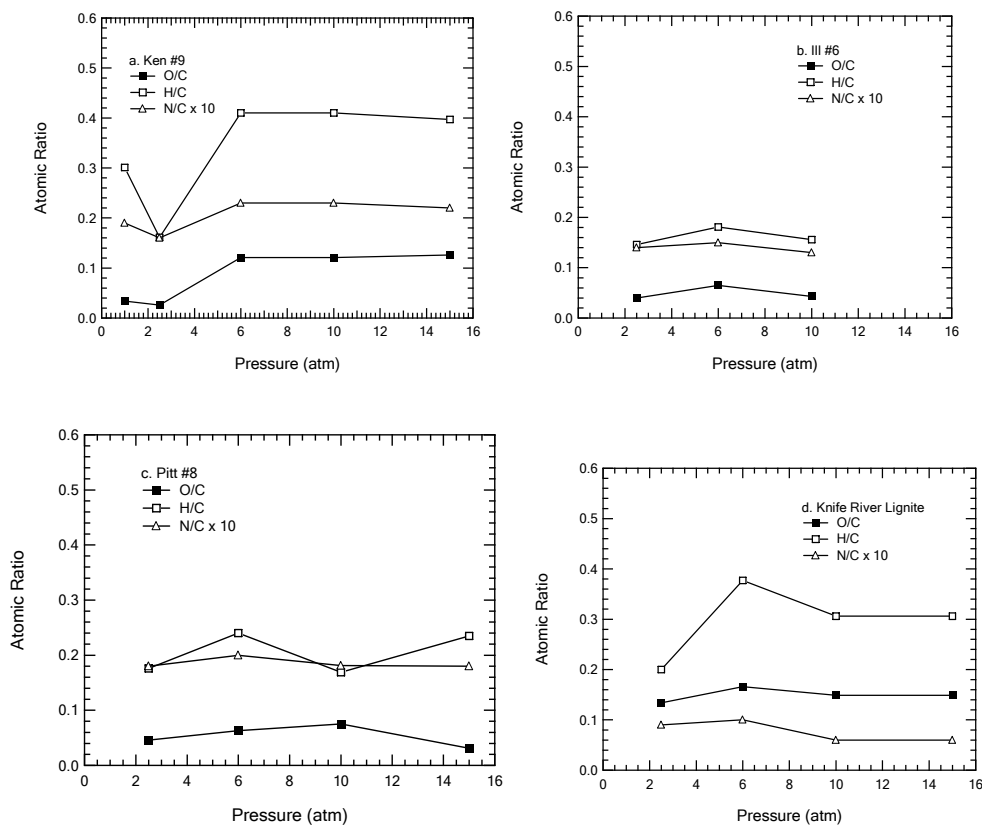


**Figure 5.5.** Elemental compositions of chars as a function of pressure. (a) Ken #9, (b) Ill #6, (c) Pitt #8, (d) Knife River Lignite.

Another factor influencing the char H/C ratios in these experiments may be the effect of residence time. The particle residence time in these experiments ranged from 0.3 s to 2.0 s when pressure was increased from 2.5 atm to 15 atm. The total mass flow rate of gas into the reactor increased only slightly with pressure in order to keep the gas temperature at 1300°C, so as pressure increased, and hence gas density increased, the velocity had to decrease. The ultimate hydrogen content of char can be affected by both

the temperature and the reaction time (Genetti et al., 1999). This residence time effect may also offset the higher H/C ratio caused by elevated pressure.

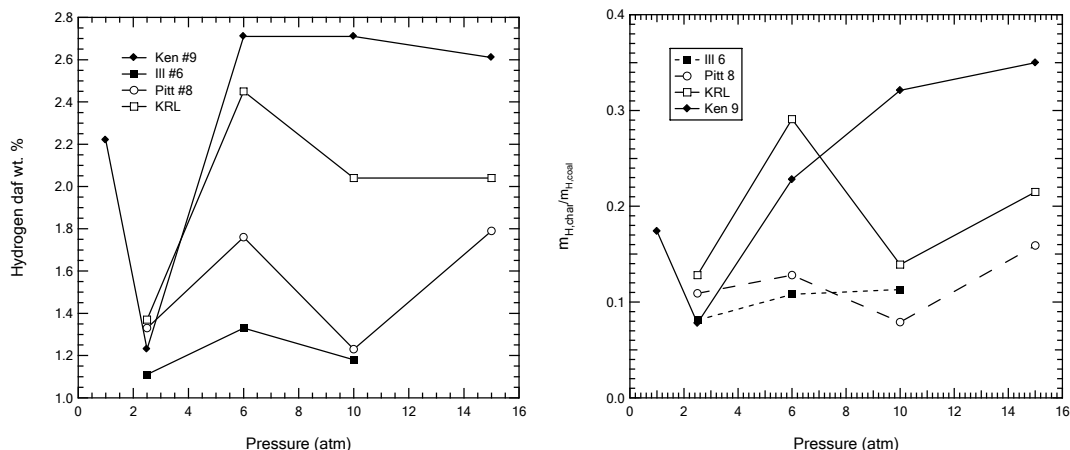


**Figure 5.6.** Hydrogen content in the chars after pyrolysis as a function of pressure (left) and fraction of the initial amount of nitrogen that remains in the char (right).

The N/C ratios in the chars did not change significantly as a function of pressure, as shown in Figure 5.7. The fraction of the initial amount of nitrogen that remains in the char was calculated from the elemental compositions of the coal and char and from the mass remaining ( $m/m_0$ ). Figure 5.7 shows that at least for two of the coals (Ken #9 and Ill #6), more nitrogen remained in the char at increased pressures. The nitrogen release data for the other two coals (Pitt #8 and KRL) are more scattered, but seem to indicate that the fraction of nitrogen remaining in the char stayed relatively constant with pressure.

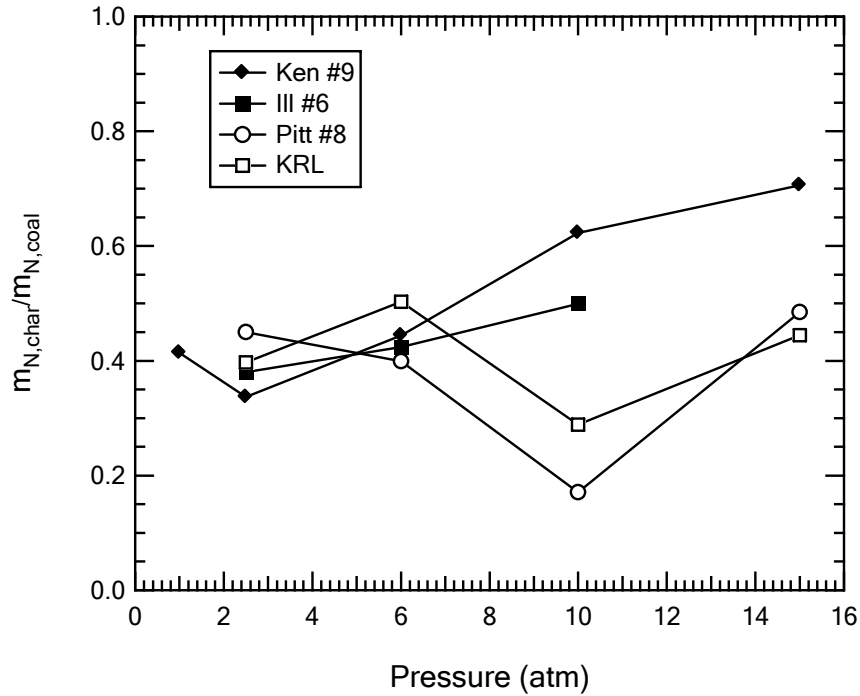


**Figure 5.7.** Fraction of initial nitrogen remaining in the char ( $m_{N,char}/m_{N,coal}$ ) after pyrolysis as a function of pressure.

## 5.5 Effects of Pressure on Coal Swelling Ratios

Figure 5.8 shows measured apparent densities as a function of pressure from 1 atm to 15 atm. Fig 5.9 shows the swelling ratios of chars collected at different pressures. The heating rate of the HPFFB char in this study was estimated to be about  $10^5$  K/s (see Figure 5.2). This heating rate is higher than in the drop tube reactor because there is no wake from the water-cooled coal injector; the particles in a FFB are convectively heated

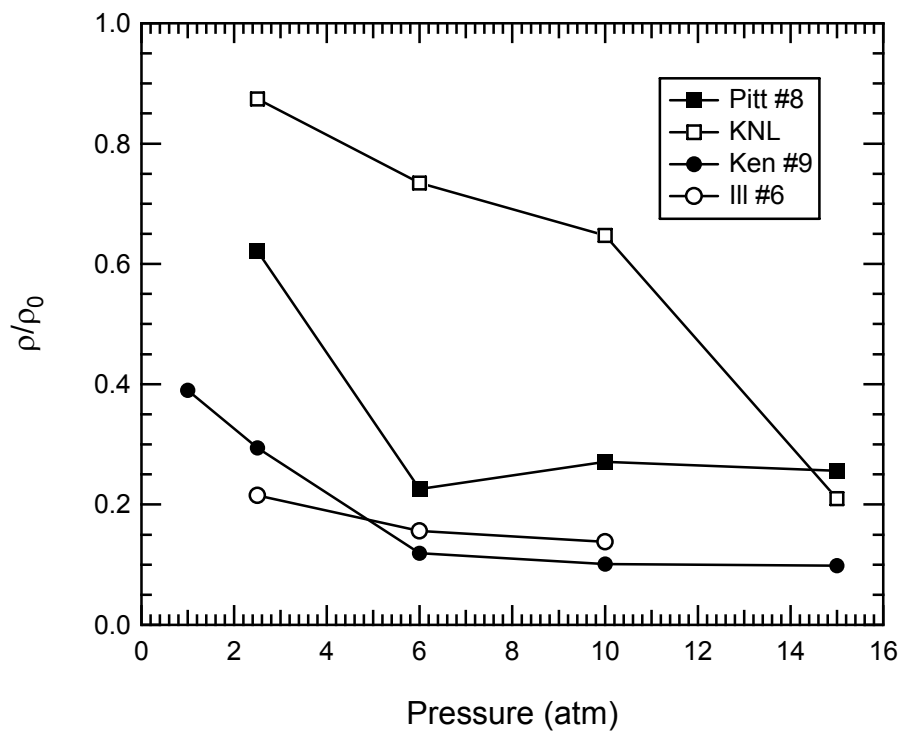


**Figure 5.8.** Apparent densities for chars prepared in the HPFFB.

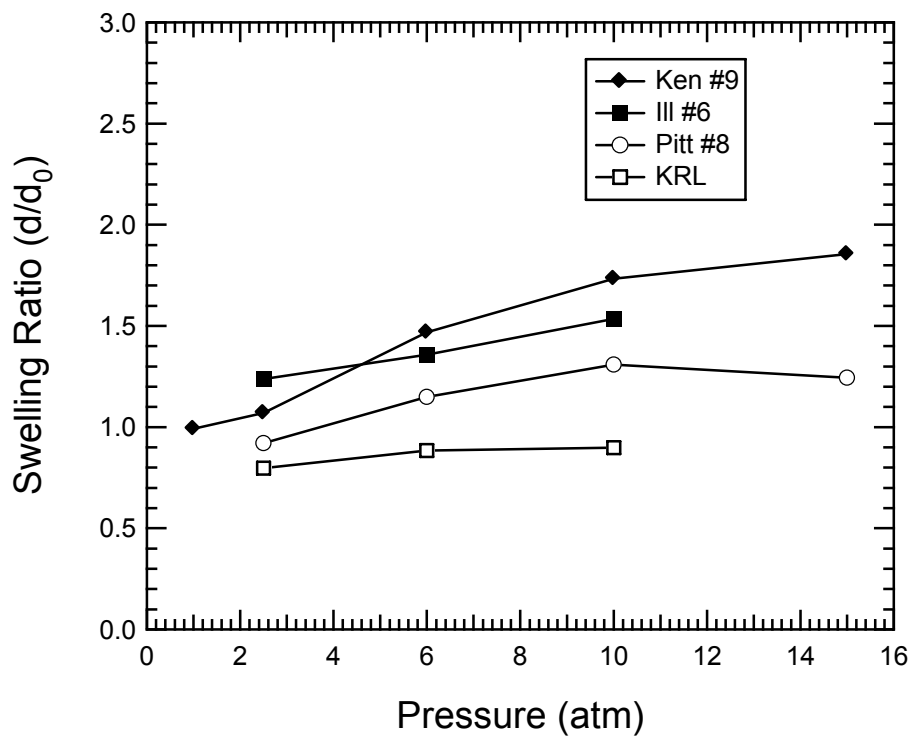


**Figure 5.9.** Swelling ratios of four coal chars as a function of preparation pressure.

as they pass through a flame front. The experimental conditions of this experiment are compared with other studies (Lee et al., 1991; Wu et al., 2000) in Table 5.3.

**Table 5.3 Comparisons of Experimental Conditions**

	Authors		
	Lee et al.(1991)	Wu et al. (2000)	Current work
Coal	Illinois No.6	Australian Bituminous coal	Three US bituminous coals and one lignite
Particle size	62 $\mu\text{m}$ mean particle diameter	63-90 $\mu\text{m}$	75 $\mu\text{m}$ average diameter
Apparatus	HEF (high-pressure entrained-flow furnace)	PDTF (pressurized drop-tube furnace)	HPFFB (high-pressure flat flame burner)
Heating rate	$\sim 10^4$ K/s	$\sim 10^4$ - $10^5$ K/s	$> 10^5$ K/s
Temperature	1189 K	1573 K	1573 K
Pressure	0.1-3.8 MPa	0.1-1.5 MPa	0.1-1.5 MPa
Atmosphere	$\text{N}_2$	$\text{N}_2$ , with $\text{O}_2$ to burn volatiles	Combustion product of $\text{CH}_4/\text{Air}$

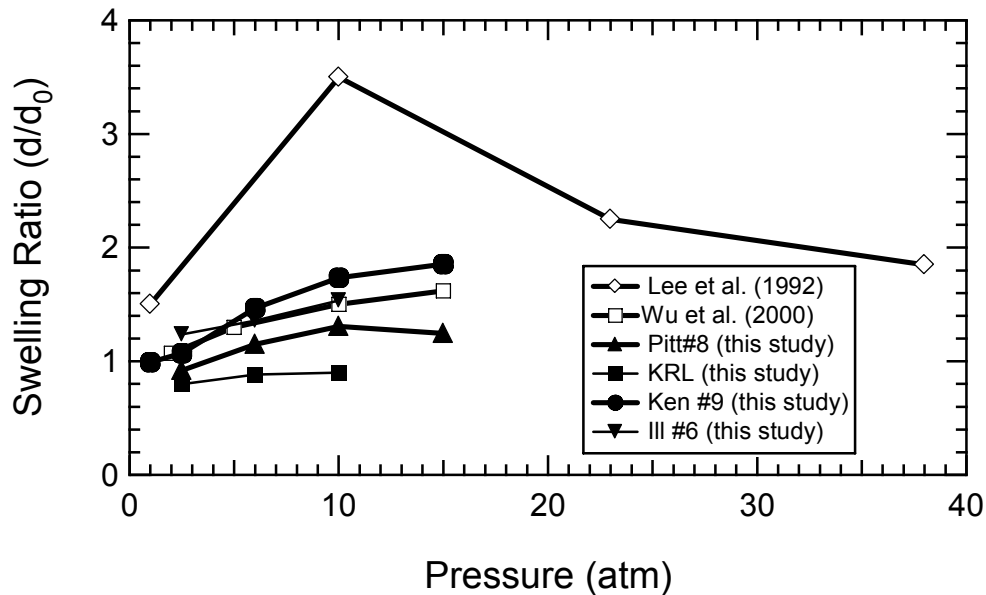


**Figure 5.10.** Comparison of swelling ratio in the HPFFB with other studies.

This high heating rate condition ( $10^5$  K/s) strongly changed the devolatilization characteristics during the early stages of coal pyrolysis, as shown by the comparison of

swelling ratios in Figure 5.10. The swelling ratios for Pitt #8 coal and Knife River lignite in the HPFFB were smaller than observed in the PDTF (Wu et al., 2000) or the high-pressure entrained-flow furnace (Lee et al., 1991). The Ken #9 and Ill #6 coals had similar or slightly larger swelling ratio than the data of Wu and coworkers, but smaller swelling ratios than the data of Lee et al. The increased swelling ratio from lignite to Ken #9 bituminous coal indicated that the effect of pressure on the coal swelling ratio is rank dependent. Similar rank dependent results were reported by Lee et al. (1991). However, there is no accepted theory of how coal rank affects the swelling ratio. In this study, coals with higher ASTM volatile contents, such as Ken #9 and Ill #6, had higher swelling ratio than the coals with lower ASTM volatile contents such as Pitt #8 and Knife River lignite. Pitt #8 coal, which has 34 wt% (daf) ASTM volatile, had a lower swelling ratio than the coal used in Wu's experiment (2000), which had 32 wt% (daf) ASTM volatile content. This was likely caused by the higher heating rate of  $10^5$  K/s of HPFFB, which was higher than the reported heating rate  $10^4\sim 10^5$  K/s of PDTF (Wu et al., 2000). This difference in heating rate was apparently counteracted by the increased volatile content of Ken #9 and Ill #6. Swelling ratios of all HPFFB chars increased with the increase of char preparation pressure. The swelling ratio of Pitt #8 coal increased when pressure increased, reaching a maximum value at 10 atm, and then dropped at 15 atm. The other coals also exhibited increasing swelling ratios within the pressure range of 1-15 atm. It is expected that the swelling ratios of these coals will increase with increasing pressure to a peak value and then decrease.

Both heating rate and pressure affect swelling characteristics during coal pyrolysis. At low heating rates (such as in a TGA, or  $\sim 1$  K/s), volatiles can diffuse

through the pores without causing an internal pressure high enough to cause the particle to swell. At moderate heating rates (such as in a drop tube, or  $10^4$  K/s), the volatiles formed in the particle interior are formed faster than when they can escape through the pores, and swelling occurs if the particle has softened. At high heating rates (approaching  $10^5$  K/s), the volatiles are formed faster than the swelling process can accommodate, and the bubbles burst. At elevated pressure, higher molecular weight tar precursors do not vaporize, causing more plasticity in softening coals. Hence if conditions are right, enhanced swelling is observed at increased pressures. However, at high heating rates, the surface tension in the bubble walls is overcome and the bubbles burst before significant swelling occurs. For low rank coals and lignites, little softening occurs, and the discharge of moisture and light gases with little tar formation can actually cause particle shrinkage. The physical structure of the char significantly affects its high temperature oxidation or gasification rate.

Comprehensive coal char oxidation models need precise prediction of the swelling ratio. A correlation of coal swelling ratio with pressure and carbon content of the parent coal was developed by Benfell (2001). This correlation predicts the change of the coal swelling ratio with increased pressure from medium heating rate coal pyrolysis ( $\sim 10^4$  K/s), but overestimates swelling ratio for high heating rate pyrolysis ( $\sim 10^5$  K/s). Since practical pulverized coal combustion occurs at high temperatures (2000 K) and heating rates ( $10^6$  K/s), such correlations should include the effects of heating rate.



## 5.6 Effects of Pressure on Char Morphology

Scanning electron micrographs (SEM) of the chars collected in this study are shown in Figures 5.11-5.15. The SEM of cross sections of Pitt #8 and Knife River lignite char samples are shown in Figure 5.12 and Figure 5.13, respectively. The Pitt #8 char particles show evidence of softening bubble formation, with large blow holes where bubbles have ruptured. The 10 atm particles seem to have smaller surface holes than the 6 atm char, which is consistent with the small increase in swelling behavior shown in Figure 5.9. As expected, the lignite chars did not show softening behavior (see Figures 5.11 and 13).

SEM images of the external surface of the Kentucky #9 chars produced at pressures of 0.85, 2.5, 6, 10, and 15 atm are shown in Figure 5.14. The letters a-e in the top left corner of each image represent increasing pressure conditions, respectively. The exterior morphology of char particles clearly changed with increasing pressure. The surfaces of chars produced at 0.85 and 2.5 atm show similar characteristics. The particles have a porous external surface, with blow holes created by volatiles as the internal particle pressure overcame the surface tension of the softened particle. Some smaller char fragments were also observed, possibly caused by fragmentation at these high heating rates. The char particle surface became less coarse as pressure increased from 6 atm to 15 atm, and bubbles were clearly visible beneath the particle surface, which implies a thin wall. Only a small number of fragments were visible at the elevated pressures, and blow holes were not observed like in the char produced at lower pressure.

Cross section SEM images of the Kentucky #9 char particles are shown in Figure 5.15. Char bubble structure appears to be affected by the pressure. The char particles

produced at lower pressure tend to have one or several large bubbles in the central area, with small bubble clusters appearing near the outer surface of the char particles (i.e., the char “skin”). For char particles produced at elevated pressures, bubbles are more evenly distributed throughout the particle interior, and the walls between pores are thinner than in the chars made at lower pressure. Similar phenomena can also be observed from Pitt #8 chars (see Figure 5.12).

The observed phenomena can be explained using char structure evolution mechanism of Yu et al. (2002) as shown in Figure 5.16. The bubble structure of chars produced at lower pressure is in the later stage of structure evolution, and chars produced at higher pressure are in the early stage. The char structure evolution is restrained by elevated pressure. Considerable amounts of volatiles are transported through bubble movement. Small bubbles are created during the initial stage of devolatilization, and then these small bubbles merge together to form larger bubbles. The larger bubbles move to the particle exterior surface and finally burst open. At high pressure, transport of bubbles is more difficult, and a char with characteristics of the early stage of bubble evolution is produced. The char structure observed illustrates one possible reason for lower mass release at elevated pressure.

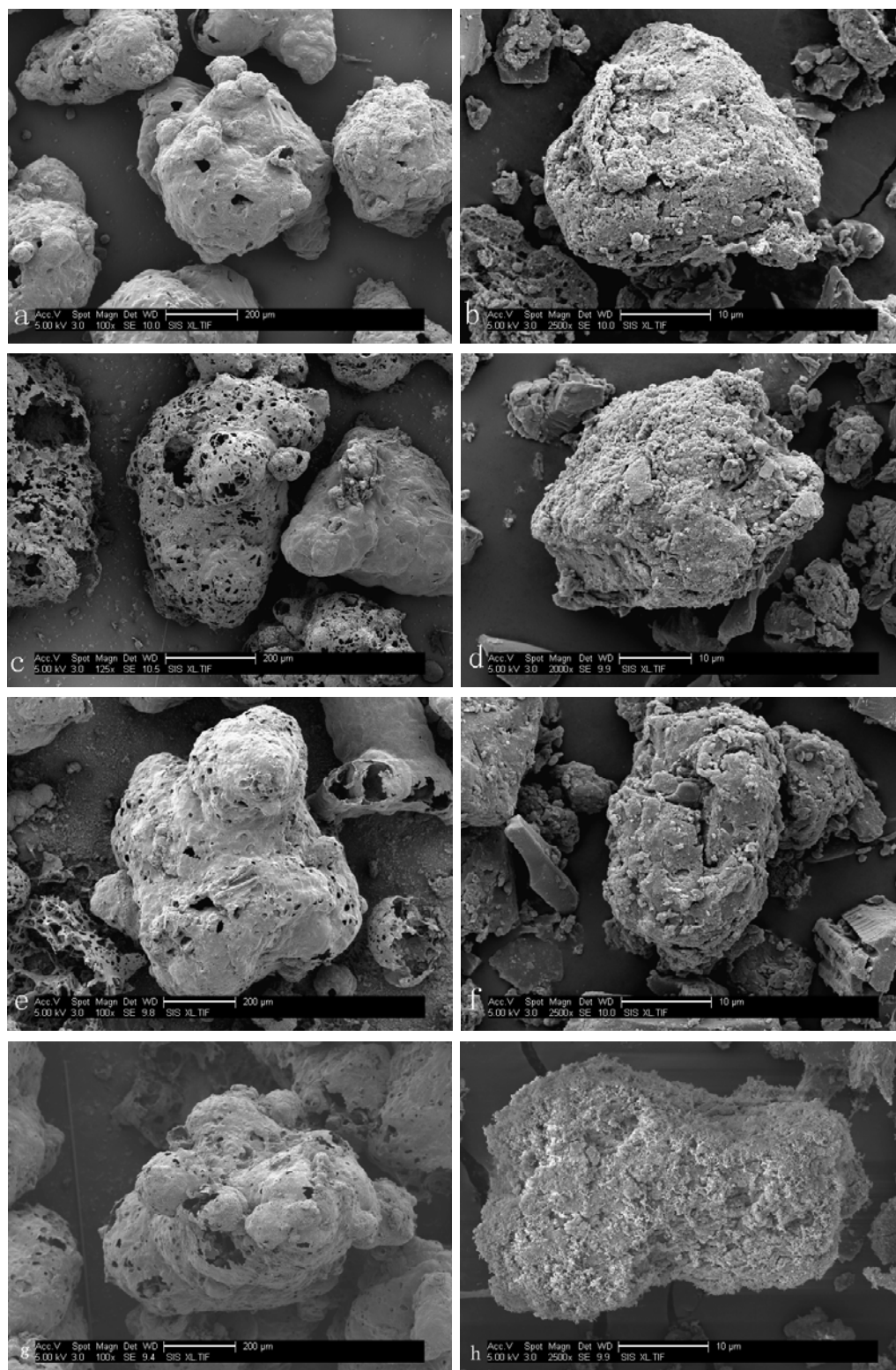


**Figure 5.11.** SEM micrograph of char produced from pyrolysis of Pitt #8 coal and Knife River Lignite. (a) Pitt #8 1 atm, (b) KRL 1 atm (c) Pitt #8 6 atm, (d) KRL 6 atm, (e) Pitt #8 10 atm, (f) KRL 10 atm, (g) Pitt #8 15 atm, (h) Pitt #8 15 atm.

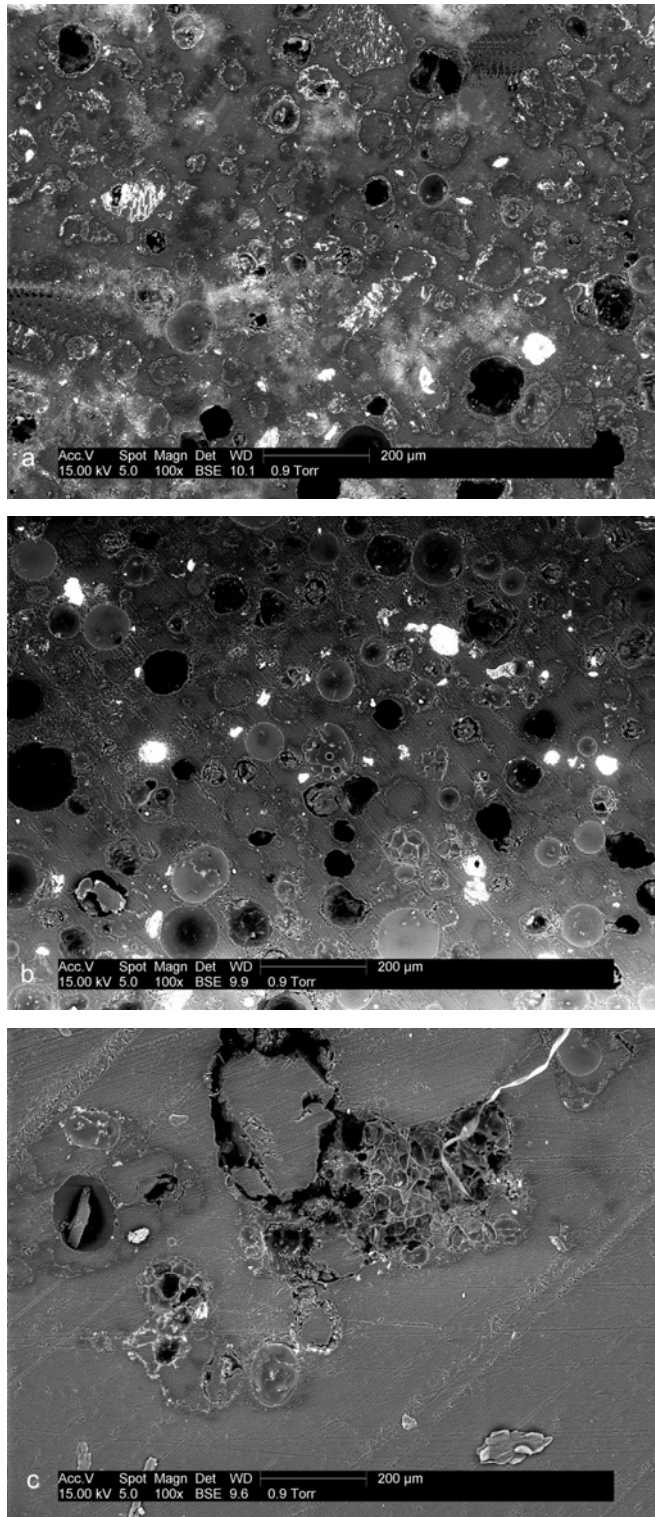


**Figure 5.12.** SEM micrograph of char cross section produced from pyrolysis of Pitt #8 coal. (a) 2.5 atm (b) 6 atm (c) 15 atm.

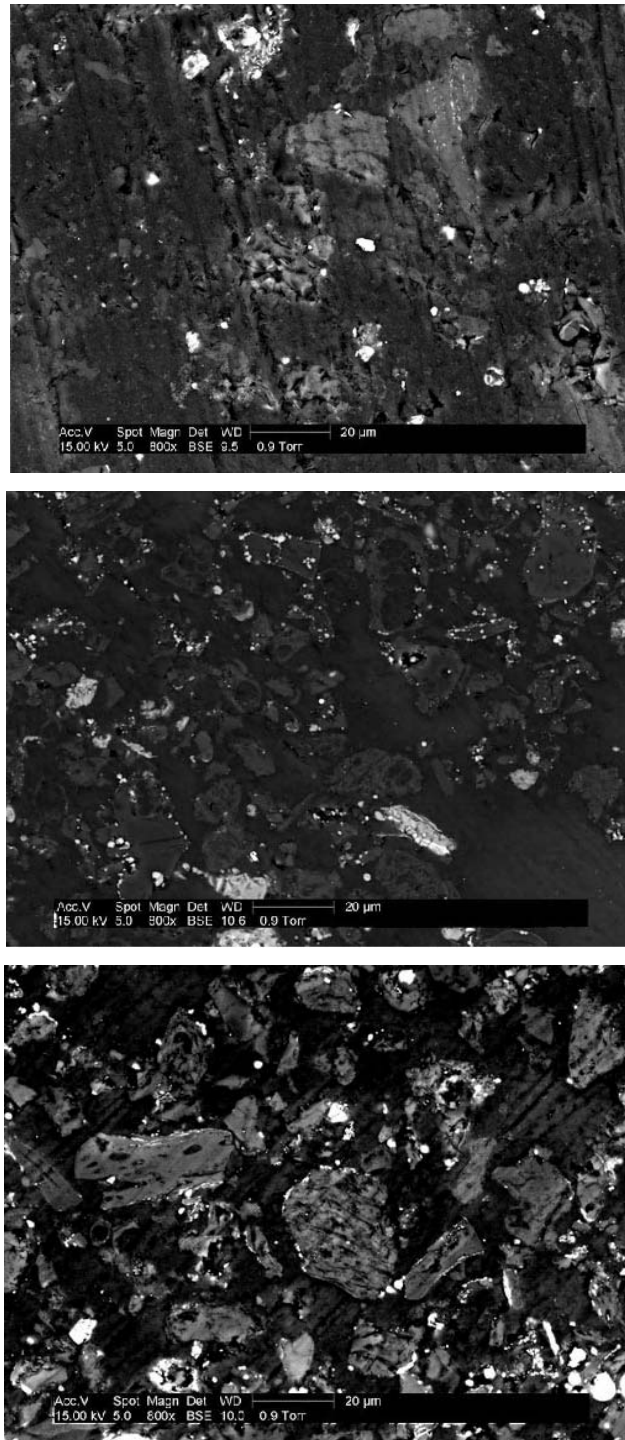


**Figure 5.13.** SEM micrograph of char cross section produced from pyrolysis of Knife River Lignite. (a) 2.5 atm (b) 6 atm (c) 15 atm.

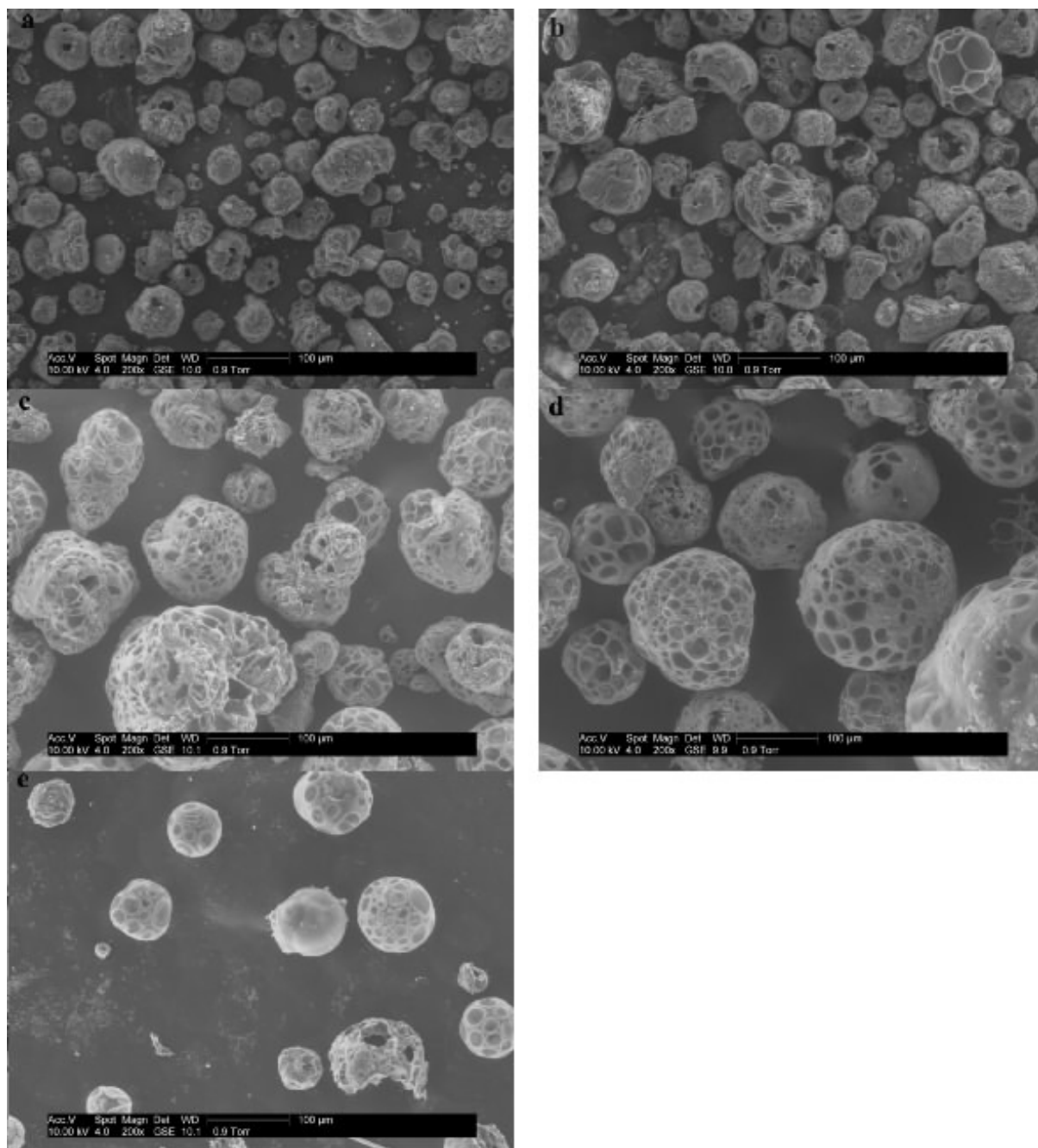


**Figure 5.14.** SEM micrograph of char produced from pyrolysis of Ken #9 coal. (a) 1 atm, (b) 2.5 atm (c) 6 atm (d) 10 atm (e) 15 atm.

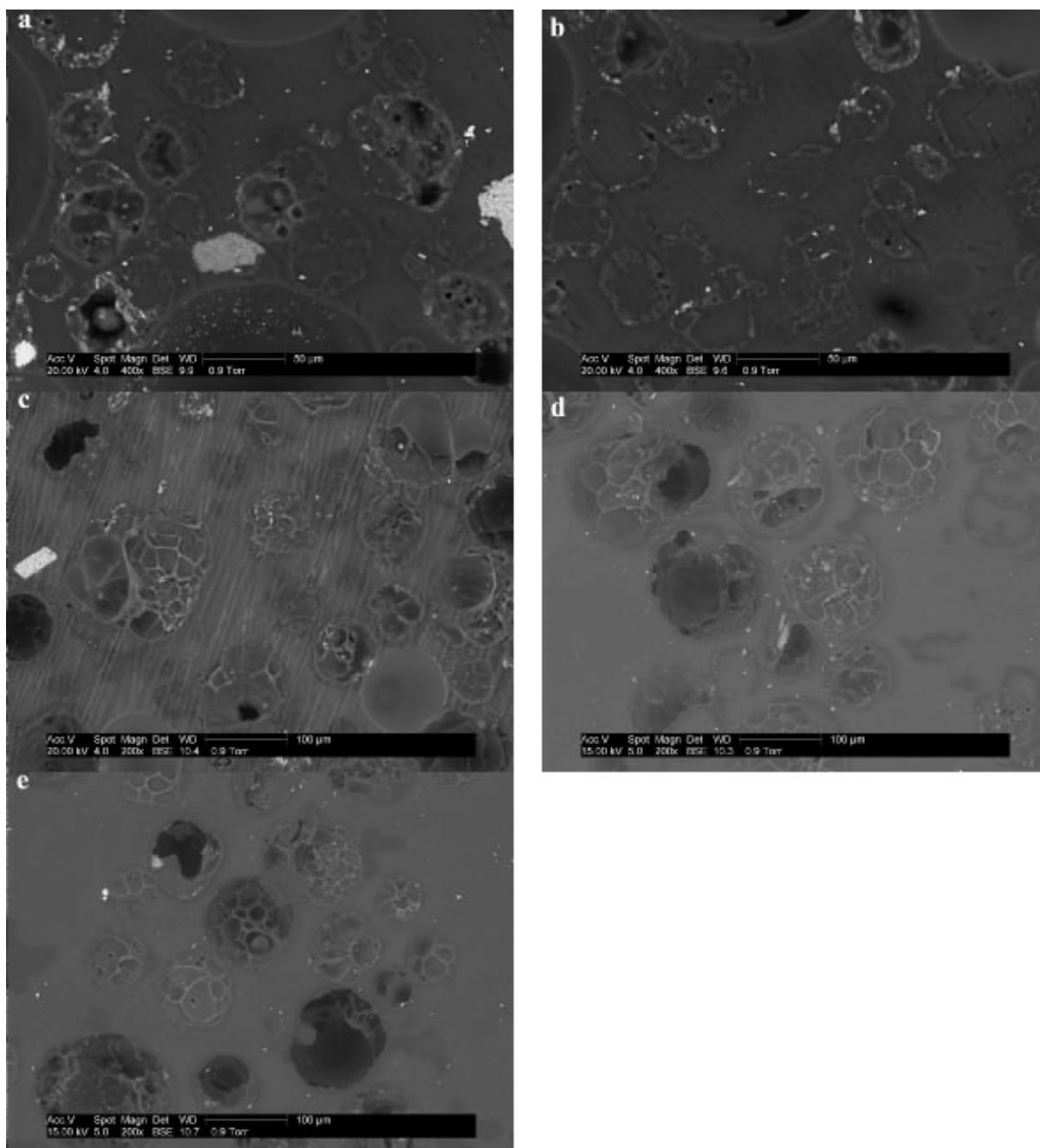


**Figure 5.15.** SEM micrograph of char cross section produced from pyrolysis of Ken #9 coal. (a) 1 atm, (b) 2.5 atm (c) 6 atm (d) 10 atm (e) 15 atm.

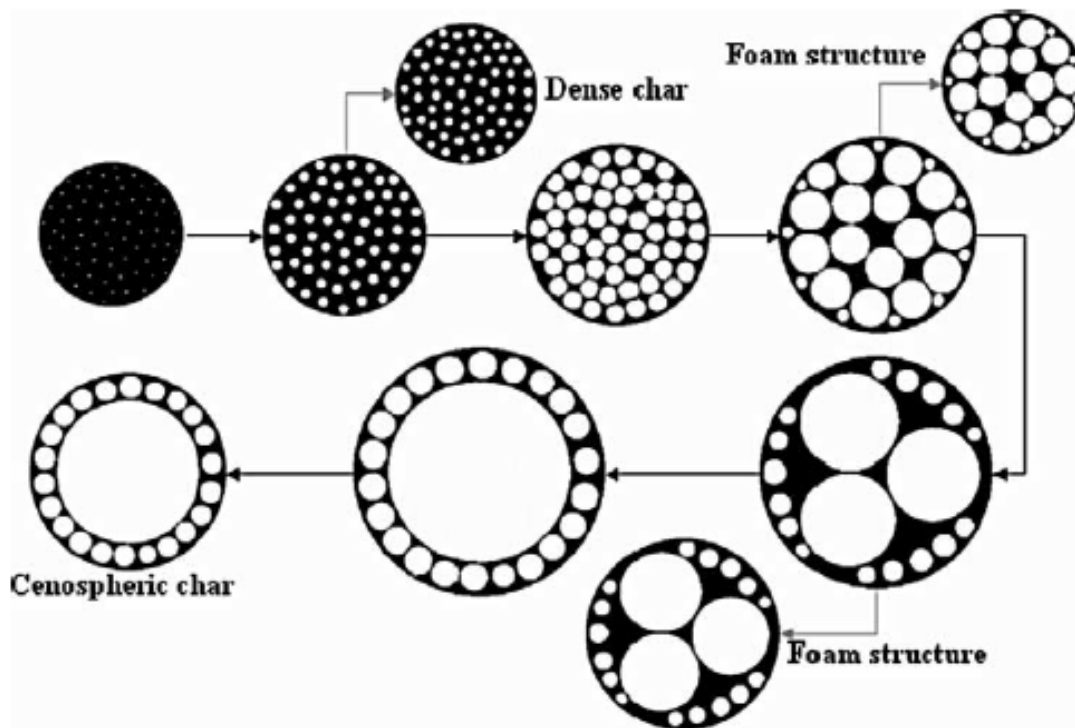


**Figure 5.16.** The proposed mechanism of char structure evolution by Yu et al. (2002)

The effect of pressure on coal particle swelling ratio was discussed previously (Figure 5.10). The swelling ratios can be related to the char morphology. Within the range of pressures tested in this study, the swelling ratios of all four coals studied increased with increasing pressure. The morphology of the Kentucky #9 char consistently illustrates the trend of increased swelling ratio with elevated pressure. At higher pressures, the char became more fluid because of the increased amount of metaplast. Bubbles were created and trapped within the particle by the increased resistance created by high pressure. These bubbles expanded and formed thinner inter-bubble walls, until a force balance was achieved with the reactor pressure exterior to the particle. At lower reactor pressures, bubbles merged or burst open because of a smaller



mass transfer resistance compared to the high-pressure condition, thus forming thicker walls and blow holes on the particle exterior surface. Therefore, smaller swelling ratios were observed at the lower pressures, and even fragments in some particles were observed. This swelling effect is governed by many factors such as coal rank, heating rate, and pressure. These same types of effects were observed in the other bituminous coals studied in this experiment. In contrast, very few changes were observed in the morphology of Knife River lignite chars as a function of pressure, since lignites do not go through a softening regime (See Figures 5.11 and 5.13).

## **5.7 Char Surface Area**

The internal surface area of char is an important factor affecting the reactivity of char oxidation or gasification, but only a few studies have reported the effect of pressure on char surface area. Lee et al. (1992) found that chars generated at higher pressure have lower N<sub>2</sub> surface areas, and that CO<sub>2</sub> surface areas increase with pyrolysis time. Similar trends were also reported by Wall et al. (2002). In contrast, Roberts et al. (2003) found that both CO<sub>2</sub> and N<sub>2</sub> surface area increased with pressure during coal pyrolysis. CO<sub>2</sub> surface areas of chars were more sensitive to increases in pressure. In the current study, both CO<sub>2</sub> and N<sub>2</sub> surface areas of chars decreased with increasing pressure (see Figure 5.17). The CO<sub>2</sub> surface area was larger than the N<sub>2</sub> surface area at all pressures, as expected. CO<sub>2</sub> surface areas are usually representative of micropore surface, and N<sub>2</sub> surface areas are representative of meso and macropores. The trend of decreased surface areas with increased pressures means that chars produced at high pressure have fewer

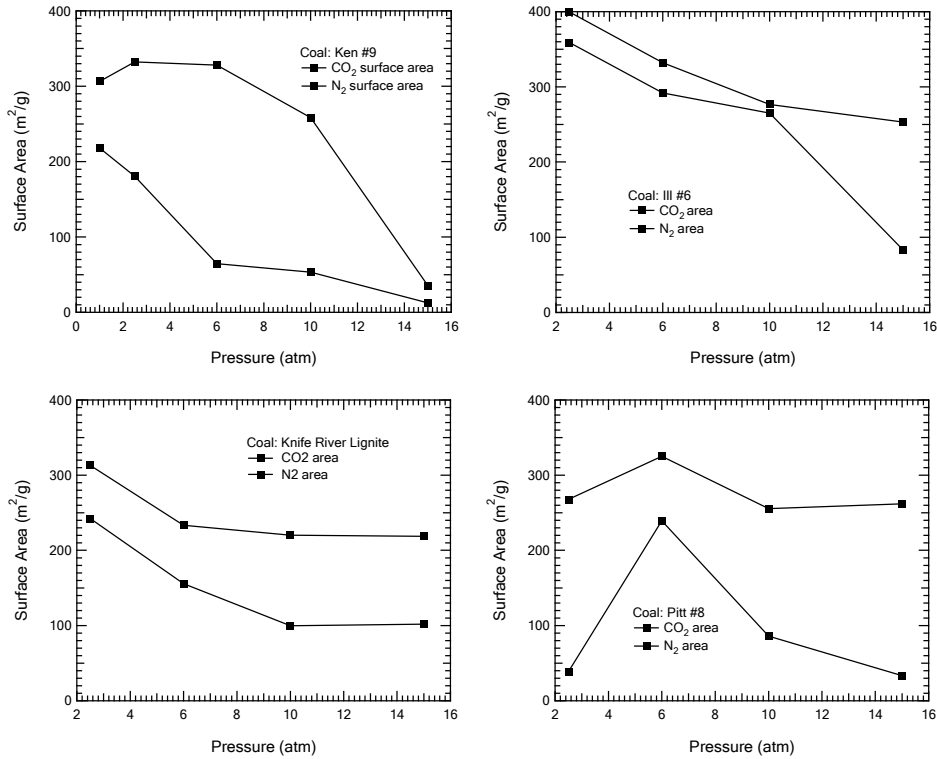


**Figure 5.17.** Surface area of chars prepared at different pressures.

micropores than low pressure chars. This trend is consistent with the SEM analysis, where high pressure chars exhibited more distinct bubbles than low pressure chars, and the texture of the solid part of the char was denser and less porous.

## 5.8 Summary of Coal Pyrolysis and Resulting Char Properties

Four coals with a broad rank distribution, including Kentucky #9, Illinois #6, Pitt #8, and Knife River Lignite, were pyrolyzed in an atmospheric flat-flame burner and a high-pressure flat-flame burner. Resulting chars were collected at pressures of 0.85, 2.5, 6, 10, and 15 atm. The chars were analyzed to find the effect of pressure on char properties.

The measured decreases in total volatiles yields with increasing pressure were predicted using the CPD model using only the elemental composition and ASTM volatiles yields of the parent coals as changeable input parameters that relate to coal chemical structure. The H/C and O/C ratios in the resulting chars initially increased with increasing pressure, but remained relatively constant at pressures from 6 to 15 atm. The H/C ratio in the char is thought to be affected by the decrease in tar yield at increased pressures, the change in the hydrogen content of the tar with pressure, and the increase in light gas yield as pressure increases. The change in residence time at different pressures in these experiments may also have played a role in the hydrogen release.

Swelling ratios of the lignite chars were less than 1.0, and only about 0.9-1.8 for the bituminous coals. All coal chars showed slight increases in swelling behavior as pressure increased. The swelling behavior observed for the Pitt #8 coal char at each pressure was lower than reported in high pressure drop tube experiments, supporting earlier work at atmospheric pressure showing that particle swelling decreases as heating rates approach  $10^5$  K/s. The morphology of chars produced at different pressures were analyzed using SEM. Chars formed at high pressure were in the early stage of foam structure evolution, while chars formed at low pressure were in later stages of foam evolution. The swelling ratio of chars increased with increasing pressure, and is attributed to bubble evolution.

Char surface areas using both CO<sub>2</sub> and N<sub>2</sub> as adsorption gases decreased with increasing pressure. The amount of micropores was less for chars produced at high pressure. The high pressure chars were more porous but had a denser framework than the low pressure chars.



## 6. Intrinsic Reactivity of Char Formed at Elevated Pressure

High-temperature, high-pressure pyrolysis experiments were conducted on two bituminous coal and one lignite. Chars were collected at different pressures in the HPFFB. These chars were then oxidized at the char formation pressure using the high-pressure Thermogravimetric Analyzer (HPTGA). Char intrinsic combustion reactivities ( $g/g_{\text{avail}}\text{-s}$ ) were determined from isothermal mass vs. time data. This chapter will discuss the data reduction procedure, the effect of pressure on resulting char reactivity, and reaction mechanisms.

### 6.1 Conditions of TGA Combustion Tests

#### 6.1.1 Char Preparation

Coal chars from Pitt #8, Ill #6, and Knife River Lignite were tested using the HPTGA. The properties of these coals were reported in the previous chapter. Chars were prepared using the procedure described in Chapter 5. All of the coals were pyrolyzed at 2.5, 6, 10, and 15 atm in the HPFFB. Resulting chars were collected, and then stored in a refrigerator until further analysis. Chars were dried at 110°C for 2 hours prior to each HPTGA test. The physical properties of these chars were reported in the previous chapter.

### 6.1.2 HPTGA Test Procedure

TGA char oxidation experiments were conducted on small amounts of sample (~4 mg) in order to minimize bed effects. Careful characterization is needed to minimize the experimental error. The HPTGA used in this study was previously used by Hecker et al. (2003) to conduct char combustion experiments at elevated pressure on char formed at atmospheric pressure. Based on their work, an experimental procedure was introduced in the current study to minimize the effect of buoyancy, flow rate, and gas composition. This procedure resulted in an intrinsic reactivity of char oxidation which was free of mass transfer effects. First of all, the total inert gas flow rate was set to 4 l/min. This flow rate was found to effectively minimize the effect of boundary diffusion, as well as to conserve helium and facilitate pressure control in the reaction chamber. Second, helium was selected as the inert gas rather than nitrogen, since helium has significantly higher thermal conductivity than nitrogen. Third, samples less than about 4 mg were found to introduce weighing errors, so 4 mg sample were used. Finally, gas compositions were carefully selected to avoid heating from char oxidation, and the reaction temperature was selected to be in the region of chemical reaction control.

Table 6.1 shows the matrix of experiments performed in the HPTGA. For the three coals examined, chars were collected in the HPFFB at four total pressures, and then tested at the same pressure in the TGA except the 2.5 atm char which was tested at 1 atm total pressure. Oxygen partial pressure and temperature were changed at each total pressure to generate the char oxidation kinetic data.

**Table 6.1 Matrix of Experiments in the HPTGA**

	P <sub>Tot</sub> = 2.5 atm	P <sub>Tot</sub> = 6 atm	P <sub>Tot</sub> = 10 atm	P <sub>Tot</sub> = 15 atm
Pitt #8	3	3	3	N/A
Ill #6	3	3	3	3
KRL	3	3	3	N/A

### 6.1.3 Kinetic Analysis

Figure 6.1 shows a typical data set obtained from the HPTGA. The weight of the basket and sample was recorded continuously by the microbalance. These data were rescaled to the initial weight of sample (without the basket). The detailed process is described in the Appendix G. The data were then fit to an experimental equation in order to reduce noise:

$$mass = A + Be^{-Ct} \quad (6.1)$$

The constants A, B, and C in equation 6.1 were obtained from a least squares analysis using Microsoft Excel. The oxidation rate of char was then calculated using:

$$-r = \frac{1}{m_{avail}} \frac{dm_{avail}}{dt} \quad (6.2)$$

An example of the HPTGA char oxidation data are shown in Figure 6.1. The weight measurements in the HPTGA are not stable at the initial stages of experiment (<30 s in this figure). The reactivity increases dramatically at late burnout levels, as seen in Figure 6.2 for char burnout levels larger than 90%. This high reactivity is caused by using the available weight in the reactivity determination (Eq. 6.2).

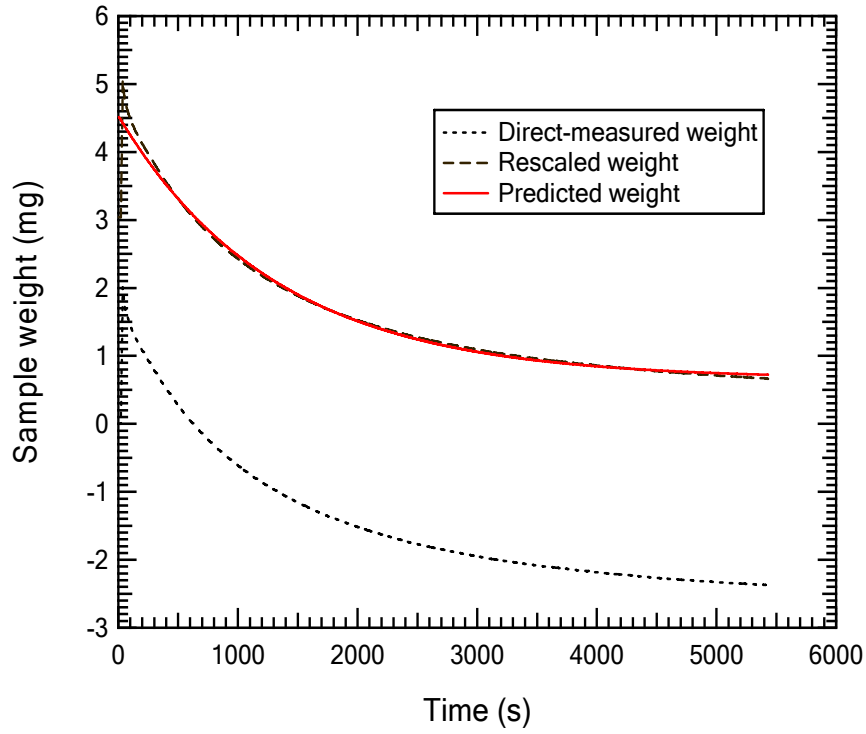


**Figure 6.1.** Measured and fitted data set obtained from a HPTGA test.

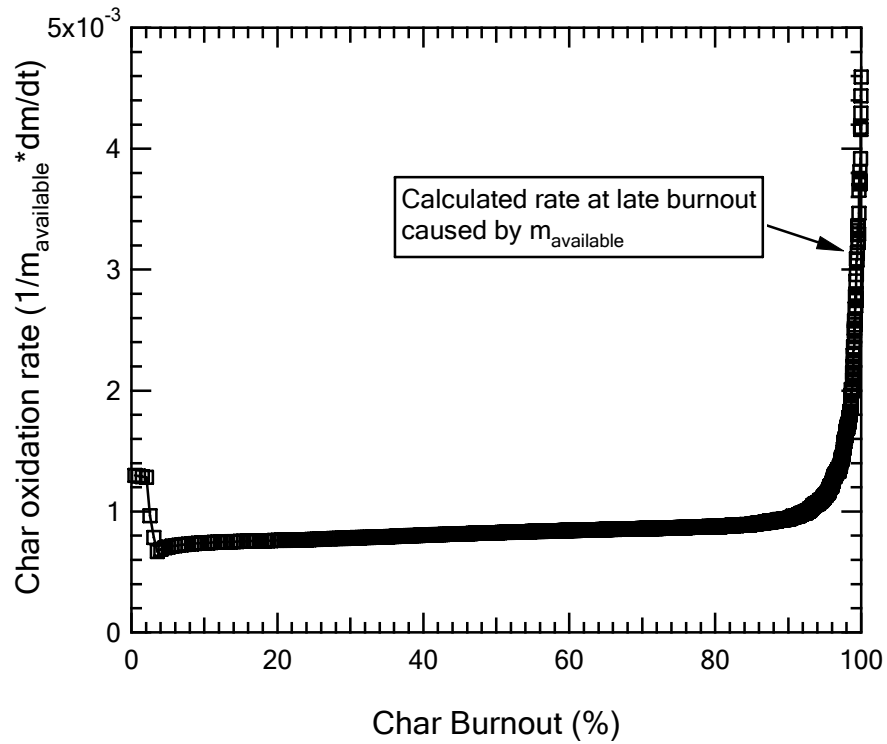


**Figure 6.2.** Char oxidation reactivity normalized by  $m_{avail}$  as a function of burnout.



The reactivity can also be interpreted using following equation:

$$-r = \frac{dx_i}{dt} = -\frac{1}{m_{initial}} \frac{dm_{avail}}{dt} \quad (6.3)$$

Figure 6.3 shows the same data processed using equation 6.3. The reactivity is not reasonable at the beginning of the test because of the instability of the microbalance. The reactivity from Eq. 6.3 during the later stages of char burnout decreases to almost zero, which is caused by full consumption of the carbonaceous material. This data processing method can help to eliminate the problem of high reaction rates at late burnouts that was shown in Figure 6.2. However, in reality, the reactivity changes with burnout based on the remaining mass. Therefore, all HPTGA rate data were normalized by the instantaneous mass in this study (according to Eq. 6.2).

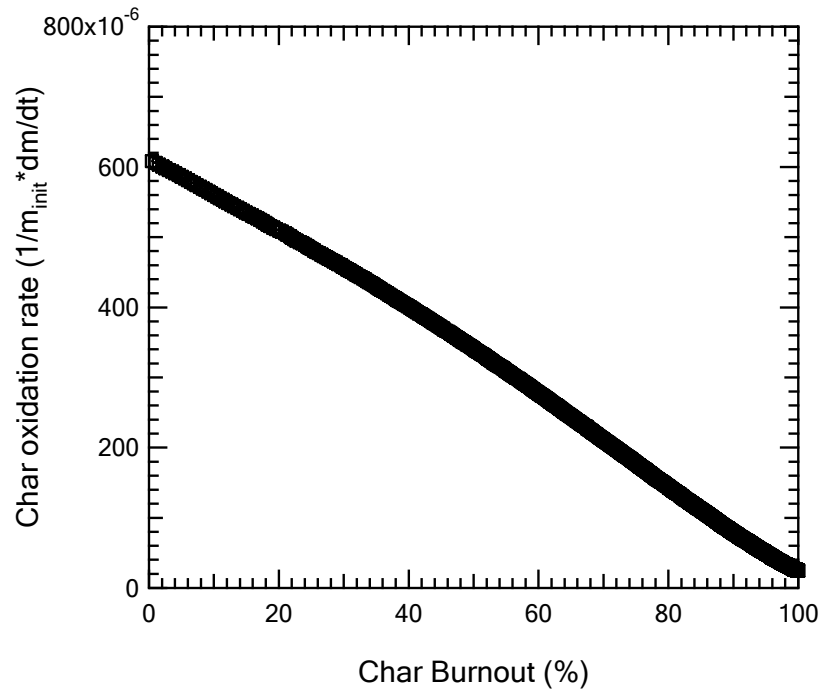


**Figure 6.3.** Char oxidation reactivity per initial mass as a function of burnout

There are wide variations in the methods used in the literature regarding how to interpret TGA data from char oxidation tests. Previous researchers have used average reactivity over a certain range of char burnout, maximum reactivity, initial char reactivity, or the reactivity at 20% burnout (Cai et al., 1996; Hecker et al., 2003; Roberts and Harris, 2000; Roberts et al., 2003). Initial reactivities vary in an unpredictable manner due possibly to movement of the sample basket or slow degassing of a small amount of pyrolysis products. Therefore, in this study, reactivities are compared at TGA char burnouts between 20% and 60%. At the end of each TGA test, the sample was burned completely at higher temperatures and O<sub>2</sub> levels in order to determine the ash content for that sample. The sample and basket were then weighed on a separate, more accurate balance, to improve the accuracy of the reactivity data. Each TGA test was repeated three times. The average reactivity value and standard deviation value were computed from the repeat samples at intervals of 5% in the char burnout, and error bars were set at  $\pm 2$  standard deviations.

The activation energy and oxygen order of n-th order rate expressions of Pitt #8 coal and Ill #6 coals were also calculated. Activation energies were determined from standard Arrhenius plots ( $\ln[\text{rate}]$  vs.  $1/T$  at constant oxygen partial pressure). Oxygen reaction orders were determined from a power-law model by determining slopes of  $\ln[\text{rate}]$  vs.  $\ln[P_{\text{O}_2}]$ . The total pressure during these TGA tests was kept the same as the char formation pressure, so as to simulate a continuous combustion process. TGA conditions used here were temperatures ranging from 693 to 753 K and oxygen partial pressures ranging from 0.2 to 0.8 atm. The low temperatures ensure that intrinsic rates were measured. Resulting O<sub>2</sub> mole fractions were 20 to 50% for the 1 atm test, and lower

than 13% for the 6, 10, and 15 atm tests. Low O<sub>2</sub> mole fractions are preferred in order to minimize the degree of char heating from the heat of the combustion.

## 6.2 Results and Discussion

### 6.2.1 Char Intrinsic Reactivity

Intrinsic reactivity data obtained in a high pressure thermogravimetric analyzer (HP-TGA) for chars prepared in the HPFFB facility were reported on a dry, ash-free basis. The effect of pressure on the resulting char combustion reactivity is shown in Figure 6.4 for the Pitt #8 coal, Figure 6.5 for the Illinois #6 coal, and Figure 6.6 for Knife River lignite. Pitt # 8 chars were oxidized in the HPTGA at a partial pressure of O<sub>2</sub> of 0.32 atm and a temperature of 715 K. The oxidation conditions of Ill #6 chars were P<sub>O<sub>2</sub></sub> = 0.4 atm and T = 693 K. KNL char oxidation conditions were P<sub>O<sub>2</sub></sub> = 0.28 atm and T = 615 K. The temperatures and oxygen concentrations were low enough for each char to avoid mass transfer effects. All of the chars were oxidized at the same total pressure as their respective char preparation pressure except for the 2.5 atm char, which was tested at 1 atm total pressure. The different oxidation conditions for different coals were used to maintain a reasonable reaction time. For example, Knife River lignite is the lowest rank coal, and hence has higher char reactivity, so the reaction temperature and oxygen partial pressure were set lower for this char.

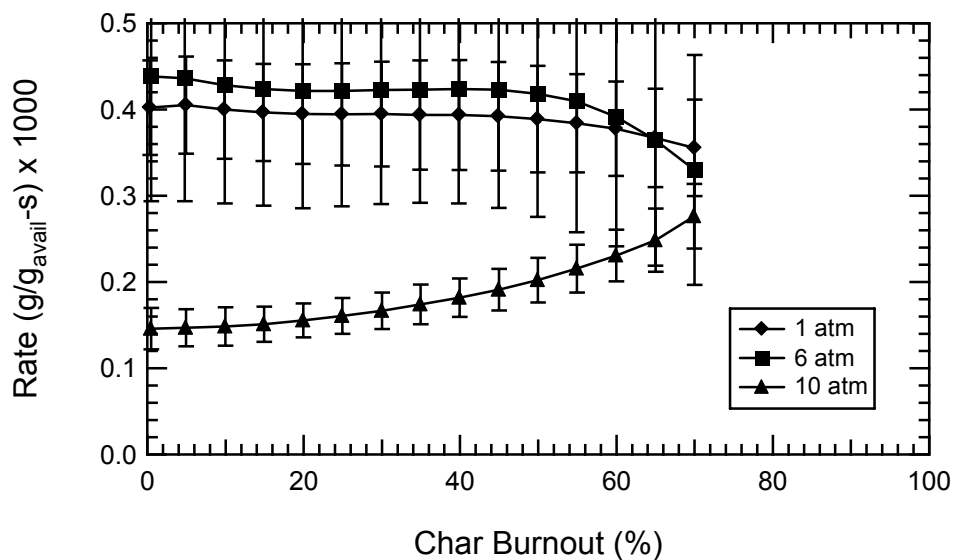


**Figure 6.4.** Pitt #8 char oxidation reactivity as a function of burnout and total pressure. The 1 atm experiments in the TGA were performed on char formed at 2.5 atm.  $T=715$  K,  $P_{O_2}=0.32$  atm.

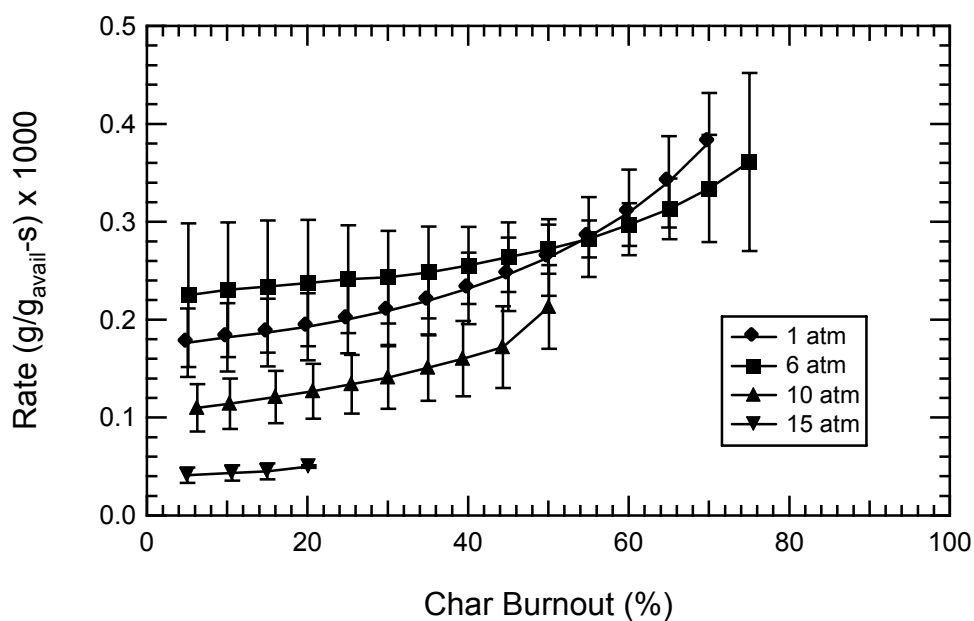


**Figure 6.5.** Ill #6 char oxidation reactivity as a function of burnout and total pressure. The 1 atm experiments in the TGA were performed on char formed at 2.5 atm.  $T=693$  K,  $P_{O_2}=0.4$  atm.

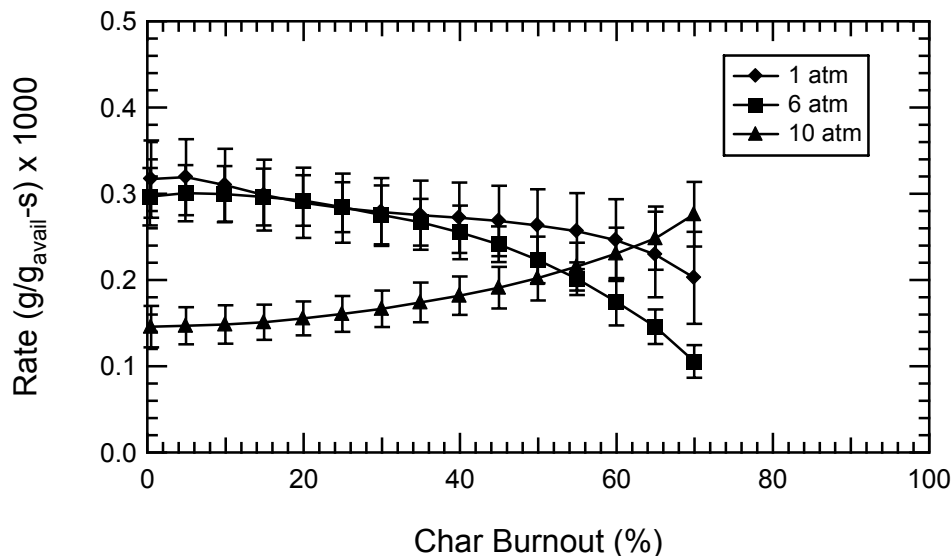


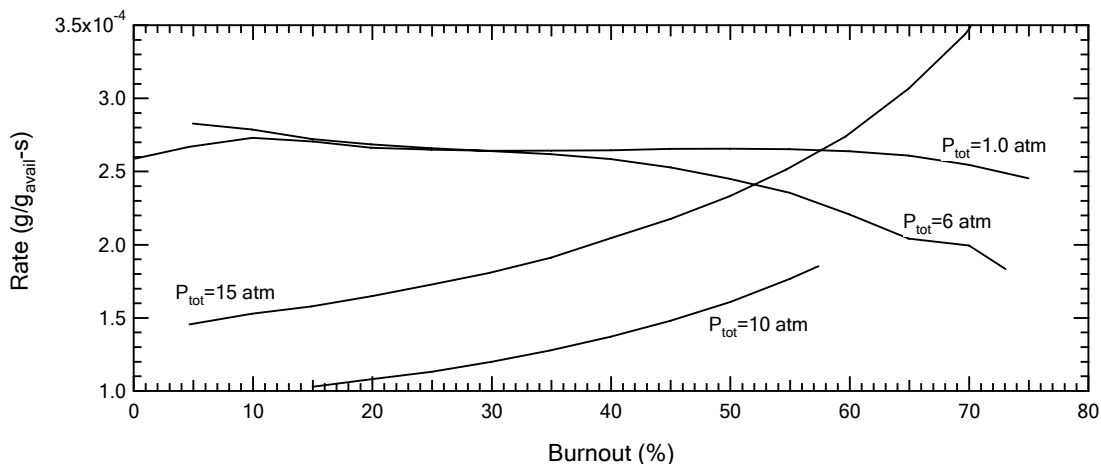
**Figure 6.6.** KRL char oxidation reactivity as a function of burnout and total pressure. The 1 atm experiments in the TGA were performed on char formed at 2.5 atm.  $T=615\text{ K}$ ,  $P_{O_2}=0.28\text{ atm}$ .

As seen in Figure 6.4, 2.5 and 6 atm Pitt #8 char reactivity curves are relatively constant for char burnouts from 0 to 50%, while the 10 atm reactivity increases with increasing burnout. Hecker et al. (2003) found that the reactivities of two coal chars (Pitt #8 and North Dakota lignite) were constant from 20-60% burnout at the pressures from 1-32 atm. Hecker's chars were produced at atmospheric pressure in a FFB and then were examined in a HPTGA.

Hecker's results also indicated that  $O_2$  reactivity for the same starting char did not change as total pressure was increased. In contrast, Figure 6.4 shows that the reactivity of the 10 atm Pitt #8 char is about 50% lower than the reactivities of the lower pressure chars. This decrease in reactivity with pressure differs from results reported by Roberts et al. (2003) that char reaction rates (defined as Eq. 6.2) didn't have a clear trend with pressure. After 60% burnout, the 6 atm HPFFB char is observed to decrease in reactivity faster than the 1 atm FFB char. At this degree of char burnout, activated sites

may have been mostly consumed and initial pore structure destroyed, causing char reactivity changes.

Another set of data were measured for Pitt #8 chars including 15 atm char. A comparison test was performed on 2.5, 6, 10, and 15 atm Pitt # 8 char at oxygen partial pressure 0.5 atm, temperature 693 K, and total pressures of 1, 6, 10, and 15 atm. The results are shown in the Figure 6.7 below. The reactivity of 15 atm char is higher than 10 atm char, and is lower than 2.5 and 6 atm char. Compared to Figure 6.4, the reactivity of 2.5 and 6 atm char in both conditions decreased with increased pressure, and reactivity of 10 and 15 atm char in Figure 6.7 decreased with increased pressure, which is consistent with the trend observed for the 10 atm char in Figure 6.4.



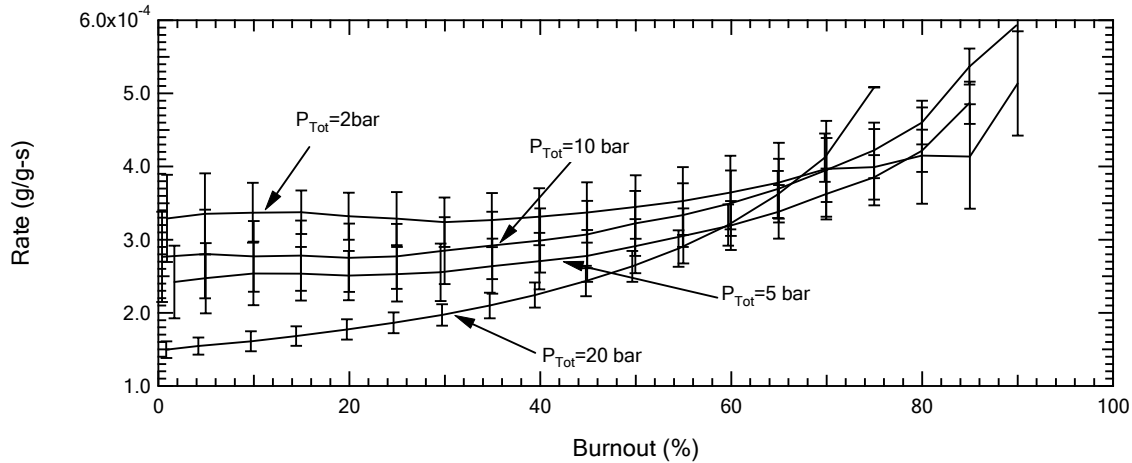
**Figure 6.7.** Pitt #8 char oxidation reactivity as a function of burnout and total pressure. The 1 atm experiments in the TGA were performed on char formed at 2.5 atm.  $T=693$  K,  $P_{O_2}=0.5$  atm.

Figure 6.5 shows the char reactivity of Ill #6 char with burnout. In general, char produced from Ill #6 coal decreased in reactivity as the pressure during pyrolysis increased, especially from 6 to 15 atm.

Figure 6.6 shows that the lignite reactivities also decrease with increasing pressure. This is an interesting result, since the lignite char does not soften and resolidify during pyrolysis, and also since the effect of pressure on lignite pyrolysis yields are thought to be minimal. Explanations for this behavior are left for further studies.

An interesting result from Figure 6.4 and 6.6 is that different pressure char reactivities show different trends with increasing burnout. Generally, reactivities of low pressure char such as 2.5 and 6 atm Pitt 8 and KRL decreased with increasing burnout, but reactivities of high pressure char such as 10 atm Pitt 8 and KRL increased with increasing burnout. The reactivities of Ill #6 char show similar trend for all four pressures tested. Since active sites were consumed when char oxidizes, the reactivity was expected to decrease, especially at the late stage of burning. However the results obtained from these chars are apparently different. The effect of experimental uncertainty has been eliminated by repeating the tests at the same condition for different kinds of chars. A possible cause of this result may be the calculation of averaging, since the late burnout has larger error bars.

The difference in how the reactivity changes with burnout for chars formed at low pressure and high pressure may also be caused by the difference in the char surface area or pore structure. Figure 6.8 shows the reactivity of Pitt #8 10 atm char as a function of burnout and total pressure used in HPTGA. The reactivity measured at high pressure for the Pitt #8 char formed at 10 atm is generally lower than the reactivity measured at low pressure. This trend contradicts the results of Hecker and coworkers (2003) obtained from char formed at 1 atm, where total pressure was shown to have no effect on char TGA reactivity. The difference between the experiments of Hecker and coworkers



**Figure 6.8.** Char HPTGA reactivity vs. Burnout and  $P_{\text{Tot}}$ , Char: Pitt #8 10 atm;  $T=700$  K;  $P_{\text{O}_2}=1$  bar.

and the results presented here is the pressure at which the chars were formed. This indicates that the effect of pressure on char physical properties may be the main contributor to the different trends observed in Figures 6.4 and 6.6. A possible mechanism may be char formed at high pressure has less internal surface area (see Figure 5.17), and thus has lower reactivity (as discussed later in this chapter). As burnout increases, some pores may open and become accessible for oxygen, which increases the reactivity at late stages of burnout. For the char formed at low pressure, most of the “oxygen-available” surface area is already accessible to oxygen; this surface area is consumed with increasing burnout, which decreases the reactivity at the late stages of burnout. Further studies, such as the change of surface area with burnout of different chars, are needed to verify this proposed mechanism.



### 6.2.2 Discussion of TGA Reactivities

The effect of pressure on resultant char reactivity has been studied under a variety of reaction conditions (Cai et al., 1996; Chitsora et al., 1987; Kajitani and Suzuki, 2003; Lee et al., 1992; Roberts et al., 2003; Sha et al., 1990; Van Heek and Muhlen, 1991). Different pyrolysis atmospheres and temperature were used; char reactivities included oxidation rates as well as H<sub>2</sub>O and CO<sub>2</sub> gasification rates. Among them, three references (Chitsora et al., 1987; Kajitani and Suzuki, 2003; Sha et al., 1990) used high temperature (700-930°C) in their reactivity tests, and hence are not used for direct comparison since mass transfer may have affected their results. Table 6.2 summarizes three studies of effects of pressure on resulting char reactivities that are comparable to this work.

Roberts et al. (2003) pyrolyzed three Australian coals at 5, 10, and 15 atm. Char oxidation reactivities were measured at 10 or 15 atm at 723K in 50 mol% O<sub>2</sub>. The initial reaction rate for one char increased with increasing pressure, while no clear trend with pressure was observed for two other chars. However, the reactivities after normalization by the char CO<sub>2</sub> surface areas were the same. Cai and coworkers (1996) examined chars formed during hydrolysis (i.e., pyrolysis in H<sub>2</sub>) as a function of pressures. They found that Pitt #8 and Linby char combustion reactivities decreased with pressure at low to medium pressures (20-30 bar), then increased at increased pressures. Lee et al. (1992) found that Illinois char reactivity generally increased with increasing char formation pressure when pressure was increased from 0 psig to 100 psig, but that this decrease was not as significant for coal pyrolysis residence times longer than 1 s. Lee and coworkers found no correlation between the micropore surface area (CO<sub>2</sub>) of chars and char oxidation reactivity.

**Table 6.2. Effects of Pressure on Resulting Char Reactivities**

	Lee et al. (1992)	Cai et al. (1996)	Roberts and Harris (2000)
Coals	Illinois No.6	Linby, Pitt #8	3 Australian thermal coals
Particle size	62 $\mu\text{m}$ mean diameter	106-150 $\mu\text{m}$	N/A
Apparatus	HEF (high-pressure entrained-flow furnace)	Wire-mesh reactor, with hydrogen as carrying gas	Pressurized flow reactor
Heating rate	$\sim 10^4$ K/s	1000 K/s	$\sim 10^4$ K/min
Temperature	1189 K	1396 K for Linby, and 973 K for Pitt #8	1373 K
Pressure	1 – 38 atm	2.5 – 150 atm	5, 10, and 15 atm
Reactivity	Char reactivity (g/g-s) increased when formation pressure increased from 0 to 100 psig, but decreased at 309 psig. No positive relation between reactivity and the micropore surface area of chars was observed.	The reactivities (g/g-s) of both char decreased when pressure increased to 20 bar, and then increased when pressure increased to higher pressure up to 150 bar.	Char apparent rates (g/g-s) vary significantly with pyrolysis pressures, whereas the intrinsic rates, which were obtained by normalizing the apparent rates by internal surface area ( $\text{g}/\text{m}^2\text{-s}$ ), are almost independent of pressure over a pressure range from 1 to 15 atm.

Generally, at low to medium pressures (1-40 atm), most of these studies showed that char reactivity decreased as char formation pressure increased. Lee et al. (1992) found that char reactivity increased with increasing pressure at low to moderate pressure. Increasing pressure is thought to decrease the tar yield, and hence increase the hydrogen content in the char. Increased hydrogen contents in chars generally translate to higher reactivities. Increased hydrogen contents in the char at increasing pressure are generally observed (see Figure 5.6). However, high-pressure also increases the fluidity of the char, making the char surface more ordered, which generally means lower reactivity. This

resolidification process can also be affected by residence time, causing lower char reactivity (Lee et al., 1992). Char surface area may also contribute to reactivity change with pressure, and will be discussed later in this chapter.

### 6.2.3 Activation Energy and Oxygen Order in the N-th Order Kinetic Rate Expression

A brief series of TGA experiments was performed on 2.5, 5, 10, and 15 atm Pitt #8 chars to determine oxygen reaction orders and activation energies, following the basic TGA test procedure of Hecker et al. (2003). Temperatures used in these TGA experiments ranged from 693 to 753 K, and oxygen partial pressures ranged from 0.2 to 0.8 atm. The total pressure used in the HPTGA is the same as the char formation pressure, except for 2.5 atm char, the HPTGA total pressure is 1 atm. The low temperatures ensured that intrinsic rates were measured (i.e., negligible effects of heat and mass transfer). The reaction orders and activation energies were calculated based on the average reactivity from 20-60 % burnout. Resulting O<sub>2</sub> mole fractions were 20 to 50% for the 1 atm test, and lower than 13% for the 6, 10, and 15 atm tests. Only three or four data points were used to calculate the kinetic parameters in this brief study; the detailed plots are shown in the Appendix G. The reaction orders and activation energies determined from this small set of experiments are shown in Table 6.3. The activation energy stays roughly constant with total pressure, although the 6 atm value is notably lower. The oxygen order is constant, which is close to Hecker's results (2003) which showed  $n=0.7$ . The exception is the 10 atm char which show  $n$  is 1.03.

**Table 6.3 Activation Energies and Oxygen Orders of Pitt #8 Coal Chars**

Total Pressure (atm)	Activation Energy (kcal/mol)	Oxygen Order
2.5	32.7	0.79
6	25.3	0.83
10	30.1	1.03
15	28.6	0.80

A similar set of TGA experiments was performed on the 2.5, and 6 atm Ill #6 chars to determine reaction orders and activation energies. TGA experiments were conducted at temperature ranging from 663-724 K and oxygen partial pressures ranging from 0.2-0.5 atm. The reaction orders and activation energies of Ill #6 coal chars are shown in Table 6.4

**Table 6.4 Activation Energies and Oxygen Orders of Ill #6 Coal Chars**

Total Pressure (atm)	Activation Energy (kcal/mol)	Oxygen Order
2.5	30.5	0.71
6	24.9	1.0

The activation energies and oxygen orders reported in Table 6.3 and 6.4 are only preliminary experimental results determined from a limited number of experiments. More extensive TGA experiments on these chars were performed and analyzed by a separated student as this dissertation was being completed, and are included in Appendix H.

#### 6.2.4 The Relationship between Surface Area and Char Reactivity

The internal surface area of the char is an important factor affecting the reactivity of char oxidation or gasification. However, only a few studies have been reported that treat the effect of pressure on char internal surface area. Lee et al. (1992) found that chars generated at higher pressures have lower N<sub>2</sub> surface areas, and that chars exhibit larger CO<sub>2</sub> surface areas with increasing pyrolysis time. Similar trends are also reported by Wall et al. (2002). In contrast, Roberts et al. (2003) found that both CO<sub>2</sub> and N<sub>2</sub> surface area increased with increasing pressure during pyrolysis, and that CO<sub>2</sub> surface areas were more sensitive to the increases in pressure. In the current study, both CO<sub>2</sub> and N<sub>2</sub> surface areas of chars generally decreased with increasing pressure, as shown earlier in Figure 5.16, with the exception of the Pittsburgh #8 data at 2.5 atm.

It is common to normalize char reactivity by the internal surface area, with either CO<sub>2</sub> or N<sub>2</sub> as the adsorption gas. The normalized reactivities were calculated using the following equation:

$$r''_{normalized} = \frac{r_{intrinsic}}{A_{CO_2 \text{ or } N_2}} \quad (6.4)$$

where  $A_{CO_2/N_2}$  is the CO<sub>2</sub> or N<sub>2</sub> surface area in m<sup>2</sup>/g, respectively. The intrinsic reactivity  $r_{intrinsic}$  is defined in Equation 6.2.

The intrinsic reactivity ( $r_{intrinsic}$ ) includes contributions by both the char surface activity and the “available” reaction area. However, it is difficult to quantify these effects individually. By normalizing the reactivity by the char internal surface area, the effect of change in char surface area on reactivity can be eliminated. It was difficult to obtain the initial char reactivity at 0% char burnout because of instabilities at the beginning of each HPTGA experiment. The intrinsic reactivities of Pitt #8, Ill #6, and KRL coal char were

therefore taken from the time at which 5% char burnout was achieved in the HPTGA. The surface areas used in the normalization were measured using the original char. These surface area values were assumed not to change after 5% char burnout at the low temperature conditions used in the HP-TGA experiments.

It is not clear in the literature which surface area measurement can be treated as the “available area” for char oxidation, even at the relatively low TGA reaction temperatures. Both  $N_2$  and  $CO_2$  surface areas were therefore used to reduce the data. The values obtained may not precisely reflect the true active surface area, but can provide a qualitative insight into the effect of char surface area on reactivity.

Figures 6.9-6.11 show HP-TGA reactivity data for the Ill #6, Pitt #8, and KRL coals, respectively. The intrinsic reactivity has units of  $g/(g\text{-sec})$  and was multiplied by  $10^3$  in this figure, while the normalized reactivity has units of  $g/(m^2\text{-sec})$  and was

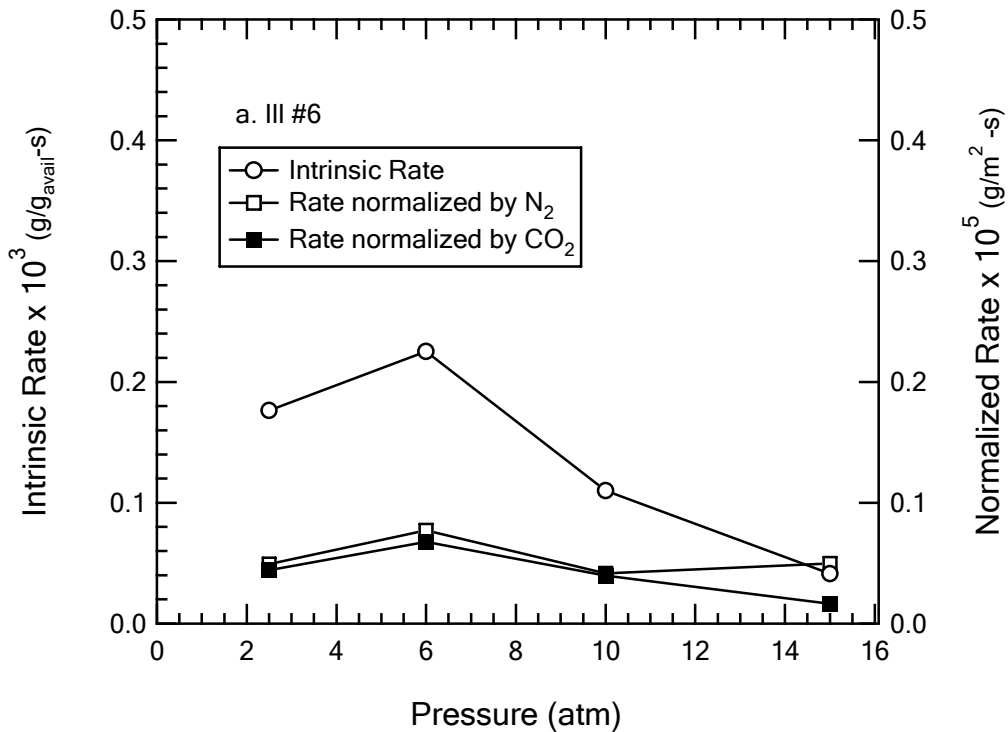


**Figure 6.9.** Ill #6 char reactivity and normalized reactivity.

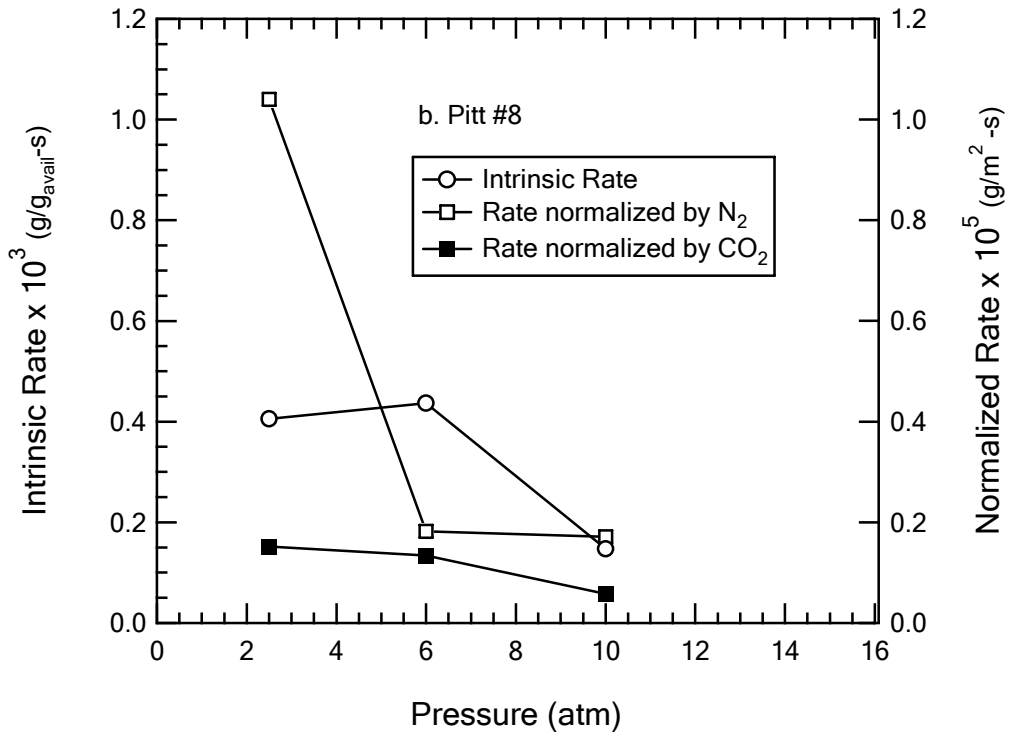


Figure 6.10. Pitt #8 Char reactivity and normalized reactivity.

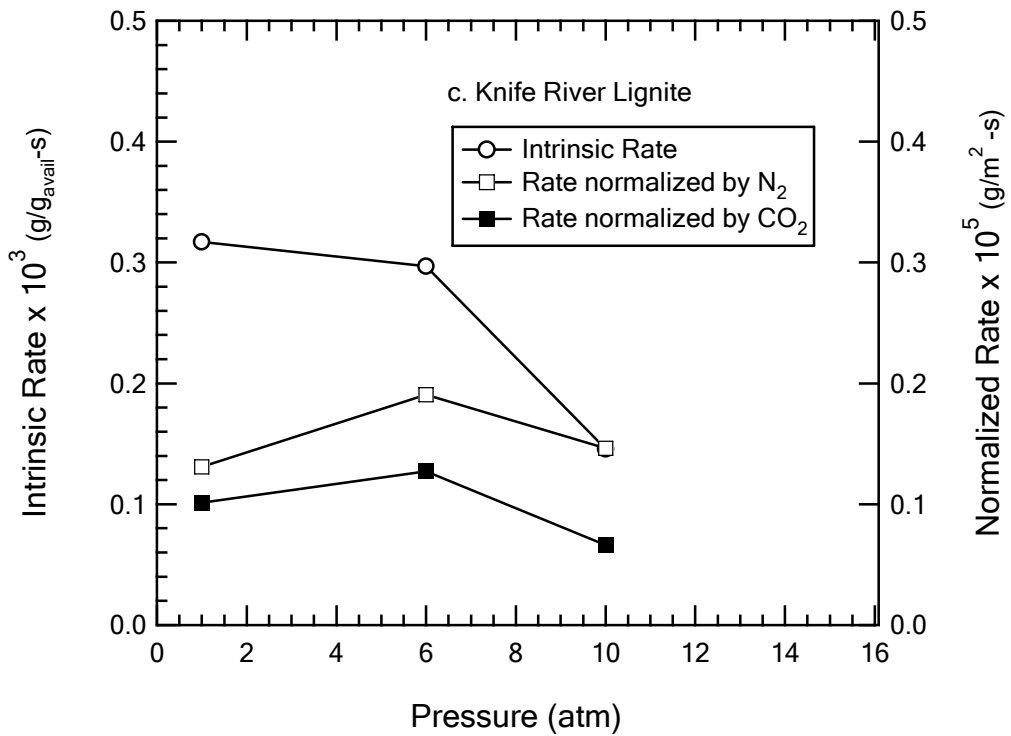


Figure 6.11. KRL char reactivity and normalized reactivity.

multiplied by  $10^5$  in these figures for comparative purposes. The normalized reactivity (by either  $\text{CO}_2$  or  $\text{N}_2$  surface area) remained relatively constant as a function of pressure for the Illinois #6 coal, Knife River lignite, and Pitt #8 except for one data point. More pressure dependence was seen in the non-normalized intrinsic reactivity for these chars.

These results imply that the decrease in intrinsic char reactivity could be due to changes in the internal surface area. Chars prepared at low pressure have larger internal surface areas available for low temperature oxidation. The temperatures used in the TGA experiments were low enough to minimize the effects of pore diffusion. Differences in char chemical structure, as indicated by the H/C and O/C ratios, can not explain the difference in reactivities observed at different pressures. H/C and O/C ratios are constant with the increased pressure (see Figure 5.5), and hydrogen and oxygen content increased with increased pressure (see Figure 5.6). This observation of the importance of internal surface area is somewhat consistent with the results of Roberts et al. (2003).

In the current study, it is hard to distinguish the relative importance of  $\text{CO}_2$  versus  $\text{N}_2$  surface area. However, close observation of the normalization of reactivity by the  $\text{N}_2$  surface area shows less dependence on pressure than that normalized by the  $\text{CO}_2$  surface area. Further studies are still required to determine the correct available surface area that describes char oxidation as a function of pressure.

### **6.3 Summary of Intrinsic Reactivities of Char Formed at Different Pressures**

TGA char oxidation reactivities were measured at the same total pressure as the char preparation pressure for Pitt #8, Ill #6, and KRL. The general trend was that the TGA reactivity on a gram per gram available basis decreased with increasing char



formation pressure. A limited number of experiments were performed to determine the oxygen order and activation energy. The Pitt #8 char intrinsic activation energy and oxygen reaction order remained relatively constant with increasing pressure, which result is consistent with the results obtained by Hecker et al. (2003) on chars formed only at atmospheric pressure.

The intrinsic reactivity (g/g-s) at 5% char burnout was normalized by N<sub>2</sub> and CO<sub>2</sub> internal surface area. The resulting normalized reactivity was found to be relatively constant with increasing pressure for N<sub>2</sub> and CO<sub>2</sub> normalizations. The fact that the normalized reactivity is approximately constant with pressure indicates that the majority of the change in char reactivity with pressure may be attributed to changes in internal surface area. The normalization of reactivity by the N<sub>2</sub> surface area shows less dependence on pressure than that normalized by the CO<sub>2</sub> surface area.

In this study, the result of decreased reactivity (g/g-s) with increased pressure is consistent with results reported by Cai et al. (1996), but is different than results reported by Lee et al. (1992) and by Roberts and Harris (2000). The observation of relatively independent normalized reactivity (g/m<sup>2</sup>-s) by char surface areas is also found by Roberts and Harris (2000), but only for CO<sub>2</sub> surface area. The experimental techniques, coal, and char formation conditions used by this study differ from these other experiments (see Table 6.2). The major difference between this study and others is that the char was tested at the same HPTGA total pressure as the char formation pressure. Because coal combustion in industrial process does not occur under different pressures, results of this study may be more useful in evaluating pressure effect in coal systems.



## 7. Elevated Pressure, High Temperature Coal Oxidation Experiments and Modeling

### 7.1 Conditions of Combustion Tests

#### 7.1.1 Experimental Conditions

All of the elevated pressure coal combustion experiments were conducted using the methane-air high-pressure flat flame burner (HPFFB) that was described in Chapter 2.

In this study, parameters such as coal type, coal size, total pressure, bulk oxygen composition, and reaction distance were varied during the experiments. Two sizes of Pitt #8 coal (63-76  $\mu\text{m}$  and 90-125  $\mu\text{m}$ ) were tested. Samples of Ill #6 coal (74-90  $\mu\text{m}$ ) char were collected at two reaction distances to test residence time effects. The test matrix for all of the coal oxidation experiments conducted is shown in Table 7.1. The post-flame  $\text{O}_2$  concentration and temperature were adjusted by changing the  $\text{CH}_4/\text{air}$  ratio. The oxygen concentration of the entraining flow gases for each condition was measured using an  $\text{O}_2$  monitor.

**Table 7.1 Matrix of Coal Oxidation Experiments<sup>a</sup>**

	P <sub>Tot</sub> = 1 atm	P <sub>Tot</sub> = 6 atm	P <sub>Tot</sub> = 10 atm
Pitt #8 (63-76 μm)	0-19.2 % O <sub>2</sub>	0-9.8 % O <sub>2</sub>	N/A
Pitt #8 (90-125 μm)	0-19.2 % O <sub>2</sub>	0-9.8 % O <sub>2</sub>	0-12.0 % O <sub>2</sub>
Ill #6 (74-90 μm) (SD*)	0-15.1 % O <sub>2</sub>	0-9.8 % O <sub>2</sub>	0-8.7 % O <sub>2</sub>
Ill #6 (74-90 μm) (LD**)	0-15 % O <sub>2</sub>	0-12.4 % O <sub>2</sub>	N/A

\* Short reaction distance

\*\* Long reaction distance

<sup>a</sup>all concentration are given in mol%

### 7.1.2 Gas Temperature Profile

The particle residence time is an important factor affecting the char burning rate. The reaction length was determined by measuring the distance from the burner to the collection probe.

Gas temperature profiles were measured for each reaction condition before char collection experiments were conducted. At each pressure, the flow rates of CH<sub>4</sub> and air were held constant, and the O<sub>2</sub> flow rate was adjusted to control the post-flame O<sub>2</sub> concentration. The flow rates of CH<sub>4</sub>, air, and O<sub>2</sub> used in different experiments are shown in Table 7.2. Thermocouple measurements of gas temperature were corrected for the effects of radiation (See Appendix A), and are shown in Fig 7.1. These temperature profiles show two characteristics: (1) the dramatic decrease of temperature versus distance from about 1700 K to 1000 K at 2.5 atm, or to 700 K at 10 atm; and (2) the fact that gas temperature profile remained relatively constant at a given pressure when the O<sub>2</sub> concentration was changed from 0-15 mol%.

**Table 7.2 Gas Flow Rates Used in the HPFFB**

	Post flame O <sub>2</sub> Concentration	CH <sub>4</sub> (l/min)	Air (l/min)	O <sub>2</sub> (l/min)
1 atm	5.8%	1.74	16.55	1
	9.8%	1.74	16.55	2
	15.1%	1.74	16.55	3.3
6 atm	3.0%	2.16	20.5	0.7
	5.0%	2.16	20.5	1.25
	10.0%	2.16	20.5	2.5
10 atm	12.4%	2.16	20.5	3.3
	5.0%	2.49	23.5	1.25
	5.7%	2.49	23.5	1.6
	9.7%	2.49	23.5	2.5
	9.9%	2.49	23.5	2.9

\* All concentrations are given in mole percent.

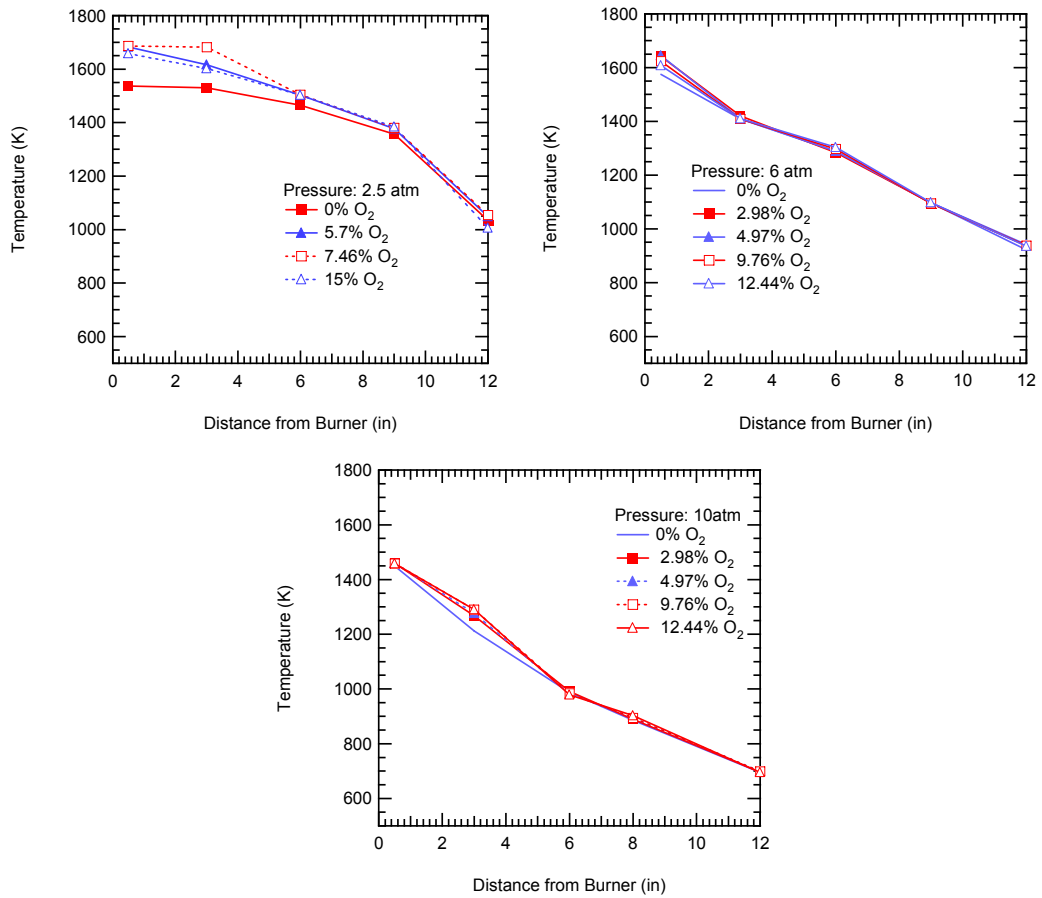


**Figure 7.1.** Measured gas temperature profiles in the HPFFB at different pressures and oxygen concentrations.

## 7.2 Experimental Results and Discussion

### 7.2.1 Variations in Char Burnout during Combustion

Figures 7.2-7.5 show the mass release for four sets of coal combustion experiments vs. O<sub>2</sub> molar fractions at different pressures. Burnout is reported here based on (a) the parent daf coal (solid lines), and (b) the initial char collected at 0.5 mol% O<sub>2</sub> (dashed lines). The change in char properties vs. post-flame O<sub>2</sub> concentration for a given is thought to be small. The data in Figure 7.2 show that the 6 atm char appears to be more reactive than 2.5 and 10 atm chars for Pitt #8. More detailed reactivity analysis will be given later in this chapter.

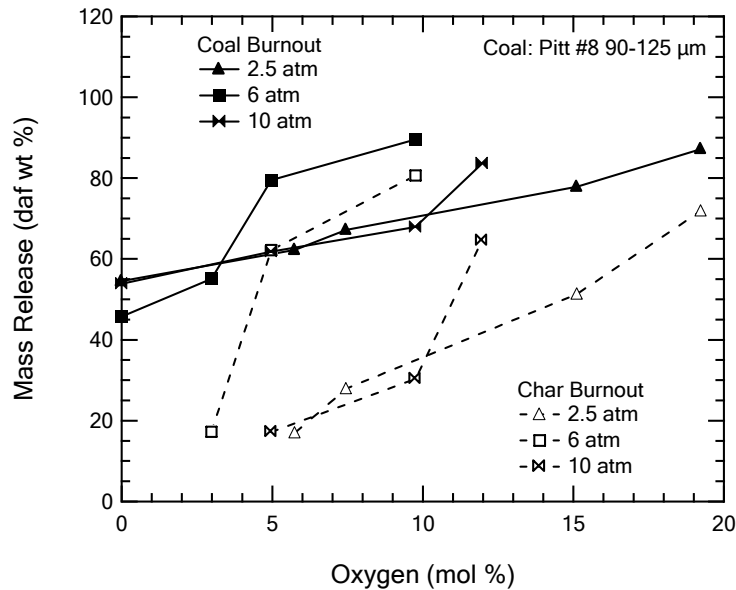


**Figure 7.2.** Measured mass release of Pitt #8 coal (90-125μm) during combustion experiments at different pressures and O<sub>2</sub> concentrations. Open symbols represent the data on a %char burnout basis, whereas closed symbols are normalized to the initial amount of dry ash-free coal.

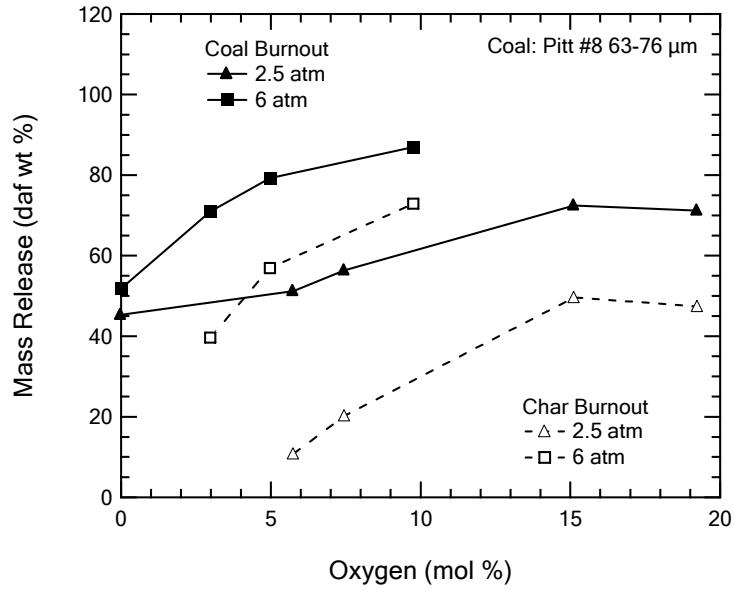


**Figure 7.3.** Measured mass release of Pitt #8 coal (63-76 $\mu\text{m}$ ) during combustion experiments at different pressures and  $\text{O}_2$  concentrations. Open symbols represent the data on a %char burnout basis, whereas closed symbols are normalized to the initial amount of dry ash-free coal.

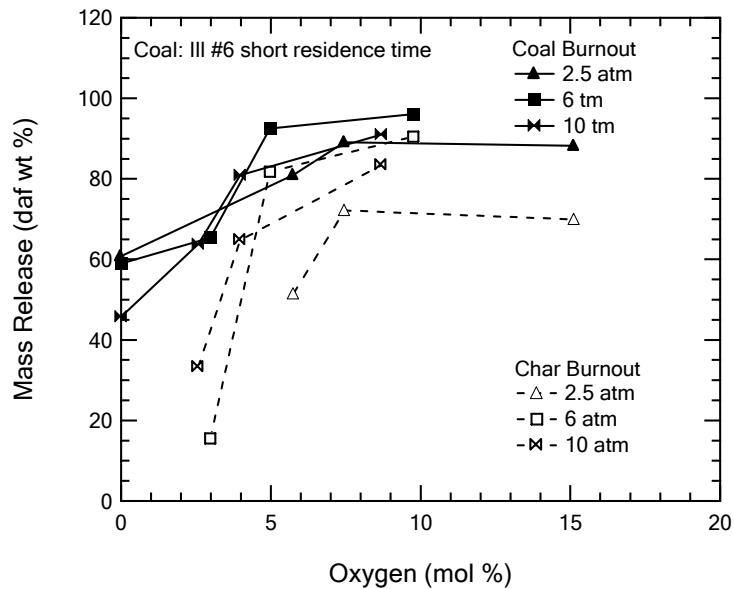


**Figure 7.4.** Measured mass release of Ill #6 coal (short reaction distance) during combustion experiments at different pressures and  $\text{O}_2$  concentrations. Open symbols represent the data on a %char burnout basis, whereas closed symbols are normalized to the initial amount of dry ash-free coal.

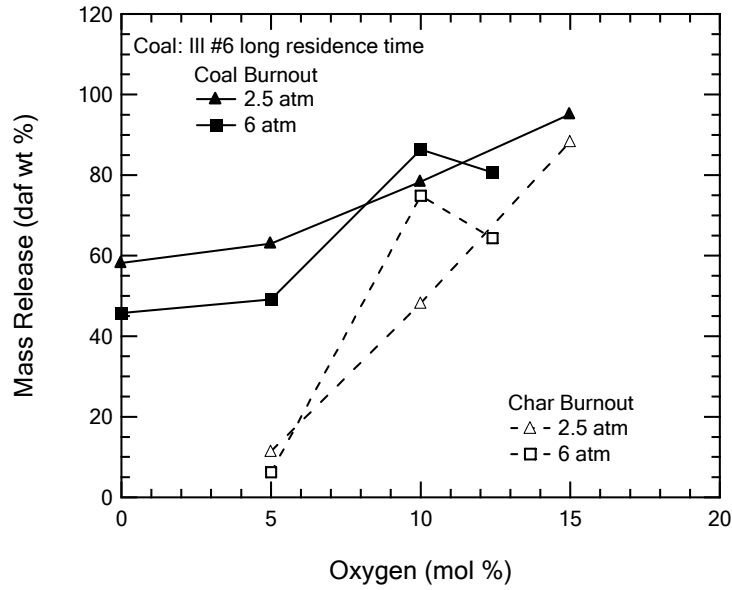


**Figure 7.5.** Measured mass release of Ill #6 coal (long reaction distance) during combustion experiments at different pressures and O<sub>2</sub> concentrations. Open symbols represent the data on a %char burnout basis, whereas closed symbols are normalized to the initial amount of dry ash-free coal.

Unfortunately, due to the constraint of achieving similar gas temperature profiles, the residence times varied for each pressure condition. This also changed the particle temperature profiles. All of these factors made it difficult to determine a single reactivity for each experiment, and hence the burnout data were modeled using the CBK model (Hurt et al., 1998), as discussed later in section 7.2.3.

### 7.2.2 Variations in Char N<sub>2</sub> BET Surface Area during Combustion

Figure 7.6 shows N<sub>2</sub> BET surface areas of chars collected at different post-flame O<sub>2</sub> conditions and pressures. In this study, higher O<sub>2</sub> concentrations corresponded to higher extent of burnout (See Figures 7.2-7.5) and lower N<sub>2</sub> surface areas. As shown for



the Pitt #8 chars, the N<sub>2</sub> surface areas initially increase vs. O<sub>2</sub> concentration for some pressure conditions and then decrease at elevated pressures.

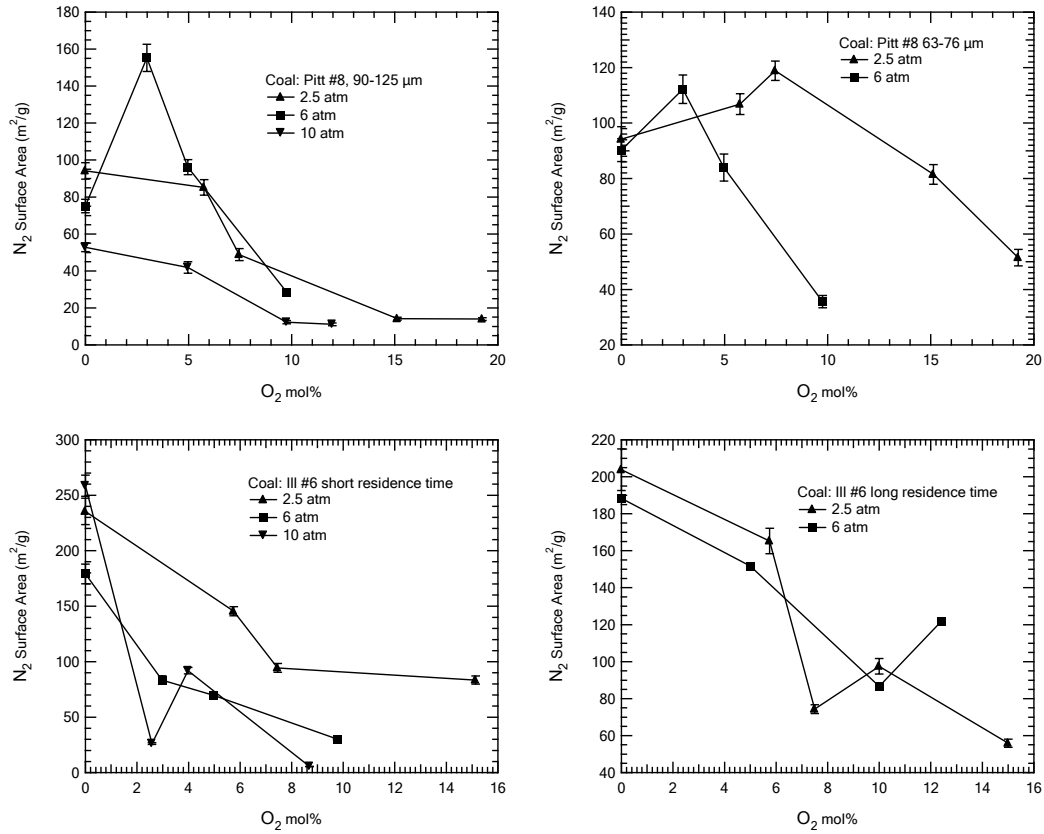


**Figure 7.6.** Nitrogen surface areas of char particles during combustion experiments at different pressures and O<sub>2</sub> concentrations.

No such initial increase in N<sub>2</sub> surface area was observed for the Ill #6 coal chars, or for some of the pressures for the Pitt #8 coal chars. For Ill #6 coal at both long and short residence time experiments, N<sub>2</sub> surface areas decrease with the increased O<sub>2</sub> molar concentrations, which corresponded to increased burnout. The change of char surface area with burnout is apparently related to the evolution of pore structure. For the Pitt #8 coal chars, the opening of closed-off pores contributes to the initial increase of surface

area, followed by decreases in surface area due to the merging and coalescing of pores (Mitchell, 2003). The evolution of pore structure with burnout of Ill #6 coal did not display the initial increase, possibly caused by the different character of the pore structure.

### 7.2.3 Variations in Char $d/d_0$ Ratio during Combustion

Values of  $d/d_0$  for the char samples, determined based on the initial coal diameter, are plotted versus the  $O_2$  concentrations in Figure 7.7. The values of  $d/d_0$  are calculated using the same method described in Chapter 2, which assumes a constant packing ratio. Values of  $d/d_0$ , with  $d_0$  from on the char produced at 0.5 mol%  $O_2$ , are plotted against char burnout in Figure 7.8. The particle diameter ratio based on coal decreased with increasing  $O_2$  concentration for all four conditions. For the Pitt #8 coal, the larger size coal reached a larger diameter ratio than the smaller size coal. The swelling ratio based on the char generally decreased with increasing char burnout. However, values of  $d/d_{char}$  greater than one were obtained, such as for the Pitt #8 90-125  $\mu m$  char. This is possibly caused by the uncertainty of reactor performance, or the effect of varying  $O_2$  content. In contrast, the diameter ratio (based on coal) of Ill #6 char in Figure 7.7 decreased quickly with increased  $O_2$  concentration, and the diameter ratio based on char decreased to 0.5 at about 85% burnout, regardless of the experimental condition or the  $O_2$  concentration.

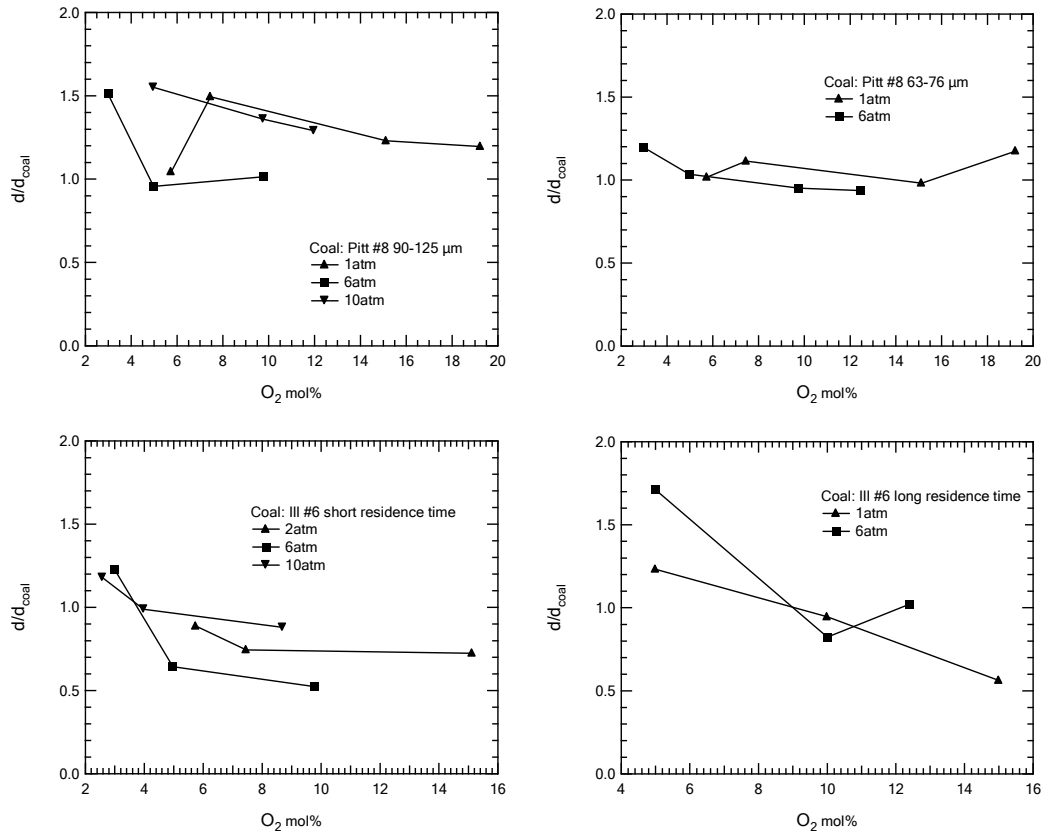


**Figure 7.7.** Diameter ratios of char particles ( $d/d_{\text{coal}}$ ) during combustion experiments at different pressures and  $\text{O}_2$  concentrations. The initial coal diameters were taken from measurements of unreacted coal. Lines are drawn between points for convenience.

### 7.3 High Temperature Char Combustion Modeling

#### 7.3.1 Modeling of Gas and Particle Temperature Profiles

The gas and particle temperature profiles are critical in order to model the char oxidation process. Gas temperature and particle velocity profiles for each condition in the HPFFB were modeled using FLUENT. The centerline gas temperature profile for each condition was measured and used to validate the reliability of the modeling results. The model assumed that the inlet natural gas is reacted instantaneously to equilibrium. The

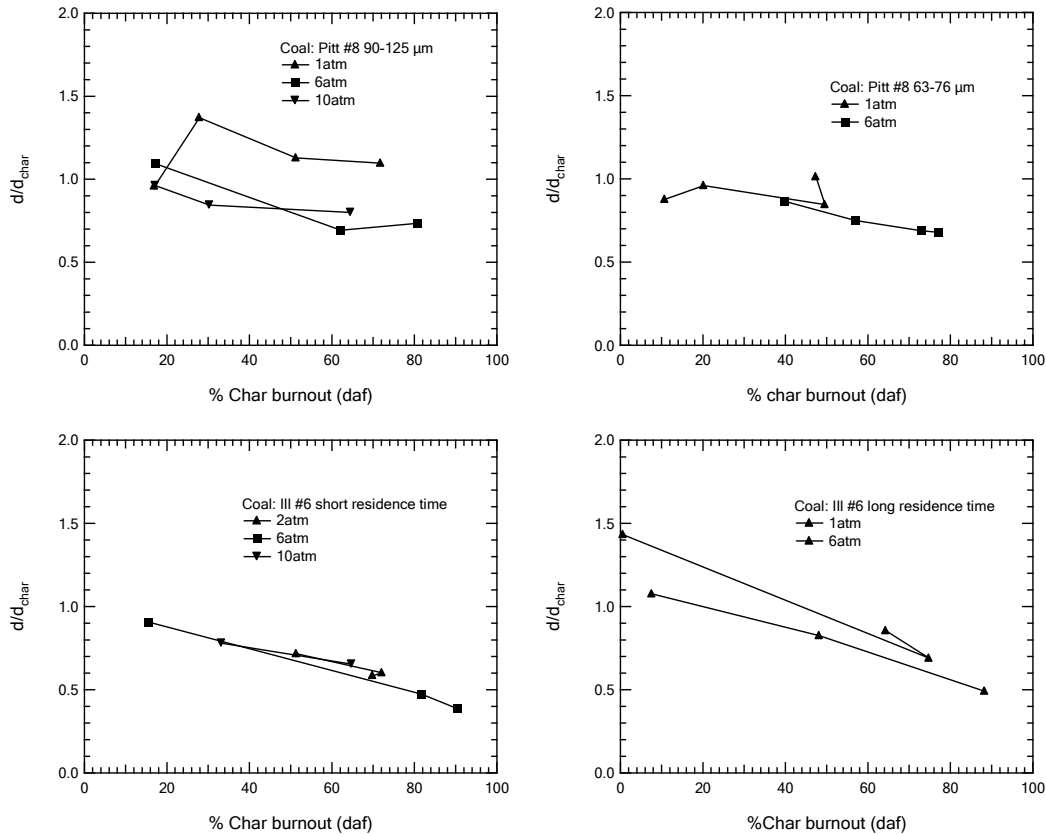


**Figure 7.8.** Diameter ratios of char particles ( $d/d_{char}$ ) during combustion experiments at different pressures and  $\text{O}_2$  concentrations. Initial char diameters for normalization are taken from char formed at 0.5 mol%  $\text{O}_2$  concentration. Lines are drawn between points for convenience.

composition of post-flame products was modeled using an equilibrium code, and was then used as input in the FLUENT calculation. The geometry of the FLUENT modeling is shown in Figure 7.9. The reaction tube length is 321 mm, and the radius is 25 mm. The radius of the feeding tube is 2.38 mm.

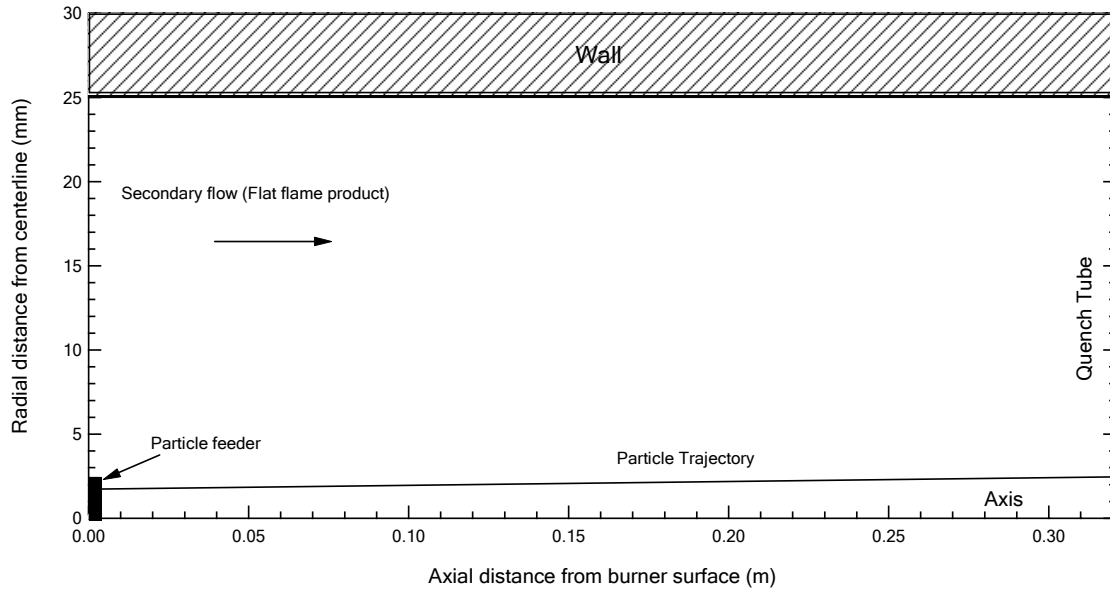


**Figure 7.9.** Geometry and particle trajectory used in the FLUENT calculations.

Coal particles entrained by  $N_2$  entered the reaction zone through a centerline feed tube. The average inlet radial entrance location of particles is assumed to be the area-averaged radius of the feeding tube, which is 1.68 mm from the centerline. Since the particle temperature is affected by the injection position, the area-averaged is reasonable based on the assumption that the particles were evenly distributed in the entraining  $N_2$  flow. Experimental observations of the particle trajectory at the outlet of the reaction tube indicated that particles flowed along the centerline. In this study, several coal particle size ranges were used, which includes 63-76  $\mu\text{m}$ , 90-125  $\mu\text{m}$ , and 74-90  $\mu\text{m}$ . Average particle sizes of 69.5  $\mu\text{m}$ , 107.5  $\mu\text{m}$ , and 82  $\mu\text{m}$  were used in the modeling. Since coal (not char) was used in combustion experiments, it is important to model both the pyrolysis and combustion reactions. In this study, the CPD model was used to calculate the time needed for coal pyrolysis. The combustion process was assumed to begin after the end of pyrolysis. The particle velocity profile was partitioned accordingly.

Figure 7.10 compares the modeled gas centerline temperature profile with the measured temperature profile at 6 atm. The other conditions are listed in the Appendix F. To simulate the dramatic heat loss occurred at elevated pressure, wall temperature was decreased with increasing reaction length. By adjusting the wall temperature profile, good agreement was achieved between the modeled and measured gas centerline temperature profile. Once the modeled gas temperature was in agreement with experimental data, the gas velocity profile from the model was used to calculate the particle velocity profile. The modeled gas temperature profile is comparable with the measured temperature profile, except for the temperature point closest to the burner. This is possibly caused by a departure of the thermocouple bead from the centerline.

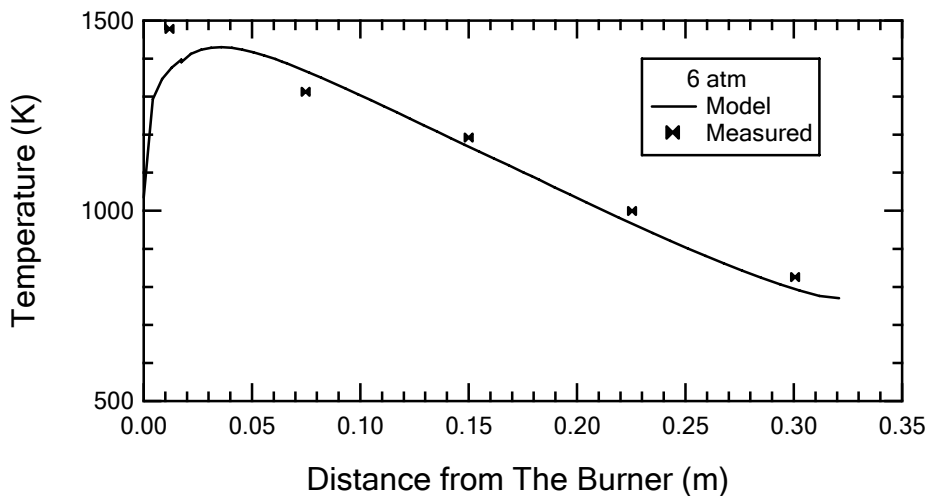


**Figure 7.10.** Measured and predicted centerline gas temperature profiles for Pitt #8 coal at 6 atm.

Figure 7.11 shows the calculated particle velocity profiles of Pitt #8 (90-125 $\mu$ m) at pressures of 2.5, 6, and 10 atm. The velocity decreased dramatically with increased pressure because the gas has a higher density at elevated pressure. In the experiment, the flow rate of inlet gas was increased somewhat to compensate for the decrease in gas

velocity. However the compensation was limited because of the necessity (a) to maintain the laminar flow pattern of the reaction gas flow, (b) to stabilize the flat flame, and (c) to achieve a similar gas temperature profile. These limitations made it impossible to perform experiments at isothermal conditions and similar residence times. The calculated temperature and velocity profiles were therefore used in char combustion modeling, and transient calculations were performed.

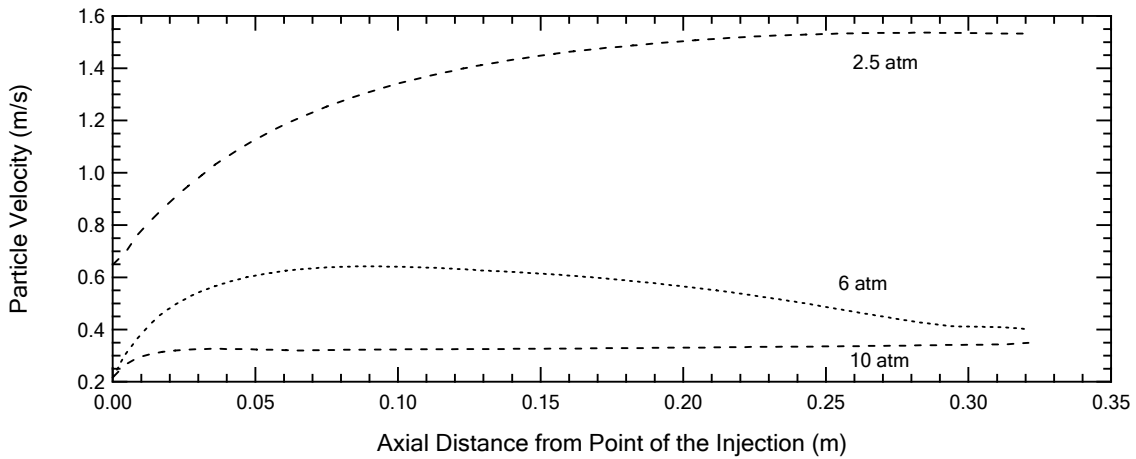


**Figure 7.11.** Predicted centerline particle velocity profiles for Pitt #8 coal.

### 7.3.2 Modeling of Char Combustion Process using n-th Order Kinetic Expressions

The  $n^{th}$  order kinetic expression, also known as the power-law kinetic expression, usually has a form:

$$r_{gas} = kP_{O_2}^n = A \exp(-E / RT) P_{O_2}^n \quad (7.1)$$

This is the most widely used kinetic form in engineering calculations to account for the oxidation of carbon:



In this section, n-th order kinetics were used to model the high-temperature, high-pressure coal combustion kinetic data obtained in this project. Char Burnout Kinetics model 8 (CBK8) was used to model the char combustion process. CBK8 is an available kinetics package that describes char oxidation relevant to pulverized fuel combustion processes (Hurt et al., 1998) that uses n-th order intrinsic kinetics. In addition, a separate version of Hurt's model that includes a 3-step surface mechanism (CBK/E) was used (Niksa et al., 2003).

Both CBK8 and CBK/E incorporate a new correlation for the coal swelling ratio (Benfell, 2001):

$$Sw_1 = \begin{cases} 8.67 - 0.0833C_{daf}, & 89 \leq C_{daf} \leq 92 \\ -0.0458 + 0.01459C_{daf}, & 72 \leq C_{daf} < 89 \\ 1.0, & C_{daf} < 72 \end{cases} \quad (7.3)$$

Where  $C_{daf}$  denotes the daf carbon content of parent coal, and  $Sw_1$  represents the swelling ratio at atmospheric pressure. A correlation which involves the effect of operating pressure is:

$$Sw = \begin{cases} Sw_1^{0.7143+2.857P_T}, & 0.1 \leq P_T \leq 0.8 \\ Sw_1^{3.5-0.625P_T}, & 0.8 \leq P_T \leq 4.0 \end{cases} \quad (7.4)$$

where  $P_T$  is the total pressure in MPa.

Figure 7.12 shows the comparison of the measured swelling ratios during devolatilization for Pitt #8 and Ill #6 coals vs. the values calculated using Benfell's correlation (Eq. 7.3 and 7.4). The results from Benfell's correlation overestimate the swelling ratios of Pitt #8 and underestimate the swelling ratios of Ill #6. This discrepancy is possibly caused by the fact that this correlation does not account for heating rate. Due



to the lack of agreement, the measured swelling ratios were used in the char combustion modeling here instead of using the correlation of Benfell.

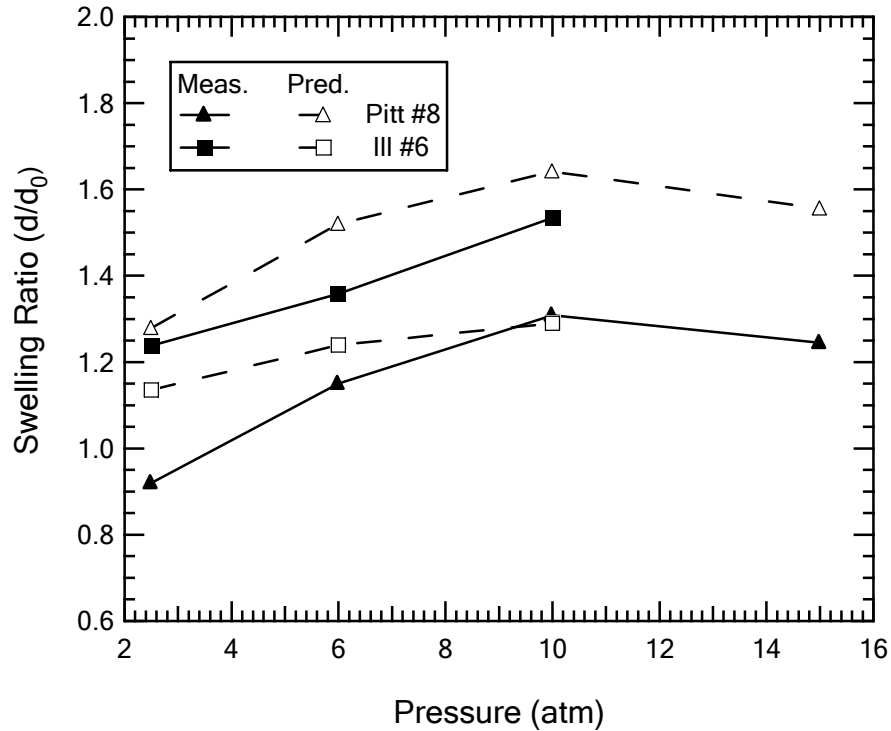


**Figure 7.12.** Comparison of swelling ratios of Benfell’s model and measured swelling ratios during devolatilization.

In the CBK8 model, the initial starting char mass subsequent to pyrolysis is input via a variable named “high-temperature volatile yield (HTVL)”. However, starting char mass changes with pressure. The most rigorous modeling effort would be to integrate a complex coal devolatilization model. In this study, coal particle temperature and velocity profiles obtained from FLUENT calculations were used as input for the CPD model. The coal pyrolysis time and volatile yield were calculated from the CPD model calculation and used as input parameters in the char combustion modeling.

CBK8 uses an n-th order relation to calculate the CO/CO<sub>2</sub> ratio, and this relation was used here. The distributed activation energy model of thermal annealing and the ash inhibition model in the CBK models were also used. The CBK models were developed from coals similar to those used in this study, and are therefore, thought to be applicable.

The n-th order combustion model of char has three parameters: (1) the pre-exponential factor A, (2) the activation energy E, and (3) the oxygen order n. The oxygen order n was assumed to be 0.5 based on Hurt's recommendation (1998). Hurt correlated the pre-exponential factor A with coal carbon mass fraction as follows:

$$A = 10^{14.969 - 0.746 \times C_{daf}} \quad (7.5)$$

The values of the pre-exponential factor (A) were calculated from Eq. 7.5 for the two coals used in this study, and are shown in the Table 7.3.

**Table 7.3 Pre-exponential Factor (A) Used in CBK8**

Coal	A (g <sub>char</sub> /(g <sub>char</sub> *sec*(mol <sub>O2</sub> /m <sup>3</sup> ) <sup>0.5</sup> ))
Pitt # 8	3.2 × 10 <sup>8</sup>
Ill # 6	1.0 × 10 <sup>9</sup>

Using a single pre-exponential factor for each coal provides a basis for comparing char reactivity, which is reflected by the activation energy only. The activation energy E was optimized to find the best fit to the measured burnout data. Figure 7.13 shows a parity plot of the best-fit vs. measured burnouts using CBK8. The agreement between the parameter fit and the data is good, especially when considering that the pyrolysis yield was calculated as well. Figure 7.14 shows the activation energies (E) used to obtain the best fit of each experimental measurement. Activation energies decrease with increasing

pressure for most char, except for the Pitt #8 large at 6 atm, which is slightly less than the activation energy of Pitt #8 char at 10 atm. Since only activation energy was changed in the modeling, this trend indicates the char intrinsic reactivity increased with increasing pressure.

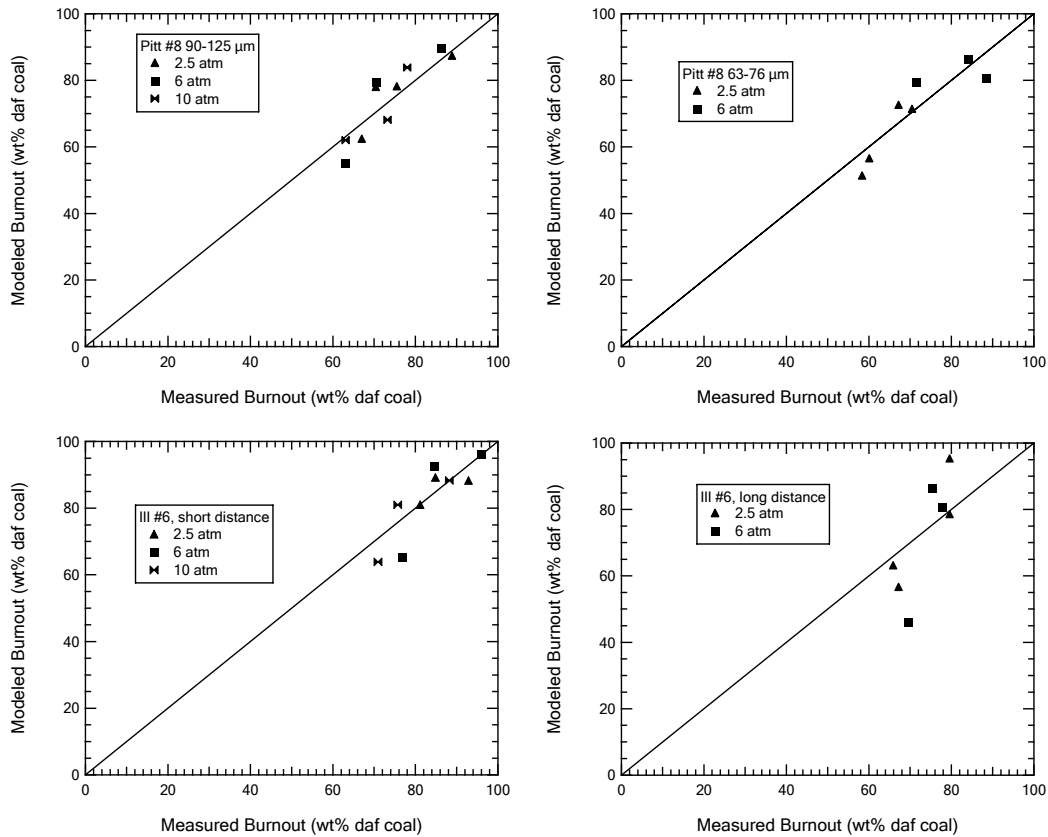


**Figure 7.13.** Modeled burnouts using of CBK8 versus measured burnouts for the four combustion conditions.

The resulting error between the modeling results of CBK 8 and the measured values of mass releases or each coal char are listed in Table 7.4. This relative error was calculated using following equation:

$$\text{Relative error} = \sqrt{\frac{\sum_{i=1}^n \left[ \frac{(p_i^p - p_i^0)^2}{p_i^0} \right]}{n}} \quad (7.6)$$

where n is the number of the data points modeled;  $p_i^p$  is the burnout prediction for the  $i^{\text{th}}$  record;  $p_i^0$  is the measured burnout value.

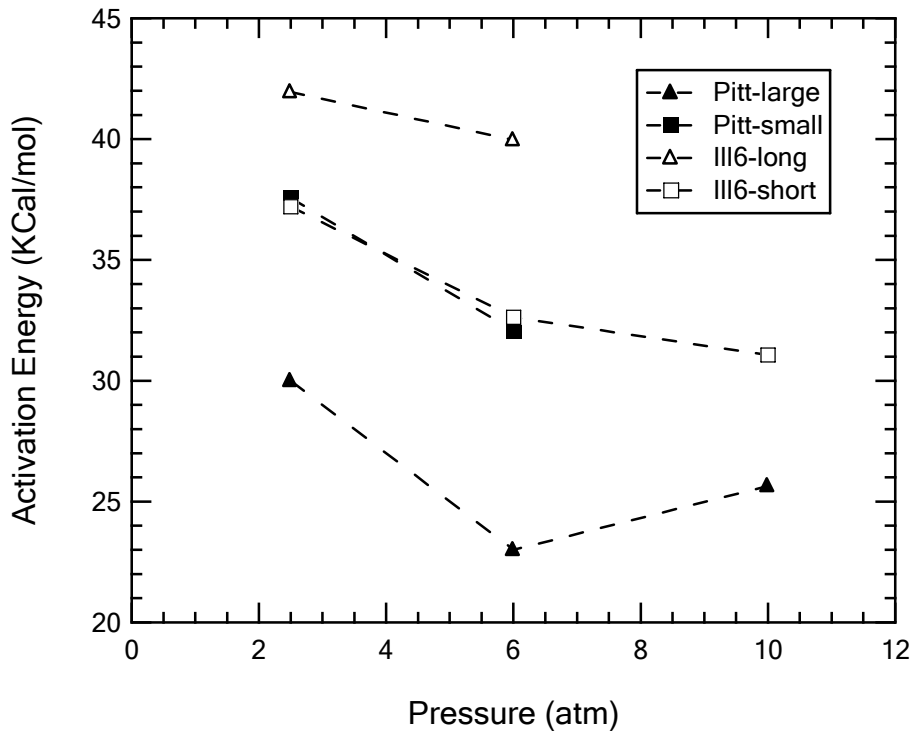


**Figure 7.14.** Modeled Activation Energy (E) determined from best fits of the data at different pressures.

**Table 7.4 Relative Error between Calculations and Measured Values of Mass Release Using the CBK8 Model**

Coal chars	Relative Error (%)
Pitt #8 large	8.0
Pitt #8 small	8.1
Ill #6 long reaction distance	7.1
Ill #6 short reaction distance	18.2

Figure 7.15 compares the activation energy (E) modeled from CBK8 with the activation energy measured from HPTGA tests, which were described in Chapter 6. For the CBK8 results, the activation energies of small size Pitt #8 and Ill #6 short distance data were used for comparison. While the data acquired from HPTGA and CBK modeling results share the same trend, the difference is also distinct (such as oxygen order for CBK8 is 0.5, and HPTGA tests have an order around 0.8). It was not possible to use the TGA data directly to model the high temperature reaction rates, due to changes in surface areas and other properties, although it will be the subject of some current research (Mitchell and Ma, 2005).

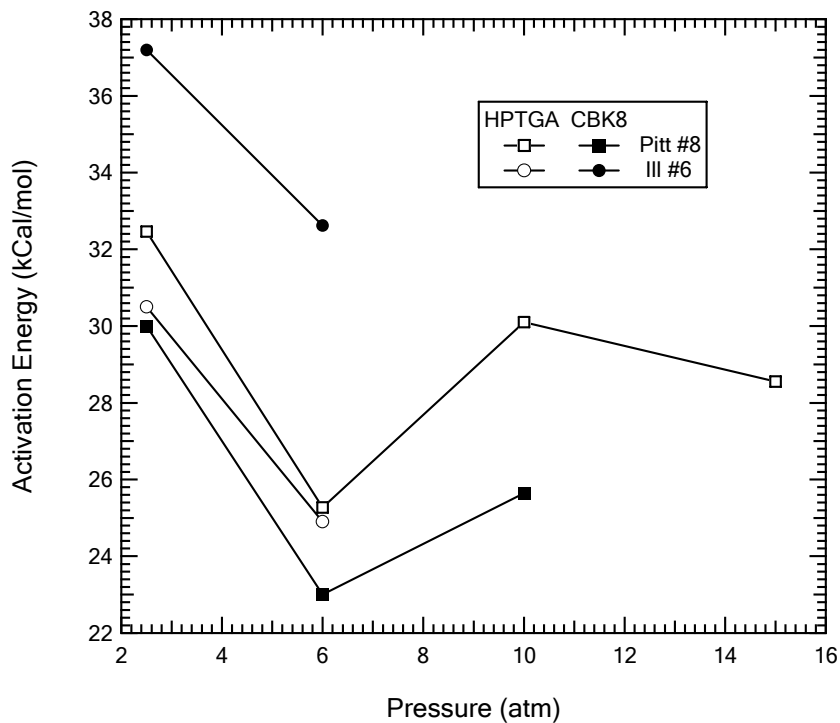
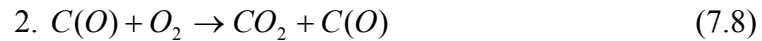


**Figure 7.15.** Comparison of Modeled Activation Energy (E) from CBK 8 with measured Activation Energy (E) from HPTGA experiments.

### 7.3.3 Modeling of Char Combustion Process using 3-Step Kinetics

The Char Burnout Kinetics Extension model (CBK/E) was developed by Hurt et al. (1998), and then was later modified to include a three-step kinetic mechanism (See Table 2.4) (Hurt and Calo, 2001):



This model was recently evaluated by comparison with several sets of high-pressure char combustion data (Niksa et al., 2003). Using one adjustable kinetic parameter  $A_{30}$  (pre-exponential factor of reaction 7.9) and default values for all other parameters, the model was shown to agree with the reported combustion behavior in many experiments. However, for low-rank coals, the reported values of  $A_{30}$  at high pressure were lower by just over half an order-of-magnitude than those at atmospheric pressure.

In the evaluation of CBK/E (Niksa et al., 2003), all of the data were obtained from combustion experiments on chars produced at atmospheric pressure. In contrast, the major objective of this study is to perform experiments on chars at the same pressure at which they were formed. The char burnout data (Figures 7.2-7.5) were modeled in this section using the CBK/E model.

Each reaction in CBK/E is a quasi-global reaction and has a pre-exponential factor  $A$  and an activation energy  $E$ . The overall rate and CO/CO<sub>2</sub> molar ratio are controlled by these parameters as follows (Hurt and Calo, 2001):

$$r = \frac{k_1 k_2 P_{O_2}^2 + k_1 k_3 P_{O_2}}{k_1 P_{O_2} + k_3 / 2} \quad (7.10)$$

$$CO / CO_2 = \frac{k_3}{k_2 P_{O_2}} \quad (7.11)$$

Among the six parameters  $A_1$ ,  $A_2$ ,  $A_3$ ,  $E_1$ ,  $E_2$ , and  $E_3$ , all activation energies were assigned based on the published char kinetic data (Niksa et al., 2003). The initial pre-exponential factor for  $k_3$  (Step 3) is used to normalize the pre-exponential factors  $k_1$  and  $k_2$ . Thus the controlling parameter for three-step mechanism is the value of pre-exponential factor of reaction 7.9 ( $A_{30}$ ). The values of  $E_1$ ,  $E_2$ ,  $E_3$ , and  $A_{20}/A_{30}$ ,  $A_{30}/A_{10}$  are listed in the Table 7.6. Note that these kinetic coefficients are very different from the TGA-derived coefficients because this is not the n-th order reaction scheme.

**Table 7.5 Kinetic Parameters Used in CBK/E**

$E_1$ (kJ/mol)	25
$E_2$ (kJ/mol)	117
$E_3$ (kJ/mol)	133.8
$A_1/A_{30}$ (bar <sup>-1</sup> )	$1.0 \times 10^6$
$A_2/A_{30}$ (bar <sup>-1</sup> )	$5.0 \times 10^4$

The CBK/E model also uses a generalized internal effectiveness factor and a power-law exponent that relates density changes to the extent of burnout. Literature values were assigned to the kinetics of other submodels such as ash inhibition model, thermal annealing model, etc. (Niksa et al., 2003). The CBK/E model was included as a subroutine in an optimization software package OptdesX (Parkinson et al., 1992) in order

to adjust the kinetic parameter ( $A_{30}$ ) within pre-set values between  $1.0 \times 10^7$  and  $1.0 \times 10^9$  (Niksa et al., 2003) to best fit the high temperature experimental data.

Figure 7.16 shows the resulting comparisons of calculated and measured burnouts for the four conditions: Pitt #8 large particle size; Pitt #8 small particle size; Ill #6 short reaction distance; and Ill #6 long reaction distance. Because  $A_{30}$  is coal rank dependent and is also affected by the char formation pressure, a unique  $A_{30}$  was calculated for different pressures at each condition by minimizing the square of the error between model predictions and the data.

Effectively,  $A_{30}$  represents the “reactivity” of the char, and CBK/E does not have a mechanism to deal with the effect of pressure on char characteristics. Therefore, the variation of  $A_{30}$  is a measure of the effect of formation pressure on char reactivity. The increase of  $A_{30}$  with increasing pressure represents the char intrinsic oxidation reactivity increases with increasing pressure. This trend is consistent with the modeling result of CBK8.

The resulting errors associated with the best fit coal burnout results from CBK/E at different conditions, as shown in Figure 7.16, are listed in Table 7.6. The optimal values of  $A_{30}$  with pressure are shown in Figure 7.17.

For four conditions tested, the Ill #6 coal burnout prediction at the short reaction distance had the maximum error (20.2%); predictions of the other three conditions had errors of about 10%. A similar result was also obtained with modeling of CBK 8 as described early in this Chapter. One possible cause for error in the model is that the mode of burning parameter was held constant at 0.2, as recommended by Hurt et al. (1998). However, it was observed that the Ill #6 char at short reaction distance exhibited



a faster decrease in particle size with increased oxygen content compared with the other conditions (see Figure 7.8). This effect of diameter change should be included for better calculations, but becomes cumbersome for true predictions unless a model describing diameter change can be used reliably.

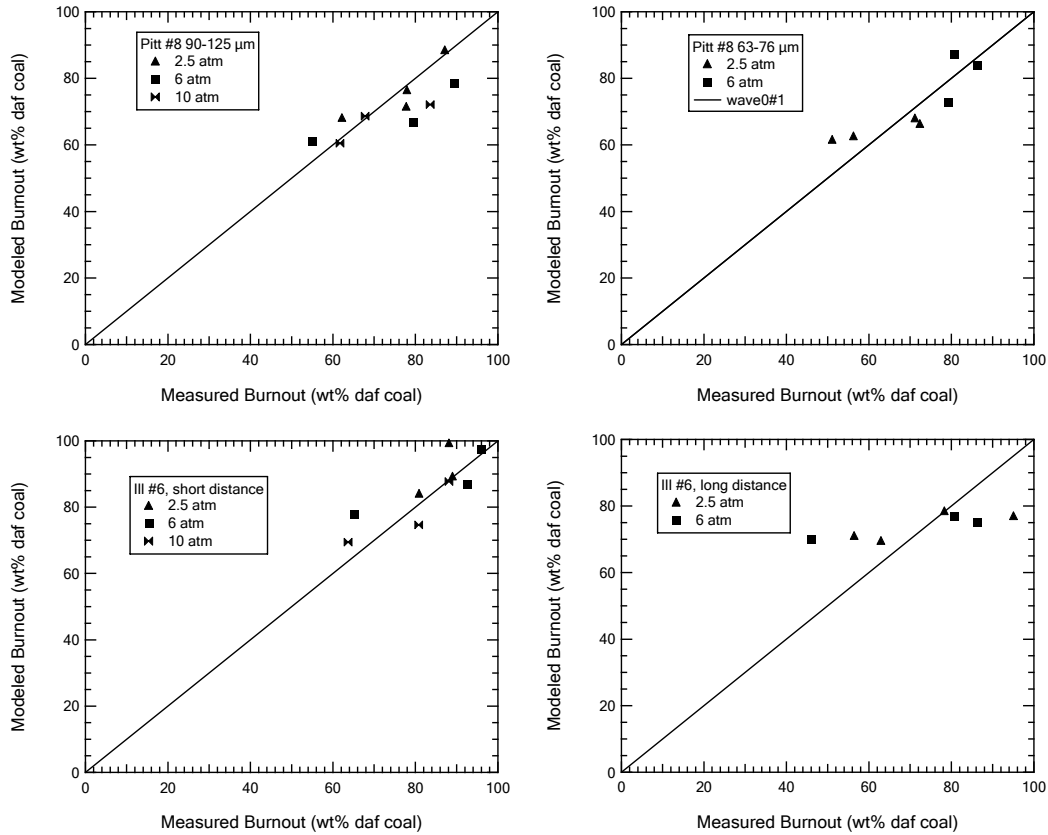


**Figure 7.16.** Predicted burnouts using CBK/E versus measured burnouts for the four combustion conditions.

**Table 7.6 Relative Error between Calculations and Measured Values of Mass Release Using the CBK/E Model**

Coal chars	Relative Error (wt%)
Pitt #8 large	10.4
Pitt #8 small	9.0
Ill #6 long reaction distance	7.9
Ill #6 short reaction distance	20.2

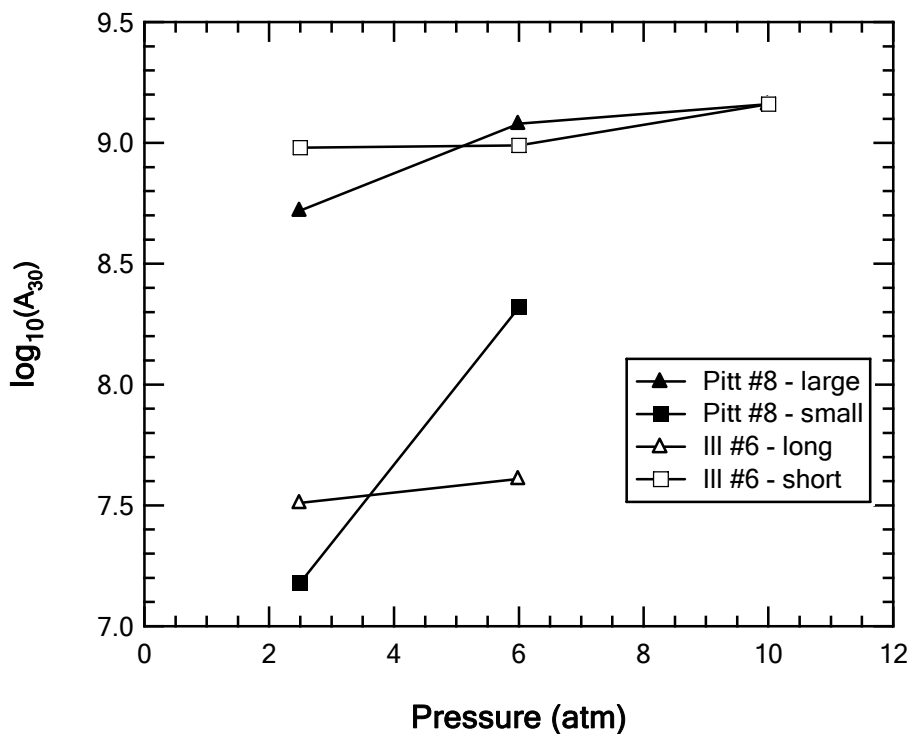


**Figure 7.17.** Best-fit values of  $A_{30}$  for the four combustion conditions.

#### 7.3.4 Discussion of Modeling Results of High Temperature Char Oxidation

Both an  $n^{\text{th}}$ -order (CBK8) and a 3-step surface mechanism (CBK/E) were used to model char combustion for two coals as a function of pressure. Initial char yields were calculated using the CPD model. The  $n^{\text{th}}$ -order modeling results indicated that activation energies decreased by about 20% as pressure increased from 2.5 to 15 atm. The values of  $E$  calculated were within the range of 100 to 180 kJ/mol (24~43 kcal/mol), which is the range of reported activation energies in most char oxidation experiments. The decreased activation energy with elevated pressure represents the increasing reactivity with increasing pressure.

Drastic changes in activation energy with pressure were reported by Monson et al. (1995). Apparent activation energies as low as 3.4 kcal/mol were reported. Their results

were influenced by using chars formed only at atmospheric pressure and by the limitations of their 2-color pyrometer.

The CBK/E model was also compared with the high pressure char oxidation data obtained in this project. Only one adjustable parameter ( $A_{30}$ ) was used in the CBK/E calculations, with 10% relative error for three conditions and 20% relative error for one condition studied. However, a different value of  $A_{30}$  was needed for each experimental condition for each coal, indicating that the effect of pressure on char properties affected reactivity as well.

These high-temperature, high-pressure char combustion experiments showed a different trend than the results obtained from low-temperature, high-pressure char combustion experiments (Chapter 6). The low-temperature experiments showed a decrease in reactivity as pressure increased. The reason for this difference is not entirely clear. It has been shown that the char internal surface area affects char intrinsic reactivity during Zone I combustion (or oxygen-complex reaction control). However, when char was burned at high-temperature (Zone II or III), where diffusion control began to dominate the reactivity, the contribution of char surface area was less important. Apparently, the chemical structure such as the active sites, which may be related to enriched hydrogen content for the char formed at high pressure, increased the oxyreactivity. The results of CBKE shows  $A_{30}$  increased with increasing pressure, which means that the C(O) desorption rate increased with increasing pressure. For example, if char formed at high pressure has more aliphatic material (matching the increased hydrogen content), more oxygen may be adsorbed on the aliphatic material. The attached C(O) may therefore have a lower desorption activation energy. A detailed study of the

chemical structure of char formed at different pressures is needed to confirm this hypothesis.

The effect of the total pressure on char oxidation kinetics has been studied for decades, and the reported results do not seem consistent. Several reviews (Hong, 1999; Niksa et al., 2003; Wall et al., 2002) and the literature review of this dissertation (Chapter 2) summarize the previous elevated pressures char oxidation studies. The char oxidation data available for comparison in this study met the requirements for complete char oxidation experiments such as high-temperature (Zone II temperature), pulverized coal size ( $<100\ \mu\text{m}$ ), and single particle behavior. All of these previous studies formed their chars at atmospheric pressure. Key findings from other experiments that meet these criteria are:

1. Monson et al. (1995) reported that char oxidation rate (area reactivity) increased with increasing pressures from 1-5 atm, then decreased at pressures from 5-15 atm at constant oxygen molar fraction;
2. Joutsenoja et al. (1999) and Saastamoinen et al. (1996) reported that char burnout rate decreased at elevated total pressure and constant oxygen partial pressure. However, at constant oxygen volume fraction (10%), the burnout rate increased when pressure was increased from 2 to 5 atm, and leveled off with further increasing of total pressure.

The diversity of different results may be caused by the experimental technique and/or the respective data analysis. Modeling of literature data is reviewed by Hong et al. (2000b) and Niksa et al. (2003).

It is well-known that char burnout is a function of char properties (e.g.,  $\rho$ , pore structure and evolution, internal surface area, and elemental composition), reaction kinetics, and reaction conditions (e.g.,  $P_{O_2}$ ,  $T_p$ , and  $P_{tot}$ ). Several theoretical factors play roles in the change of char reaction rate with increasing pressure:

1. Bituminous coal chars undergo a plasticity stage during pyrolysis, thus char formed at high pressure has a more oriented surface (Niksa et al., 2003) and lower surface area, which is associated with lower reactivity.
2. Char formed at high pressure has higher hydrogen content, which may be related to more reactive char.
3. Elevated total pressure can restrain the gas diffusion coefficient, thus decreasing the global reactivity at high temperature (Zone II or Zone III combustion).
4. At constant total pressure, increased oxygen partial pressure ( $P_{O_2}$ ) increases the char oxidation reactivity until the char surface is saturated. At high temperature, a higher  $P_{O_2}$  is needed to achieve surface saturation because of the increased reaction rate (or faster desorption of surface complexes) (Roberts and Harris, 2000).
5. The effect of mineral matter is primarily responsible for the high-reactivity of low-rank coal, especially at low temperatures, although this effect becomes less important at high temperatures. The role of catalytic mineral matter at high pressure is still unclear (Niksa et al., 2003).

The complexity of char combustion reactions makes it difficult to develop a comprehensive model to include all mechanisms. The CBK8 model used an n-th order

reaction mechanism, but activation energy needs to be changed as a function of pressures. The CBK/E model was a good attempt at using a surface mechanism, but still required one adjustable parameter  $A_{30}$  that was a function of pressure. Hurt developed correlations for  $A_{30}$  based on pressure and coal type, but notes that a complete mechanistic description is still unavailable (Niksa et al., 2003). However, this mechanism (in CBK/E) may be useful for engineering calculations over a wide range of conditions.

It should be pointed out this was the first attempt to study effects of pressure on whole coal combustion process including coal devolatilization and char combustion. The results presented here are different than previously published high pressure char combustion data because this study measured char reaction rates at the pressure at which the char was formed, rather than forming the initial char at atmospheric pressure. This study was also performed at higher particle heating rates than other studies, which reduced char swelling and affected char morphology. These results are therefore more realistic and closer to industrial processes than other studies.

#### **7.4 Summary of High Temperature Char Combustion Experimental and Modeling Results**

High-pressure, high-temperature char combustion experiments were performed in an HPFFB for two coals: Pitt #8 and Ill #6. Char samples were collected and analyzed.

The following phenomena were observed:

- (1) Within the total pressure range from 2.5 to 10 atm, char burnout increased with increasing  $O_2$  concentration at constant total pressure.
- (2)  $N_2$  surface area for Pitt #8 chars increased at early stages of burnout and then decreased with increasing burnout.  $N_2$  surface areas for Ill #6 chars always decreased with increasing burnout. The evolution of pore structure

with burnout probably contributed to the change of  $N_2$  surface area. The difference in the surface area behavior between the two coals may be caused by the different character of pore structure.

- (3) The particle diameter ratio based on coal ( $d/d_{\text{coal},0}$ ) decreased with increasing  $O_2$  concentration for all four conditions. For the Pitt #8 coal, the larger size coal achieved a larger swelling ratio than the smaller size coal. The diameter ratio based on the char ( $d/d_{\text{char},0}$ ) generally decreased with increasing char burnout. The diameter ratio (based on coal) of Ill #6 char decreases quickly with increased  $O_2$  concentration, and the diameter ratio based on char decreased to 0.5 at about 85% burnout rate, regardless of the experimental condition or the  $O_2$  concentration.

The gas temperature and velocity profiles were modeled using Fluent. The coal pyrolysis process was modeled using the CPD model. The results from these two models were used as input parameters for the char burnout model. Both  $n^{\text{th}}$ -order kinetics and 3-step surface kinetics were used to model the experimental results. Only one kinetic parameter was used to fit the experimental char burnout data:

1. Activation energy ( $E$ ) was used as a fitting parameter for the  $n^{\text{th}}$ -order kinetic model (CBK8), and
2.  $A_{30}$  was used as a fitting parameter for the 3-step model (CBK/E).

Both CBK8 and CBK/E achieved with 10% relative error for three conditions and 20% relative error for one condition with the char combustion data. The modeling results showed that the char oxidation rate increased with increasing total pressure. A different value of  $E$  or  $A_{30}$  was necessary for each pressure condition for each coal. This means

that a one-point calibration is necessary for every condition before CBK/E or CBK8 is capable of predicting char burnout.

The result obtained here indicates that char reactivity constant increases with increasing total pressure, which is different than reported by some investigators. This difference is likely due to the fact that most previous investigators produced their starting char at atmospheric pressure only, rather than at the pressure where reactivity was measured (as was done in this study). The pressure during pyrolysis affects the char morphology and hydrogen content, which in turn affect apparent char reactivity.



## 8. Summary and Conclusions

The objective of this project was to characterize high pressure high heating rate coal pyrolysis and char combustion, with emphasis on improving understanding of the effect of pressure on coal pyrolysis and char combustion, and on improving coal char high pressure combustion models. The results of this project will be useful in designing high-pressure entrained flow gasifiers and other advanced coal conversion systems. These objectives were reached through the following accomplishments.

### 8.1 Accomplishments

1. A high-pressure flat flame burner system was designed, constructed, and used to perform devolatilization and high temperature reactivity tests. A  $\text{CH}_4/\text{air}/\text{O}_2$  flame was operated under slightly fuel lean or oxidizing atmosphere to provide a high-temperature, high-pressure environment. This burner was able to achieve particle heating rates of  $10^5$  K/sec and a high-temperature gas environment. Coal rank, oxygen mole fraction, and reaction distance were chosen as variables to study the effect of pressure on coal pyrolysis and char combustion.

2. Sixteen pyrolysis tests were completed. Chars were generated from four typical coals from a wide range of rank and origin at high heating-rate, high-temperature, and high-pressures, including four different pressures (2.5, 6, 10, and 15 atm). The products of these pyrolysis experiments were quenched with cold nitrogen gas after a short time at high temperature. These pyrolysis tests captured the evolution of the char chemical and structural characteristics during rapid pyrolysis at different pressures for coals of varying rank.
3. A series of high-pressure TGA tests were performed to determine intrinsic reactivities of chars and to find the effect of pressure on char reactivity. By keeping the total pressure the same as the char formation pressure, the effects of formation pressure on char intrinsic reactivities were studied.
4. Forty-three high temperature coal combustion tests were performed to study the effect of pressure on oxidation reactivities of char. The reaction products were collected and analyzed to provide high-temperature reactivities.
5. The process of high-temperature, high-pressure char combustion was modeled. Both an  $n^{\text{th}}$  order kinetics model and a three-step kinetic model were used to correlate the data collected in this study. The effect of pressure on char reactivity was analyzed.

## 8.2 Summary of Results

### 8.2.1 Effects of Pressure on Char Properties

Four coals with a broad rank distribution, including Kentucky #9, Illinois #6, Pitt #8, and Knife River Lignite, were pyrolyzed in an atmospheric flat-flame burner, and in a high-pressure flat-flame burner. Resulting chars were collected at pressures of 0.85, 2.5, 6, 10, and 15 atm. The chars were analyzed to characterize the effect of pressure on char properties.

The measured decreases in total volatiles yields with increasing pressure were predicted using the CPD model using only the elemental composition and ASTM volatiles yields of the parent coals as changeable input parameters that relate to coal chemical structure. The measured H/C and O/C ratios in the resulting chars initially increase with increasing pressure, but remain relatively constant at pressures from 6 to 15 atm. The H/C ratio in the char is thought to be affected by, 1) the decrease in tar yield at increased pressures, 2) the change in the hydrogen content of the tar with pressure, and 3) the increase in light gas yield as pressure increases. The change in residence time at different pressures in these experiments may also have played a role in the hydrogen release.

Swelling ratios of the lignite chars were less than 1.0, and only about 1.3-1.8 for the bituminous coals. All coal chars showed slight increases in swelling behavior as pressure increased. The swelling behavior observed for the Pitt #8 coal char at each pressure was lower than reported in high pressure drop tube experiments, supporting earlier work at atmospheric pressure showing that particle swelling decreases as heating rates approach  $10^5$  K/s. The morphology of chars produced at different pressures were

analyzed using SEM. Chars formed at high pressure were observed to be in the early stage of foam structure evolution, while chars formed at low pressure were in later stages of foam evolution. The swelling ratio of chars increased with increasing pressure, and is attributed to bubble evolution.

Char surface areas were measured using both CO<sub>2</sub> and N<sub>2</sub> as adsorption gases, and decreased with increasing pressure. The amount of micropores was less for chars produced at high pressure. The high pressure chars were more porous than the lower pressure chars, but had a more dense framework.

### 8.2.2 Effects of Pressure on Char Intrinsic Reactivity

TGA char oxidation reactivities were measured at the same total pressure as the char preparation pressure. The general trend was that the TGA reactivity on a gram per gram available basis decreased with increasing char formation pressure for both Pitt #8 and Knife River lignite coal chars. The Pitt #8 char intrinsic activation energy and oxygen reaction order remained relatively constant (~0.8) with increasing pressure.

The intrinsic reactivity on a g/g<sub>avail</sub>-s basis at 5% char burnout was normalized by the N<sub>2</sub> and CO<sub>2</sub> internal surface area. The resulting normalized reactivity was found to be relatively constant with increasing pressure for both the N<sub>2</sub> and CO<sub>2</sub> normalizations. The fact that the normalized reactivity is constant with pressure seems to indicate that the majority of the change in char reactivity with pressure can be attributed to changes in internal surface area. The normalization of reactivity by the N<sub>2</sub> surface area shows less dependence on pressure than that normalized by the CO<sub>2</sub> surface area.

### 8.2.3 Effects of Pressure on High Temperature Char Characteristics

High-pressure, high-temperature char combustion experiments were performed in a HPFFB for two coals: Pitt #8 and Ill #6. Char samples were collected and analyzed. The following phenomena were observed:

- Within the total pressure range from 2.5 to 10 atm, char burnout increased with increasing O<sub>2</sub> concentration at constant total pressure.
- N<sub>2</sub> surface areas for Pitt #8 chars increased at early stages of burnout and then decreased with increasing burnout. N<sub>2</sub> surface areas for Ill #6 chars always decreased with increasing burnout. The evolution of pore structure with burnout contributed to the change of N<sub>2</sub> surface area. The difference in the surface area behavior between the two coals may be caused by the difference of pore structure.
- The particle diameter ratio based on coal ( $d/d_{\text{coal},0}$ ) decreased with increasing O<sub>2</sub> concentration for all four conditions. For the Pitt #8 coal, the larger size coal achieved a larger swelling ratio than the smaller size coal. The diameter ratio based on the char ( $d/d_{\text{char},0}$ ) generally decreased with increasing char burnout. The diameter ratio (based on coal) of Ill #6 char decreases quickly with increased O<sub>2</sub> concentration, and the diameter ratio based on char decreased to 0.5 at about 85% burnout rate, regardless of the experimental condition or the O<sub>2</sub> concentration.

#### 8.2.4 The Modeling of High-Temperature Char Combustion

The gas temperature and velocity profiles were modeled using Fluent. The coal pyrolysis process was modeled using the CPD model. The results from these two models were used as input parameters for the char burnout model. Both n-th order kinetics and 3-step surface kinetics were used to model the experimental results. Only one kinetic parameter was used to fit the experimental char burnout data:

- Activation energy (E) was used as a fitting parameter for the n<sup>th</sup>-order kinetic model (CBK8), and
- $A_{30}$  was used as a fitting parameter for the 3-step model (CBK/E).

Both CBK8 and CBK/E achieved with 10% relative error for three conditions and 20% relative error for one condition with the char combustion data. The modeling results showed that the char oxidation rate increased with increasing total pressure. A different value of E or  $A_{30}$  was necessary for each pressure condition for each coal. This means that a one-point calibration is necessary for every condition before CBK/E or CBK8 is capable of predicting char burnout.

The result obtained here that char reactivity constant increases with increasing total pressure is different than reported by some investigators and of the TGA results reported in this study. Some of that difference may be due to the fact that many previous investigators produced their starting char at atmospheric pressure only, rather than at the pressure where reactivity was measured (as was done in this study). The pressure during pyrolysis affects the char morphology and hydrogen content, which in turn affect apparent char reactivity.

### 8.3 Principal Conclusions

This study of the effect of pressure on coal pyrolysis, resulting char properties, and char high-temperature combustion reactivity, has given rise to the following conclusions:

1. The volatiles yield decreased with increasing pressure, which can be reasonably predicted by the CPD model. The H/C and O/C ratios in the resulting chars initially increased with increasing pressure, but remained relatively constant at pressures from 6 to 15 atm.
2. The major effect of pressure on char properties was the change of physical structure. All coal chars showed slight increases in swelling behavior as pressure increased. High heating rates in this study caused lower swelling ratios for most of the coals tested than those reported in drop tube reactors. Chars formed at high pressure were apparently in the early stage of foam structure evolution, while chars formed at low pressure were in later stages of foam evolution. Char surface areas using both CO<sub>2</sub> and N<sub>2</sub> as adsorption gases decreased with increasing pressure. The amount of micropores was less for chars produced at high pressure. The high pressure chars were more porous than the lower pressure chars, but had a denser framework.
3. TGA reactivity on a gram per gram available basis decreased with increasing char formation pressure for Pitt #8, Ill #6, and Knife River lignite coal chars. Based on limited experiments, the Pitt #8 char intrinsic activation energy and oxygen reaction order remained relatively constant with increasing pressure. However the normalized reactivity was found to be relatively constant with

increasing pressure for both the N<sub>2</sub> and CO<sub>2</sub> normalizations. The fact that the normalized reactivity is constant with pressure indicates that the majority of the change in char reactivity with pressure may be attributed to changes in internal surface area.

4. Char burnout increased with increasing O<sub>2</sub> concentration at constant total pressure. The particle diameter ratio of Ill #6 based on coal ( $d/d_{\text{coal},0}$ ) decreased with increasing O<sub>2</sub> concentration, while the particle diameter ratio of Pitt #8 is relatively constant with increasing O<sub>2</sub> concentration.
5. The modeled activation energies of Pitt #8 and Ill #6 coal using CBK8 have similar trends with activation energies measured using HPTGA.
6. The modeling results showed that the char oxidation rate constant increased with increasing total pressure. A different value of E or A<sub>30</sub> for n<sup>th</sup> order or 3-step kinetic models was necessary for each pressure condition for each coal. This means that a one-point calibration would be necessary for every condition before CBK/E or CBK8 would be capable of predicting char burnout.

#### **8.4 Limitations and Recommendations**

The effect of pressure on the coal combustion and gasification process has been studied for decades, but questions remain. The current study used a unique experiment involving a high-pressure flat-flame burner. The results confirm some of what has been reported in previous studies, and also revealed new phenomena. Several limitations and recommendations are presented here to help improving future research in the area of



high-pressure coal combustion.

(1) Improve the HPFFB experiment system. The most challenging task of this project was to develop the HPFFB. However, the temperature profile in the axial direction of the reactor was not constant at high pressure. This non-uniform profile may be due to the following reasons:

- Dramatic heat loss through reactor insulation layer at high pressure. This problem was also addressed by Monson (1992), and may be caused by the performance degradation of the insulation material with increased pressure. A possible solution is replacing the current micro-porous insulation with rigid, denser insulation.
- The effect of buoyancy. In the current setting, a down-fired burner was used. The buoyancy counteracted the flow, and this effect is more evident at high pressure. The buoyancy also caused higher temperature of the burner surface and thus shortened the life of the burner. A future renovation could use an up-fired burner. This will improve the performance and decrease the high-temperature erosion of the burner

(2) The residence time in these tests could be only modestly adjusted by moving the burner. Experimental errors in residence time estimation accumulate at long residence times. Therefore, an improved reaction system that allows more flexible reaction distance could provide shorter residence times, and thus reduce the experimental error.

(3) The char collection efficiency needs to be improved. It was observed that some char particles were deposited at the connection of the reaction tube and the

collection probe. This phenomenon is possibly caused by the decreased flow velocity at high pressure, causing more interaction with local recirculation zones at the top of the collection probe. An improvement in collection efficiency is possible by redesigning the burner system to reduce the particle deposition in this region.

- (4) If char collection efficiency can be improved, it may be better to use char in the high-pressure combustion experiments instead of using coal. This will decrease the modeling difficulty and increase the sensitivity of the effect of pressure on the char combustion process.
- (5) Char samples collected in this study were characterized using different technologies. However, more comprehensive analysis of char samples, such as char porosity, image analysis for char physical structure, char surface area, and char chemical structure, are still needed to better understand the effect of pressure.
- (6) Particle temperature needs to be measured to build a more reliable CO/CO<sub>2</sub> ratio model. This study uses a model based on kinetic data measured at atmospheric pressure (Hurt and Mitchell, 1992). The simultaneous measurement of mass release and particle temperature at high pressures can test the applicability of this model.

## References

- Alvarez, D., A. G. Borrego and R. Menendez, "Unbiased Methods for the Morphological Description of Char Structures," *Fuel*, **76**: 1241 (1997).
- Anthony, D. B. and J. B. Howard, "Coal Devolatilization and Hydrogasification," *AIChE J.*, **22**: 625-656 (1976).
- Arendt, P. and K. H. Heek, "Comparative Investigation of Coal Pyrolysis under Inert Gas and H<sub>2</sub> at Low and High Heating Rates and Pressures up to 10 MPa," *Fuel*, **60**: 779-787 (1981).
- Aris, R. The Mathematical Theory of Diffusion and Reaction in Permeable Catalysts. Oxford, UK, Clarendon Press (1957).
- Back, M. H., "The Kinetics of the Reaction of Carbon with Oxygen," *Can. J. Chem.*, **75**: 249-257 (1997).
- Bailey, J. G., A. G. Tate, C. Diessel and T. F. Wall, "A Char Morphology System with Applications to Coal Combustion," *Fuel*, **69**, (225) (1990).
- Banin, V. R. M. and B. Veeffkind, "Kinetic Study of High-Pressure Pulverized Coal Char Combustion: Experiments and Modeling," *Fuel*, **76**: 945-949 (1997).
- Bautista, J. R., W. B. Russel and D. A. Saville, "Time-Resolved Pyrolysis Product Distribution of Softening Coals," *Ind. Eng. Chem. Fundm.*, **25**: 536-544 (1986).
- Benfell, K. E., Assessment of Char Morphology in High Pressure Pyrolysis and Combustion, PhD Thesis, Department of Geology, The University of Newcastle (2001).
- Benfell, K. E., G.-S. Liu, D. Roberts, D. J. Harris, J. A. Lucas, J. G. Bailey and T. F. Wall, "Modelling Char Combustion: the Influence of Parent Coal Petrography and Pyrolysis Pressure on the Structure and Intrinsic Reactivity of its Char," *Proc. of the Comb. Inst.*, **28**: 2233-2241 (2000).

- Bischoff, K. B., "Effectiveness Factor for General Reaction Rate Forms," *AIChE J.*, **11**: 351-355 (1965).
- Brunauer, S., P. H. Emmett and E. Teller, "Adsorption of Gases in Multimolecular Layers," *J. Am. Chem. Soc.*, **60**: 309 (1938).
- Cai, H. Y., A. J. Guell, I. N. Chatzakis, J. Y. Lim, D. R. Dugwell and R. Kandiyoti, "Combustion Reactivity and Morphological Change in Coal Chars: Effect of Pyrolysis Temperature, Heating Rate and Pressure," *Fuel*, **75**: 15-24 (1996).
- Campbell, P. A., R. E. Mitchell and L. Ma, "Characterization of Coal Char and Biomass Char Reactivities to Oxygen," *Proc. of the Comb. Inst.*, **29**: 519-526 (2002).
- Carberry, J. J. Chemical and Catalytic Reaction Engineering. New York, McGraw Hill (1976).
- Chitsora, C. T., H.-J. Muhlen, K. H. v. Heek and H. Juntgen, "The Influence of Pyrolysis Conditions on the Reactivity of Char in H<sub>2</sub>O," *Fuel Process. Technol.*, **15**: 17-29 (1987).
- Cloke, M., E. Lester and W. Gibb, "Characterization of Coal with Respect to Carbon Burnout in P.F.-Fired Boilers," *Fuel*, **76**: 1257-1267 (1997).
- Du, Z., A. F. Sarofim and J. P. Longwell, "Activation Energy Distribution in Temperature-programmed Desorption: Modeling and Application to the Soot Oxygen System," *Energy & Fuels*, **4**, (3): 296-302 (1990).
- Du, Z., A. F. Sarofim, J. P. Longwell and C. A. Mims, "Kinetic Measurement and Modeling of Carbon Oxidation," *Energy & Fuels*, **5**: 214-221 (1991).
- Essenhigh, R. H., Chemistry of Coal Utilization (Chapter 19). M. A. Elliott, New York, (1981).
- Essenhigh, R. H., "An Integration Path for the Carbon-Oxygen Reaction with Internal Reaction," *Proc. of the Comb. Inst.*, **22**: 89-96 (1988).
- Essenhigh, R. H., "Rate Equation for the Carbon-Oxygen Reaction: An Evaluation of the Langmuir Adsorption Isotherm at Atmospheric Pressure," *Energy & Fuels*, **5**: 41-46 (1991).
- Essenhigh, R. H., F. D. and K. H. E., "Combustion Characteristics of Carbon: Influence of the Zone I -Zone II Transition on Burnout in Pulverized Coal Flames," *Energy & Fuels*, **13**: 955-960 (1999).
- Essenhigh, R. H. and A. M. Mescher, "Influence of Pressure on the Combustion Rate of Carbon," *Proc. of the Comb. Inst.*, **26**: 3085-3094 (1996).

- Essenhigh, R. H. and G. C. Yorke, "Reaction Rates of Single Coal Particles: Influence of Swelling, Shape, and Other Factors," *Fuel*, **44**: 177-186 (1965).
- Fatemi, M. Effect of Pressure on Pyrolysis of a Sub-Bituminous Coal in an Entrained-Flow Reactor. Am. Chem. Soc. Div. Fuel Chem., **32**: 117-124 (1987).
- Fletcher, H. T., A. R. Kerstein, R. J. Pugmire and D. M. Grant, "Chemical Percolation Model for Devolatilization. 2. Temperature and Heating Rate Effects on Product Yields," *Energy & Fuels*, **4**: 54 (1990).
- Fletcher, T. H., "Time-Resolved Particle Temperature and Mass Loss Measurements of a Bituminous Coal During Devolatilization," *Comb. and Flame*, **78**: 223-236 (1989).
- Fletcher, T. H., "Compilation of Devolatilization Data Obtained at the Combustion Research Facility, Sandia National Laboratories," Livermore, California, (1991).
- Fletcher, T. H., "Swelling Properties of Coal Chars During Rapid Coal Pyrolysis and Combustion," *Fuel*, **72**, (11): 1485-1495 (1993).
- Fletcher, T. H. and D. R. Hardesty, "Milestone Report for DOE's Pittsburgh Energy Technology Center," *contract FWP 0709*, Sandia Report No. SAND92-8209 available NTIS, (1992).
- Fogler, H. S. Elements of Chemical Reaction Engineering. Englewood Cliffs, New Jersey, PTR Prentice Hall (1992).
- Froment, G. F. and K. B. Bischoff. Chemical Reactor Analysis and Design. New York, John Wiley and Sons (1979).
- Gale, T. K., C. H. Bartholomew and T. H. Fletcher, "Decreases in the Swelling and Porosity of Bituminous Coals During Devolatilization at High Heating Rates," *Comb. and Flame*, **100**: 94-100 (1995).
- Gao, H., S. Murata, M. Nomura, M. Ishigaki, M. Qu and M. Tokuda, "Experimental Observation and Image Analysis for Evaluation of Swelling and Fluidity of Single Coal Particles Heated with CO<sub>2</sub> Laser," *Energy & Fuels*, **11**: 230-238 (1997).
- Genetti, D., T. H. Fletcher and R. J. Pugmire, "Predicting <sup>13</sup>C NMR Measurements of Chemical Structure of Coal Based on Elemental Composition and Volatile Matter Content," *Energy & Fuels*, **13**: 60-68 (1999).
- Grant, D. M., T. H. Fletcher, R. J. Pugmire and A. R. Kerstein, "Chemical Model of Coal Devolatilization using Percolation Lattice Statistics," *Energy & Fuels*, **3**: 175 (1989).

- Gray, D., J. G. Cogoli and R. H. Essenhigh, "Problems in Pulverized Coal and Char Combustion," *Advances in Chemistry Series*, **132**: 72 (1976).
- Griffin, T. P., J. B. Howard and W. A. Peters, "Pressure and Temperature Effects in Bituminous Coal Pyrolysis: Experimental Observations and a Transient Lumped-parameter Model," *Fuel*, **73**: 591-601 (1994).
- Hambly, E. M., The Chemical Structure of Coal Tar and Char During Devolatilization, Master Thesis, Chemical Engineering Department, Brigham Young University (1998).
- Harris, D. J. and J. H. Patterson, "Use of Australian Bituminous Coals in IGCC Power Generation Technologies," *Aust. Inst. Of Energy J.*, **13**: 22 (1995).
- Haynes, B. S., "A Turnover Model for Carbon Reactivity I. Development," *Comb. and Flame*, **126**: 1421-1432 (2001).
- Haynes, B. S. and T. G. Newbury, "Oxyreactivity of Carbon Surface Oxides," *Proc. of the Comb. Inst.*, **28**: 2197-2203 (2000).
- Hecker, W. C., M. P. Madsen, M. R. Sherman, J. W. Allen, R. J. Sawaya and T. H. Fletcher, "High Pressure Intrinsic Oxidation Kinetics of Two Coal Chars," *Energy & Fuels*, **17**: 427-432 (2003).
- Hill, C. G. J. An Introduction to Chemical Engineering Kinetics and Reactor Design. New York, John Wiley and Sons (1977).
- Hong, J., Modeling Char Oxidation as a Function of Pressure Using an Intrinsic Langmuir Rate Equation, PhD Dissertation, Chemical Engineering Department, Brigham Young University (1999).
- Hong, J., W. C. Hecker and T. H. Fletcher, "Improving the Accuracy of Predicting Effectiveness Factors for m-th Order and Langmuir Rate Equations in Spherical Coordinates," *Energy & Fuels*, **14**: 663-670 (2000a).
- Hong, J., W. C. Hecker and T. H. Fletcher, "Modeling High Pressure Char Oxidation Using Langmuir Kinetics with an Effectiveness Factor," *Proc. of the Com. Inst.*, **28**: 2215-2223 (2000b).
- Hurt, R. H., "Structure, Properties, and Reactivity of Solid Fuels," *Proc. of the Com. Inst.*, **27**: 2887-2904 (1998).
- Hurt, R. H. and J. M. Calo, "Semi-Global Intrinsic Kinetics for Char Combustion Modeling," *Comb. and Flame*, **125**: 1138-1149 (2001).

- Hurt, R. H. and B. S. Haynes, "On the Origin of Power-Law Kinetics in Carbon Oxidation," *Proc. of the Com. Inst.*, **30**, (2): 2161-2168 (2004).
- Hurt, R. H. and R. E. Mitchell, "On the Combustion Kinetics of Heterogeneous Char Particle Populations," *Proc. of the Com. Inst.*, **24**: 1233-1241 (1992).
- Hurt, R. H., J. Sun and M. Lunden, "A Kinetic Model of Carbon Burnout in Pulverized Coal Combustion," *Comb. and Flame*, **113**: 181-197 (1998).
- Joutsenoja, T., J. Saastamoinen, M. Aho and R. Hernberg, "Effects of Pressure and Oxygen Concentration on the Combustion of Different Coals," *Energy & Fuels*, **13**: 130-145 (1999).
- Kajitani, S. and N. Suzuki. Study on Coal Pyrolysis Property in Pressurized Entrained Flow Coal Gasifier. 12th Int. Conf. on Coal Sci., Cairns, Australia: No. 10C4 (2003).
- Khan, M. R. and R. G. Jenkins, "Thermoplastic Properties of Coal at Elevated Pressures : 1. Evaluation of a High-pressure Microdilatometer," *Fuel*, **63**: 109 (1984).
- Laurendeau, N. M., "Heterogeneous Kinetics of Coal Char Gasification and Combustion," *Prog. in Energy and Comb. Sci.*, **4**: 221-270 (1978).
- Lee, C. W., R. G. Jenkins and H. H. Schobert, "Structure and Reactivity of Char from Elevated Pressure Pyrolysis of Illinois No.6 Bituminous Coal," *Energy & Fuels*, **6**: 40-47 (1992).
- Lee, C. W., A. W. Scaroni and R. G. Jenkins, "Effect of Pressure on the Devolatilization and Swelling Behaviour of a Softening Coal during Rapid Heating," *Fuel*, **70**: 957-965 (1991).
- Lester, E. and M. Cloke, "The Characterisation of Coals and Their Respective Chars Formed at 1300°C in a Drop Tube Furnace," *Fuel*, **78**: 1645 (1999).
- Lester, E., M. Cloke and M. Allen, "Char Characterisation Using Image Analysis Techniques," *Energy & Fuels*, **10**: 696 (1996).
- Lester, T. W., W. R. Seeker and J. F. Merklin, "The Influence of Oxygen and Total Pressure on the Surface Oxidation Rate of Bituminous Coal," *Proc. of the Com. Inst.*, **18**: 1257 (1981).
- Levenspiel, O. The Chemical Reactor Omnibook. Corvallis, Oregon, OSU Book Stores, Inc. (1993).
- Levenspiel, O. Chemical Reaction Engineering (3rd ed.). New York, Chemical Reaction Engineering (3rd ed.) (1999).

- Liu, Y.-L., R. Malhotra and S. Niksa, "Impact of Pressure Variations on Coal Devolatilization Products. 1. Detailed Product Distributions from 0.1 MPa," *Energy & Fuels*, **18**: 508 (2004).
- Ma, J., Soot Formation from Coal Pyrolysis, PhD Dissertation, Chemical Engineering Department, Brigham Young University (1996).
- Manton, N., J. Cor, G. Mul, D. Eckstrom, R. Malhotra and S. Niksa, "Impact of Pressure Variations on Coal Devolatilization Products. 2. Detailed Product Distributions from 1.0 MPa," *Energy & Fuels*, **18**: 520-530 (2004).
- Marsh, H., "How Oxygen Molecules Gasify Carbons," *Spec. Publ.-Chem. Soc.*, **32**: 133-74 (1978).
- Marsh, H. and T. Siemieniewska, "The Surface Areas of Coals as Elaluated from the Adsorption Isotherms of Carbon Dioxide using the Dubinin-Polanyi Equation," *Fuel*, **44**: 355 (1967).
- Matsuoka, K., Z.-x. Ma, H. Akiho, Z.-g. Zhang, A. Tomita, T. H. Fletcher, M. A. Wojtowicz and S. Niksa, "High-pressure Coal Pyrolysis in a Drop Tube Furnace," *Energy & Fuels*, **17**: 984-990 (2003).
- Mehta, B. N. and R. Aris, "Communication on the Theory of Diffusion and Reaction-VII: The Isothermal P-th Order Reaction," *Chemical Engineering Sci.*, **26**: 1699 (1971).
- Mitchell, R. E., "Characterization of Variations in Char Reactivity and Mode of Particle Buring During Combustion of Pulverized Solids," *Final report for NSF Grant # CTS-9903403*, Stanford, California, (2003).
- Mitchell, R. E. and L. Ma. On the Burning Behaviors of Pulverized Coal and Biomass Chars. The 19th Annual ACERC Conference, Provo, UT, USA (2005).
- Monson, C. R., Char Oxidation at Elevated Pressures, PhD Dissertation, Mechanical Engineering Department, Brigham Young University (1992).
- Monson, C. R., G. J. Germane, A. U. Blackham and L. D. Smoot, "Char Oxidation at Elevated Pressure," *Comb. and Flame*, **100**: 669-683 (1995).
- Moors, J. H. J., Pulverised Char Combustion and Gasification at High Temperature and Pressure, PhD Thesis, Technique University of Eindhoven (1998).
- Niksa, S., "Predicting the Devolatilization Behavior of Any Coal from Its Ultimate Analysis," *Comb. and Flame*, **100**, (384-394) (1995).



- Niksa, S., G. Liu and R. H. Hurt, "Coal Conversion Submodels for Design Applications at Elevated Pressures. Part I. Devolatilization and Char Oxidation," *Prog. in Energy and Comb. Sci.*, **29**, (5): 425-477 (2003).
- Oh, M. S., W. A. Peters and J. B. Howard, "An Experimental and Modeling Study of Softening Coal Pyrolysis," *AIChE J.*, **35**: 775 (1989).
- Parkinson, A., R. Balling, J. Free, J. Talbert, D. Davidson, G. Gritton, L. Borup and B. Busaker, "OptdesX A Software System For Optimal Engineering Design," (1992).
- Perry, S., A Global Free-Radical Mechanism for Nitrogen Release During Devolatilization Based on Coal Chemical Structure, PhD Dissertation, Chemical Engineering Department, Brigham Young University (1999).
- Ranish, J. M. and P. L. J. Walker, "High Pressure Studies of the Carbon-Oxygen Reaction," *Carbon*, **31**: 135-141 (1993).
- Reichelt, T., T. Joutsenoja, H. Spliethoff, K. R. G. Hein and R. Hernberg, "Characterization of Burning Char Particles Under Pressurized Conditions by Simultaneous *in situ* Measurement of Surface Temperature and Size," *Proc. of the Com. Inst.*, **27**: 2925-2932 (1998).
- Robert, J. F. and C. H. Bartholomew. Introduction to Industrial Catalytic Processes, Fundamentals and Practice, Chapman and Hall (1997).
- Roberts, D. G. and D. J. Harris, "Char Gasification with O<sub>2</sub>, CO<sub>2</sub>, and H<sub>2</sub>O: Effects of Pressure on Intrinsic Reaction Kinetics," *Energy & Fuels*, **14**: 483-489 (2000).
- Roberts, D. G., D. J. Harris and T. F. Wall, "On the Effects of High Pressure and Heating Rate during Coal Pyrolysis on Char Gasification Reactivity," *Energy & Fuels*, **17**: 887-895 (2003).
- Saastamoinen, J. J., M. J. Aho, J. P. Hamalainen, R. Hernberg and T. Joutsenoja, "Pressurized Pulverized Fuel Combustion in Different Concentrations of Oxygen and Carbon Dioxide," *Energy & Fuel*, **10**: 121-133 (1996).
- Seebauer, V. P. J. and G. Staudinger, "Effects of Particle Size, Heating Rate and Pressure on Measurement of Pyrolysis Kinetics by Thermogravimetric Analysis," *Fuel*, **76**: 1277-1282 (1997).
- Sha, X. Z., Y. G. Chen, J. Cao, Y. M. Yang and D. Q. Ren, "Effects of Operating Pressure on Coal Gasification," *Fuel*, **69**: 293 (1990).
- Shan, G., A Comprehensive Model for Coal Devolatilisation, PhD Thesis, Chemical Engineering Department, The University of Newcastle, Australia (2000).

- Sheng, C. and J. L. T. Azevedo, "Modeling the Evolution of Particle Morphology During Coal Devolatilization," *Proc. of the Com. Inst.*, **28**: 2225 (2000).
- Smith, I. W., "The Combustion of Coal Char: A Review," *Proc. of the Com. Inst.*, **11**: 1045-1065 (1982).
- Smith, J. M. Chemical Engineering Kinetics. New York, New York, McGraw-Hill (1981).
- Smoot, L. D., "International Research Centers' Activities in Coal Combustion," *Prog. in Energy and Comb. Sci.*, (24): 409-501 (1998).
- Smoot, L. D. and P. J. Smith. Coal Combustion and Gasification. New York, Plenum Press (1985).
- Solomon, P. G. and D. G. Hamblen. Chemistry of Coal Conversion. New York, Plenum Press (1985).
- Solomon, P. R. and T. H. Fletcher, "Impact of Coal Pyrolysis on Combustion," *Proc. of the Com. Inst.*, **25**: 463-474 (1994).
- Strezov, V., J. A. Lucas and T. F. Wall. Effect of Pressure on the Swelling of Density Separated Coal Particles. Int. Symp. on Utilisation of Coal and Biomass, Newcastle, Australia: ISUCB-03 (2003).
- Sun, C. L., Y. Q. Xiong, Q. X. Liu and M. Y. Zhang, "Thermogravimetric Study of the Pyrolysis of Two Chinese Coals Under Pressure," *Fuel*, **76**: 639-644 (1997).
- Suuberg, E. M., W. A. Peters and J. B. Howard, "Product Compositions and Formation Kinetics in Rapid Pyrolysis of Pulverized Coal," *Proc. of the Com. Inst.*, **17**: 117-120 (1979).
- Suuberg, E. M., M. Wojtowicz and J. M. Calo, "Reaction Order for Low Temperature Oxidation of Carbon," *Proc. of the Com. Inst.*, **22**: 79-87 (1988).
- Takematsu, T. and C. Maude. Coal Gasification for IGCC Power Generation. London (1991).
- Thiele, E. W., "Relation between Catalytic Activity and Size of Particle," *Ind. Eng. Chem. Fundm.*, **31**: 916 (1939).
- Tsai, C. and A. W. Scaroni, "The Structural Changes of Bituminous Coal Particles during the Initial Stages of Pulverized-Coal Combustion," *Fuel*, **66**: 200 (1987).
- Van Heek, K. H. and H.-J. Muhlen. Fundamental Issues in Control of Carbon Gasification Reactivity, Kluwer Academic Publishers (1991).

- Walker, P. L. J., F. J. Rusinko and L. G. Austin. Gas Reactions of Carbon. New York, Academic Press (1959).
- Wall, T. F., G.-s. Liu, H.-w. Wu, D. G. Roberts, K. E. Benfella, S. Gupta, J. A. Lucas and D. J. Harris, "The Effects of Pressure on Coal Reactions during Pulverised Coal Combustion and Gasification," *Prog. in Energy and Comb. Sci.*, **28**: 405-433 (2002).
- Wu, H., G. Bryant, K. Benfell and T. Wall, "An Experimental Study on the Effect of System Pressure on Char Structure of an Australian Bituminous Coal," *Energy & Fuels*, **14**: 282-290 (2000).
- Yeasmin, H., J. F. Mathews and S. Ouyang, "Rapid Devolatilisation of Yallourn Brown Coal at High Pressures and Temperatures," *Fuel*, **78**: 11-24 (1999).
- Yu, J., J. Lucas, V. Strezov and T. Wall, "Swelling and Char Structures from Density Fractions of Pulverized Coal," *Energy & Fuels*, **17**: 1160-1174 (2003).
- Yu, J.-L., V. Strezov, J. Lycas, G.-S. Liu and T. Wall, "A Mechanistic Study on Char Structure Evolution During Coal Devolatilization - Experiments and Model Predictions," *Proc. of the Com. Inst.*, **29**: 467-473 (2002).
- Zhang, H., Nitrogen Evloution and Soot Formation During Secondary Coal Pyrolysis, PhD Dissertation, Department of Chemical Engineering, Brigham Young University (2001).
- Zhang, H. and T. H. Fletcher, "Nitrogen Transformations during Secondary Coal Pyrolysis," *Energy & Fuels*, **15**: 1512-1522 (2001).
- Zhuang, Q., T. Kyotani and A. Tomita, "Dynamics of Surface Oxygen Complexes during Carbon Gasification with Oxygen," *Energy & Fuels*, **9**, (4): 630-634 (1995).
- Zhuang, Q., T. Kyotani and A. Tomita, "Desorption Behavior of Surface Oxygen Complexes on Carbon in an Inert Gas and in O<sub>2</sub>-Gasification Atmosphere," *Energy & Fuels*, **10**: 169-172 (1996).
- Zygourakis, K., "Effect of Pyrolysis Conditions on the Macropore Structure of Coal-Derived Chars," *Energy & Fuels*, **7**: 33-41 (1993).



## **Appendices**



## Appendix A: Temperature Correction

A type-B thermocouple was inserted from the bottom of the pressurized chamber to measure the centerline gas temperature profiles at different temperature settings. The measured temperature (bead temperature) was then corrected to account for radiation losses between the bead and the wall of the reactor. The correction is based on the energy balance on the thermocouple bead.

Assume the thermocouple bead has attained equilibrium and conduction along the bead wires is neglected, an energy balance can be established on the bead.

$$h(T_{gas} - T_{bead}) = \varepsilon\sigma(T_{bead}^4 - T_{wall}^4) \quad (A.1)$$

where  $h$  is the convective heat transfer coefficient,  $\varepsilon$  is the thermocouple bead emissivity,  $\sigma$  is the Stefan-Boltzmann constant,  $T_{bead}$  is the bead temperature,  $T_{wall}$  is the wall temperature and  $T_{gas}$  is the actual gas temperature. Emissivity is assumed as 0.4, obtained from silica coating. A value of 1100 °C is used for the wall temperature. The value of  $h$  can be calculated from the Nusselt number:

$$h = Nu(T_f) \cdot \frac{k_f(T_f)}{D_b} \quad (A.2)$$

where  $T_f$  is the film temperature in the boundary layer,  $k_f$  is the thermal conductivity of the gas evaluated at  $T_f$ , and  $D_b$  is the diameter of the bead. A measured value of 1.9 mm for  $D_b$  is used in the correction.  $T_f$  is estimated by averaging the gas temperature and the bead temperature.  $k_f$  is calculated by weighing thermal conductivity of the four major components in the gas, namely  $\text{CO}_2$ ,  $\text{N}_2$ ,  $\text{H}_2\text{O}$ , and  $\text{O}_2$ .

The Nusselt number is estimated by a correlation with Reynolds number and Prandtl number in equation A.3.

$$Nu(T_f) = 2.0 + (0.4 \text{Re}_{T_f}^{1/2} + 0.06 \text{Re}_{T_f}^{2/3}) \text{Pr}^{0.4} \left(\frac{\mu}{\mu_s}\right)^{2/4} \quad (\text{A.3})$$

$$\text{Re}_{T_f} = \frac{D_b v_\infty \rho_f(T_f)}{\mu_f(T_f)} \quad (\text{A.4})$$

$$\text{Pr}_{T_f} = \frac{C_p(T_f) \cdot \mu_f(T_f)}{k_f(T_f)} \quad (\text{A.5})$$

where  $\text{Re}_{T_f}$  is the Reynolds number based on the bead diameter at temperature  $T_f$ ,  $\text{Pr}$  is the Prandtl number,  $\mu$  is the viscosity of the gas at the gas temperature, and  $\mu_s$  is the viscosity of the gas at the bead temperature. Also  $v_\infty$  is the terminal velocity of the flowing gas,  $\rho$  is the density,  $C_p$  is the heat capacity and  $\mu$  is the viscosity, and  $k_f$  is thermal conductivity. The value of  $v_\infty$  is calculated using mass conservation and measured gas temperature. Density is estimated by assuming ideal gas behavior. Heat capacity, viscosity, and thermal conductivity are obtained using a polynomial correlation based on BYU Dipper database.

The bead temperature is first used to evaluate the gas properties in the boundary layer. The gas temperature is then calculated iteratively until a certain convergence



criterion is reached. The corrected centerline gas temperature profiles were used to perform further modeling.



## **Appendix B: Operation Procedure of HPFFB**

Instructions for operating the high-pressure flat-flame-burner are outlined below.

### **Startup**

1. Check to make sure that the reactor is assembled and that cooling water is flowing to the collection system.
2. About twelve hours before the experiment, turn on the reactor heater to 1200°C (the default heating rate is 100 K/Hr). Burner should be removed from the furnace and mounted before experiment to reduce the corrosion caused by high-temperature.
3. Set the outlet pressure of the fuel, air, and nitrogen to the value that is 5 atm (70 psi) higher than process pressure, for example, 15 atm for a 10 atm experiment.
4. Weigh filters and put them in place. Wrap the collection system with heating tape to avoid condensation of vapor produced by methane combustion.
5. Check that the valve for “Filter #3” is pointing horizontally to the right, that the valve to the cyclone and the two Y valves are open.
6. Close the valve on the primary inlet (green).

7. Open the primary bypass valve.
8. Set the flow controller for secondary gas (Nitrogen). Set flow controllers for fuel (natural gas) and oxidizer (air) to initial flow rates. Open valves of secondary gas and air.
9. Open valve of fuel. Now the initial ignition condition is ready. The flame can be ignited by the high-temperature heater about 30 sec after the fuel valve is turned on.
10. After 10 minutes of flame stabilizing, increase fuel and oxidizer flow rates synchronously to the operation conditions; this process may take 20-30 minutes.
11. Wait for flame temperature to increase and stabilize. The flame noise should disappear when the flame is stable.
12. Put coal in the feeder.
13. Put feeder on reactor.
14. Attach the primary inlet gas to feeder
15. Attach vibrator and tighten feeder while vibrator is running.
16. Slowly open injection probe valve.
17. Close bypass valve on the primary inlet and wait several seconds.
18. Check for leaks of primary gas.
19. Move feeder close to coal entrance.
20. Check all flows, temperatures, and pressures.
21. Feed the coal and record time.

### **At the End of a Run**

1. Close the injection probe valve. Turn off the vibrator, and the primary gas flow.

2. Unplug the heating tape; the collection system may be extremely hot.
3. Turn off the CH<sub>4</sub> and O<sub>2</sub> flows (if used in experiment). Keeps air flow running to ensure the cooling of the burner surface.
4. Close the char leg valve.
5. Turn off the quench flow.
6. Change the setpoint of pressure controller to 0, Wait the system pressure drop to about 20 psi. The pressure regulator valve has a large pressure drop so it is very slow to vent when system is lower than this pressure. Then you need to open the sampling valve to decrease system pressure.
7. When pressure drops to 0~5psi, disconnect the flexible stainless pipe from the two tar leg filters. Wait a few minutes for system pressure drops to 0.
8. Carefully disconnect the tar legs filters, use caution when disconnect the first filter because system may still be pressurized.
9. Disconnect the flexible pipe from the char leg filter, and then remove this filter.
10. Remove the virtual impactor and cyclone collector. Retrieve char sample collected in the cyclone collector. Char sample should be sealed in a container and stored in refrigerator for further analysis.
11. Turn off the secondary air flow. Disconnect the flexible pipes from the burner. Remove the burner, clean it for next experiment. Lower the setpoint of temperature controller to 25°C (do not turn off the temperature controller).
12. Collect the deposits on the filter papers if needed. Clean all of the parts of collection system.

13. Close the valves of all gas cylinders.

## Appendix C: Experimental Pyrolysis and Combustion Conditions

Pyrolysis experiments were performed at four pressures (2.5, 6, 10, and 15 atm). For each pressure, the flow rates of CH<sub>4</sub>, air were varied to ensure a similar temperature profiles. Table C.1 lists the details for the HPFFB experimental pyrolysis conditions.

**Table C.1 Summary of settings used during HPFFB pyrolysis experiments**

Condition	Flow rate of CH <sub>4</sub> (l/min)	Flow rate of air (l/min)	Primary N <sub>2</sub> flow rate (cc/min)
2.5 atm	1.74	16.55	150
6 atm	2.16	20.5	200
10 atm	2.49	23.5	250
15 atm	2.85	28.5	330

Combustion experiments were performed at three pressures (2.5, 6, and 10 atm). The flow rates of Methane, air, and O<sub>2</sub> were varied at different pressures and oxygen molar fractions. The conditions are listed in Table C.2.

**Table C.2 Summary of settings used during HPFFB combustion experiments**

Condition	O <sub>2</sub> molar fractions (mol %)	Flow rate of CH <sub>4</sub> (l/min)	Flow rate of air (l/min)	Flow rate of O <sub>2</sub> (cc/min)	Primary N <sub>2</sub> flow rate (cc/min)
2.5 atm	5.75	1.74	16.55	1.0	150
	9.76	1.74	16.55	2.0	150
	15.13	1.74	16.55	3.3	150
	19.24	1.74	16.55	4.94	150
6 atm	2.98	2.16	20.5	0.7	200
	4.97	2.16	20.5	1.25	200
	9.76	2.16	20.5	2.50	200
10 atm	2.58	2.49	23.5	0.75	250
	9.76	2.49	23.5	2.9	250
	11.97	2.49	23.5	3.6	250



## Appendix D: Tabulation of Experimental Data of High-pressure Pyrolysis

**Table D.1 Ultimate and proximate analyses of four coal samples**

Coal	Rank	d (μm)	Proximate Analysis (Wt %)			Ultimate Analysis (wt%, daf)				
			Moisture	Ash (dry)	VM (daf)	C	H	N	S	O <sup>a</sup>
Pitt #8	HvA-Bit	63-90	1.44	10.72	34.34	84.58	5.47	2.00	0.49	7.44
Ken #9	HvB-Bit	44-74	8.21	8.43	42.11	76.72	5.27	1.81	3.72	12.48
Ill #6	HvC-Bit	74-90	3.31	9.35	53.83	78.02	5.45	1.36	4.14	10.59
Knife River	Lignite	45-75	11.91	20.38	47.86	62.23	4.23	0.95	1.28	31.30

a.  $O = 100 - (C + H + N + S)$

**Table D.2a Summary of Elemental Compositions for the HPFFB Pyrolysis Tests  
Pitt #8 (Bituminous)**

Formation Pressure (atm)	Ash (wt %, dry)	C (wt %, daf)	H (wt %, daf)	N (wt %, daf)	S (wt %, daf)	O (wt %, daf, by diff.)
2.5	15.8	90.52	1.33	1.93	0.62	5.59
6	21.1	88.07	1.76	2.01	0.72	7.44
10	13.0	87.48	1.23	1.85	0.68	8.76
15	15.6	91.63	1.79	1.97	0.83	3.77

**Table D.2b Summary of Ash, Mass Release, Density, Swelling Ratio for the FFB Tests Pitt #8 (Bituminous)**

Formation Pressure (atm)	m/m <sub>0</sub> (daf) (Ave.)	m/m <sub>0</sub> (daf) (Tracer Ti)	m/m <sub>0</sub> (daf) (Tracer Al)	m/m <sub>0</sub> (daf) (Tracer ash)	Tap Density (g/ml)	d/d <sub>0</sub>	Surface Area (N <sub>2</sub> ) (m <sup>2</sup> /g)	Surface Area (CO <sub>2</sub> ) (m <sup>2</sup> /g)
2.5	0.49	0.41	0.54	0.48	0.31	0.92	39.00	267.70
6	0.34	0.31	0.39	0.34	0.11	1.15	239.50	325.20
10	0.61	0.57	0.62	0.61	0.14	1.31	85.80	255.50
15	0.49	0.46	0.50	0.52	0.13	1.25	33.50	262.00

**Table D.3a Summary of Elemental Compositions for the HPFFB Pyrolysis Tests Ken #9 (Bituminous)**

Formation Pressure (atm)	Ash (wt %, dry)	C (wt %, daf)	H (wt %, daf)	N (wt %, daf)	S (wt %, daf)	O (wt %, daf, by diff.)
1 (FFB)*	19.5	88.38	2.22	1.98	3.40	4.03
2.5	20.3	91.63	1.23	1.69	2.33	3.12
6	19.6	79.38	2.71	2.13	2.99	12.79
10	14.8	79.38	2.71	2.13	2.99	12.79
15	12.8	78.96	2.61	2.03	3.08	13.31

\* Produced from an atmospheric FFB

**Table D.3b Summary of Ash, Mass Release, Density, Swelling Ratio for the FFB Tests Ken #9 (Bituminous)**

Formation Pressure (atm)	m/m <sub>0</sub> (daf)	m/m <sub>0</sub> (daf) (Tracer Ti)	m/m <sub>0</sub> (daf) (Tracer Al)	m/m <sub>0</sub> (daf) (Tracer ash)	Tap Density (g/ml)	d/d <sub>0</sub>	Surface Area (N <sub>2</sub> ) (m <sup>2</sup> /g)	Surface Area (CO <sub>2</sub> ) (m <sup>2</sup> /g)
1 (FFB)*	0.379	0.32	0.39	0.43	0.258	0.991	218.1	306.6
2.5	0.360	0.41	0.38	0.30	0.194	1.070	180.4	332.4
6	0.377	0.35	0.39	0.38	0.079	1.468	64.6	328.0
10	0.529	0.59	0.49	0.50	0.067	1.734	53.4	258.6
15	0.628	0.63	0.65	0.60	0.065	1.856	12.6	35.6

\* Produced from an atmospheric FFB

**Table D.4a Summary of Elemental Compositions for the HPFFB Pyrolysis Tests III #6 (Bituminous)**

Formation Pressure (atm)	Ash (wt %, dry)	C (wt %, daf)	H (wt %, daf)	N (wt %, daf)	S (wt %, daf)	O (wt %, daf, by diff.)
2.5	20.06	91.04	1.11	1.45	1.52	4.88
6	20.77	87.77	1.31	1.55	1.73	7.64
10	17.65	90.58	1.21	1.38	1.69	5.14

**Table D.4b Summary of Ash, Mass Release, Density, Swelling Ratio for the FFB Tests III #6 (Bituminous)**

Formation Pressure (atm)	$m/m_0$ (daf)	$m/m_0$ (daf) (Tracer Ti)	$m/m_0$ (daf) (Tracer Al)	$m/m_0$ (daf) (Tracer ash)	Tap Density (g/ml)	$d/d_0$	Surface Area (N <sub>2</sub> ) (m <sup>2</sup> /g)	Surface Area (CO <sub>2</sub> ) (m <sup>2</sup> /g)
2.5	0.392041	0.39	0.38	0.41	0.138	1.238	359	399.5
6	0.410448	0.43	0.41	0.39	0.107	1.358	292	332.2
10	0.542653	0.64	0.51	0.48	0.088	1.514	265	276.7

**Table D.5a Summary of Elemental Compositions for the HPFFB Pyrolysis Tests Knife River (Lignite)**

Formation Pressure (atm)	Ash (wt %, dry)	C (wt %, daf)	H (wt %, daf)	N (wt %, daf)	S (wt %, daf)	O (wt %, daf, by diff.)
2.5	36.5	81.98	1.37	0.85	1.11	14.70
6	33.5	78.01	2.45	0.94	1.33	17.27
10	35.3	80.20	2.04	0.58	1.20	15.97
15	26.1	80.20	2.04	0.58	1.20	15.97

**Table D.5b Summary of Ash, Mass Release, Density, Swelling Ratio for the FFB Tests Knife River (Lignite)**

Formation Pressure (atm)	m/m <sub>0</sub> (daf)	m/m <sub>0</sub> (daf) (Tracer Ti)	m/m <sub>0</sub> (daf) (Tracer Al)	m/m <sub>0</sub> (daf) (Tracer ash)	Tap Density (g/ml)	d/d <sub>0</sub>	Surface Area (N <sub>2</sub> ) (m <sup>2</sup> /g)	Surface Area (CO <sub>2</sub> ) (m <sup>2</sup> /g)
2.5	0.445	0.82	0.52	0.44	0.473	0.798	242.5	313.0
6	0.507	0.45	0.58	0.51	0.398	0.884	155.8	233.4
10	0.470	0.38	0.57	0.47	0.350	0.899	99.8	220.1
15	0.724	0.76	0.68	0.71	0.114	1.511	102.0	218.7

## Appendix E: Tabulation of Experimental Data of High-temperature Combustion

**Table E.1a Summary of Elemental Compositions for the HPFFB Combustion Tests  
Pitt #8 (90-125  $\mu\text{m}$ )**

Pressure (atm)	O <sub>2</sub> mol% (Reaction Condition)	C (wt%) (dry)	H (wt%) (dry)	N (wt%) (dry)	S (wt%) (dry)	O (wt%) (dry)	Ash (wt%) (dry)
2.5 atm	0.00%	71.35	1.61	1.71	0.68	3.75	20.88
	5.75%	72.78	2.37	1.70	0.714	4.22	18.19
	7.46%	71.37	4.03	1.72	1.28	7.45	14.13
	15.13%	69.52	3.61	1.63	1.01	4.10	20.11
	19.24%	65.46	3.58	1.49	0.95	10.57	17.92
6 atm	0.00%	70.81	1.80	1.74	0.83	-2.66*	27.47
	2.98%	74.69	1.93	2.01	0.57	-0.68*	21.47
	4.97%	58.94	0.70	1.30	0.47	0.92	37.64
	9.76%	49.40	0.58	1.11	0.28	-5.48*	54.09
10 atm	0.00%	76.083	1.07	1.608	0.589	7.619	13.03
	4.97%	65.57	1.75	1.86	0.8	5.84	24.16
	9.57%	50.87	0.82	1.15	0.87	7.32	38.94
	9.76%	61.40	1.78	1.65	0.37	7.10	27.67
	11.97%	46.49	0.63	0.94	0.61	9.68	41.62

**Table E.1b Summary of Mass Release, Tap Density, Diameter Ratios for the HPFFB  
Combustion Tests Pitt #8 (90-125  $\mu\text{m}$ )**

Pressure (atm)	O <sub>2</sub> mol% (Reaction Condition)	m/m <sub>0</sub> (daf)	Tap Density (g/ml)	$\rho/\rho_0$	Diameter ratio d/d <sub>0</sub>
	coal		0.70		
2.5	0%	0.46	0.25	0.35	1.09
	5.75%	0.38	0.33	0.47	0.93
	7.46%	0.33	0.15	0.22	1.15
	15.13 %	0.22	0.18	0.26	0.95
	19.24 %	0.13	0.22	0.32	0.74
	0%	0.54	0.08	0.12	1.38
	2.98 %	0.44	0.09	0.13	1.51
	4.97 %	0.20	0.16	0.23	0.96
	9.76 %	0.10	0.07	0.10	1.01
	0%	0.44	0.07	0.11	1.61
10	4.97 %	0.38	0.07	0.10	1.55
	9.76 %	0.31	0.09	0.13	1.36
	11.97 %	0.17	0.06	0.08	1.29

\*Sample was collected from the oxygen molar fraction condition.

**Table E.1c Summary of N<sub>2</sub> Surface Area for the HPFFB Combustion Tests Pitt #8 (90-125 μm)**

2.5 atm		6 atm		10 atm	
O <sub>2</sub> mol%	N <sub>2</sub> Area(m <sup>2</sup> /g)	O <sub>2</sub> mol%	N <sub>2</sub> Area(m <sup>2</sup> /g)	O <sub>2</sub> mol%	N <sub>2</sub> Area(m <sup>2</sup> /g)
0	94.2±4.48	0	75.1±3.58	0	52.9±2.37
5.75	85.2±4.17	2.98	155.3±7.34	4.97	41.9±3.11
7.46	48.9±3.24	4.97	96.2±4.06	9.76	12.3±0.86
15.13	14.1±0.74	9.76	28.7±0.86	11.97	11.1±0.78
19.24	14.0±0.74				

**Table E.2a Summary of Elemental Compositions for the HPFFB Combustion Tests Pitt #8 (63-76 μm)**

Pressure (atm)	O <sub>2</sub> mol% (Reaction Condition)	C (wt%) (dry)	H (wt%) (dry)	N (wt%) (dry)	S (wt%) (dry)	O (wt%) (dry)	Ash (wt%) (dry)
	Coal	74.58	4.87	1.69	1.53	6.61	10.72
2.5	0.00%	71.80	1.21	1.67	1.02	6.00	18.30
	5.75%	75.45	0.90	1.71	0.81	1.18	19.95
	7.46%	75.11	0.88	1.73	0.65	-1.21	22.84
	15.13%	66.46	0.97	1.39	0.53	-1.49	32.15
	19.24%	63.92	0.91	1.36	0.46	2.70	30.65
6	0.00%	78.10	1.26	1.70	0.40	-3.04	21.58
	2.98%	60.25	1.19	1.42	0.83	4.18	32.14
	4.97%	59.11	1.08	1.43	0.66	-2.47	40.19
	9.76%	46.40	0.74	1.08	0.40	-0.26	51.64
	12.44%	46.73	0.64	1.02	0.27	-0.77	52.12

**Table E.2b Summary of Mass Release, Tap Density, Diameter Ratios for the HPFFB Combustion Tests Pitt #8 (63-76  $\mu\text{m}$ )**

Pressure (atm)	O <sub>2</sub> mol% (Reaction Condition)	m/m <sub>0</sub> (daf)	Tap Density (g/ml)	$\rho/\rho_0$	Diameter ratio d/d <sub>0</sub>
	coal		0.70		
2.5	0.00%	0.54	0.24	0.34	1.16
	5.75%	0.48	0.32	0.46	1.02
	7.46%	0.41	0.21	0.29	1.11
	15.13%	0.27	0.19	0.27	0.98
	19.24%	0.28	0.12	0.17	1.18
6	0.00%	0.44	0.12	0.17	1.38
	2.98%	0.25	0.10	0.15	1.20
	4.97%	0.18	0.11	0.16	1.04
	9.76%	0.11	0.09	0.13	0.95

**Table E.2c Summary of N<sub>2</sub> Surface Area for the HPFFB Combustion Tests Pitt #8 (63-76  $\mu\text{m}$ )**

2.5 atm		6 atm	
O <sub>2</sub> mol%	N <sub>2</sub> Area(m <sup>2</sup> /g)	O <sub>2</sub> mol%	N <sub>2</sub> Area(m <sup>2</sup> /g)
0	94.2±4.48	0	90.3±4.12
5.75	106.8±3.76	2.98	112.2±5.12
7.46	118.9±3.52	4.97	84.0±4.89
15.13	81.5±3.57	9.76	35.6±2.21
19.24	51.5±2.98		



**Table E.3a Summary of Elemental Compositions for the HPFFB Combustion Tests III #6 (Short Distance)**

Pressure (atm)	O <sub>2</sub> mol% (Reaction Condition)	C (wt%) (dry)	H (wt%) (dry)	N (wt%) (dry)	S (wt%) (dry)	O (wt%) (dry)	Ash (wt%) (dry)
2.5	0.0%	72.78	0.89	1.16	1.22	3.90	20.06
	5.8%	62.02	0.44	0.93	1.11	0.12	35.38
	7.5%	51.29	0.93	0.90	0.99	-1.85	47.75
	15.1%	59.81	1.20	1.10	1.14	-10.50	47.24
6	0.0%	69.54	1.05	1.23	1.37	6.04	20.77
	3.0%	68.44	1.77	1.34	1.59	2.22	24.64
	5.0%	31.83	0.80	0.59	2.41	3.47	60.89
	9.8%	24.67	0.64	0.48	1.49	2.42	70.31
10	0.0%	74.59	0.97	1.14	1.39	4.26	17.65
	2.6%	68.31	1.63	1.64	1.70	0.24	16.48
	4.0%	56.31	1.48	1.37	3.60	-0.80	23.04
	8.7%	45.87	1.03	1.34	3.21	10.51	38.04

**Table E.3b Summary of Mass Release, Tap Density, Diameter Ratios for the HPFFB Combustion Tests III #6 (Short Distance)**

Pressure (atm)	O <sub>2</sub> mol% (Reaction Condition)	m/m <sub>0</sub> (daf)	Tap Density (g/ml)	$\rho/\rho_0$	Diameter ratio d/d <sub>0</sub>
	coal		0.64		
2.5	0.0 %	0.39	0.14	0.22	1.24
	5.75 %	0.19	0.17	0.27	0.89
	7.46 %	0.11	0.17	0.27	0.75
	15.13 %	0.11	0.19	0.30	0.72
6	0 %	0.41	0.10	0.16	1.34
	2.98 %	0.34	0.11	0.17	1.23
	4.97 %	0.07	0.16	0.25	0.64
	9.76 %	0.03	0.19	0.30	0.52
10	0%	0.54	0.09	0.14	1.54
	2.58 %	0.36	0.11	0.17	1.24
	3.98 %	0.19	0.11	0.17	0.99
	8.69 %	0.12	0.13	0.20	0.88

**Table E.3c Summary of N<sub>2</sub> Surface Area for the HPFFB Combustion Tests III #6 (Short Distance)**

2.5 atm		6 atm		10 atm	
O <sub>2</sub> mol%	N <sub>2</sub> Area(m <sup>2</sup> /g)	O <sub>2</sub> mol%	N <sub>2</sub> Area(m <sup>2</sup> /g)	O <sub>2</sub> mol%	N <sub>2</sub> Area(m <sup>2</sup> /g)
0	235.4±11.87	0	179.1±8.96	0	258.6±9.52
5.75	145.4±4.12	2.98	83.4±3.78	2.58	26.2±0.86
7.46	94.3±3.95	4.97	69.7±2.36	3.98	91.8±2.89
15.13	83.5±3.58	9.76	30.4±0.87	8.69	5.6±0.15

**Table E.4a Summary of Elemental Compositions for the HPFFB Combustion Tests III #6 Long Distance)**

Pressure (atm)	O <sub>2</sub> mol% (Reaction Condition)	C (wt%) (dry)	H (wt%) (dry)	N (wt%) (dry)	S (wt%) (dry)	O (wt%) (dry)	Ash (wt%) (dry)
2.5	0.0%	72.13	1.17	1.35	1.17	1.47	22.72
	5.7%	73.05	1.09	1.22	1.31	4.42	18.92
	7.5%	69.04	0.552	1.067	0.548	9.59	19.20
	10.0%	60.22	1.43	1.19	1.00	2.71	33.46
	15.0%	30.67	0.48	0.51	0.28	0.10	67.97
6	0.0%	60.38	1.51	1.38	1.53	9.63	25.57
	5.0%	69.23	2.32	1.63	1.35	9.45	16.02
	10.0%	50.10	1.54	1.18	1.78	1.30	44.09
	12.4%	49.43	1.30	1.14	2.14	10.36	35.64

**Table E.4b Summary of Mass Release, Tap Density, Diameter Ratios for the HPFFB Combustion Tests III #6 (Long Distance)**

Pressure (atm)	O <sub>2</sub> mol% (Reaction Condition)	m/m <sub>0</sub> (daf)	Tap Density (g/ml)	$\rho/\rho_0$	Diameter ratio d/d <sub>0</sub>
	coal		0.69		
2.5	0 %	0.42	0.16	0.23	1.15
	5.7%	0.37	0.16	0.24	1.19
	7.5%	0.43	0.16	0.23	1.23
	10%	0.22	0.17	0.24	0.95
	15%	0.05	0.19	0.27	0.56
6	0 %	0.54	0.12	0.18	1.20
	5%	0.51	0.07	0.11	1.61
	10%	0.14	0.16	0.23	0.82
	12.4%	0.19	0.12	0.18	1.02

**Table E.4c Summary of N<sub>2</sub> Surface Area for the HPFFB Combustion Tests III #6 (Long Distance)**

2.5 atm		6 atm	
O <sub>2</sub> mol%	N <sub>2</sub> Area(m <sup>2</sup> /g)	O <sub>2</sub> mol%	N <sub>2</sub> Area(m <sup>2</sup> /g)
0	203.8±11.21	0	188.3±5.1
5.7	165.2±6.81	5	151.8±0.22
7.5	74.4±2.39	10	86.6±2.24
10	97.5±4.15	12.4	121.6±3
15	56.0±2.22		



## **Appendix F: Gas Field Simulations for HPFFB Tests**

In order to find the particle temperature and velocity profile, Fluent 6 was used to calculate the properties of gas field. In the modeling of this process, several assumptions were used to simplify the calculation.

- (1) The axi-symmetric cylindrical coordinates was used in the modeling. This assumption avoided the 3-D modeling and maintained the rationality because radial transport is negligible.
- (2) The secondary flow is formed by arrays of flamelets. It was observed that the length of flamelets is about 2 mm at atmospheric pressure. So it was reasonable to assume the product gas achieved equilibrium instantly after gas flow left the burner surface. The composition of product gas was calculated using equilibrium program NasaLewis. It was also assumed the flow velocity is even distributed among the burner surface since the hypodermic tubes function as a distributor.
- (3) Coal particle was assumed to be injected at the area-averaged location of the entraining tube. Since the primary gas flow has a large affect on the particle heating history, an area-averaged location best represents the average property of particles injected.

(4) The temperature drop along the axis direction was caused by heat loss through the reactor wall. Since the degradation of the insulation performance is unknown, a fixed linear temperature boundary condition was applied to the reactor wall. A guessed wall temperature profile was used at first, and calculated centerline temperature profile was compared to the measured centerline temperature profile. The case with the best matched centerline temperature profile was used to output the wall boundary temperature profile. This temperature profile then was used to calculate the gas field properties needed.

The geometry of HPFFB assumed for the simulations is shown in Figure F.1, with the boundary conditions indicated. The reaction zone was restricted from the burner surface and feeding tube outlet to the inlet surface of quenching tube. Five boundary conditions were assumed during FLUENT modeling. The reactor wall is a fixed temperature, with a user-defined linear temperature profile. The outflow boundary is applied to the outlet of reaction zone, or the inlet of the quench tube. The burner centerline was defined as a symmetry axis. Both primary flow inlet and secondary flow inlet (burner) were defined as mass flow inlets.

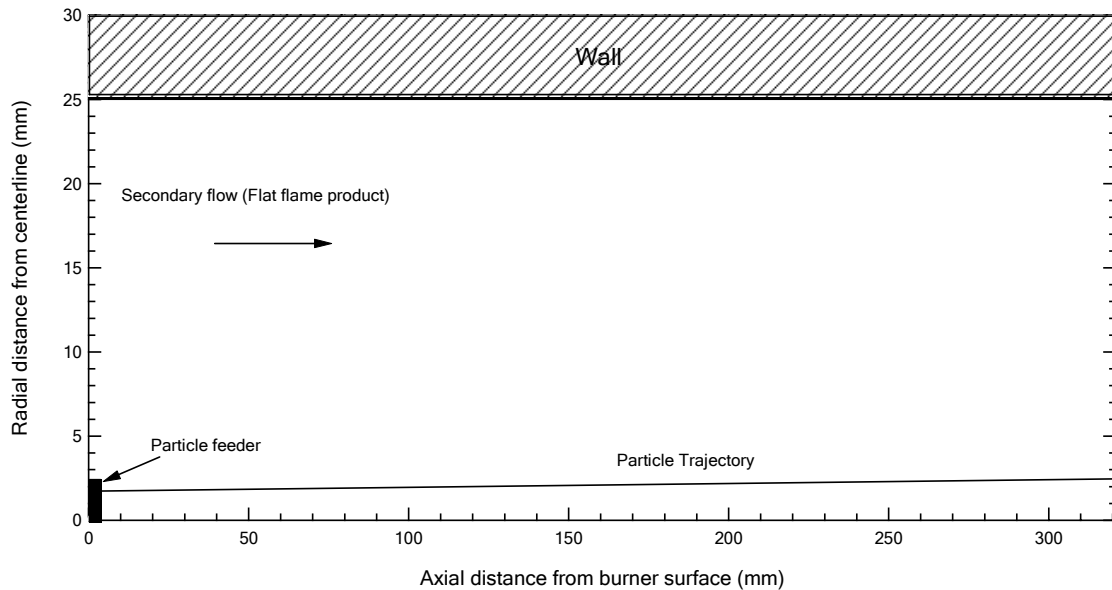


**Figure F.1.** Schematic of axi-symmetric slice of the HPFFB including the dimensions and geometry assumed in order to model gas flow field on FLUENT.

The entire flow field was divided into 18,480 cells: 440 cells along the drop tube length and 42 cells along the drop tube radius. Doubled sided successive ratios were applied for all of the edges to enhance the precision of calculation of the corners.

The boundary conditions assumed for primary and secondary flow assumed in FLUENT simulation are listed in Table F.1.

**Table F.1**

**Summary of Boundary Conditions Assumed for HPFFB Gas Field Simulations**

HPFFB Condition	<b>2.5 atm</b>	<b>6 atm</b>	<b>10 atm</b>	<b>15 atm</b>
Primary Inlet Temperature (K)	500	500	500	500
Primary flow rate (g/s)	2.083e-3	4.00e-3	4.167e-3	4.167e-3
Secondary Inlet Temperature (K)	1573	1550	1450	1450
Secondary flow rate (g/s)	0.376	0.491	0.534	0.645

The secondary flow rates were calculated using an equilibrium code. The flow rates of CH<sub>4</sub>, air, and the total mass flow rates used in pyrolysis tests are listed in Table

F.2. The mass flow rates of the major products gas and oxygen in the products of the matched pressures are also listed in Table F.2. The compositions of the products gas were used as the gas material in the FLUENT simulation.

**Table F.2 Flow Rates Used in the HPFFB Pyrolysis Tests**

Condition	2.5 atm	6 atm	10 atm	15 atm
CH <sub>4</sub> (slpm)	1.74	2.16	2.49	2.85
Air (slpm)	17.5	21.5	25	28.5
Total flow rate (g/sec)	0.312E-3	0.416E-3	0.521E-3	0.687E-3
H <sub>2</sub> O flow rate (g/sec)	0.45E-01	0.59E-01	0.65E-01	0.75E-01
CO <sub>2</sub> flow rate (g/sec)	0.54E-01	0.71E-01	0.77E-01	0.91E-01
N <sub>2</sub> flow rate (g/sec)	0.27	0.35	0.38	0.47
O <sub>2</sub> flow rate (g/sec)	0.14e-2	0.18E-02	0.14E-02	0.75E-02

The wall temperature profiles used for pyrolysis tests at four pressures are listed in Table F.3. Figure F.2-F.4 show the comparison of measured centerline temperatures and predicted temperatures. Fig 5.5 shows the particle residence time vs. distance for the Pitt #8 90-125 μm size particle.

**Table F.3 Summary of Wall Temperature Profiles Assumed for HPFFB Gas Field Simulations in the Pyrolysis Tests**

Pressures (atm)	Temperature Profile (K)
2.5	1573-2034.26 × L
6	1550-3224.29 × L
10	1450-3271.02 × L
15	1450-2959.50 × L

\* L (m) is the distance to the burner surface.



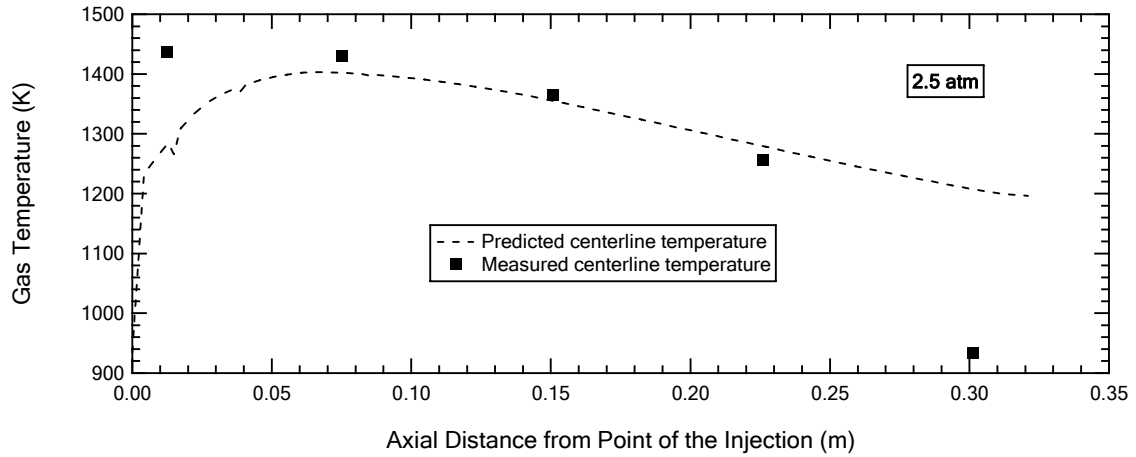


**Figure F.2.** Measured (symbols) and predicted (dashed line) centerline gas temperature profiles for the 2.5 atm HPFFB condition.

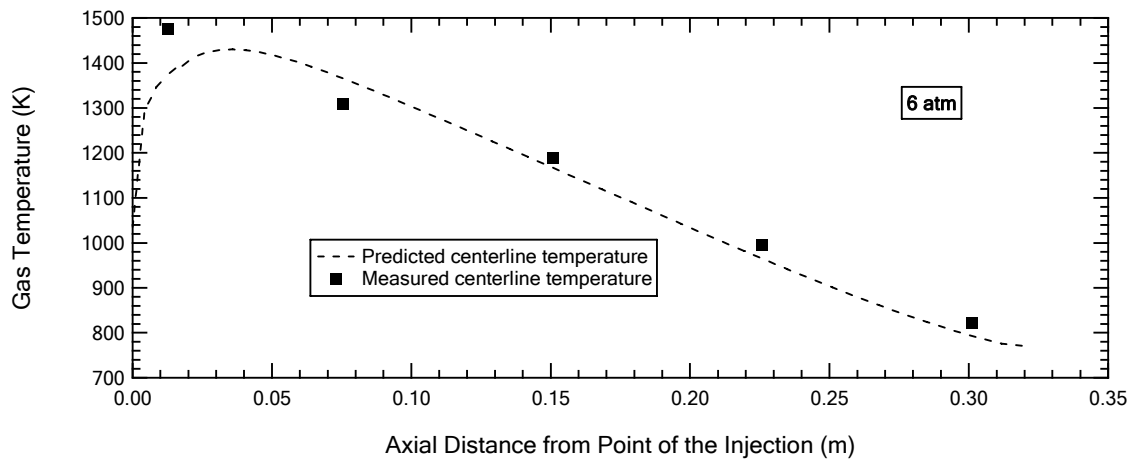


**Figure F.3.** Measured (symbols) and predicted (dashed line) centerline gas temperature profiles for the 6 atm HPFFB condition.

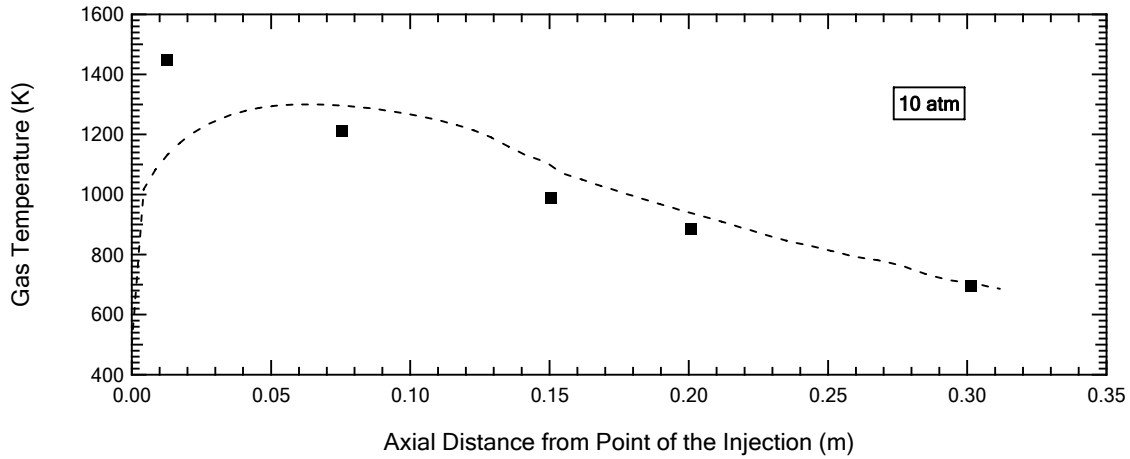


**Figure F.4.** Measured (symbols) and predicted (dashed line) centerline gas temperature profiles for the 10 atm HPFFB condition.

Fig F.5 shows the particle residence time vs. distance for pyrolysis condition.

Since the particle sizes of different coals are close, same profiles were used to calculate for all four coals.

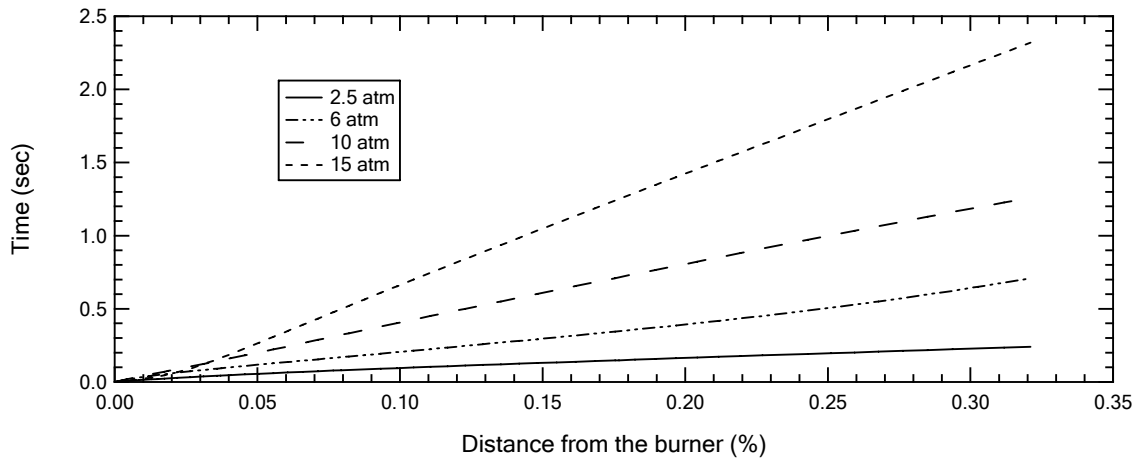


**Figure F.5.** Predicted Ill #6 particle residence time for the 2.5 atm, 6 atm, 10atm, and 15 atm HPFFB pyrolysis condition..

Figure F.6, 7, and 8 show the residence time of Ill #6 long distance, Pitt #8 large size, and Pitt #8 small size vs. the length from the burner respectively in the HPFFB combustion tests.

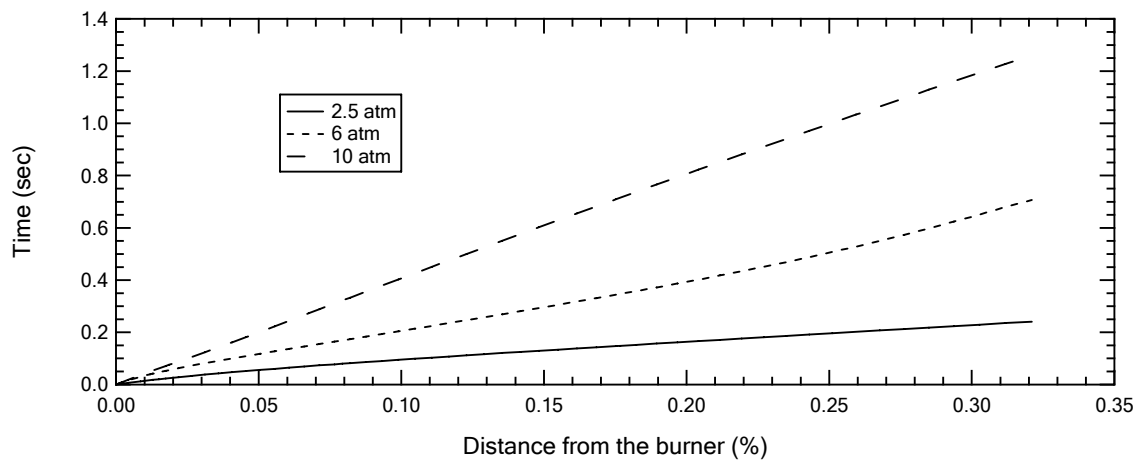


**Figure F.6.** Predicted III #6 particle residence time for the 2.5 atm, 6 atm, and 10 atm HPFFB combustion condition.

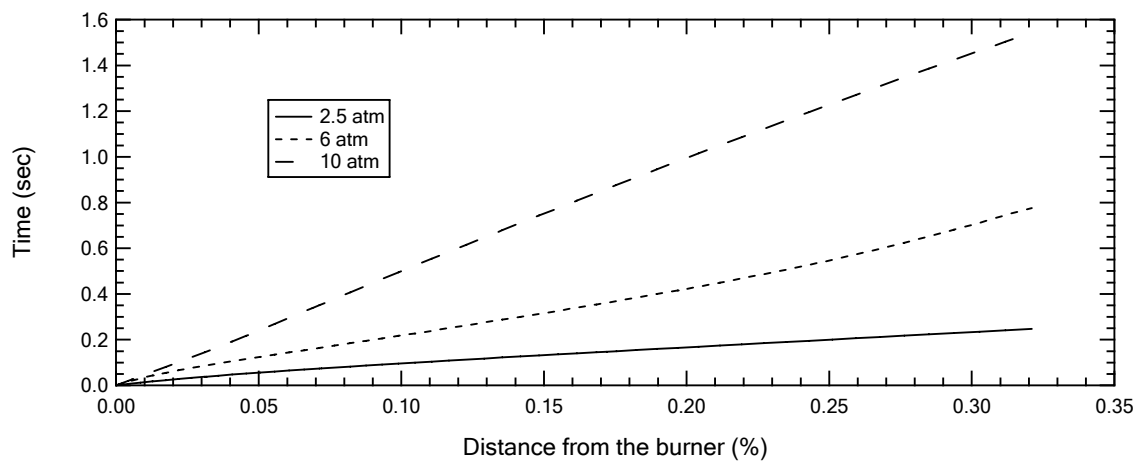


**Figure F.7.** Predicted Pitt #8 small size particle residence times for the 2.5 atm, 6 atm, and 10 atm HPFFB combustion condition.

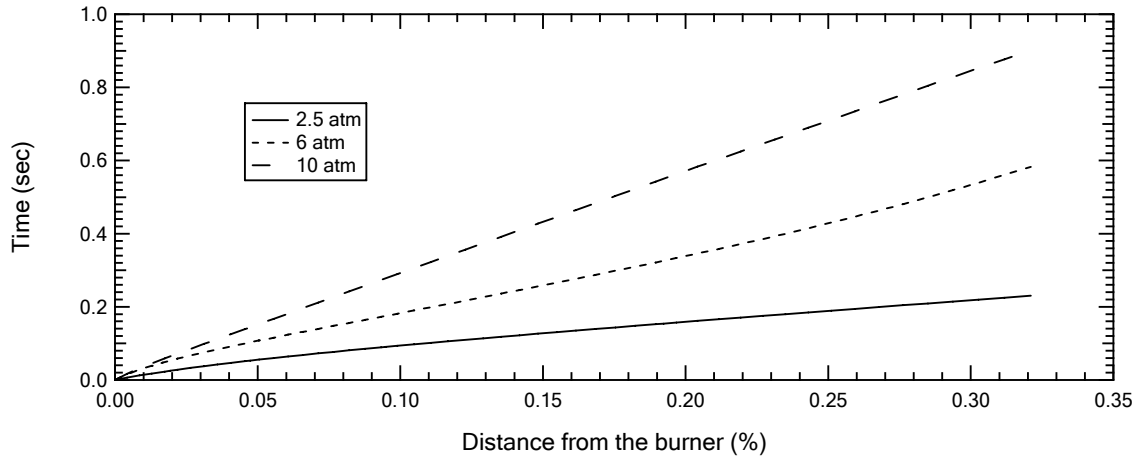


**Figure F.8.** Predicted Pitt #8 large size particle residence times for the 2.5 atm, 6 atm, and 10 atm HPFFB combustion condition.

## Appendix G: Detailed HPTGA Tests Results

This section contains 1) the rescaling process of data obtained from HPTGA measurements, 2) detailed plots that determined the activation energies and oxygen orders for the HPTGA test results of Chapter 6.2.3. Figures G.1-4 are plots for Pitt #8 char made from 2.5, 6, 10, and 15 atm respectively; and Figures G.5-6 are for Ill #6 char from 2.5 and 6 atm. The reaction conditions used in HPTGA tests are listed in Table G.1.

The HPTGA used in this study measured the change of weight as a function of time. It was necessary to rescale the weight to “true” weight. Before each HPTGA test, sample was dried, cooled down, and then weighed using a separate high-precision ( $10^{-3}$  mg) balance, here defined as  $m_{\text{true1}}$ . After the HPTGA test, the residue was retrieved, and also measured using the same balance, here defined as  $m_{\text{true2}}$ . To avoid the instability, the balance was left on during the tests. The weight measured by the HPTGA changed from a relative weight ( $m_{\text{HPTGA1}}$ ) to the residue weight ( $m_{\text{HPTGA2}}$ ). Then a ratio was calculated as:

$$Ratio = \frac{(m_{\text{true1}} - m_{\text{true2}})}{(m_{\text{HPTGA1}} - m_{\text{HPTGA2}})} \quad (\text{G.1})$$

If two consecutive measured are defined as  $m_n$  and  $m_{n+1}$ , and the corrected weight of  $m_{\text{HPTGA2}}$  is  $m_{\text{true2}}$ . The next point before this point is calculated using equation:

$$m_n = m_{n+1} + (m_n - m_{n+1}) \times \text{ratio} \quad (\text{G.2})$$

here  $n+1$  points to the last measured data. The remained values can be calculated by altering  $n$ . These calculations can rescale the measured to correct weights.

**Table G.1 Summary of Reaction Conditions used in HPTGA Tests**

Char	P <sub>Tot</sub> (atm)	Tests Series 1*	Tests Series 2**
Pitt #8 (2.5 atm)	1	P <sub>oxygen</sub> =0.2 atm T=420, 450, and 480 °C	T=420 °C P=0.2, 0.4, and 0.5 atm
Pitt #8 (6 atm)	6	P <sub>oxygen</sub> =0.5 atm T=420, 450, 465, and 485 °C	T=420 °C P=0.4, 0.5, and 0.8 atm
Pitt #8 (10 atm)	10	P <sub>oxygen</sub> =0.5 atm T=420, 450, and 480 °C	T=420 °C P=0.2, 0.4, and 0.8 atm
Pitt #8 (15 atm)	15	P <sub>oxygen</sub> =0.5 atm T=420, 450, and 480 °C	T=420 °C P=0.4, 0.5, and 0.8 atm
Ill #6 (2.5 atm)	1	P <sub>oxygen</sub> =0.2 atm T=405, 420, 435, and 450 °C	T=420 °C P=0.2, 0.25, 0.3, and 0.4 atm
Ill #6 (6 atm)	6	P <sub>oxygen</sub> =0.2 atm T=390, 398, 405, and 420 °C	T=420 °C P=0.194, 0.275, 0.357, and 0.433 atm

\* Test series 1, Constant O<sub>2</sub> partial pressure, varied temperature.

\*\* Test series 2, Constant temperature, varied O<sub>2</sub> partial pressure.

For Figures G.1-6, the left figures are  $\ln(-\text{rate})$  vs.  $1/T$ , the activation energy of respective char is  $\text{slope} \times (-R)$ . The right figures are  $\ln(-\text{rate})$  vs.  $\ln(P_{\text{oxygen}})$ , the slope of line is the oxygen order. Figures G.7-18 show the reactivity vs. burnout for four Pitt #8

chars and 2 Ill #6 chars. Figures G.19- 23 is the comparison of the reactivity vs. burnout curves of Pitt #8 char made at 2.5, 6, 10, and 15 atm.

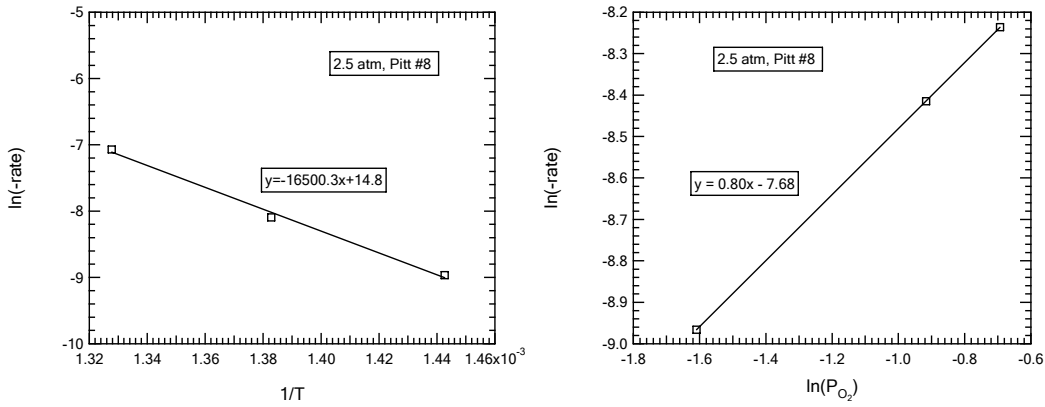


**Figure G.1.** The plots to calculate activation energy and oxygen order of Pitt #8 char (2.5 atm). Left: activation energy; right: oxygen order.

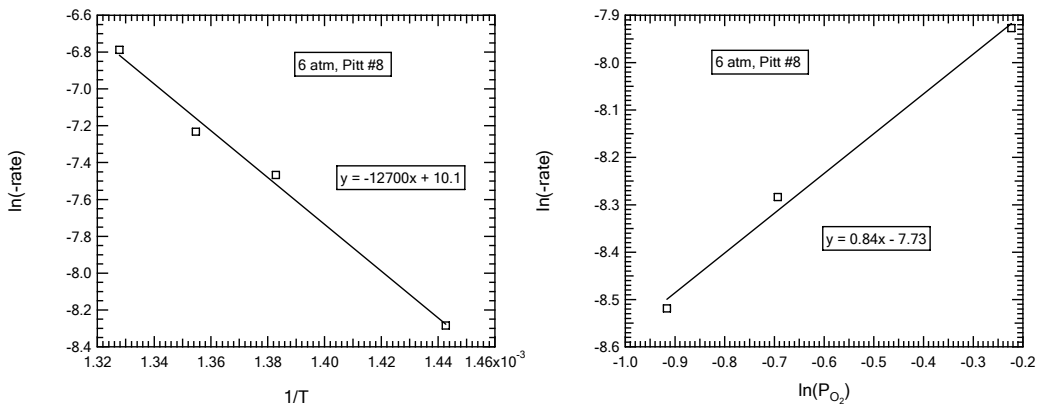


**Figure G.2.** The plots to calculate activation energy and oxygen order Pitt #8 char (6 atm). Left: activation energy; right: oxygen order.

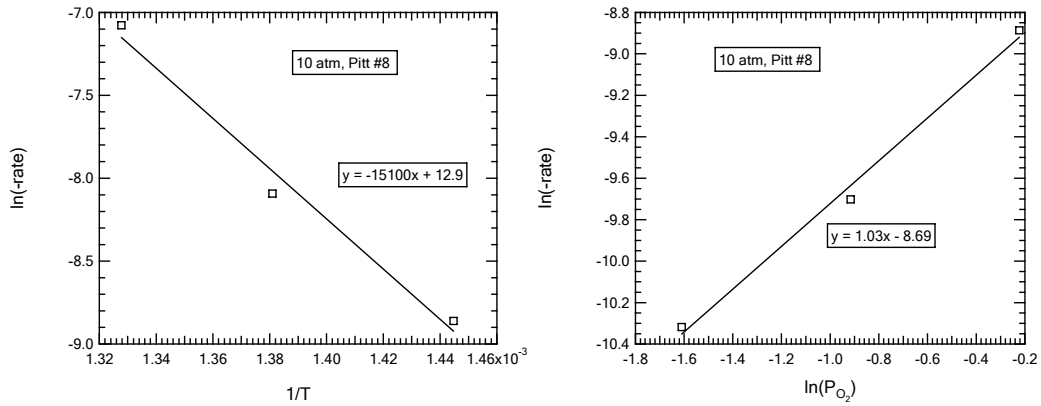


**Figure G.3.** The plots to calculate activation energy and oxygen order Pitt #8 char (10atm). Left: activation energy; right: oxygen order.

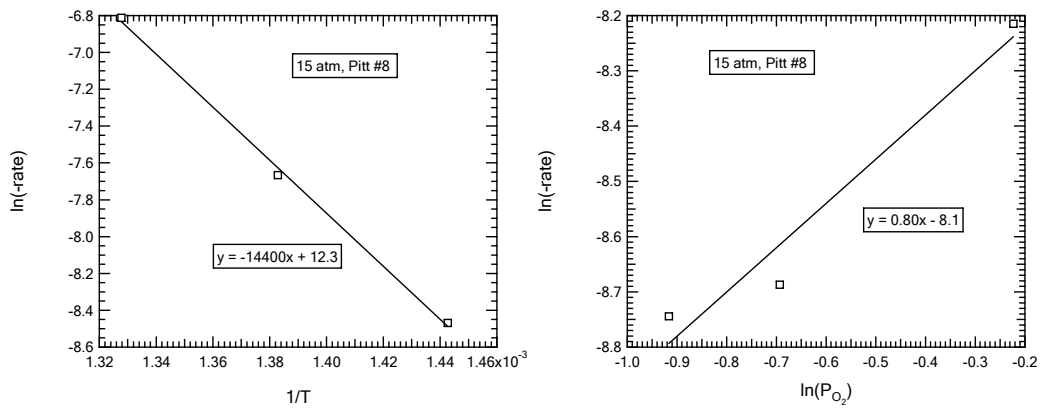


**Figure G.4.** The plots to calculate activation energy and oxygen order Pitt #8 char (15atm). Left: activation energy; right: oxygen order.



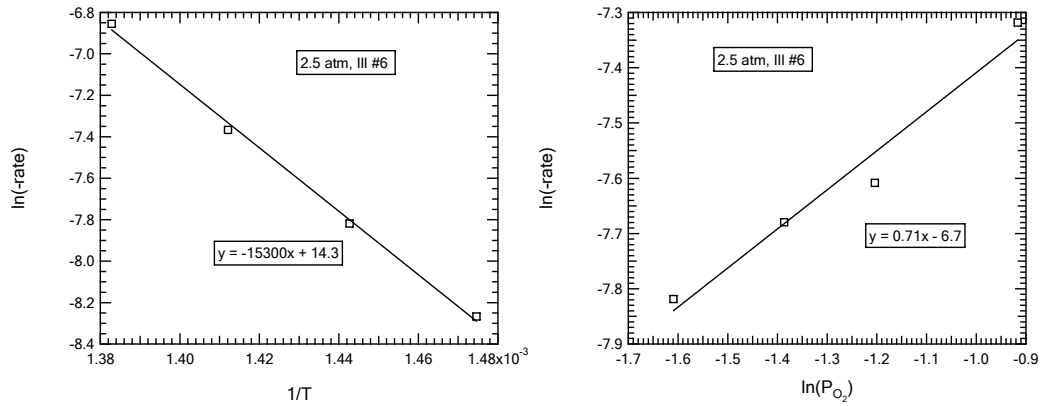


**Figure G.5.** The plots to calculate activation energy and oxygen order III #6 char (2.5atm). Left: activation energy; right: oxygen order.

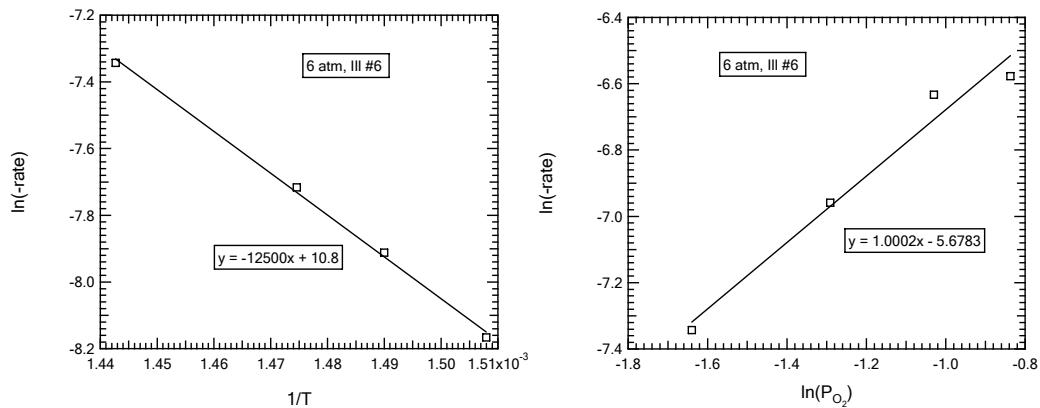


**Figure G.6.** The plots to calculate activation energy and oxygen order III #6 char (6atm). Left: activation energy; right: oxygen order.

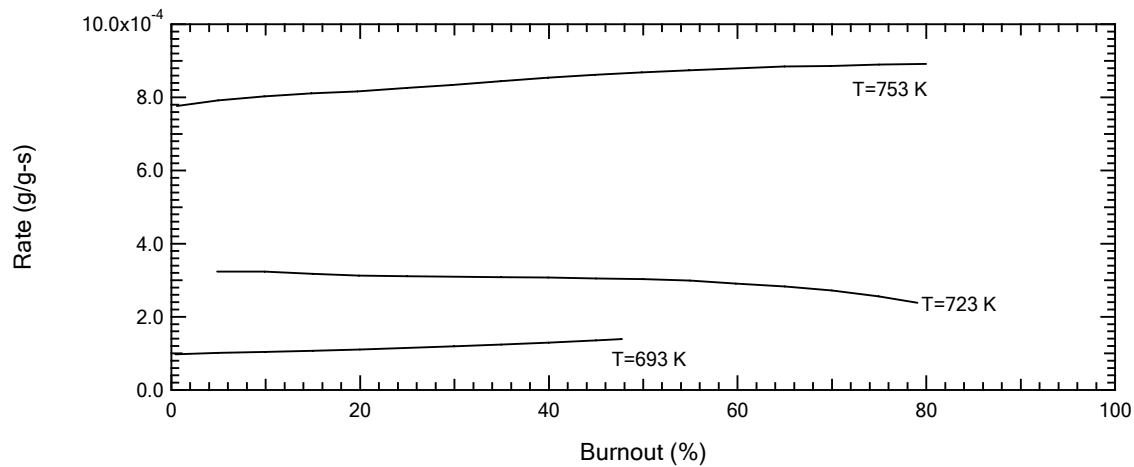


**Figure G.7.** Char HPTGA reactivity vs. Burnout  
 Char: Pitt #8 2.5 atm;  $P_{\text{tot}}=1$  atm,  $P_{\text{O}_2}=0.2$  atm.

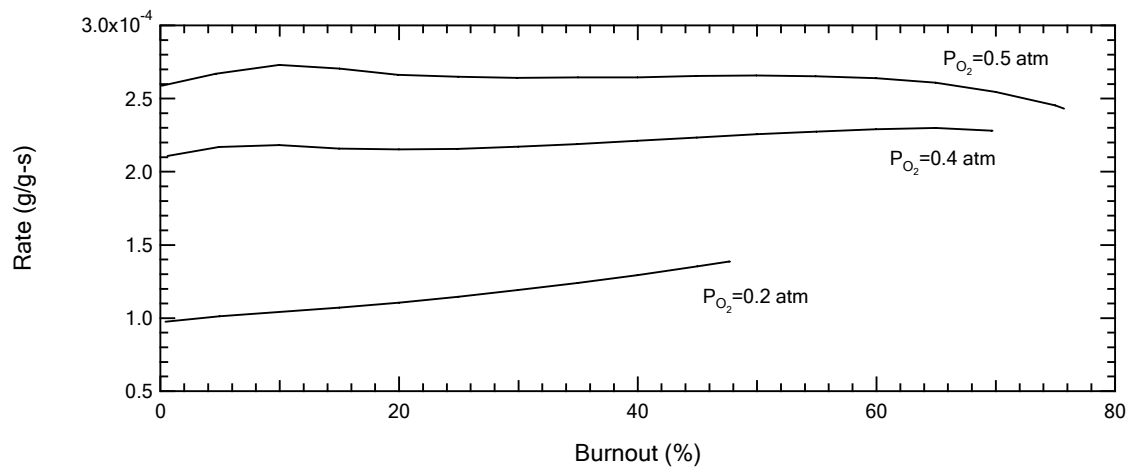


**Figure G.8.** Char HPTGA reactivity vs. Burnout  
 Char: Pitt #8 2.5 atm;  $T=693$  K;  $P_{\text{tot}}=1$  atm.

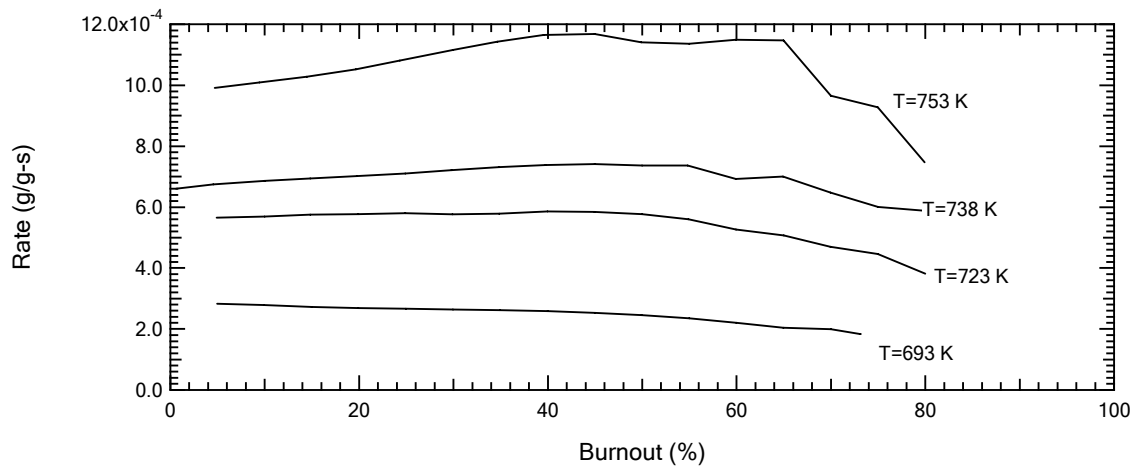


**Figure G.9.** Char HPTGA reactivity vs. Burnout  
 Char: Pitt #8 6 atm;  $P_{O_2}=0.5$  atm;  $P_{tot}=6$  atm.

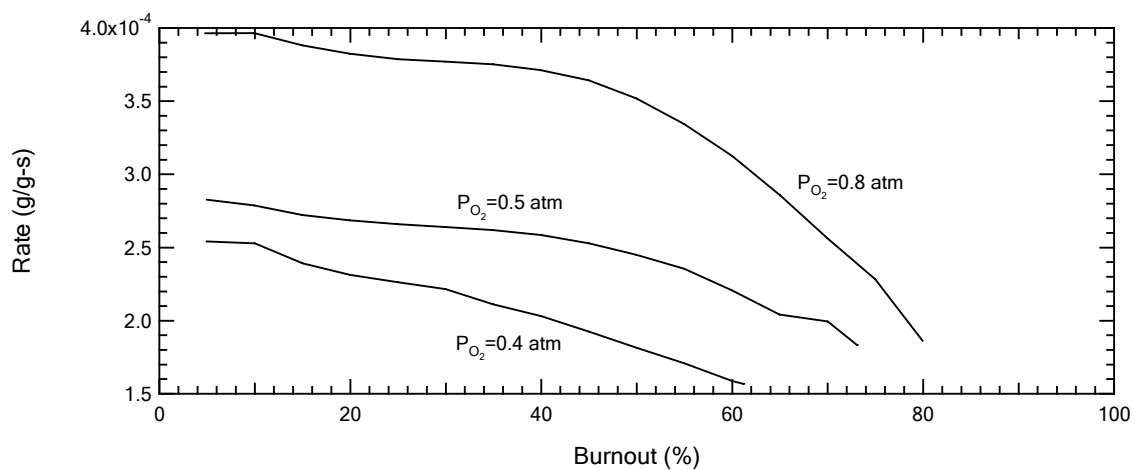


**Figure G.10.** Char HPTGA reactivity vs. Burnout  
 Char: Pitt #8 6 atm;  $T=693$  K;  $P_{tot}=6$  atm.

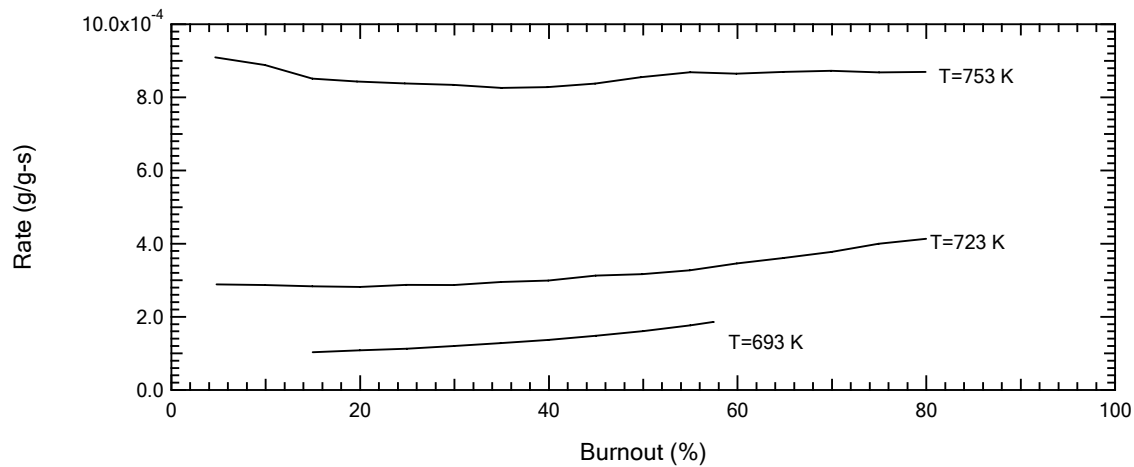


**Figure G.11.** Char HPTGA reactivity vs. Burnout  
Char: Pitt #8 10 atm;  $P_{O_2}=0.5$  atm;  $P_{tot}=10$  atm.

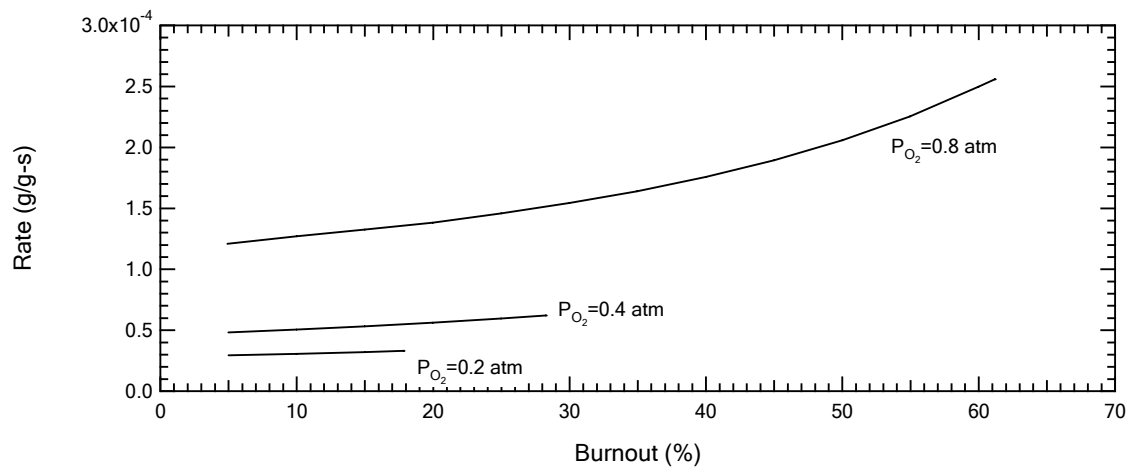


**Figure G.12.** Char HPTGA reactivity vs. Burnout  
Char: Pitt #8 10 atm;  $T=693$  K;  $P_{tot}=10$  atm.

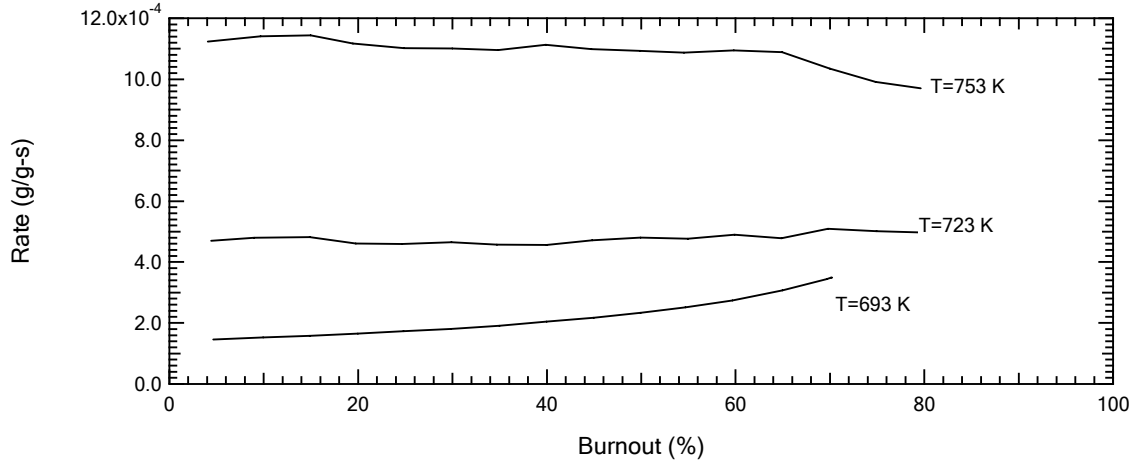


**Figure G.13.** Char HPTGA reactivity vs. Burnout  
Char: Pitt #8 15 atm;  $P_{O_2}=0.5$  atm;  $P_{tot}=15$  atm.

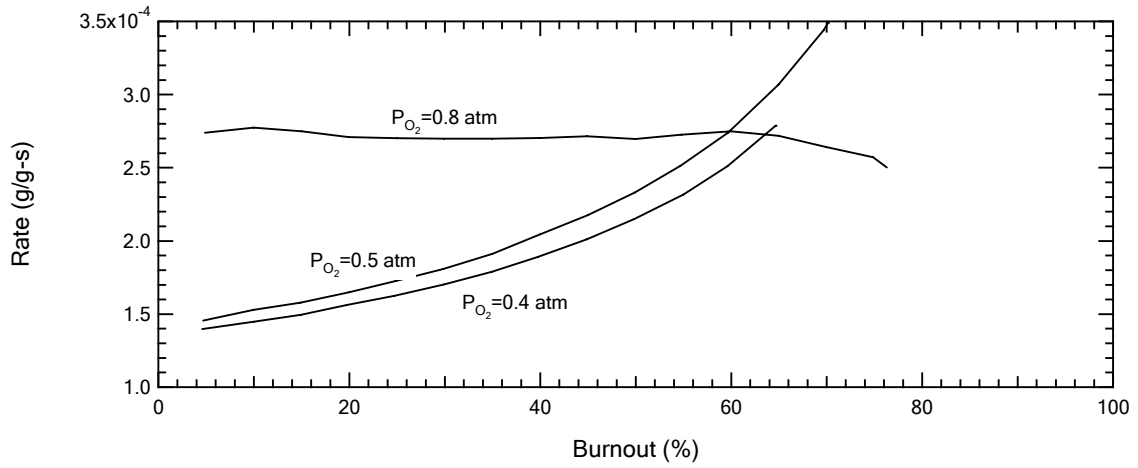


**Figure G.14.** Char HPTGA reactivity vs. Burnout  
Char: Pitt #8 15 atm; T=693 K;  $P_{tot}=15$  atm.

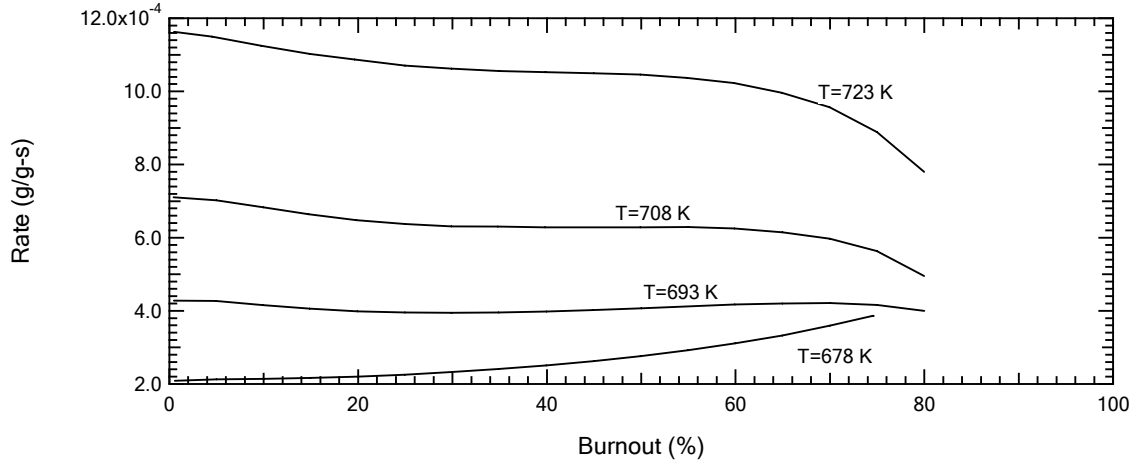


**Figure G.15.** Char HPTGA reactivity vs. Burnout  
 Char: Ill #6 2.5 atm;  $P_{O_2}=0.2$  atm;  $P_{tot}=1$  atm.

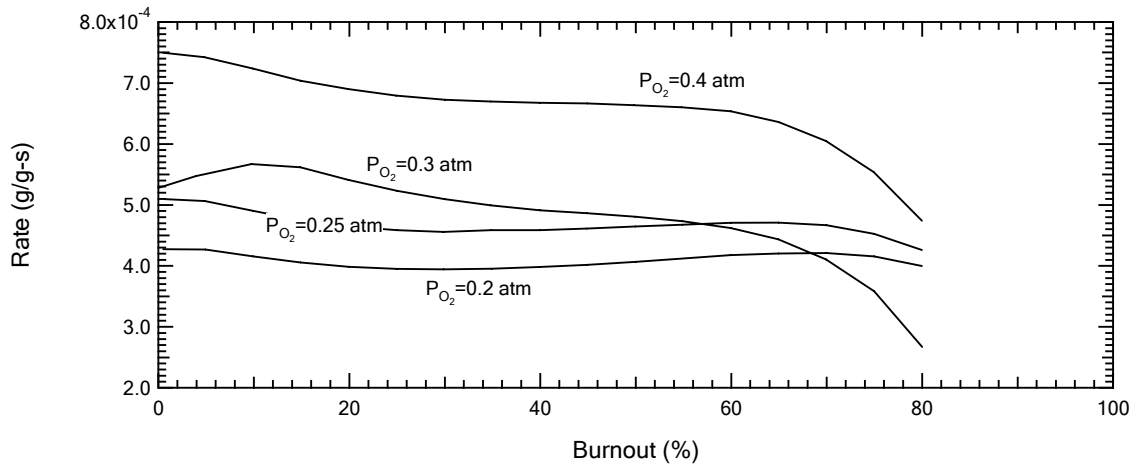


**Figure G.16.** Char HPTGA reactivity vs. Burnout  
 Char: Ill #6 2.5 atm;  $T=693$  K;  $P_{tot}=1$  atm.

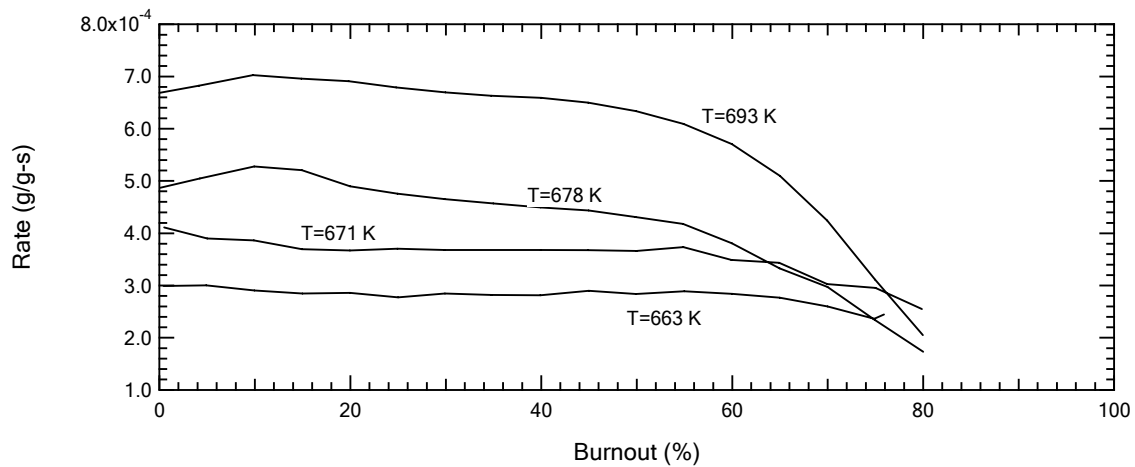


**Figure G.17.** Char HPTGA reactivity vs. Burnout  
 Char: Ill #6 6 atm;  $P_{O_2}=0.2$  atm;  $P_{tot}=6$  atm.

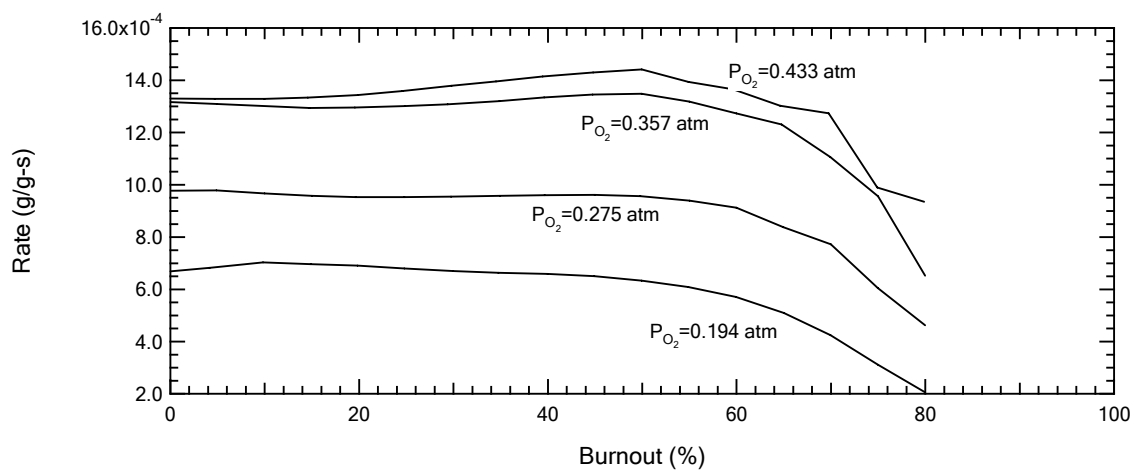


**Figure G.18.** Char HPTGA reactivity vs. Burnout  
 Char: Ill #6 6 atm;  $T=693$  K;  $P_{tot}=6$  atm.

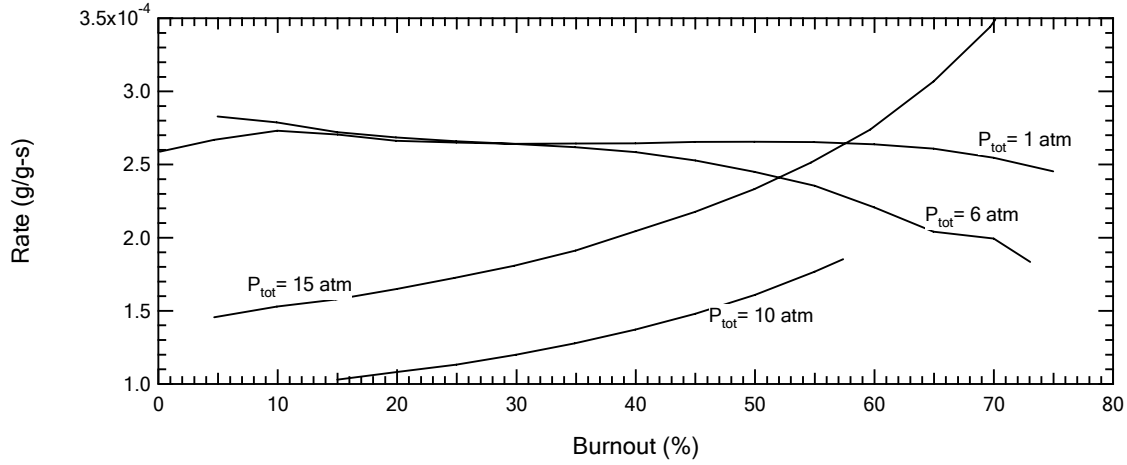


**Figure G.19.** Char HPTGA reactivity vs. Burnout  
 Char: Pitt #8 2.5, 6, 10, and 15 atm; T=693 K; P<sub>O2</sub>=0.5 atm.

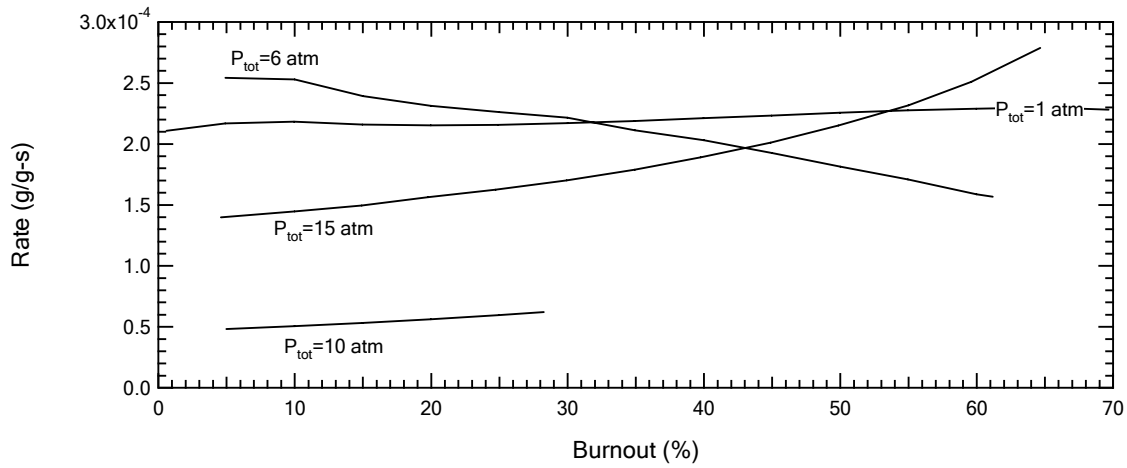


**Figure G.20.** Char HPTGA reactivity vs. Burnout  
 Char: Pitt #8 2.5, 6, 10, and 15 atm; T=693 K; P<sub>O2</sub>=0.4 atm.



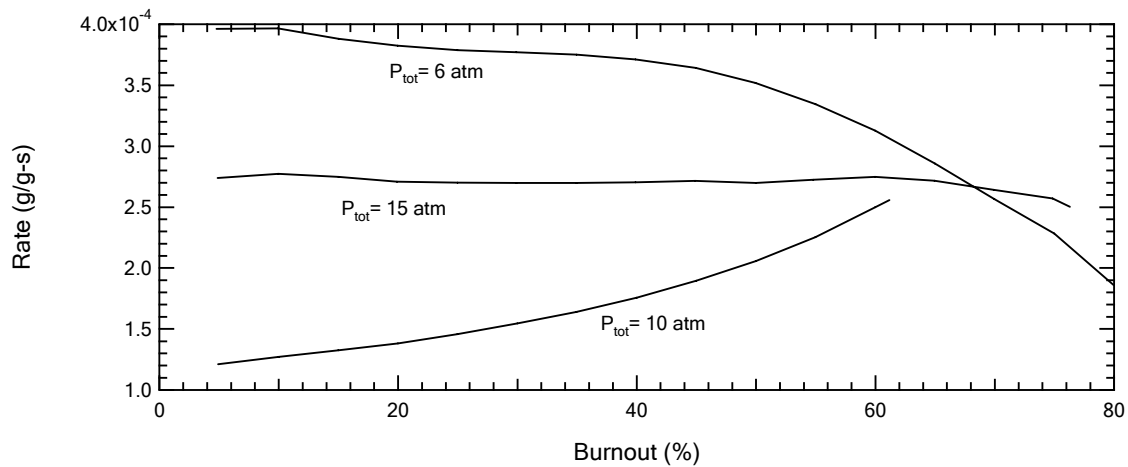


**Figure G.21.** Char HPTGA reactivity vs. Burnout  
 Char: Pitt #8 6, 10, and 15 atm; T=693 K; P<sub>O<sub>2</sub></sub>=0.8 atm.

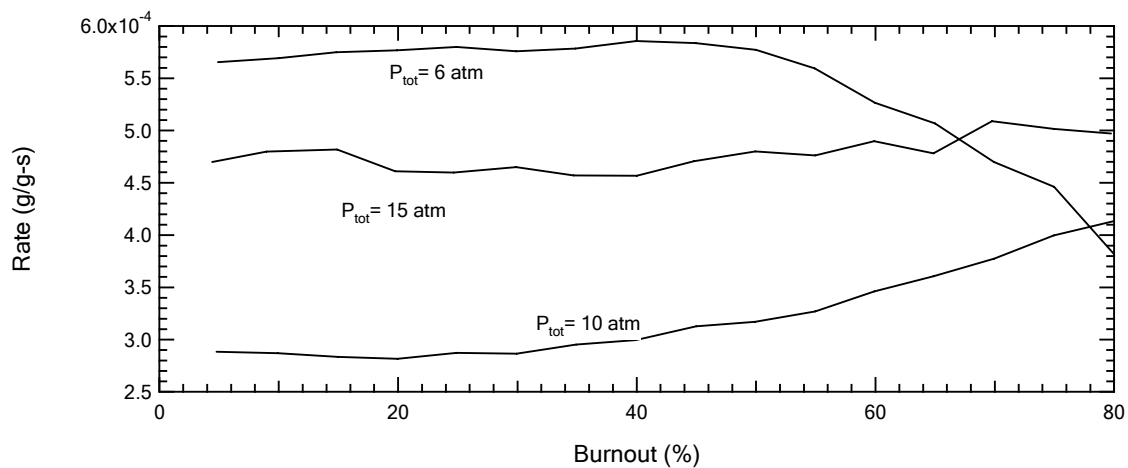


**Figure G.22.** Char HPTGA reactivity vs. Burnout  
 Char: Pitt #8 6, 10, and 15 atm; T=723 K; P<sub>O<sub>2</sub></sub>=0.5 atm.

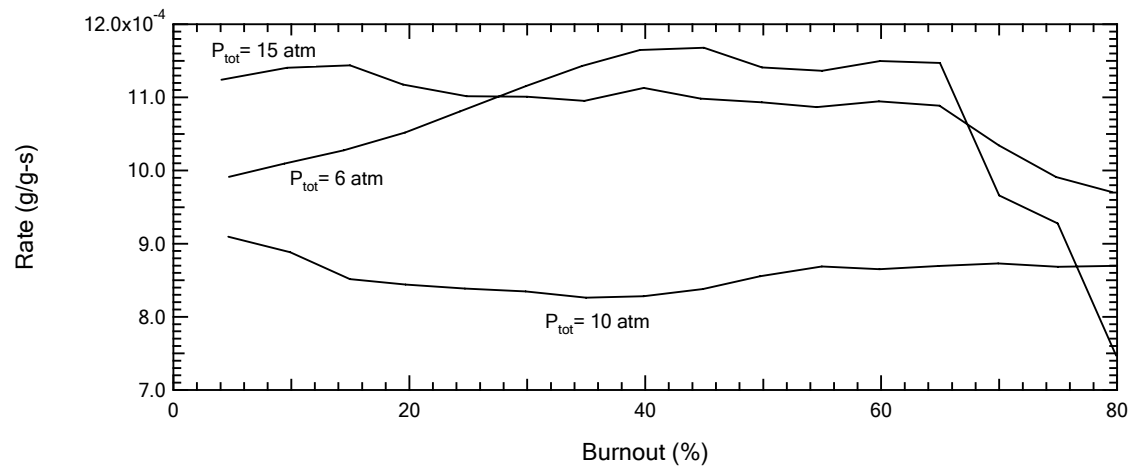


**Figure G.23.** Char HPTGA reactivity vs. Burnout  
 Char: Pitt #8 6, 10, and 15 atm; T=753 K; P<sub>O<sub>2</sub></sub>=0.5 atm.

## Appendix H: Additional HPTGA Tests Results

This section documents results of HPTGA tests performed on the Pitt #8 char sample collected in this study. The HPTGA tests were performed by Ben Christensen, and supervised by William C. Hecker. Figures H. 1-6 show the data acquired. The reaction conditions of each test are show in the title of each figure. Figures H.7 and H.8 shown the Arrhenius plots for calculating activation energy using the average rate from 20-40% burnout.

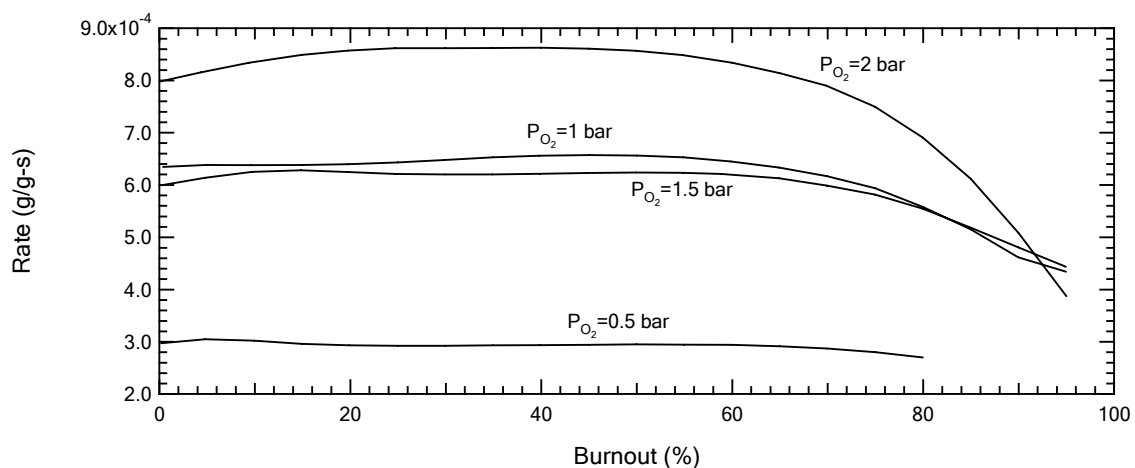


**Figure H.1.** Char HPTGA reactivity vs. Burnout and P<sub>O<sub>2</sub></sub>  
Char: Pitt #8 2.5 atm; T=700 K; P<sub>tot</sub>=2.5 bar.

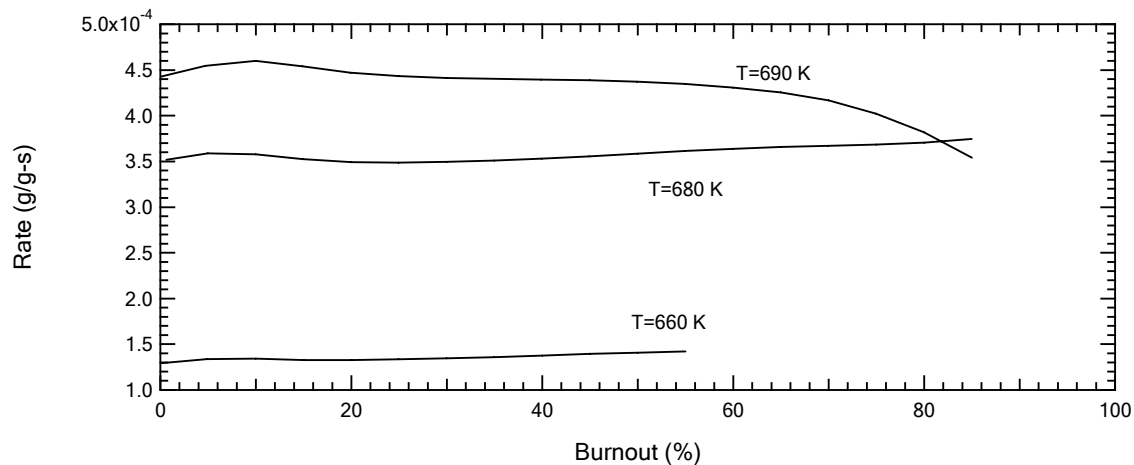


**Figure H.2.** Char HPTGA reactivity vs. Burnout and T  
 Char: Pitt #8 2.5 atm;  $P_{\text{tot}}=2.5$  bar;  $P_{\text{O}_2}=1$  bar.

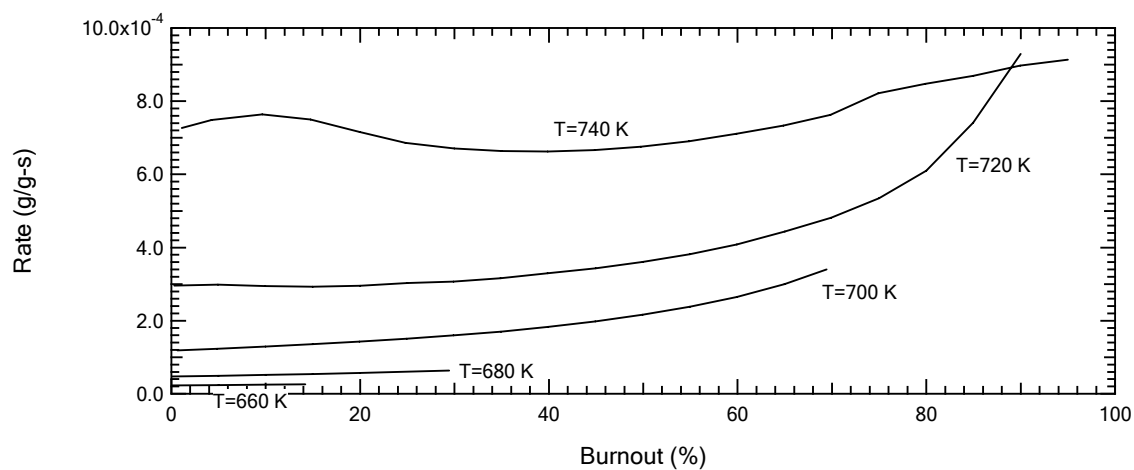


**Figure H.3.** Char HPTGA reactivity vs. Burnout and T  
 Char: Pitt #8 6 atm;  $P_{\text{tot}}=6$  bar;  $P_{\text{O}_2}=1$  bar.

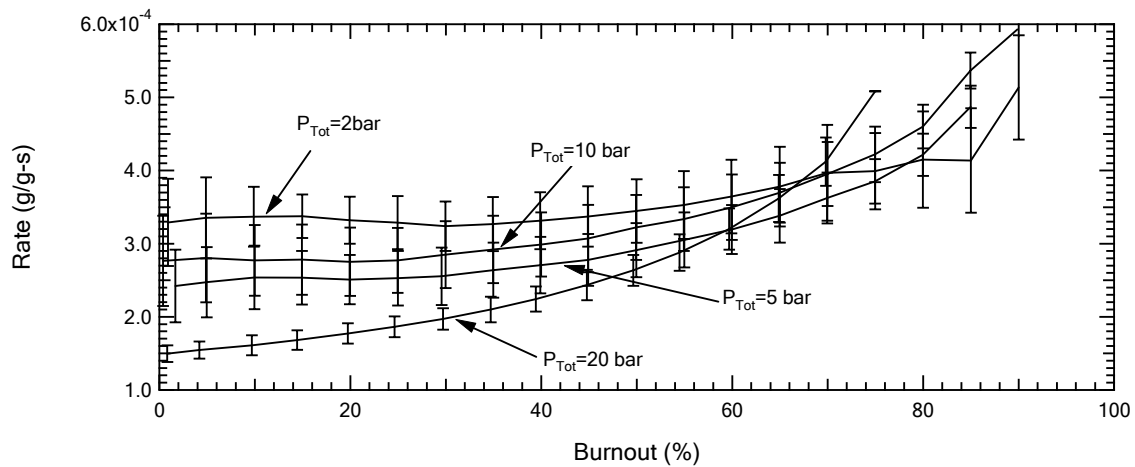


**Figure H.4.** Char HPTGA reactivity vs. Burnout and  $P_{tot}$   
 Char: Pitt #8 10 atm;  $T=700$  K;  $P_{O_2}=1$  bar.

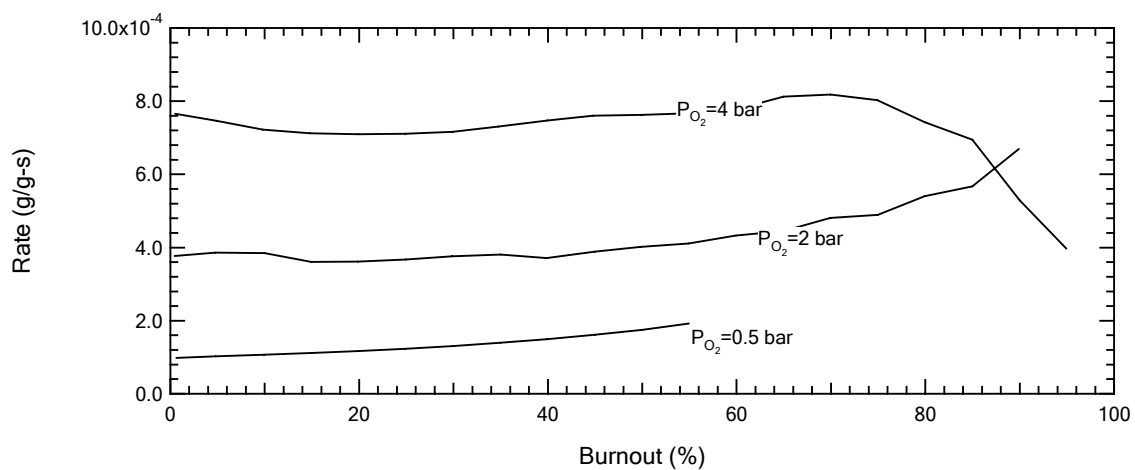


**Figure H.5.** Char HPTGA reactivity vs. Burnout and  $P_{O_2}$   
 Char: Pitt #8 10 atm;  $T=700$  K;  $P_{tot}=10$  bar.

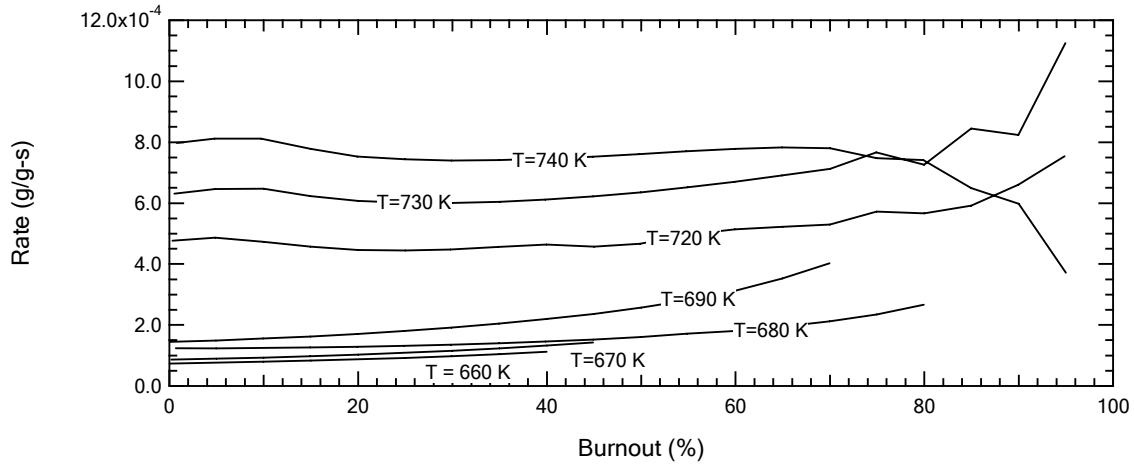


**Figure H.6.** Char HPTGA reactivity vs. Burnout and T  
 Char: Pitt #8 10 atm;  $P_{\text{tot}}=10$  bar;  $P_{\text{O}_2}=1$  bar.

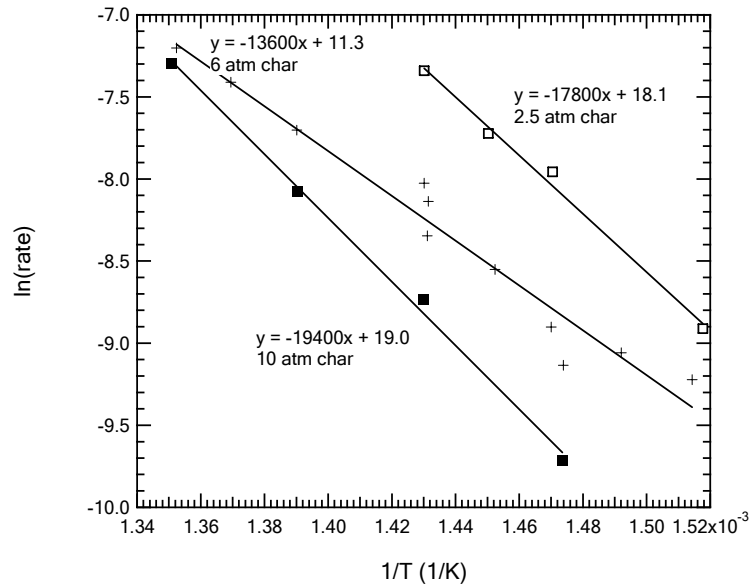


**Figure H.7.** Arrhenius plot for calculating activation energy, 20-40% Burnout

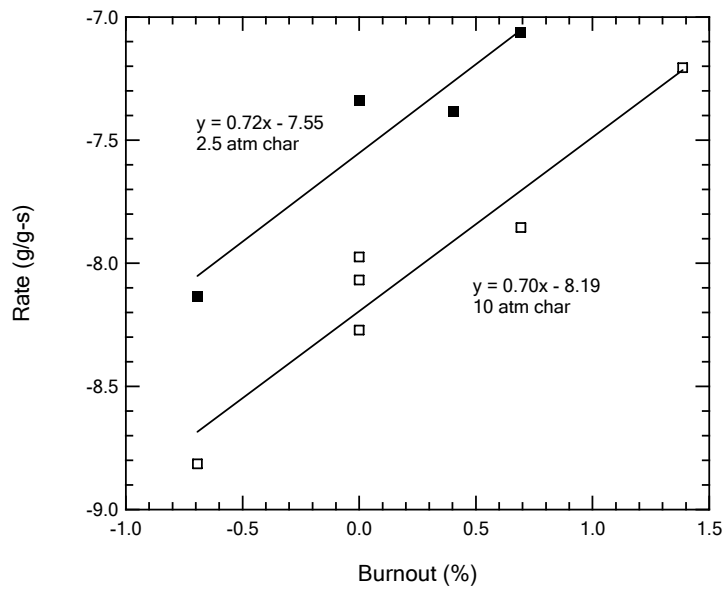


**Figure H.8.** Arhenius plot for calculating oxygen reaction order, 20-40% Burnout





## Appendix I: Sample CPD Model Input Files

A sample input file for the CPD version cpdcp (which calculates particle temperatures given gas velocity and temperature as a function of distance) with the free radical mechanism nitrogen model implemented is shown below. The model is given on the accompanying CD.

```
0.5          !p0          III #6
.0           !c0
5.2          !sig+1
381.4        !mw
40.5         !mdel (7 will be subtracted internally to the CPD model)

2.602e15     !ab
55400        !eb
1800         !ebsig
0.9          !ac=rho
0            !ec
3.e15        !ag
69000        !eg
8100         !egsig
3.e15        !Acr (pre-exponential factor for crosslinking rate)
65000        !Ecr (Activation energy for crosslinking rate)

2.5          !pressure (atm)
```

20	!number of time points
0, 500	!time(ms),temp(K)
2.35455,	509.135
3.17879,	528.189
5.01606,	545.279
6.46903,	562.371
8.17303,	577.826
10.1649,	605.013
15.927,	698.914
18.1587,	736.626
20.7916,	786.043
25.2759,	864.164
29.1419,	931.899
34.0617,	1008.62
40.1644,	1087.99
45.0307,	1144.49
49.043 ,	1185.18
55.0176,	1235.54
60.1314,	1271.61
65.1662,	1301.73
70.1549,	1327.21

## Appendix J: Sample CBK Model Input Files

A sample input file for the CBK version 8 (which calculates particle temperatures, particle mass at given gas temperature as a function of time) is shown below. The model is given on the accompanying CD.

```
84.58 ! coalC; percentage coal carbon content, daf
5.47 ! coalH; percentage coal hydrogen content, daf
10.72 ! coalASH; percentage coal ash content, dry basis
34.34 ! ASTM volatile matter (%daf), for estimation of flame VM
55.17 ! percentage high temperature volatile loss, daf (0 - 100).
0.92 ! linear swelling factor
50000. ! K2OBYK3O, ratio of step 2 to step 3 preex. factors. Units: (mol/cm3)-N
1E-6 ! K3OBYK1O, ratio of step 3 to step 1 preex. factors. Units: (mol/cm3)-1
32000. ! E3, intrinsic step 3 activation energy, cal/mol 133.8KJ/mol
28000. ! E2, intrinsic step 2 activation energy, cal/mol 117 KJ/mol
6000. ! E1, intrinsic step 1 activation energy, cal/mol 25KJ/mol
-1 ! initial fuel density, daf g/cc
1 ! number of particle size bins
107.5 1.0 ! diameter and mass fraction (0-1) in diameter bins, um
200. ! Ac
9000. ! Ec
1.0 ! zn, intrinsic reaction order for step 2
0.2 ! alpha, mode of burning parameter
12. ! TaubyF, parameter in effective diffusivity expression
0.17 ! TPorfilm, porosity of THICK ash film (and final ash particle)
5.0 ! ash grain size (um)
0.005 ! thermal conductivity of ash, cal/cm-s-C
1 ! Itraj, a switch, 1 prints single particle trajectories, 0 not
2.5 ! total pressure, atm
```

```

0.01  ! time step, sec
18    ! Intstep, number of time steps
1423  ! initial particle temperature, K
1423  0.0575 500 ! Tg(K) Pox (atm) Tenv (K) (Environmental variables)
1408  0.0575 500
1391  0.0575 500
1372  0.0575 500
1351  0.0575 500
1329  0.0575 500
1305  0.0575 500
1281  0.0575 500
1255  0.0575 500
1230  0.0575 500
1205  0.0575 500
1180  0.0575 500
1156  0.0575 500
1134  0.0575 500
1115  0.0575 500
1100  0.0575 500
1089  0.0575 500
1084  0.0575 500

```

A sample input file for the CBK version E (which calculates particle temperatures, particle mass at given gas temperature as a function of time) is shown below. The model is given on the accompanying CD.

```

84.58 ! coalC; percentage coal carbon content, daf
5.47  ! coalH; percentage coal hydrogen content, daf
10.72 ! coalASH; percentage coal ash content, dry basis
34.34 ! ASTM volatile matter (%daf), for estimation of flame VM
55.17 ! percentage high temperature volatile loss, daf (0 - 100).
0.92  ! linear swelling factor
50000. ! K2OBYK3O, ratio of step 2 to step 3 preex. factors. Units: (mol/cm3)-N
1E-6   ! K3OBYK1O, ratio of step 3 to step 1 preex. factors. Units: (mol/cm3)-1
32000. ! E3, intrinsic step 3 activation energy, cal/mol 133.8KJ/mol
28000. ! E2, intrinsic step 2 activation energy, cal/mol 117 KJ/mol
6000.  ! E1, intrinsic step 1 activation energy, cal/mol 25KJ/mol
-1     ! initial fuel density, daf g/cc
1      ! number of particle size bins
107.5  1.0 ! diameter and mass fraction (0-1) in diameter bins, um
200.   ! Ac
9000.  ! Ec

```

1.0 ! zn, intrinsic reaction order for step 2  
0.2 ! alpha, mode of burning parameter  
12. ! TaubyF, parameter in effective diffusivity expression  
0.17 ! TPorfilm, porosity of THICK ash film (and final ash particle)  
5.0 ! ash grain size (um)  
0.005 ! thermal conductivity of ash, cal/cm-s-C  
1 ! Itraj, a switch, 1 prints single particle trajectories, 0 not  
2.5 ! total pressure, atm  
0.01 ! time step, sec  
18 ! Intstep, number of time steps  
1423 ! initial particle temperature, K  
1423 0.0575 500 ! Tg(K) Pox (atm) Tenv (K) (Environmental variables)  
1408 0.0575 500  
1391 0.0575 500  
1372 0.0575 500  
1351 0.0575 500  
1329 0.0575 500  
1305 0.0575 500  
1281 0.0575 500  
1255 0.0575 500  
1230 0.0575 500  
1205 0.0575 500  
1180 0.0575 500  
1156 0.0575 500  
1134 0.0575 500  
1115 0.0575 500  
1100 0.0575 500  
1089 0.0575 500  
1084 0.0575 500